PRODUCTION AND NATURE OF HIGHLY LUMINESCENT SPARK-PROCESSED POROUS OXIDES OF SILICON AND OTHER ELEMENTS

By

MICHAEL EMERY STORA

A DISSERTATION PRESENTED TO THE GRADUATE SCHOOL
OF THE UNIVERSITY OF FLORIDA IN PARTIAL FULFILLMENT
OF THE REQUIREMENTS FOR THE DEGREE OF
DOCTOR OF PHILOSOPHY

UNIVERSITY OF FLORIDA

2000

Copyright 2000

by

Michael Emery Stora

Dedicated to my parents, Michelle Monique and Emery Lester Stora

ACKNOWLEDGEMENTS

First and foremost, I would like to express my appreciation and heartfelt thanks to Dr. Hummel who has served as my research advisor, graduate advisor, supervisor, supervisory committee chairman, and mentor. His enthusiasm, support, interest, and humor have been invaluable to me. I also wish to thank Dr. Ludwig for his friendship, creativity, and technical contributions.

I thank Drs. Holloway and DeHoff for both serving on my supervisory committee and for their influence as professors. It was a pleasure to learn from both of them as their classes were among the most interesting and productive I have taken.

I graciously thank Drs. Sigmund and Srivastava for their service on my supervisory committee.

I am grateful to my current and former coworkers including Nigel Shepherd, William "Grif" Wise, Jeliazko Polihronov, David Burton, Damien "Cross" Reardon, Jon Hack, Dr. Sung-Sik Chang, and Dr. David Malone for both their technical contributions and valued friendship. I also wish to thank Dr. Philip Rack, Dr. Jonathan Gorrell, Jay Lewis, and Loren Reith, for their friendship and constant willingness to help.

Dr. Holloway's secretary, Ludie, deserves special recognition for being the de facto "secretary" for all of us graduate students.

I am grateful to the staff and graduate students of the University of Rochester's Center for Photo-Induced Charge Transfer, particularly Steve Atherton and Chris Collison, for the equipment-time and training they so graciously provided,

Dr. Robert Walko at Sandia National Laboratories and Dr. Sey-Shing Sun at Planar Systems for their help with constructing electroluminescent devices, and Dr. Regina Müller-Mach at Agilent Technology for help with photoluminescence excitation measurements. I also wish to thank Drs. Gerd Müller and B. C. Blasse for their interest and helpful advice and Dr. Herbert Ruefer at Wacker-Chemitronic for supplying the large quantities of silicon wafers used in this study.

My thanks go to all my friends in the UF Kodenkan Jiu-Jitsu Club and UF Judo Club who are too numerous to list. I owe a great deal to Professors Alex Limbaugh, Donald Cox, and Bill Beach, and Senseis Margaret Limbaugh, Kevin Book (deceased), and John Nelson whose lessons of hard work, discipline, and dedication were as important as any academic lesson.

Thanks to my college roommates and long-time friends Dr. Dmitry Golovko and "soon-to-be Dr." David Harrison for the friendship and encouragement they have given me over the years.

Last, but certainly not least, I wish to thank my parents, to whom this study is dedicated, and my fiancée Heather Rose for the undying love and support they have given me.

TABLE OF CONTENTS

page

ACKNOWLEDGEMENTS iv

ABSTRACT viii

CHAPTERS

1 INTRODUCTION 1

2 CONVENTIONS AND ORGANIZATION 5

Units of Measure 5
Definitions and Rules 10
Organization of Experimental Results 13

3 BACKGROUND AND LITERATURE REVIEW 14

Review of Spark-Processed Silicon Literature 14
Other Literature on Spark-Processing and Sparks in General 57
Review of Quantum Size-Effect Literature 61
Review of Defects in Silica and Silicon Oxynitrides 71
Review of an Important Transient Defect in Silica 75
General Review of Luminescence Processes 93

4 MATERIALS, METHODS, AND EQUIPMENT 107

5 RESULTS: PROCESSING PARAMETERS OF SPARK-PROCESSED SILICON 119

Electrical, Temporal, and Physical Processing Parameters 119
Chemical Processing Parameters 180

6 RESULTS: MICROSCOPY AND CHEMICAL SPECTROSCOPIES OF SPARK-PROCESSED SILICON 209

Scanning Electron Microscopy (SEM) 209
Fourier Transform Infrared Spectroscopy (FTIR) 215
Secondary-Ion Mass Spectroscopy (SIMS) 220

7 RESULTS: OTHER SPARK-PROCESSED ELEMENTS 235

Preliminary Exploration 235
Additional Work with Selected Elements 258
Chemical Processing Parameters 265

8 RESULTS: OTHER LUMINESCENT SPECTROSCOPIES 300

Variable Excitation Power 300
High-Temperature Photoluminescent Spectroscopy 306
Photoluminescent Excitation Spectroscopy (PLE) 326
Time-Resolved Photoluminescent Spectroscopy (TRPL) 336

9 RESULTS: MISCELLANEOUS 367

Useful Results 367
Interesting Results 371
Uninteresting Results 372

10 FURTHER DISCUSSION 374

Final Word on Quantum Dots 374
Integrating Results from Multiple Chapters 376

11 SUMMARY AND CONCLUSIONS 389

12 FUTURE WORK 393

APPENDICES

A ELECTROLUMINESCENCE AND PHOTOCONDUCTIVITY 395

B CALIBRATION OF THE PL SYSTEM 402

C COMPUTER PROGRAMS 416

REFERENCES 429

BIOGRAPHICAL SKETCH 438

Abstract of Dissertation Presented to the Graduate School
of the University of Florida in Partial Fulfillment of the
Requirements for the Degree of Doctor of Philosophy

PRODUCTION AND NATURE OF HIGHLY LUMINESCENT SPARK-PROCESSED POROUS OXIDES OF SILICON AND OTHER ELEMENTS

By

Michael Emery Stora

December, 2000

Chairman: Professor Rolf E. Hummel
Major Department: Materials Science and Engineering

Spark-processed silicon (sp-Si) is a novel nano-porous material with unique optical and magnetic properties. Sp-Si exhibits two broad, intense, room-temperature photoluminescence (PL) bands, which are located near 370 nm and 530 nm when excited by 325 nm UV light. These are known as the UV/blue band and the green band, respectively. In addition, a number of other elements have been show to exhibit significant PL when spark-processed.

Several PL spectroscopic methods were used to characterize sp-Si and other spark-processed materials. These included continuous-wave PL (CWPL), time-resolved PL (TRPL), PL excitation spectroscopy (PLE), and temperature-dependent PL measurements. In addition scanning electron microscopy (SEM), Fourier transform infrared spectroscopy (FTIR), and secondary-ion mass spectroscopy (SIMS) were utilized.

The influences of the chemical, physical, electrical, and temporal processing parameters on the PL of sp-Si and other spark-processed elements were extensively explored and characterized. Both PL bands of sp-Si as well as similar bands in sp-Ge, sp-Al, and sp-Ta were found to be strongly dependent on the presence of nitrogen in the processing ambient. The PL of sp-Si and several other spark-processed materials was found to exhibit extremely fast sub-10 ps lifetimes. Longer-lived components attributed to trapping and evidence of competition between the two PL bands of sp-Si indicate charge transfer between separate absorption and emission mechanisms.

A model for the PL mechanisms of sp-Si is proposed. This model explains the observed properties of both PL bands of sp-Si and may be extended to other spark-processed materials. Absorption of UV light is attributed to a stable version of a normally metastable defect found in silica, and many other materials, known as the self-trapped exciton (STE). The rapid melting and solidification during spark-processing is believed to "quench-in" this defect. PL emission is the result of charge transfer of carriers from STEs to nitrogen-related deep defect states within the silica band-gap. The UV/blue band is attributed to defects containing nitrogen and the green band is attributed to more complicated defects containing two or more nitrogen atoms, similar in nature to the N-N nearest-neighbor center in GaP.

CHAPTER 1
INTRODUCTION

Silicon has dominated the semiconductor industry for more than half and century. While other materials are often used for high power switching and rectification, the role of silicon in the microelectronics industry is of paramount importance. The vast majority of integrated circuit technology is based on silicon [Pea88]. Silicon is economical (costing about a tenth as much as gallium arsenide, its nearest competitor) and easy to manufacture. The technology to dope silicon with a number of donor and acceptor elements is mature and well behaved. The most significant advantage of silicon is that it has a stable, adherent, and easily grown oxide that is epitaxial and self-passivating (especially for the (100) crystal orientation) [May90]. This oxide may be selectively patterned and etched by hydroflouric (HF) acid, which crystalline silicon resists. Finally, silicon is non-toxic and silicon production and processing has a minimal impact on the environment. This is not true of gallium arsenide. These technical advantages, combined with the maturity of, and investment in, silicon-based technology make it likely that silicon will remain the dominant semiconductor material for the foreseeable future.

Despite its advantages, silicon has major limitations. It is both a low band-gap and indirect band-gap material. It is limited to very inefficient optical emission in the near-infrared (IR) region of the electromagnetic spectrum. It is poorly suited to both electro-optical communication and display technology. For these reasons, gallium arsenide and other III-V (or II-VI) semiconductors and their alloys are typically used in applications where light emission is necessary, while other non-semiconductor technologies dominate the display market. Photonics (the integration of photo-optics and electronics) promises to help overcome basic speed and bandwidth limitations of electronic communications, not only over long distances, as common today, but on the inter-chip and intra-chip levels as well. This will only become economically and technically feasible when a phosphor materials technology is developed that is completely compatible with silicon-based microelectronics. For these reasons, the development of silicon-based phosphors has generated much excitement for a number of years.

In order to be successful, such a material must have a higher effective band-gap and a much higher radiative efficiency than silicon. The second issue can be addressed by doping silicon with isoelectronic centers or activators, but this actually decreases the energy of emission. For a time in the nineties, it appeared that porous silicon (PS), offered the solution to both issues. PS was discovered by Uhlir [Uhl56] and its efficient room temperature photoluminescence (PL) was reported by Canham [Can90]. While the mechanisms for the luminescence of PS are still controversial, practical photonic devices have never materialized and the excitement has largely diminished.

A new material, known as spark-processed silicon (sp-Si) was discovered by Hummel and Chang in 1992 [Hum92]. It is a highly luminescent porous oxide produced by an electrical discharge between an anode and a silicon cathode in air or a mixture of nitrogen and oxygen. While sp-Si and PS have some superficial similarities, they exhibit different emission wavelengths, emission time constants, stability under annealing and ultraviolet (UV) exposure, microstructure, and other important properties [Lud96a, Cha94]. Sp-Si and PS are very different materials with unique properties which likely result from unique mechanisms.

Despite its efficient PL, useful electroluminescence (EL) from sp-Si has proven elusive. While strong PL is no guarantee of useful EL (it is not even a prerequisite), a more detailed understanding of the nature and mechanisms of the PL of sp-Si may allow the design of more intelligent approaches to generate EL in sp-Si or a future material derived from sp-Si.

The author has undertaken this study to better understand the nature of sp-Si and its luminescent properties. This endeavor consists of two main thrusts: correlating the properties of sp-Si to the conditions under which it was produced and attempting to glean an understanding of the mechanisms responsible for the luminescence of sp-Si. The former involves the development of new precision production techniques to accurately quantify and verify the previously reported properties of sp-Si as well as to conduct new experiments by taking advantage of the new degrees of freedom offered by these techniques. The latter involves attempting to identify the species and mechanisms responsible for the PL of sp-Si by conducting various experiments to find evidence that may suggest, support, or exclude proposed models.

In an attempt to further understand the properties of sp-Si, the author conducted spark-processing on a number of other elements besides silicon. It was discovered that strong, stable, room temperature PL is not unique to silicon. In fact, every elemental semiconductor and semi-metal (with the exception of selenium, which is too flammable to spark-process), as well as a number of metals, exhibit PL after spark-processing. In addition, the PL of several of these spark-processed materials was found to be dependent on the presence of nitrogen in the processing ambient, indicating that a common mechanism may be involved. Thus, spark-processing of materials other than silicon evolved from a limited exploration to become an integral part of this study.

The two goals of this endeavor have been met. The processing parameters of sp-Si and their influence on its properties have been extensively explored. Not only are the absorption and emission mechanisms of sp-Si well characterized, but the author is also able to present a comprehensive theory for the luminescence of several spark-processed materials.

CHAPTER 2
CONVENTIONS AND ORGANIZATION

Units of Measure

Physical Units of Measure

The author uses units of measurement pragmatically. Preference is given to the International System of Units (SI), or "Metric System," when there is no obvious alternative. SI-derived units such as the cgs (centimeter-grams-seconds) System are used when these are more appropriate to the scale of the measurement than SI units. As all the experiments reported in this study were performed in the United States, the American version of the Imperial, or "English" system of units cannot be ignored. In most cases, equipment and supplies were manufactured to US specifications. It is difficult for the reader to have such measurements arbitrarily converted to SI units only for the sake of conformity, as some authors do. Because SI and SI-derived units are the standard for scientific literature, whenever an Imperial unit is used, a Metric equivalent will follow in parentheses. If this is a scientifically important measurement, significant digits will be stated and preserved in the conversion. If this is a nominal measurement, than the metric conversion will be nominal as well. An example of this is the size of semiconductor wafers, which are usually manufactured in even-inch diameters. For example: "the 4" (10 cm) silicon wafer was . . . " While the wafer may very well have been manufactured to very high tolerances (4.00", for example), 4" is a standard size and terminology used in industry. The metric conversion is equally nominal (10 cm, not 10.16 cm).

Units of pressure deserve some special consideration. Most American literature uses pounds per square inch (psi) for pressure above atmosphere and torr (mtorr, μtorr) for vacuum. The torr is a SI-derived unit defined as the pressure necessary to support a 1 mm column of mercury against gravity. However, torr is not a very common unit in international literature. It is also not particularly practical (there are 760 torr in an atmosphere (atm)). The SI unit of pressure is the Pascal (Pa), but this is not particularly practical for vacuum, and not very common in the literature. This study will use a cgs unit, the bar (mbar, μbar) for vacuum as well as pressure above atmosphere, which is very common in international literature. The μbar is a dyne cm^{-2}. It is quite convenient and intuitive, as 1 bar is very close to 1 atmosphere (0.9869 atm--within about 1%) and 1 mbar is very close to 3/4 of a torr (0.7453 torr--within less than 1%). Atmosphere, or atm, in this study always refers to the SI standard atmosphere and not the technical atmosphere. The technical atmosphere is defined as one kilogram-force (the weight of one kilogram mass on earth) per square centimeter. It is essentially equal to the pressure exerted per 10 meter depth of fresh water. While it is a very convenient engineering unit, and deserves much more acceptance in the opinion of the author, it is relatively unknown and will not be used in order to avoid misunderstandings.

Unless otherwise stated, absolute vacuum serves as the common reference point for all pressure measurements in this study, both vacuum and above atmosphere. For example, 1.5 atmospheres means 0.5 atmospheres above atmospheric pressure.

Optical Units of Measure

Units of optical intensity are quite simple but are the cause of much confusion. The author uses the following rules.

If no units are given for an "intensity", the number represents uncorrected instrumental units (typically counts for a photomultiplier or charge-plate detector).

Quantum units represent the number of light quanta (photons) emitted at a particular wavelength per unit time. These differ from instrumental counts in that they take into account a wavelength-dependent correction for the sensitivity of the instrument.

Radiometric units are units of optical power (watts, for example) at a particular wavelength. These are related to quantum units by the wavelength dependence of the energy of a photon (the amount of energy carried by a photon is inversely proportional to its wavelength). This is rigorously defined as the radiant flux (intensity integrated over a sphere), but the author will use the term intensity as it is so often used in the literature. Many sources indicate that the use of watts for radiant flux is to be deprecated, but this has not stopped their almost universal use. The alternative is the clumsy ergs per second. There is often a reality gap between the people who propose standards and those who must use them.

Photopic units are obtained from radiometric units by taking into account the wavelength-dependent sensitivity of the vision of a "typical" (and gender-less) human being. The term photometric is more commonly encountered in the literature, but could refer to either the photopic vision of the retinal cones (which dominates at light levels above 1 millilambert (mL)), or the scotopic vision of the retinal rods (which dominates at low light levels and is more sensitive in the blue). The author prefers the term photopic to prevent this ambiguity. These units indicate the apparent brightness of a light source at a given wavelength. Photopic units are derived by multiplying radiometric units by a correction curve known as "The International Standard Eye", or more formally, The Relative Luminosity Function of the Commission Internationale de L'Eclairage (CIE) [Ber76, Sze81]. As the sensitivity of the eye varies with viewing angle, this curve was defined for light entering the eye in a 2° acceptance angle (other curves exist for larger angles). This curve peaks at 555 nm, which is close to the peak wavelength of sunlight, and resembles a slightly asymmetrical Lorentzian curve with a greater half-width in the long-wavelength direction, and a slight shoulder near 450 nm. It has finite values from 380 nm to 770 nm and is defined as zero outside of this range. The proper term for these units is luminous flux, which is measured in lumens (lm). It is neither an Imperial nor an SI unit, but was defined as the apparent brightness of 1/680th of a watt of light at 555 nm. Luminous flux density can be measured in footcandles (fc), lux (lx), or phot (ph) in the Imperial, SI, and cgs systems, respectively. Flux can also be measured per unit solid angle and per unit solid angle per unit area, with and without factors of π, giving rise to candelas (cd), stilbs (sb), nits (nt), footlamberts (fL), lamberts (L), and apostilbs (asb). There is no equivalent set of radiometric units for these as people just use "watts per . . ." If all this gets confusing, the reader should just keep in mind that these units were contrived from psychometric measurements made on small groups of volunteers in the early years of the 20th Century. There is really no underlying physical meaning behind these units for the reader to understand.

It is common to see statements in the literature referring to intensity (power or its photopic equivalent) at a particular wavelength. The author has essentially done the same thing in the proceeding paragraphs. This is rather sloppy, because, except in the case of a theoretically monochromatic light source, power is actually proportional to the area under the curve of the intensity vs. photon energy plot. This is usually referred to as the "integrated intensity" in the literature. In addition, most authors use the area under the curve of the intensity vs. wavelength plot, which is not really the same thing. Such imprecisions are common to every field of scientific study and are generally not problematic if the reader is cognizant of them.

When conducting photoluminescence (PL) measurements, it is generally not possible or even desirable to know exactly how the measured quantities correspond to true quantum or radiometric units as long as it is known that they are related by an unknown linear proportionality constant. This is often due to uncertainty over the spatial distribution of emitted light as well as arbitrary sensitivity adjustments made to the instruments (such as the adjustment of optical slits, detector alignment, and geometry). In such cases, the units of measure are referred to as arbitrary units. If intensity is measured at different wavelengths, it makes sense to refer to arbitrary quantum units or arbitrary radiometric units, etc. However, if intensity is measured at only one wavelength while some other parameter is varied, there is no difference between these wavelength-dependent arbitrary units (one arbitrary constant is as good as another). In such cases, only the term "arbitrary units" will be used.

As a final note on optical measurements, it should be pointed out that the peak location of an optical band may be reported in nanometers (nm) or electron-volts (eV). These are inversely proportional to each other with a proportionality constant of 1240 nm eV.

Definitions and Rules

Stages of Apparatus Development

In the experimental chapters of this study, the reader will encounter the terms Stage I, Stage II, and Stage III. These refer to the degree of sophistication of the equipment and instrumentation as it evolved during the course of the experimental work and will be defined in detail in Chapter 4. In summary: Stage I involved spark-processing with a Tesla coil, DC power supply, or pulsed high voltage supply from a video monitor. Stage II involved the use of a sophisticated controllable spark-current supply that was relatively insensitive to changes in experimental parameters. In addition, the spark current could be crudely measured. Stage III involved the ability to precisely measure and control the spark current to completely separate it from other processing variables. In addition, Stage III involved the implementation of means to prevent nonlinearities in the PL system resulting from chromatic aberrations and scattering/diffraction at small slit openings. This finally allowed good calibration curves to be made for the PL system which can be applied to Stage III measurements with great confidence and to Stage I/II measurements with a fair degree of confidence.

Rules for Figures

When multiple PL spectra or peak intensities are presented in one figure, it is to be assumed that these were measured at identical conditions or that the author has corrected for varying conditions so that the intensities may be compared with meaning. When PL spectra are in different figures, it should be assumed that their intensities are not directly comparable unless otherwise stated. The term "normalized", when applied to a PL spectrum or other data, means that the largest value of the dependant variable was set to 1 and that all other data points were scaled accordingly. The term "self normalized", when applied to multiple spectra or other data sets, means that each one was individually normalized to 1 with different scaling factors. In the case of PL spectra, this allows peak shape, width, and location to be compared independent of peak intensity.

Except in the background and literature review chapter (Chapter 3), when the intensities, peak intensities, or peak wavelengths of more than one PL band of a sample or samples are shown in a figure, the shortest peak-wavelength data are denoted by squares and the longer peak-wavelength data are denoted by circles. When applicable, the shortest peak-wavelength data points are connected by a solid line and the longer peak-wavelength data points are connected by a dashed line. When only one dependant variable is plotted, squares and solid lines are used. In the case of the UV/blue and green bands (to be defined) of spark-processed silicon (sp-Si), the UV/blue is represented by squares and solid lines and the green is represented by circles and dashed lines.

Multiple PL spectra are often presented in figures by two-dimensional (2-D) projections of three-dimensional (3-D) parameter spaces. In general, the X-axis represents the processing variable in question, the Y-axis represents wavelength, and the vertical Z-axis represents intensity. The orientation of the Z-axis is never changed (increases vertically). However, in order that the reader obtain a clear view of the data, the azimuthal angle and rotation about the Z-axis vary from figure to figure. In many cases, this results in the unfortunate but necessary reversal of the direction of increasing numerical values of one or both of the X and Y-axes. This is better than having one set of data obscure another and is not a problem if the reader looks closely at the figure. The projections are made with no perspective (infinite horizon, or "cubic perspective") and the "back planes" are drawn to assist the eye of the reader.

These 3-D figures may represent two or more samples or measurements per approximate value of a processing parameter. In these cases, the author is forced to resort to the use of color so that the reader can clearly differentiate between them. Highly contrasting solid colors are used. For the case of PL spectra, the spectrum with the highest peak intensity (of the shortest wavelength band if more than one) is assigned the color blue followed by red, purple, and green in that order. Even for the microfilm-reader, who will see shades of gray, this arrangement is superior to the use of black and white.

In addition, color is used in any graph where two or more dependent variable data sets overlap in a figure or are otherwise hard to follow with the eye. In the case of the PL peak intensities of the UV/blue and green bands of sp-Si plotted as a function of a processing variable, the colors used are blue and green, respectively.

There are three possible standards for the scale and range of a particular parameter's axis in a figure. The first is a fixed range for all figures, the second is to scale the axis to the distribution of the data in each figure, and the third is to adjust the range and scale of the axis to best show the trend of the data that the author wishes to demonstrate (a smaller range to amplify a small trend, or a larger range to hide scatter when there is no trend). The author feels that the third approach is misleading. In the case of the location of the peak intensity of PL bands, the first approach is impractical, leaving only the second method. Accordingly, in such figures, the Y-axis is scaled to the distribution of the data.

Organization of Experimental Results

Due to the large number of experimental parameters varied in this study and the sheer quantity of data to be analyzed, there are several experimental chapters, each of which may contain its own introduction/motivations, experimental, results, and discussion sections. It would be unwieldy to attempt this with one chapter for each where the discussion would be too far removed from most of the corresponding results (particularly figures). The experimental chapters are arranged in a logical order and the discussion sections will be cumulative (each may refer to previous chapters). This is important because the results build on each other and, in many cases, experiments were designed based on previous results. Following these experimental chapters is a further discussion chapter (Chapter 10) covering all the previous chapters as well as the summary and conclusions chapter (Chapter 11) and a future work chapter (Chapter 12).

Because this is a scientific study with the primary goal of understanding the nature of the luminescence of spark-processed materials, the author chose to use separation of variables (scientific method) rather than the Taguchi method. Instead of a uniform-density parameter space, the author endeavored to find a set of optimal or near-optimal values to serve as the origin of the parameter space and to fill it with data points along one axis (parameter) at a time. If it is ever desirable to produce spark-processed materials for commercial uses, the empty areas of the parameter space, which represent simultaneous large deviations from the standard values of multiple variables, may have to be explored.

CHAPTER 3
BACKGROUND AND LITERATURE REVIEW

Review of Spark-Processed Silicon Literature

Hummel and Chang first observed photoluminescence from spark-processed silicon (sp-Si) in 1992 [Hum92]. The vast majority of literature on sp-Si and spark-processing in general has been published by Hummel and associated researchers and students, a group that includes the author. Work by other groups has concentrated on areas not directly related to this dissertation. These include work on the electroluminescence of sp-Si [Yua95], doping of sp-Si with hydrocarbons [Rut94], and doping of sp-Si with rare earth elements [Stj97].

Due to the relative novelty of the field and the fact that most of the work on sp-Si has been done locally, the traditional concept of a "literature review" chapter is of limited applicability. This section will cover the majority of the work done by others while reserving most of that done by the author for later chapters. However, both were conducted concurrently and neither category was done in an intellectual vacuum. While most of the content to be presented herein is unpublished, work by others has strongly influenced the author and the author has played a part in the research to be presented in this section. The following sections will cover work by other research groups on sp-Si, work in closely related fields, and other work applicable to the understanding of this presentation.

The majority of work published by Hummel, Ludwig, et al., has been periodically assembled in large review articles [Hum01, Lud96a, Lud97] and this background draws heavily on these three publications. The literature will be presented in the as published state. Much of this information is confirmed by the author's research, but in some cases it must be modified or even contradicted. Some of these instances will be alluded to in this background section. Such comments and criticisms will be indented, single-spaced, and in a bold font to clearly differentiate them from the review.

Introduction to Spark-Processed Silicon

Spark-processing substantially modifies the properties of materials. Spark-processed silicon has been shown to exhibit intense room-temperature photoluminescence (PL), electroluminescence (EL), and cathodoluminescence (CL) in the visible part of the electromagnetic spectrum as well as in the near UV and near IR. Sp-Si also exhibits some novel magnetic properties.

When excited with 325 nm light from a He-Cd laser, sp-Si exhibits either or both of two intense PL peaks. These have been located at approximately 385 nm and 525 nm in the published literature and are known as the UV/blue peak and the green peak, respectively. Several processing parameters influence the absolute and relative intensities of these two bands and will be discussed.

> **Measurements by the author combined with detailed calibrations of the PL system place these peaks at about 372 nm and 531 nm when plotted in radiometric (power) units and 373 nm and 542 nm when plotted in quantum units.**

Much has been published about the major differences between the production, properties, luminescence, and mechanisms of sp-Si and another material known as porous silicon (PS), which is produced by a wet chemical or electrochemical etch [Can90]. Electropolishing of Si predates the discovery of luminescence by decades

[Uhl56, Tur58]. There is little in common between these materials, and PS will not be discussed to any significant degree in this study. Ludwig has dealt with these distinctions in great detail [Lud96a]. It should be pointed out however, that when excited by 325 nm light, sp-Si exhibits similar photoluminescent intensities (at significantly different wavelengths) to PS samples purported to have quantum efficiencies of approximately 5%. The conclusion has been drawn that sp-Si has similar quantum efficiencies [Hum95a, Hum95b].

Theoretical models to explain above band-gap luminescence in modified semiconductors with nanoscale features traditionally fall into three main categories: (1) a classical quantum confinement model [Can90, Bru94, Cal94], (2) a surface-modified quantum model [Koc93, Cam86], and (3) models based on molecular species and localized defects (many of which will be discussed in a later section).

The first category of theories predicts a widening of the optical band-gap of semiconductors due to physical confinement of carriers in quantum wells, wires, or dots (one, two, or three-dimensional confinement). These models usually use a classical particle in a box approach [Oha90] or an effective mass approximation approach [Bru86, Kay88]. In addition, materials with an indirect optical band-gap (like silicon) can assume a pseudo-direct behavior due to Heisenberg-related smearing of the momentum of confined carriers [San92].

The second category also involves broadening of the optical gap of nanocrystalline semiconductors, but rather than a direct recombination mechanism across this gap, the enlarged gap hosts optically active tail states associated with the surface interface of the quantum dot and the surrounding material. The high surface to volume ratio of nanoscale particles makes such a mechanism plausible.

The third category assumes either the presence of luminescing molecular species present in the matrix (often complexes of Si, O, and H known as siloxenes) [Fuc93, Tam94] or luminescence from highly localized defects in the oxide itself [Tsy94, Pro93].

Production of Spark-Processed Silicon

The method of producing sp-Si samples in the majority of published work has evolved from the use of a Tesla coil or DC high voltage supply to the use of the pulsed high voltage output of the flyback coil from a cathode ray tube (CRT). The spark intensity varies from one CRT to another. The open circuit voltage is approximately 15 kV. The repetition rate of the high voltage pulses is equal to the horizontal scan rate of the CRT. This is 16 kHz for a television (525 columns X 30 frames per second) and is about 19 kHz for a VGA monitor. The pulses are applied between an anode (often a sharp tungsten tip) and the silicon to be processed, which forms the cathode, see Figure 3-1. They have typically been separated by a gap on the order of 1 mm. The pulse width created when driving a spark gap with a VGA monitor has been quoted as being 10 ns or 20 ns [Lud96a, Hum01]. Based on the assumption that the power supply charges the capacitance of the spark gap (estimated to be 30 pF) to the full potential of 15 kV after which it discharges across the gap in 10 ns, Ludwig calculated a value of 45 amps for the instantaneous current of each pulse.

This analysis is inherently flawed and will be addressed in Chapter 5.

Spark-processing is done in air or a mixture of pure gases. As it requires a discharge, it cannot be done in a vacuum. In air or mixtures of nitrogen and oxygen it

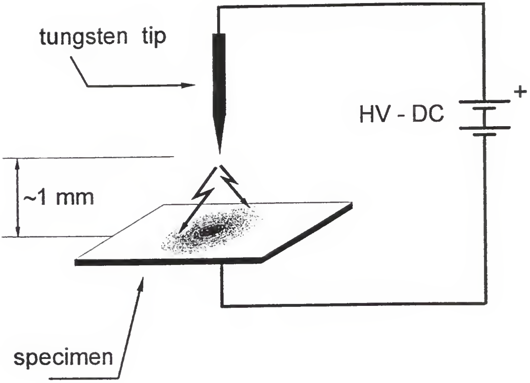

Figure 3-1: Schematic representation of the preparation of spark-processed materials. High-voltage DC pulses cause a discharge between an anode tip and the substrate (cathode). Adapted from Lud96b with permission.

results in the build-up of a circular whitish-gray porous oxide layer on the surface of the silicon. When the power source is a monitor, the growth rate is about 3-5 μm/min. and the central region is often surrounded by a light brown ring that is substantially thinner than the central region (this is not always true of samples produced by the author, but depends on the processing conditions).

Very little surface modification occurs when the sample is the anode and the tip the cathode. It is believed that gas molecules are positively ionized and accelerated toward the cathode transferring kinetic energy to the substrate surface. When a high-voltage DC potential is applied between two tungsten electrodes in air, the cathode glows red hot and the anode remains relatively cool. The cathode is consumed at a much greater rate.

This rapid transfer of kinetic energy melts and/or evaporates the silicon and ejects a plume of material, which reacts with the ambient gases and recondenses on the substrate, see Figure 3-2. The deposited material is constantly bombarded by more ions and more material deposits on top of it. The result is a nanoporous matrix composed largely of silicon-rich silica with a quantity of embedded silicon nanoparticles.

The luminescence has been reported to vary with a number of processing parameters. The area and thickness of the porous region increases with processing time. A linear relationship between PL intensity and processing time has been reported. The resulting PL appears to be unaffected by the doping type, doping level, or crystalline orientation of the wafer during processing [Cha94].

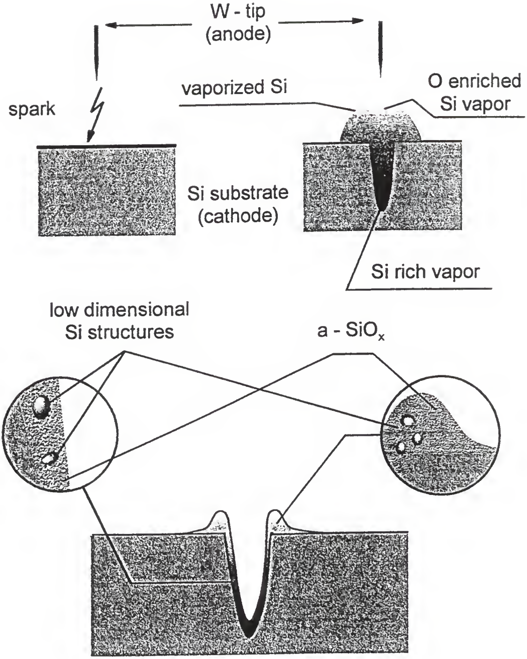

Figure 3-2: Schematic representation of the formation of silicon nanoparticles within a silicon-rich silica matrix during spark-processing. Adapted from Lud96b with permission.

Morphology of Spark-Processed Silicon

Figure 3-3a shows a plan view scanning electron microscopy (SEM) micrograph of sp-Si processed with a Tesla coil power source. Figures 3-3c and 3-4 show cross-sections of the substrate and porous region. The porous region consists of deposited clusters surrounding deep "worm-holes". These holes appear to be channels through which the spark reaches the more conductive substrate. In this example, they are about 15 μm in diameter and 200 μm in length. Ludwig believed that these channels represent the volume eroded by a single pulse and has calculated an evaporation rate of 8 g/s and a current density of 10^7 A/cm^2 [Lud97].

> **The author believes that these channels result from the gradual deposition of material around the discharge sites. As the thickness builds up, the spark is drawn to the least resistive paths to the substrate and repeatedly strikes areas with less coverage. This causes growth near these areas, limiting their size. As a result, long narrow channels form through the porous region. The author neither believes that the pore volume represents the amount of material removed by a single discharge, nor that the pore diameter indicates the diameter of the plasma channel, which is likely to be highly forked at the substrate end.**

Figure 3-3b shows a high resolution transmission electron microscopy (TEM) micrograph of a sp-Si sample produced using a Tesla coil. Silicon particles with diameters in the nanometer range can be seen (four are outlined in ink). The crystalline orientation appears to be random and the particles are surrounded by an amorphous matrix. Also in the figure are electron diffraction patterns of the silicon-rich region in the upper right of the figure and of the amorphous region in the lower left. These confirm that the silicon is crystalline but randomly oriented and the

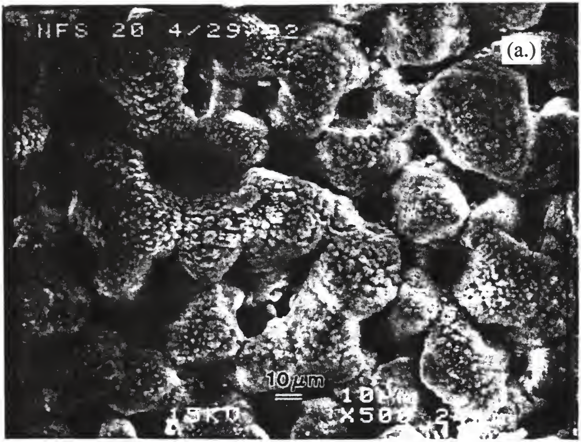

Figure 3-3: Micrographs of sp-Si:

- **(a)** SEM plan view. Adapted from Hum93 with permission.
- **(b)** TEM. Some nanocrystals have been outlined. Satellite pictures show electron diffraction patterns taken at locations indicated on the micrograph. CR = crystalline and AM = amorphous. Adapted from Hum93 with permission.
- **(c)** SEM cross-section at a fresh fracture. Adapted from Hum93 with permission.

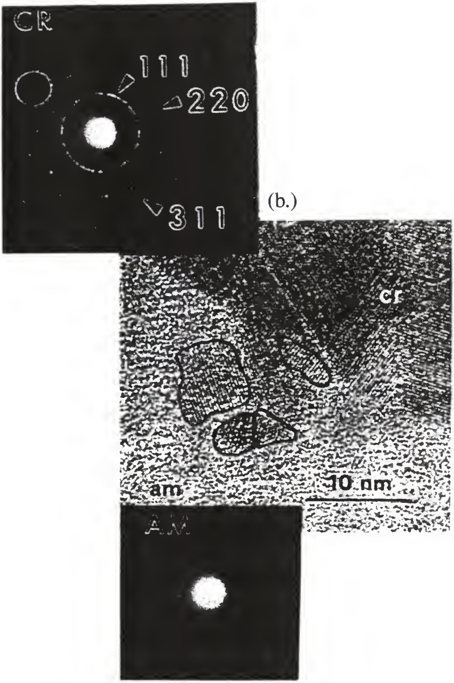

Figure 3-3—continued

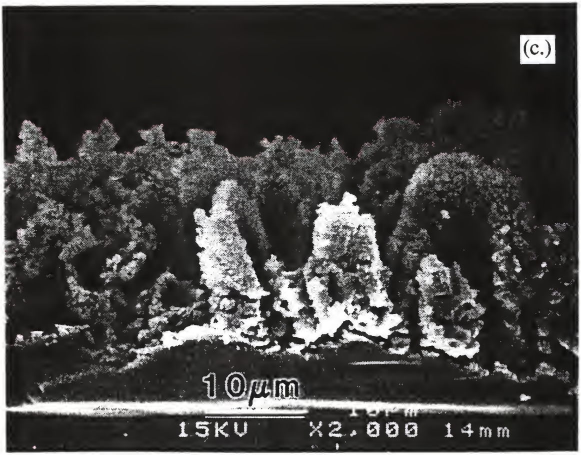

Figure 3-3--continued

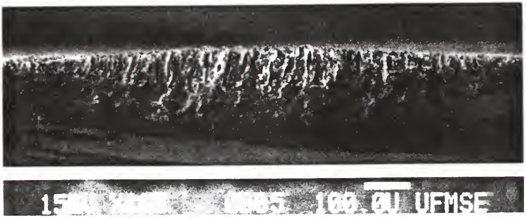

Figure 3-4: Cross-sectional SEM micrograph of sp-Si taken at a fresh fracture. Adapted from Lud96a with permission.

matrix is amorphous. The X-ray energy dispersion spectrum of the amorphous region indicates that it is largely silica (SiO_2) [Cha94].

The presence of silicon nanoparticles has been confirmed by the observation of their expected effect on the Raman spectra (Stokes shift) of sp-Si vs. bulk silicon [Cha94]. Campbell and Fauchet describe how the Raman peak shift and line width depend on particle size and shape [Cam86]. This is caused by phonon confinement. In addition, relaxation of momentum conservation of optical phonons in nanoparticles may cause splitting, resulting in a double Raman peak [Tsu92, Wu_95]. Figure 3-5a shows the Raman peak for bulk silicon at 520.9cm^{-1}. Figure 3-5b shows the corresponding peak of a green luminescing sample that is shifted toward lower energies and broadened. Figure 3-5c shows the shifted, broadened, and split peak for a UV/blue luminescing sample. In this case, both single peak and double peak best-fit Gaussian deconvolutions are superimposed on the data. Both samples were produced by monitor sparking. The degree of shift and broadening is consistent with spherical particles of 3-5 nm in diameter [Cam86, Sui92].

While nanoparticles are present, there seems to be no correlation between the size of the nanoparticles and the color or intensity of the PL. A more detailed study found no significant difference between the Raman shift and broadening between UV/blue and green sp-Si samples [Rup97]. Furthermore, the less luminescent edge or "halo" regions of monitor-sparked samples appear to have a smaller particle size than the center of the porous region, which is highly luminescent. The sizes of the particles detected in this study, regardless of region, ranged from 8 to15 nm. These are much too large to be the cause of either PL band. Finally, the observed Raman peak shifts and broadenings were not consistent with one another. This is very strong evidence that quantum size effects are not responsible for the PL of sp-Si.

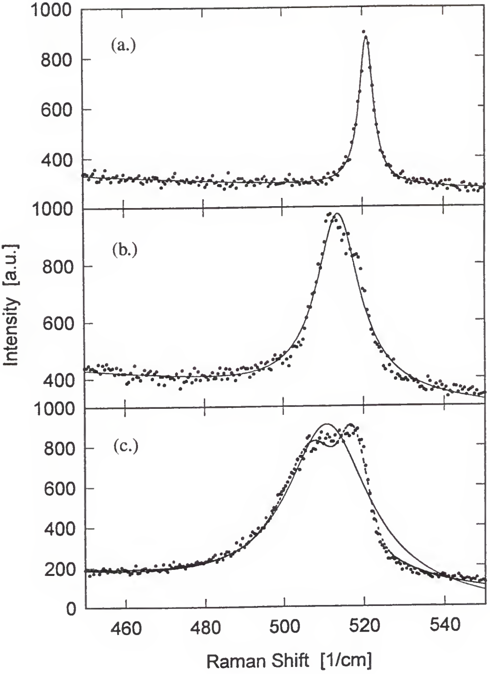

Figure 3-5: Room temperature Raman shifts (λ_{exe} = 488 nm, 400 W cm^{-2}):

(a) crystalline Si - 520.9 cm^{-1} peak, 4.0 cm^{-1} FWHM

(b) green luminescing sp-Si - 513.8 cm^{-1} peak, 6.5 cm^{-1} FWHM

(c) UV/blue luminescing sp-Si - 510.9 cm^{-1} peak, 24.0 cm^{-1} FWHM

Single Lorentzian fit shown for all samples (solid line), double Lorentzian fit shown for (c) (dotted line). Adapted from Hum95a with permission.

Composition of Spark-Processed Silicon

X-ray photoelectron spectroscopy (XPS) has been performed on monitor sparked sp-Si samples. The core binding energies of the Si 2p electrons have been found to be 103.4 eV [Kur97]. This is very close to that of silicon in the +4 valence state as measured in amorphous SiO_2 (103.3 eV). This implies that the majority component of the sp-Si surface is near-stoichiometric silica.

Small-spot XPS has been conducted on the cross-section of a freshly fractured sample that was processed in air, and reveals that the composition varies with depth [Lud96b]. The resulting depth profile is shown in Figure 3-6. The concentration of SiO_2 is essentially 100% at the surface and falls monotonically as the depth increases until the substrate is reached. The spark-processed layer in question was 250 μm in depth. The concentration of crystalline silicon increases monotonically from 0% at the surface to 100% at the interface with the substrate. The depth profile of two minor constituents differed. The first represents silicon whose signal is charge shifted. This must be due to isolated islands or clusters of silicon not connected to the substrate and surrounded by an insulating matrix. These first appear at a depth of about 50 μm, and constitute about 13 at% (atomic percent) of the sample from about 100 μm to 200 μm. The charge shifted signal finally disappears at the interface with the substrate. Finally, nitrogen in concentrations as high as 6 at% is found at similar depths. This signal is also exhausted at the interface with the substrate. Within the detection limit of the instrument (approximately 1 at%), the surface appears to be pure SiO_2. Depth resolved X-ray emission spectroscopy results are consistent with only silica to a depth of at least 200 nm (10 keV beam) [Lud96b].

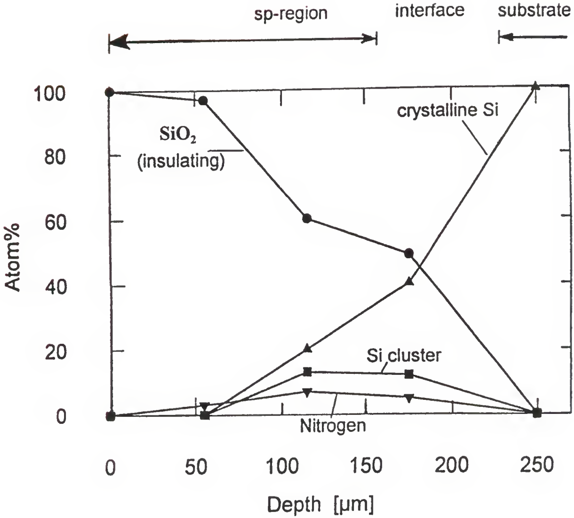

Figure 3-6: Composition of sp-Si as a function of depth as derived from small-spot XPS measurements. Adapted from Lud96b with permission.

Transmission and diffuse reflection Fourier transform infrared spectroscopy (FTIR) spectra were taken for a monitor-sparked sample in the "fresh" state (Figure 3-7a), after annealing at 600 °C in air for 20 h (Figure 3-7b), after an additional 24 h anneal at 800 °C (Figure 3-7c), and for another sample sparked in a stream of flowing nitrogen (Figure 3-7d). The first three spectra show strong vibrational modes associated with Si and O. These are labeled on the figure. Structures in the 3600 cm^{-1} to 3750 cm^{-1} range assigned to vibrational frequencies of OH groups including the ≡Si-O-H group (silanol) are present and are shaded in the figure. It is clearly seen that the strength of these modes decreases with annealing. OH groups are known to desorb at temperatures above 450 °C. A number of hydrogen related vibrational modes that are seen in porous silicon produced by a wet etching process are not seen in sp-Si. These include the scissors and wagging modes of the Si-H bond at 910 cm^{-1} and 630-670 cm^{-1}, respectively, as well as a Si-O-H mode at 870 cm^{-1}. A strong N_2 related vibrational mode is seen in all four spectra indicating that nitrogen is incorporated in sp-Si processed in either air or nitrogen.

Optical Properties

Room temperature photoluminescence

Sp-Si prepared in air using a monitor as a power supply exhibits two primary photoluminescence (PL) bands under 325 nm excitation. A peak maximum near 385 nm is known as the UV/blue band and a peak near 525 nm is known as the green band. These are shown in Figure 3-8a and 3-8b. A tail extending into the red can be seen in samples exhibiting only the UV/blue peak. This peak can be resolved into a discrete peak near 650 nm when sp-Si is excited by the 488 nm or 514.5 nm line of an

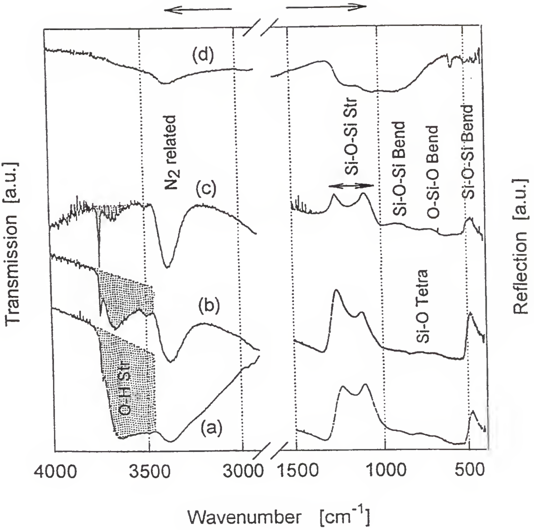

Figure 3-7: FTIR spectra of:

(**a**) freshly sparked sp-Si produced in air

(**b**) same sample annealed for 20 h at 800 °C in air

(**c**) same sample after an additional 24 h anneal at 800 °C in air

(**d**) sp-Si produced in UHP nitrogen (99.999% pure)

Adapted from Hum95a with permission.

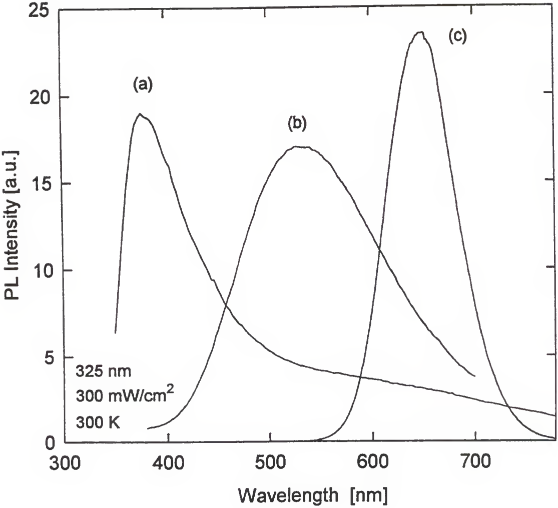

Figure 3-8: Room-temperature PL spectra of: (325 nm 0.3 W cm^{-2} excitation)

(**a**) UV/blue luminescing sp-Si

(**b**) green luminescing sp-Si

(**c**) red PL of PS shown for comparison

Adapted from Lud97 with permission.

Argon ion laser as well as when PL is measured at high temperatures. Hummel has assigned this luminescence to a specific radiative transition rather than to an extended distribution of states [Hum01]. The peak intensities of the UV/blue and green peaks are similar. When excited by about 5 W of 488 nm laser light, the red peak has similar intensities to the other peaks when excited by about 20 mW of 325 nm laser light. This indicates a room temperature quantum efficiency ratio of about 1:250. It is possible that the tail also exists in green samples, but it cannot be individually resolved.

The relative proportions of the UV/blue and green peaks can be changed by varying several processing parameters. A more intense spark produces more green and less blue. A large heat-sink under the sample produces more blue. Blowing a stream of air on the sample during processing almost guarantees a blue emitting sample. Heating the substrate during processing enhances the green at the expense of the blue. It is likely that temperature is the common factor in all these observations. While a sample can exhibit a superposition of the UV/blue and green peaks, there is never a peak in between or a shift in the peak locations beyond that expected by the mathematical addition of the two curves.

The PL peak of an anodically etched porous silicon sample purported to have 5% external quantum efficiency is shown in Figure 3-8c. This was measured under identical conditions as the sp-Si peaks. The intensity of PS is comparable to both UV/blue and green sp-Si leading to the published assertion that the quantum efficiency of sp-Si is in the neighborhood of 5%.

> **The methods reported in this dissertation allow the creation of UV/blue sp-Si several times brighter than samples of this vintage. For the green PL, they can be over an order of magnitude brighter. However, when the author attempted to make a direct**

> **measurement of the quantum efficiency of a typical green sample, the result was only about 1/3%. The brightest green samples are about 5 times more intense than a typical green sample, which indicates a quantum efficiency of approximately 1 - 2%. This is still quite high, and due to the methodology of the measurements, is probably a conservative or "worst case" value. This issue is addressed in Chapter 9.**

Both major PL peaks vary linearly in intensity with excitation powers varying from 0.01 $mWcm^{-2}$ to 10 $mWcm^{-2}$. The spectral shape is also preserved.

These PL bands of sp-Si cannot be accounted for by currently known PL bands in stoichiometric and non-stoichiometric silica and other glasses. In Figure 3-9, the primary peaks of sp-Si are represented by curves (a) and (b). Also shown on this graph are a number of silica-related peaks. These samples were measured under identical conditions and include: (c) X-ray damaged borosilicate glass exposed to 40 keV X-rays, (d) 99.999% pure silica powder, (e) Silicon-rich silica created by Si ion-implantation (25 keV, 2×10^{11} cm^{-2}), and finally, (f) industrial grade fused silica. Within the high bandgap of silica (9 eV for crystalline silica, about 8 eV for dense amorphous thermal silica) there are reported luminescent bands at 185 nm, 264 nm, 288 nm, 400 nm, 563 nm, and 650 nm [Fri85, Pio90, Sta87]. These have been assigned to defect states as they have been found to increase in PL intensity under X-ray, gamma, or neutron irradiation of silica. These bands have been successfully excited by below-gap photon energies. 165 nm, 240 nm, 258 nm, and 620 nm absorption bands have been found in silica. Photon energies over 5.0 eV (248 nm) are reportedly necessary to activate luminescence at 264 nm, and 288 nm. These are associated with triplet-to-singlet and singlet-to-singlet transitions of electrons in Si-Si bonds across an oxygen vacancy [Toh89b, Jon76]. The 460 nm luminescence is seen in Si-rich silica containing a low concentration of OH groups. The 650 nm emission

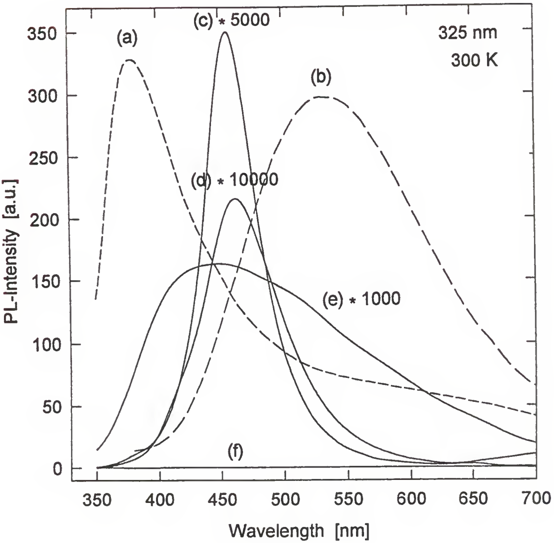

Figure 3-9: PL spectra of various samples measured under identical conditions:

(a) UV/blue luminescing sp-Si

(b) green luminescing sp-Si

(c) X-ray damaged borosilicate glass

(d) SiO_2 powder (99.999% pure)

(e) Si ion-implanted fused SiO_2

(f) fused SiO_2

Numbers indicate multiplication factors. Adapted from Hum95a with permission.

band has been attributed to a non-bridging oxygen hole center (NBOHC) [Sta87, Gri91] or an oxygen interstitial [Lud95a, Sku84, Pro94, Shi94]. It is associated with the 258 nm and 620 nm absorption and is unique among defects in silica due to its small relaxation (most others have Stokes shifts of 2 eV or more). This band is rapidly degraded under UV excitation [Hum95b].

It appears that the existing literature on silica cannot explain the main PL peaks of sp-Si. Also, He-Cd laser radiation (325 nm) is well below the peak absorption energy associated with all of the known emission bands except the one at 650 nm. Finally, under 325 nm excitation, the PL of monitor produced sp-Si is at least three or four orders of magnitude more intense than that from these various defects in silica and glasses.

Thermal dependence of the PL of sp-Si

The PL spectra of monitor-sparked sp-Si samples were measured at a variety of temperatures. Samples with UV/blue or green luminescence lose intensity above room temperature and gain intensity below room temperature, see Figure 3-10. The peak location and shape of the UV/blue luminescence is unchanged, while the green peak is blue-shifted and broadened by increasing temperature. As in the case of lower energy excitation, the red tail of UV/blue sp-Si can be resolved as a separate peak at high temperature. This band appears to be less susceptible to thermal quenching than the main part of the spectrum. The optical band-gaps of Si. SiO_2, and silicon quantum dots all decrease (red shift) with increasing temperature [Blu74, Thu75]. This is not observed in either primary peak. The blue shift of the green peak with increasing temperatures resembles the behavior of some silicon oxynitrides and

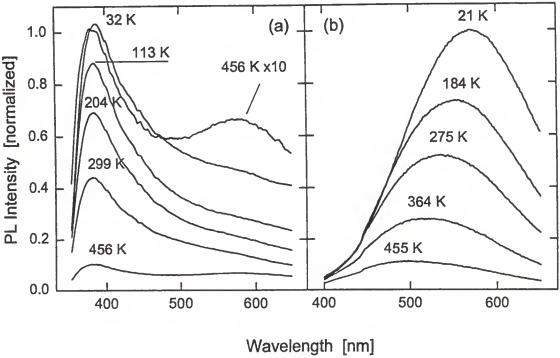

Figure 3-10: Temperature dependence of the PL spectra of:

(a) UV/blue luminescing sp-Si

(b) green luminescing sp-Si

Measurement temperatures are indicated adjacent to curves. Adapted from Lud96b with permission.

non-stoichiometric silicon nitride excited by below band-gap energies [Aus60, Wak95].

The integrated PL intensity is plotted as a function of inverse temperature in Figure 3-11a. At temperatures as low as 25 K, the PL intensity of sp-Si is 10 to 20 times more intense than at room temperature. Above room temperature, the PL is thermally quenched with activation energies of 156 meV for the UV/blue peak and 241 meV for the green peak. These values indicate a high degree of localization. The scale of this localization can be estimated by assuming that these activation energies correspond to excitonic binding energies. Using a simple electrostatic potential model ($\Delta E = (4\pi\varepsilon\varepsilon_0)^{-1}e^2d^{-1}$) and an average of the two values, a carrier separation distance, d, can be estimated to be 0.6 nm in Si (ε=12) and 1.9 nm in SiO_2 (ε=3.9). The lattice constant of Si is 0.543 nm by comparison. There are a number of ways to trap and localize defects besides classical excitons, but this exercise demonstrates a very high degree of localization, nevertheless.

Below room temperature, the activation energies vary with temperature. Such effects are generally attributed to the thermal emptying of exponential band-tails or other localized states that are inhomogeneously broadened. Such a phenomenon has been seen in band-tail to band-tail luminescence in *a*-Si:H [Col80]. In such cases, the intensity varies with temperature according to the equation $I(T) = I_o / (1 + ce^{T/T_o})$, where c is a constant. T_o is the characteristic temperature, which is a measure of the disorder in the system. It is related to the degree of inhomogeneous broadening and is proportional to the "width" of the density of band-tail states. If $I_o / I(T) - 1$ is plotted logarithmically vs. temperature then a straight line should result according to the theory. T_o can be determined from the slope of the line. As seen in Figure 3-11b, the thermal data for sp-Si fits this model very closely. In its simplest form, this model

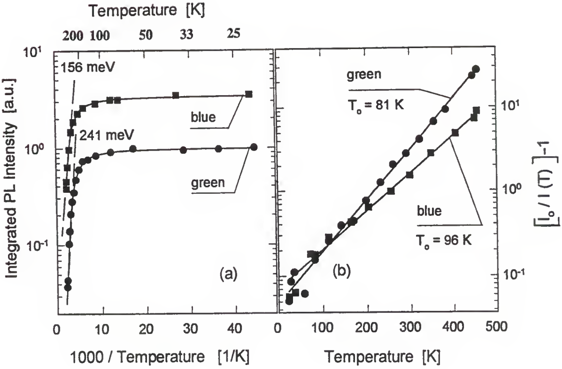

Figure 3-11: Temperature dependence of sp-Si PL:

(**a**) Temperature dependence of the integrated PL intensity of UV/blue and green luminescing sp-Si. Activation energies of thermal quenching are shown.

(**b**) Plot of $[I_0/I(T)] - 1$ vs. temperature for the same data. Characteristic temperatures are shown (see text).

Adapted from Aug96 with permission.

also predicts a redshift with increasing temperature as the band-tail states closest to the mobility edges are thermalized first. At higher temperatures, the remaining occupied band-tail states lie further in the gap and have less potential energy. However, real systems can be more complex. An inhomogeneously broadened state might not lie near a mobility edge and might depopulate by a different mechanism. In the case of SiN_X, a red shift is seen at small values of X, a blue shift at high X, and no shift at all at some intermediate X value. Thus, neither the lack of a shift in the case of the UV/blue peak, nor the blue shift of the green peak can be taken as a significant contradiction of the theory. The excellent fit of the integrated intensities indicates that either exponential band-tails or exponentially broadened interband states are involved in both species of luminescence. Measured values of the characteristic temperature of the PL of sp-Si have varied from 70 K to 110 K. This indicates a higher degree of disorder and band broadening than in PS where T_o is in the range of 40 K to 70 K [Ros93, Mus93]. It should also be noted that in PS, PL intensity is actually decreased at very low temperatures and has a maximum between 100 K and 200 K [Zhe92, Per92]. Thus, luminescence in PS is thermally activated. In sp-Si, thermal quenching predominates at all temperatures measured.

Figure 3-11a is actually highly misleading. By putting straight lines and the activation energies on this Arrhenius-plot, Augustin strongly implies that these energies were derived from a slope in this I(T) vs. 1/T plot. Correspondence with Ludwig verified that these energies are in fact derived from the slope of an $I_o / I(T) - 1$ vs. 1/T plot (not shown). This treatment is a consequence of the following theory for the change in PL intensity during thermal quenching: $I(T) = I_o [(\tau_r^{-1}) / (\tau_r^{-1} + \tau_n^{-1})]$, where τ_r and τ_n are the time constants of the radiative process and non-radiative processes. In processes that are not thermally activated, τ_r usually is relatively insensitive to temperature and τ_n is strongly temperature dependent. Some manipulation of the previous equation yields: $(\tau_n^{-1} / \tau_r^{-1}) = I_o / I(T) - 1$. The ratio on the left can be approximated by an exponential giving: $\exp(-E_a/K_bT) \approx I_o / I(T) - 1$, where E_a is the activation energy for the non-radiative process. This model is much simpler than the treatment of Collins and is often not sufficient for amorphous or disordered materials [Col80]. However, at sufficiently high temperatures, this thermally activated quenching usually predominates and E_a approaches a constant value.

Stability of sp-Si

Sp-Si is highly stable against degradation by UV light exposure, thermal annealing, and HF acid etching. Figure 3-12 shows how the PL intensity of sp-Si compares to that of PS with continued 325 nm UV excitation. Curves (a) and (b) represent typical sp-Si samples. Curve (c) represents a sp-Si sample annealed in 900 °C air for three hours. It is even more stable than freshly produced sp-Si. Curve (d) represents a sp-Si sample produced in UHP nitrogen. Curves (e) and (f) represent two typical PS samples. All curves are self-normalized to an intensity of 1 at zero time. The difference between sp-Si and PS is stunning, especially after the logarithmic intensity axis is taken into account.

Figure 3-13a shows how the PL intensity of sp-Si is influenced by annealing in ultrapure nitrogen. For each data point, the same sample was introduced to the furnace at the indicated temperature and held for 30 minutes. It was then removed, allowed to cool to room temperature, and the PL spectrum was measured. Each successive data point from low to high temperature indicates several accumulative annealings at the indicated temperatures. The green peak is relatively stable until 600

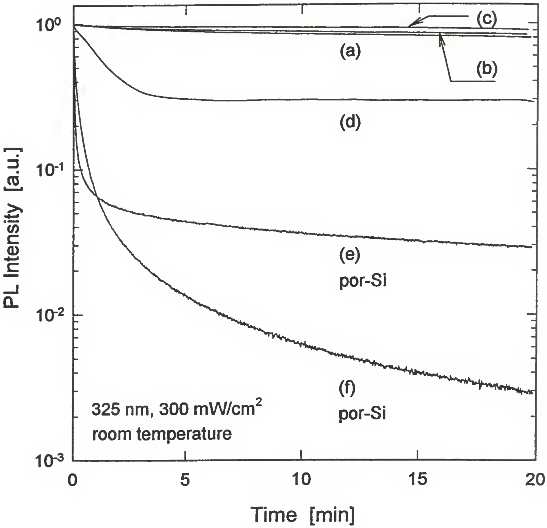

Figure 3-12: Degradation of PL as a function of time of exposure to 325 nm 0.3 W cm^{-2} laser light:

(a) UV/blue luminescing sp-Si

(b) green luminescing sp-Si

(c) UV/blue luminescing sp-Si annealed in air for 3 h at 900 °C

(d) sp-Si produced in UHP nitrogen (99.999% pure)

(e) and **(f)** porous Si samples for comparison

Adapted from Hum 95b with permission.

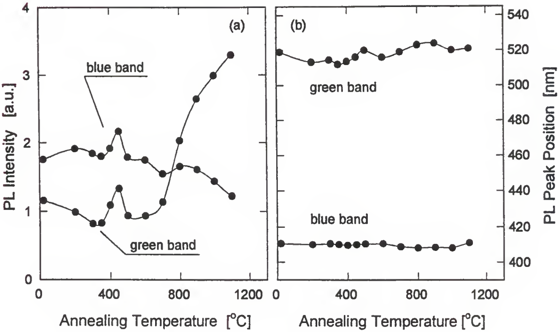

Figure 3-13: Annealing characteristics of sp-Si (consecutive anneals of the same sample in UHP nitrogen (99.999% pure) for 30 min. at each temperature):

(a) PL peak intensities of UV/blue and green PL bands

(b) PL peak positions of UV/blue and green PL bands

All data was taken at room temperature with 325 nm excitation. Adapted from Hum95a with permission.

°C and begins to increase with annealing, tripling in intensity by 1,100 °C. The UV/blue peak remains relatively stable until 900 °C when it begins to decrease somewhat, loosing less than half its intensity by 1,100 °C. The apparent peak locations of both bands are independent of annealing temperatures as seen in Figure 3-13b (410 nm and 520 nm are instrumental locations of the peaks before correction). The apparent increase in PL around 400 °C has been attributed to quenching of non-radiative centers from "naked" silanol groups. This is seen in the 460 nm defect luminescence in silica, see Figure 3-14. The silica sample was boiled in pure deionized water for 5 hours to saturate dangling silicon bonds with -OH groups. From room temperature to about 110 °C, the surface of silica is believed to be covered with chemisorbed -OH groups which are in turn covered by physisorbed H_2O. This combination does not provide good surface passivation. The H_2O desorbs between 200-250 °C leaving an -OH terminated surface that provides excellent passivation. Between about 450-600 °C, the -OH groups desorb, and the passivation is lost. Thus, similar peaks in the annealing curves are seen between 400 °C and 450 °C for the UV/blue and green peaks of sp-Si as well as the much less intense defect-related luminescence in silica. The double line in the figure indicates the temperature above which there should be no chemisorbed -OH groups. It is believed that silanol groups enhance the luminescence of sp-Si within a narrow temperature range, but are not directly responsible for either luminescent band. It should be noted that no difference was seen for sp-Si after boiling in water vs. a standard air-sparked sp-Si sample, indicating that dangling bonds are already passivated in sp-Si prepared in damp Florida air.

The PL from sp-Si has been found to be remarkably stable against HF etching. HF etches SiO_2 quickly, indicating that the excess silicon and nitrogen in the bulk

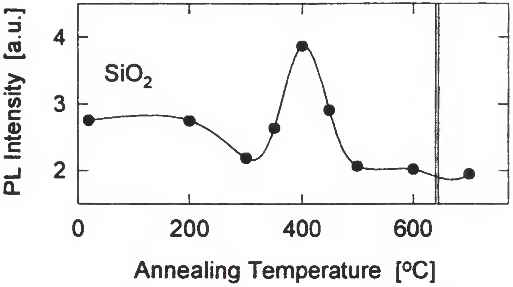

Figure 3-14: PL peak intensities of 460 nm defect luminescence in silica after consecutive anneals of the same sample in UHP nitrogen (99.999% pure) for 30 min. at each temperature. Adapted from Hum95c with permission.

slow etching substantially [Cha94]. Because of this, it has been concluded that the PL of sp-Si is a bulk, and not surface, phenomenon.

PL lifetimes of sp-Si

Nanosecond PL decay was originally reported for the PL band of sp-Si. More recent measurements by the author have revealed much faster picosecond luminescence using equipment with a much faster time resolution. This will be discussed in detail in Chapter 8.

However, the original published conclusions about the speed of these processes in sp-Si are still true (perhaps more so) and will be presented in this review. The fast response suggests that recombination is based on geminate carriers recombining at highly localized luminescent centers.

The ps decay of sp-Si is much faster than red-luminescing PS [Ook92] and defects in a-SiO_2 [Toh89c], which are both in the 1 - 10 μs range. It is also three orders of magnitude faster than the 10 ns decay observed in blue-luminescing highly oxidized PS [Koc93, Kov94]. The 1.9, 2.2, 2.7, and 3.1 eV transitions in silica have reported time constants on the order of 10 μs, 100 ns, 10 ms, and 100 μs, respectively [Sta87, Nis92, Sku78, Sku84, Sku92]. All of these mechanisms are excluded as likely candidates to explain the UV/blue and green PL of sp-Si.

Effects of processing parameters on luminescence

The intensity and color of the PL emission from sp-Si depend on several experimental parameters including the pressure of the gas ambient, the total processing time, and the substrate temperature. Two of the most important parameters are the spark current and the chemical composition of the gas ambient. Figure 3-15 shows how the UV/blue and green PL intensity change with gas

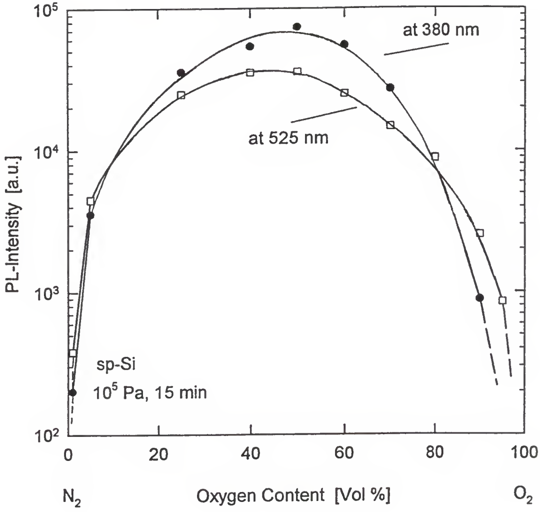

Figure 3-15: Peak intensities of UV/blue and green PL bands as a function of the composition of the gas ambient during processing. X-axis shows the percentage of UHP oxygen. The balance is UHP nitrogen. Adapted from Hum98 with permission.

composition between pure N_2 and pure O_2. Both gases must be present during processing for either of these dominant bands to exist in a sample [Hum98]. Samples sparked in pure O_2 exhibit only an orange/red peak at 1.9 eV (650 nm) which is 4-6 orders of magnitude smaller in intensity than the PL from a typical sp-Si sample. This peak has been attributed to nonbridging oxygen hole center (NBOHC) defects in silica. The samples represented by this figure were spark-processed with a monitor as a power source, which is essentially a constant-voltage supply. Oxygen is more readily ionized than nitrogen. It is clear to the casual observer that as the nitrogen concentration is increased the spark intensity rapidly decreases. Thus, without the luxury of a constant current source, this experiment cannot differentiate between two of the most important parameters (gas composition and current). With such a constant-voltage supply, the intensity of both peaks is maximized at N_2:O_2 ratios near 1:1. While nitrogen has been shown to passivate non-radiative centers in Si [Luc95], it appears to play a more direct role in the luminescence of sp-Si.

The PL intensity of sp-Si increases with processing time, see Figure 3-16 [Aug96]. This can be explained by the continuous production of luminescing centers. This increase is not accompanied by any change in the peak location. If the luminescence were due to quantum dots of continuously decreasing size, one would expect both a blue shift and nonlinear intensity increase. According to one model [Hyb94] quantum dot optical transition probability (and thus, the efficiency) varies with diameter by $1/d^6$.

As previously mentioned, heating the substrate is known to increase the intensity of the green peak at the expense of the UV/blue peak. Figure 3-17 shows the intensity of the green peak as a function of substrate temperature. Without a constant-current supply, increasing substrate temperature can increase the current as

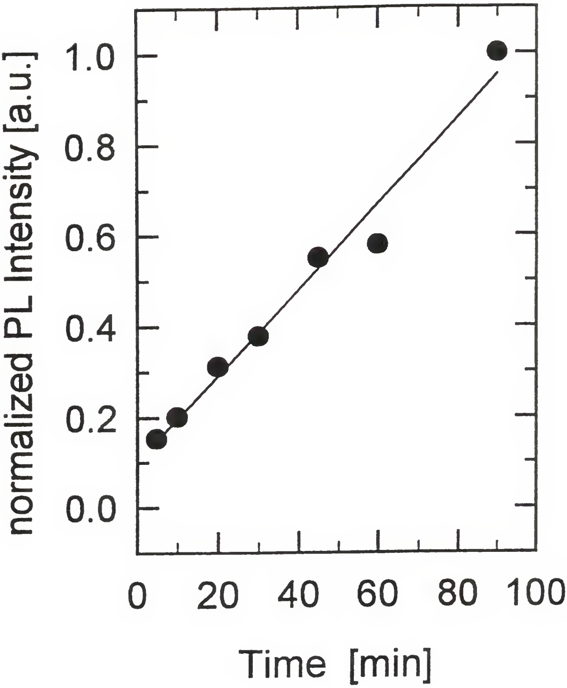

Figure 3-16: Intensity of the UV/blue PL peak of sp-Si as a function of processing duration. Adapted from Aug96 with permission.

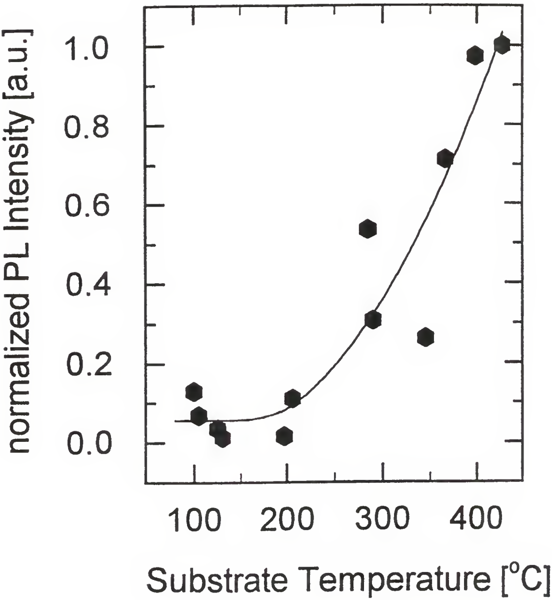

Figure 3-17: Intensity of the green PL peak of sp-Si as a function of the substrate temperature during processing. Adapted from Aug96 with permission.

well because the intrinsic carrier concentration of the silicon increases. However, because of the large relative increase of the green peak compared to the UV/blue peak, there is definitely evidence of a thermal component to this effect.

If the spark-processing is done in flowing air, the intensity of the UV/blue peak is observed to increase with increasing air velocity. Figure 3-18 shows the increase in PL intensity as a function of the air pressure applied to a nozzle blowing on the sample during spark-processing. Such "spray cooling" is known to be a highly efficient method of cooling a small area, and this effect is probably thermal in nature. It is not due to additional oxygen from the flowing air. X-ray emission measurements indicate that sp-Si processed in flowing air is less oxidized than that processed in stagnant air, a somewhat counterintuitive observation [Kur97].

As briefly mentioned, variations in the substrate including the type and concentration of dopants (n-type and p-type) do not effect the peak locations of the PL bands in sp-Si. However, a substantial difference in current can result.

Tungsten has proven to have excellent properties for use as an anode material for spark processing, and it is often used for this reason. This led to the argument that the UV/blue luminescence of sp-Si originates from tungsten contamination [Vep97]. The luminescence of sp-Si sparked using a variety of anode materials exhibited identical peak locations and similar PL intensities [Hum98]. The anode materials included W, Ti, Mo, V, Ni, and, most importantly, Si. Some electrodes oxidized more easily than others, and some exhibited an adherent insulating oxide which "choked off" the spark. Differences in current can explain the observed differences in intensity. These experiments conclusively rule out the role of contamination from the anode as a mechanism for the UV/blue and green peaks of sp-Si.

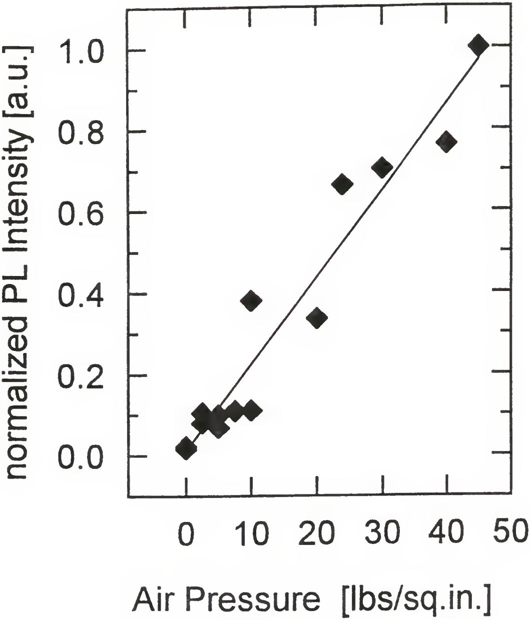

Figure 3-18: Peak intensity of the UV/blue band of sp-Si as a function of the air pressure used for spray cooling of the area being processed. Adapted from Aug96 with permission.

Cathodoluminescence of sp-Si

Sp-Si is known to exhibit two cathodoluminesence (CL) peaks near 480 nm and 650 nm [Lud95a]. This luminescence is commonly observed in silica and glasses and is easily explained. It appears to have no relation to the PL of sp-Si. It is beyond the scope of this study to go into the CL in detail, but it should be pointed out that the penetration depth of electrons (10 KeV was used for the CL work) is only a few μm, while silica is nearly transparent to 325 nm UV light. CL is therefore believed to be a surface (or near-surface) phenomenon, while PL is a bulk phenomenon.

Electroluminescence of sp-Si

Some work has been done by the author on electroluminescence of sp-Si and will be covered in Appendix A. In brief, thin film AC EL devices were found to be very inefficient and produce a faint greenish luminescence. No meaningful spectra could be taken of such a dim source. Roughly half (apparently the younger half) of people asked to observe it could see it in a darkroom. Thick film (high frequency) AC devices based on sp-Si in an oil dielectric worked significantly better (intense enough to measure) but were short lived. The EL spectrum in this case is very similar to the CL spectrum. It should also be noted that a much more intense and stable broad red/IR luminescence has recently been observed by Nigel Shepherd, a member of the same research group as the author, in a DC device based on metal contacts over an extremely thin spark-processed layer (sparked for only seconds). Previously, Yuan and Haneman observed visible PL in a similar system [Yua95]. However, as the author was not involved in this work and the EL peaks appear totally unrelated to the PL, these results will not be discussed here.

Doping sp-Si with rare-earth elements

Sp-Si has been doped with highly luminescent Ce, Eu, and Tb salts [Hum01]. This is also beyond the scope of this study except to note that the PL of these narrow line emitting elements becomes very broad when they are dispersed in a sp-Si matrix. The emission of Eu in sp-Si:Eu has a full-width at half-maximum of 200 nm. This demonstrates that the disorder in sp-Si is great enough to inhomogeneously broaden a very specific state into a wide PL band. Thus, a distribution of states is not needed to explain the broad PL bands in undoped sp-Si.

Spark-processing of materials other than silicon

Spark-processing leads to visible PL in a large variety of materials including Ge, Sb, Bi, Sn, Te, As, and GaAs [Lud94, Lud95b]. With the exception of GaAs, this was the work of the author and will be covered in the experimental section. However, certain aspects of sp-Ge and sp-Zn have also been studied by others, particularly Chang [Cha00a, Cha00b].

Three deconvoluted PL peaks are reported in air-sparked sp-Ge near 420 nm (blue), 520 nm (green), and 620 nm [Cha00a/Figure 3-19]. The author consistently observes the first two peaks in sp-Ge but never the third. Chang sparked primarily in air, while the majority of the author's work was in mixtures of UHP N_2 and UHP O_2, which may explain the difference. The overall PL intensity increases at low temperatures (as low as 21 K) and the increase is greater for the blue peak than the green peak. Furthermore, the blue band of sp-Ge also maintains its peak location at all temperatures (as does the yellow 620 nm band). This thermal behavior is very similar to that of sp-Si.

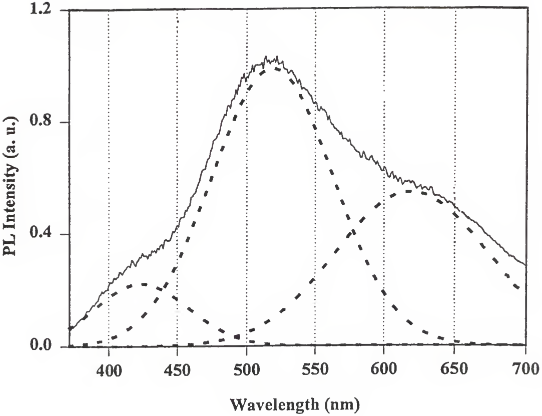

Figure 3-19: PL spectrum of sp-Ge (solid line) and Gaussian deconvolution (dashed lines) of same into three distinct peaks. Adapted from Cha00b with permission.

Several spark-processed metals exhibit visible PL and will be discussed in this study. With the exception of recent conference proceedings [Sto00], only sp-Zn has been covered in the literature [Cha00b]. Unlike sp-Si and other sp-materials including some metals, the PL of sp-Zn can be readily explained. A UV/blue 380 nm PL peak is attributed to a direct band-edge transition of ZnO [Sze81], while a broad green 540 nm PL peak is attributed to any of many well-documented non-stoichiometric defects in ZnO [Van96, Pro95, Xu_96, Byl78, Ort97, Liu92].

Laser-processing of silicon

Pulsed laser ablation of silicon in an atmosphere containing nitrogen and oxygen (lp-Si) results in PL similar to, but substantially weaker than, the UV/blue peak that results from spark-processing [Hum00]. Lp-Si exhibits no green peak analogous to that of sp-Si.

Magnetic Properties of Sp-Si

Sp-Si exhibits unique magnetic properties that can best be described as being strongly paramagnetic with a narrow, but clearly discernable, ferromagnetic hysteresis loop [Hac97]. It is likely that spark-processing produces such a high concentration of paramagnetic centers that their unpaired electrons are close enough to couple, giving rise to a ferromagnetic exchange energy. Electron Paramagnetic Resonance (EPR) studies indicate the presence of approximately 3.8×10^{20} unpaired spins/cm^3 associated with the E' center in silica. The E' center is one of the major sources of unpaired spins in silica. The remanent magnetization (a measure of the ferromagnetic behavior), the total magnetization (a measure of the paramagnetic behavior) and the strength of the EPR signal (a measure of unpaired spin density) correlate to one another and all decrease rapidly with annealing above 600 °C. This magnetic behavior appears to be independent of the PL mechanism, which is not strongly effected by annealing in this temperature range.

The PL intensity of the UV/blue peak increases slightly when the PL is measured in a magnetic field as high as 2×10^4 Oe. When the field is reduced, a permanent reduction in intensity of around 6% is observed. This trend continues when the field is reversed, see Figure 3-20 [Hum00]. This phenomenon is not easily explained, but it is interesting to note that it does not occur to the green peak of sp-Si. This is further evidence that the mechanisms for the two peaks are different.

No peak splitting is observed in the PL bands of sp-Si at high magnetic fields, but it is unlikely that this effect could be observed even if present given the broad nature of these bands.

Finally, it should be noted that once a sample is exposed to a magnetic field over 10^4 Oe, it no longer displays a ferromagnetic hysteresis loop.

Other Literature on Spark-Processing and Sparks in General

Three papers on spark-processing and spark erosion not published by researchers at the University of Florida are of interest and are discussed in this section. St. John performed spark processing on silicon covered by erbium nitrate salts [Stj97]. The erbium was incorporated into the sp-Si structure and found to be coordinated to oxygen and exhibit broadened PL. These results are consistent with those discussed in the previous section.

Hsu reported the formation of titanium-rich titanium carbide nanoparticles produced by spark erosion of titanium electrodes in an organic solvent [Hsu95]. The reaction between Ti and C is thought to occur in the vapor phase. A bimodal size

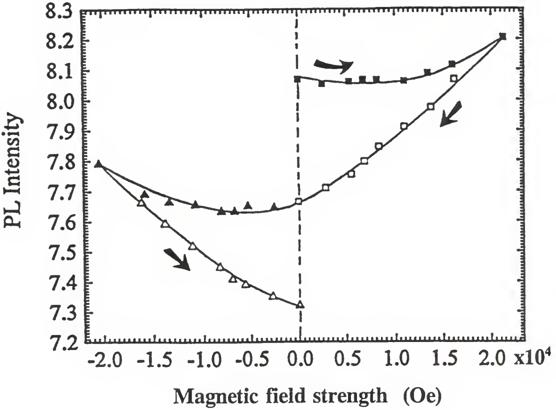

Figure 3-20: Evolution of the peak intensity of the UV/blue PL band of sp-Si with exposure to a varying magnetic field. Adapted from Hum00 with permission.

distribution of particles was found. 5-50 nm particles were attributed to the rapid condensation of TiC and Ti vapor while larger 5-20 μm particles were attributed to solidification of remelted TiC:Ti.

Zhang reported on a novel method of performing spark erosion by electrical discharge machining (EDM) with a constant voltage supply [Zha97]. An ultrasonic repetition rate of sparks was achieved by vibrating the cutting electrode at ultrasonic frequency. While this paper belongs to a very different field than spark-processing, a thorough explanation of the processes that occur in a spark discharge is discussed in detail.

If a potential below the breakdown voltage is applied between two electrodes in air, a tiny current will flow. The conductivity is provided by gas molecules that are ionized by various forms of ionizing radiation including UV light and cosmic rays. This current is stable if the potential is unchanged and is sometimes referred to as the "hidden current".

If the potential is increased further, a halo-discharge occurs. Here the current is large enough to cause some additional ionization. However, even at this stage, there is not enough current to create a specific ionization channel and the halo expands in a diffuse manner.

If the potential is increased further still, the halo-discharge becomes a self-continuous discharge. The production rate of charged particles overcomes the de-ionization rate and the number of ionized particles increases dramatically with time. This rapid increase in current is known as the spark discharge phase. The entire spark discharge phase lasts about 10^{-7} to 10^{-5} seconds. During this short period, a large amount of energy is released resulting in highly localized heating. This creates a tremendous overpressure. Typical temperatures and pressures are on the order of

10,000 K and hundreds of atmospheres. A shock wave travels away from the spark column through the surrounding gas.

When the number of ionized particles again reaches equilibrium, the final stage is reached. This is known as the arc discharge phase and is stable as long as the potential is maintained. In this phase, many ionizations and recombinations occur in equilibrium and the current and total number of ions are constant. The arc can last a long time and results in significant melting and/or evaporation of the cathode surface (the heavy ions striking the cathode carry much more momentum than the electrons striking the anode). When the potential is reduced below the point necessary to maintain an arc, the hot column of gas rapidly cools resulting in a sudden reduction of pressure to near vacuum. This, in turn, collapses forming another shock wave.

If a series of spark and arc discharges occur repeatedly, a large amount of melted and vaporized material can be produced. The free material is drawn into the gap by the vacuum associated with the end of the arc discharge and blown outward by the shock wave associated with the spark discharge. At the same time, ions are being produced and the cathode is being melted/evaporated (mostly in the arc phase). This repetition results in a continuous mixing and remixing of molecules from the gas phase and the cathode in an environment with an abundance of available thermal and electrical energy to drive chemical reactions.

Understanding the nature of sparks and how they develop and progress in time provides the necessary background needed to interpret the microstructure of sp-Si and the effects of changing the spark-processing parameters on the PL of sp-Si. These processing parameter variations will be presented in detail in Chapter 5 and newer SEM micrographs of sp-Si will be presented in Chapter 6.

Review of Quantum Size-Effect Literature

While a very strong case against the involvement of quantum confinement or "quantum dots" in the PL of sp-Si has been made in the literature, the topic deserves a closer second look, if only for the reason that nanoscale silicon structures are present in the material.

Radiative Lifetimes in Quantum Systems

The radiative lifetimes of sp-Si will be discussed in Chapter 8. It is difficult to compare the lifetime of sp-Si to published lifetimes of quantum structures, because there is substantial disagreement among the published lifetimes for both experimental and theoretical treatments of quantum systems.

Beginning with the experimental papers: Bimberg observed lifetimes of "dozens of picoseconds" in GaAs/AlGaAs and InAs/GaAs quantum dots [Bim97]. It should be pointed out that these materials already exhibit efficient direct PL in the bulk without quantum effects and the PL was only in the range of 1.1 to 1.3 eV even for dot diameters as small as 0.5 to 2.5 nm.

Linnros prepared Si nanoparticles in a SiO_2 matrix by ion-implantation of Si into silica [Lin97]. The dosage was varied by changing the thickness of an amorphous silicon (a-Si) implantation mask above the silica layer. Phase segregation of the excess Si was achieved with a 1 hour 1100 °C anneal under N_2. The resulting PL wavelength varied with the implantation dose (longer wavelength for more Si) and was believed to correlate with particle size. In all cases, the PL decay took the form of a stretched exponential similar to that reported for PS. The primary exponential time constants decreased exponentially with increasing PL energy from 20 to 50 μs for 1.45 eV PL to 5 to 15 μs for 1.9 eV PL. The extended tails were attributed to interactions between adjacent quantum dots. The PL was believed to be excitonic even at room temperature.

Okamoto observed low temperature PL in 2D Si/SiO_2 single quantum wells at low temperature (2 K) [Oka97]. A small size-dependent PL peak was seen superimposed on a much larger size-independent peak which was located at 1.6 eV and had a decay time of 1.1 ms. The size-dependent portion had the following locations and decay times: 1.8 eV and 0.3 ms for a 0.6 nm well, 1.7 eV and 0.6 ms for a 1 nm well, and 1.5 eV (no decay time reported) for a 1.3 nm well. Stokes shifts for resonant excitation were from 0.1 eV to just under 0.4 eV, which is consistent with theoretically expected exciton binding energies in quantum dots. The majority of the luminescence was attributed to defects at the Si/SiO_2 interface while the small size-dependent portion was attributed to a quantum size effect.

Min et al. prepared Ge quantum dots in SiO_2 by ion-implantation of a super-saturated concentration of Ge [Min96]. No correlation was seen between nanocrystal size and the peak energy and lifetimes of the PL. In addition, the PL shows only weak temperature dependence, which is inconsistent with the published theory for Ge quantum dots. The PL was identical to that seen in silica damaged from Xe implantation with no quantum dots present. The luminescence was attributed to radiative defect centers in the SiO_2 matrix.

In a theoretical paper, Takagahara and Takeda used first-principle calculations to describe the development of pseudo-direct behavior in quantum dots of indirect-gap materials such as Si and Ge [Tak92]. The interesting claim is made that the resulting band folding in a nanocrystal is similar to the local action of an isoelectronic center such as the nitrogen impurity in GaP:N. The calculated lifetimes were found to vary from the ns range for 1 nm dots to the ms range for 3 nm dots of either Si or Ge. Effective gaps were calculated to be 1.5 eV for 3 nm particles for both Si and Ge. To achieve 3.0 eV gaps, sizes as small as 1.3 nm in Si and 1.7 nm in Ge were needed.

The large disagreement in time constants for processes attributed to quantum confinement makes it difficult to argue that a process is not due to such effects based on a measured time constant. However, there seems to be no experimental evidence of time constants in the 1-10 ps range for known, well-characterized, quantum structures. This is important because, as will be shown in Chapter 8, the primary time constants of sp-Si are in this sub-10 ps range.

Particle Size vs. Energy Gap

Several of the papers in the preceding section also discuss the correlation between PL peak wavelengths and particle size or the lack of such agreement. It is evident, even in theoretical models, that very small particles would be needed to account for the UV/blue peak in sp-Si. Takagahara's calculation that a 1.3 nm Si quantum dot would have an absorption band-gap of 3.0 eV is in close agreement with the simpler effective mass approximation model. If one considers the high Stokes shift observed in quantum systems (hundreds of meV) and the fact that the UV/blue emission of sp-Si (with 325 nm excitation) is at 3.3 eV (not 3.0 eV), then a gap on the order of 4 eV would be necessary for a quantum dot model of this PL band. This would correspond to a particle size significantly smaller than 1 nm. In addition, there seems to be a wavelength vs. particle size discrepancy between theoretical papers and experimental reports in the literature. The wavelengths often do not correlate well to particle size, or when they do, they are often longer for a given particle dimension than predicted by theory.

It is interesting that even in a very well characterized system, such as that studied by Okamoto, where some luminescence that correlated with size was found, it appeared to contribute only slightly to the total luminescence intensity. Thus, assigning the PL bands of sp-Si to non-size effect related systems is not necessarily a challenge to the validity of quantum theories. Such phenomena may simply be masked by more prominent ones.

Papers by Gotza and Wu and their coworkers provide more examples of well-defined quantum structures that fail to produce observable luminescence. Gotza et al. prepared arrays of free-standing isolated 2-3 nm diameter silicon wires using reactive ion etching of silicon-on-insulator wafers followed by a self-limiting oxidation [Got98]. The buried insulator layer not only isolated the wires electrically from the substrate, but served as an effective etch stop. These wires were then passivated by a layer of a-SiN_x:H followed by an anneal in a reducing atmosphere (forming gas). Under 325 nm excitation, a broad luminescence could be seen with a peak wavelength which depended on the value of x in the SiN_x:H capping layer. In addition, PL bands were observed at 400 nm, 480nm, 560 nm, and 650 nm. All of these emission bands were attributed to various defect states in SiN_x and SiO_2. Wu et al. observed PL spectra from nanocrystalline Si:H that has no correlation with particle size, even for mean particle sizes as low as 2.2 nm [Wu_98]. The PL was attributed to the radiative recombination of carriers at interface defects in the nanocrystalline silicon.

Excitonic Nature of Quantum Dots

Several of the papers already discussed report or predict that various nanoparticle systems show excitonic behavior, even at room temperature. According to Yip, quantum systems should exhibit strong Stark-effect red-shifting and intensity quenching due to an applied electric field:

> In response to an electric field, the electron and hole eigenstates follow the contours of the linear energy gradient in opposing directions so that a large red-shift necessarily induces a strong polarization of the eigenstates with the corresponding reduction in the oscillator strength of the absorption resonance. [Yip98, 802]

The same should follow for the emission resonance as well, which differs only by the Stokes shift corresponding to the exciton binding energy. While Yip worked with InAsP/InP and InAsP/InGaP quantum wells, this quenching may be expected to be even more prominent in indirect-gap materials that rely on relaxation of the momentum selection rules for luminescence. By reintroducing a spatial dependence to the eigenstates that increases the expectation value of the hole/electron separation distance, the external field decreases the localization of the system. In addition to the decrease in resonance that occurs in direct-gap quantum systems, there should be an additional decrease in the oscillator strength from the loss of Heisenberg-related momentum smearing.

There is a strange disagreement about the quantum confined Stark-effect in the literature. In bulk (non-quantum) semiconductors which show excitonic behavior (often at low temperatures), the Stark-effect results in a blue-shift because the binding energy of the exciton subtracts from the gap energy. When the exciton is destroyed by the electric field, the emission energy increases by an amount equal to the binding energy. Haung describes the same phenomenon in quantum confined systems

[Hau89]. While this blue shift contradicts the red-shift described by Yip et al., Haung confirms that highly confined quantum systems are excitonic at room temperature and that moderate electric fields cause large decreases in the oscillator strength of such systems. While the author finds the argument of Yip more compelling, it may not be necessary to resolve the red/blue-shift dispute for purposes of this study.

If a distribution of quantum dot sizes were responsible for either broad PL band in sp-Si, it may be impossible to observe any Stark red or blue-shift because its magnitude may be insignificant compared to the total width of the band. However, intensity quenching would apply to each nanoparticle in isolation and should be seen. A total lack of any Stark-effect quenching in the UV/blue band sp-Si will be reported in Chapter 9.

Limitations of the Various "Size-Effect" Models

An ideal theory would be capable of predicting the whole range of semiconductor properties from a single atom to an infinite bulk crystal. This is clearly not available. Different approaches are used for different scales or ranges. Bloch functions do a good job of predicting the band structure of infinite crystals, other models can account for surface relaxation in finite crystals, etc. The quantum confinement approach, especially in its simplest form (the particle in a box) seeks to extrapolate the behavior of small particles from their bulk properties. At the other extreme end of the spectrum, molecular models seek to explain the behavior of molecules and small clusters by building them up from individual atoms and atomic bonds. More sophisticated "quantum" models blur the line as to exactly what category they belong to. Of course, the natural system is not changing, only the model. The ultimate test of any model is how well it works at predicting the behavior of real systems. A number of papers, considered under the broad umbrella of quantum confinement literature, blur these lines between the molecular approach and the quantum size effect approach.

Khurgin reports that real Si/SiO_2 quantum dot systems do not exhibit luminescence that corresponds well to the ideal model where the blue shift is inversely proportional to the square of the particle diameter [Khu96]. After acknowledging that this lack of correlation has led to models based on oxidation and surface states, Khurgin suggests that the discrepancy may be accounted for by considering that a majority of the luminescence may come from a small portion of the size distribution of particles. A model similar to the effective mass approximation, but that takes into account all three lattice directions, demonstrates that the oscillator strength (OS) of luminescence depends only on the smallest dimension of a nanoparticle, not on the average dimension. Furthermore, the OS is proportional to d^{-6}, where d is the smallest dimension. With such a nonlinear relationship, the mean particle size measured by Raman or other means is less important than the size of the smallest population of particles, which will contribute most of the luminescence. While the author agrees with this in principle, the d^{-6} relationship is questionable as nowhere in the derivation did Khurgin account for the finite barrier of a Si/SiO_2 quantum dot. A more rigorous treatment by Hybersten finds that the OS of a quantum dot varies with d^{-6} only for the idealized case of an infinite barrier and with as little as d^{-3} for finite barriers [Hyb94]. Finally, Khurgin et al. achieved a close fit to empirical results by assuming a 2 nm size distribution about the mean. These results fit data for systems exhibiting luminescence between 1.7 and 2.7 eV. Despite the good fit between this modified theory and the observations, Khurgin has an excellent grasp of the limitations of the quantum confinement model:

> It is important to note that this statement is not contradictory to the alternative model: since size of the NC's [nanocrystals] is of the same order of magnitude as the size of the exciton in the silicon oxide or siloxene, and/or the spatial extent of the surface state, the probability of electron-hole recombination determined by the volume in which they are confined, should be roughly the same for the exciton, surface state, or quantum confinement. In this respect, making the distinction between the quantum confinement, surface state, and defect makes very little sense on the nanometer scale. [Khu96, 1243]

Quantum Dots as Large Molecules

Three papers that blur traditional lines are discussed in this subsection.

In the first paper, Delley uses a density functional approach to calculate the (absorption) band-gaps of small silicon structures ranging from a single silicon atom to a 3 nm (706 Si atom) nanoparticle as well as an extrapolation all the way up to bulk silicon [Del93]. The claim is made that dangling bonds would completely mask the effective band gap, so all dangling bonds were considered to be hydrogen terminated. After correcting for self-energy considerations using a Green's function dynamically screened interaction approximation, the calculated band-gaps at both extreme ends of the size scale are very close to the known values (within 0.1 eV for bulk Si and within 0.3 eV for pentasilane). Through a symmetry consideration, the model also predicts the pseudo-direct gap behavior that occurs in small particles. This may be about as close as one can get to an ideal model for Si particles of all scales, at least in these respects. The model predicts that the band-gap varies with $N^{-1/3}$ where N is the number of Si atoms in the cluster (this is essentially d^{-1} for spherical clusters) while the OS is nearly constant for clusters of 1-30 atoms and decreases exponentially with the number of atoms above 30. A band-gap of over 6 eV is calculated for a single silicon atom and a band-gap of 2.5 eV is calculated for a 3 nm (706 atom) nanoparticle. The latter is claimed to correspond to the smallest observed particles at the time of submission and to be in agreement with the observed absorption energy values.

In the second paper, Ebihara reports on the PL and EL of polydihexylsilane (PDHS) [Ebi97]. While no models are presented, if the preceding papers are accurate, such a small molecule is the logical extension of the concept of a silicon quantum dot to smaller sizes and higher energies. PL emission is reported to be at 3.35 eV (370 nm) at 77 K and 3.23 eV (384 nm) at 4.2 K. The quantum efficiency is less than 0.1% at 300 K and it increases to almost 0.7% at temperatures near 4.2 K. The trend is fairly linear. At room temperature, this peak is close in energy to the UV/blue peak of sp-Si but, as will be seen in Chapter 8, the thermal quenching of sp-Si is nonlinear. Also, Ludwig observed no thermal shift in the UV/blue peak, but the author did observe a blue shift with increasing temperature.

In the third and final paper, Filonov presents a fascinating report on the calculated electronic properties of Si_{14} clusters with varying degrees of oxygen involvement [Fil98]. The Si_{14} cluster is highly symmetric and corresponds to a silicon nanoparticle about 0.8 nm in diameter. Filonov starts with a fourteen atom lattice "fragment" with a vertical direction corresponding to the bulk Si <111> axis and atoms at their standard diamond lattice sites. There are 16 Si-Si bonds and 24 dangling bonds that are hydrogen terminated. This initial molecule is, thus, $Si_{14}H_{24}$. The effect of adding oxygen to the structure is determined by building additional prototype molecules one additional oxygen atom at a time. Two possibilities were studied: replacing terminating hydrogens by -OH groups and inserting -O- bridges between Si-Si bonds. The second scheme is limited to the addition of 16 oxygens, one into each of the 16 Si-Si bonds, and the decision was made to limit the number of oxygen atoms incorporated by both schemes to 16. To this end, 21 prototype molecules were constructed: $Si_{14}H_{24}$, $Si_{14}H_{24-x}(OH)_x$ with x between 1 and 16, and $Si_{14}H_{24}O_x$ with x between 1 and 16 (the following values of x were skipped in both cases: 2, 4, 7, 9, 11, and 13). The latter structure essentially approaches a silica, not silicon, quantum dot. For each x value, the lattice relaxation of the structure is estimated using an MM2 routine and the lowest energy locations for the oxygen atoms are selected. The candidate structures are then further optimized using molecular orbital theory. The specific theory used was MO LCAO theory using the Modified Neglect of Diatomic Overlap-Parametric Method 3 (MNDO-PM3) in the restricted Hartree-Fock approximation. Only valence electrons were considered as individual bodies. Core electrons were modeled as part of the nucleus. This method allowed both the ground and excited states to be modeled, neatly giving absorption, emission, and Stokes shift energies for every structure. The simplest $Si_{14}H_{24}$ structure has an absorption band-gap of about 4.4 eV and an emission energy of 3.7 eV, giving fairly close agreement with more common quantum confinement models.

Hydrogen replacement by -OH groups at the surface resulted in little change in the emission energy of the cluster but there was a continuous decrease in the absorption energy with increasing -OH incorporation. This also resulted in a decreasing Stokes shift with more -OH that was attributed to a decrease in physical relaxation of the excited state due to mutual repulsion among the electronegative -OH groups at the surface. The addition of bridging -O- in the bulk of the dot gave significantly different results. The Stokes shift was essentially constant for values of x between 0 and 10, which is attributed to the lack of influence of the oxygen on the surface that undergoes relaxation. The bulk is already too tightly bonded to suffer significant relocation of atoms. The conclusion is made that the Stokes shift in a quantum dot is essentially a function of surface termination. As x approaches 10, the absorption and emission energies decrease in a linear fashion. With x between 14 and 16, the energy levels are radically different (they suddenly increase about 2 eV) and the Stokes shift is tiny. It is actually negative when x is 16, indicating that the ground state is unstable. When x is 12, the energies and Stokes shift are intermediate between the two forms. It is in this range that the molecule looses its silicon character and takes on properties similar to silica. The overall ground state energies of the oxygen-incorporated structures are lower than those of the -OH terminated ones and are more likely to occur in nature.

The excitation and emission wavelengths and constant Stokes shift of the bridging oxygen-incorporated structure are remarkably similar to the behavior of the UV/blue peak of sp-Si when excited by various wavelengths. However, this is only true over a limited range of excitation energies so it is probably a coincidence. This will be addressed in detail in Chapter 10.

Review of Defects in Silica and Silicon Oxynitrides

Before concluding that known defects in silica and silicon oxynitrides are not responsible for the luminescence of sp-Si, one should consider some broader luminescence literature beyond that which was reviewed in publications by Hummel, Ludwig, et al. This review will concern itself with the phenomenological characteristics of such luminescence only, instead of attempting to review the theory of the luminescence from defects that do not apply to sp-Si. Absorption bands at 165 nm, 240 nm, 258 nm, and 620 nm have already been discussed as well as emission bands at 185 nm, 264 nm, 288 nm, 400 nm, 563 nm, and 650 nm. All of these have been ruled out as candidates for the UV/blue (375 nm) or green (525 nm) emission bands of sp-Si. Some additional emission bands, as well as additional evidence regarding these already presented, are discussed.

Low-Energy Emission Bands

States with emission energies of 2 eV or less are often reported for silica. Three common examples are 1.7 eV (729 nm), 1.9 eV (653 nm), and 2.0 eV (620 nm). Kenyon observed all three emission peaks in silicon-rich silica [Ken96]. The 1.7 eV peak was attributed to oxygen deficient centers (ODCs), while there was no attribution for the 2.0 eV peak. Interestingly, the 1.9 eV center was attributed to quantum structures because it is red-shifted and looses intensity with annealing. However, this band may be the same as the previously discussed 650 nm band. Tohmon also observed 1.9 eV luminescence and claimed that it is a well-known oxygen vacancy related defect [Toh89a]. Shimizu-Iwayama observed the 2.0 eV and 1.7 eV bands but not the 1.9 eV band in ion-implanted SiO_2:Si [Shi94]. The 2.0 eV center was destroyed by annealing at 600 °C and its intensity followed that of the electron spin resonance (ESR) signal of the E' center (believed to be a Si dangling bond at an oxygen vacancy) in SiO_2. The 1.7 eV emission was attributed to carrier recombination at defects on the surface of Si nanoparticles. Clearly, there is disagreement among the authors regarding the source of sub 2.0 eV luminescence in silica. However, as the primary peaks of sp-Si are above this energy range, they can be ruled out nevertheless.

Involvement of Other Elements

Several authors have reported on emission related to impurities in silica or luminescence from silicon oxynitrides. Augustine observed 2.2 eV emission (564 nm) under 2.54 eV (488 nm) excitation from $SiO_xN_y{:}H$ plasma-enhanced chemical vapor deposition (PECVD) films made with a N_2O source [Aug95]. This luminescence increased 10 times after a 20 minute rapid thermal anneal (RTA) and was attributed to bandtail-to-bandtail emission of the oxynitride. Stathis observed the ESR signal of a photoinduced defect in silica that he attributed to nitrogen involvement [Sta84]. Two models were proposed: $\equiv\mathrm{Si{-}O{-}N{-}O{-}Si}\equiv$ and $\equiv\mathrm{Si{-}O{-}N{-}Si}\equiv$. Finally, Poumellec reports 7 absorption bands and associated emission bands in $SiO_2{:}Ge$ [Pou97]. Clearly, the incorporation of other elements into silica can be significant. In sp-Si, likely elements for incorporation are nitrogen, tungsten (already ruled out as contributing to luminescence), and carbon (from organic contamination). The luminescence of sp-Si produced in mixtures of nitrogen and carbon dioxide are reported in Chapter 5. Carbon is associated with a third peak in sp-Si located near, but distinguishable from, the green peak. This peak is not seen in samples not deliberately processed in carboniferous gases, even when a measurable amount of carbon contamination is present. This leaves only nitrogen as a viable candidate for the UV/blue and green emission peaks.

Higher-Energy Emission Bands

Gee and Imai both observed similar defects in silica irradiated by much different means [Gee79, Ima88]. In neutron irradiated silica, Gee observed the 4.3 eV (288 nm) emission band previously reported in this chapter and found it to be associated with a 7.6 eV excitation peak attributed to an ODC. Imai observed this same emission and excitation peak in silica exposed to ArF excimer laser radiation. An excitation band for the same emission was also found at 5.0 eV. All three peaks were reduced in intensity after annealing in oxygen. Tohmon placed these absorption peaks at 7.6 eV and 5.2 eV and claimed three associated emission peaks at 4.3 eV, 2.7 eV (459 nm), and 1.9 eV (653 nm) [Toh89]. Imai attributed the 7.6 eV absorption to a relaxed oxygen vacancy and the 5.0 absorption to an unrelaxed vacancy. In an unrelaxed oxygen vacancy, the Si atoms are near the same positions they would occupy without a missing oxygen. The unbound electrons on the Si atoms have a pseudo-bonding interaction with each other over such a long distance (≡Si• •Si≡). The potential of this system is rather high when the separation is large. If the Si atoms are displaced somewhat, the system can reach a lower potential energy configuration known as the relaxed vacancy. In the literature, the unrelaxed vacancy is sometimes represented by ≡Si/ \Si≡ to distinguish it from the relaxed vacancy: ≡Si—Si≡. As these states do not reproduce the observed excitation spectrum of sp-Si (to be presented in Chapter 8), these defects can be ruled out as well. However, a related defect will be discussed in the next section.

Several authors report absorption bands in silica near 5 eV. Tohmon observed a 5.25 eV absorption associated with 3.1 eV (400 nm) emission that he attributed to 2-coordinated silicon with two excess electrons. [Toh89] While this emission peak is near that of the UV/blue band of sp-Si when excited by 325 nm (3.8 eV) light, it will be shown that this is not the case when sp-Si is excited by energies closer to 5 eV. Kohketsu also observed similar peaks at 5.17 eV and 5.06 eV [Koh89]. The former is associated with emission at 4.3 eV (288 nm) and 3.1 eV (400 nm), and the latter is associated with emission at 4.2 eV (295 nm) and 3.0 eV (413 nm). The decay of the

3.1 eV band had a time constant of 80 μs, which will be shown to be completely incompatible with the UV/blue emission from sp-Si. Kohketsu attributed the former to excess Si in SiO_2 and the latter to small Si clusters containing at least 4 Si–Si bonds. Bagratashvili reported absorption bands at 248 nm (5.0 eV) and 242 nm (5.12 eV) that he associated with emission peaks at 280 nm (4.4 eV) and 455 nm (2.7 eV) for the former, and 296 nm (4.2 eV) and 396 nm (3.1 eV) for the latter. The former was attributed to simple ODCs while the latter was attributed to ODCs associated with germanium impurities. The 455 nm emission was reported to increase in intensity as the temperature was increased from 290 K to 514 K. This is in contrast to the peaks of sp-Si, which are thermally quenched, not activated. Finally, Griscom reported these absorption peaks at 5.0 eV and 5.15 eV [Gri91]. Clearly, there is much disagreement in the literature on these similar peaks. None of which appear to fit the behavior sp-Si. Griscom also discusses a 3.8 eV absorption band that may be linked to peroxy linkages or interstitial Cl_2 molecules.

Review of an Important Transient Defect in Silica

The observed properties and theory of one particular defect should be discussed in detail, because, as will be shown, its absorption curve matches the excitation spectrum of the green PL peak of sp-Si. This transient defect found in both crystalline and amorphous silica is believed to be the self-trapped exciton (STE).

An excellent review of the properties and theory of the STE has been written by Itoh [Ito89]. While the band-gap of silica in either the amorphous or crystalline form is a matter of some debate, SiO_2 of both varieties appears to have a direct transition at 10.4 eV. Even the question of how to define a band-gap in an amorphous material is controversial. The author prefers to call the separation between the mobility edges the "gap" and consider local tail states to be within the gap. Often quoted numbers such as 8 eV for amorphous and 9 eV for crystalline silica are for indirect transitions and may include a significant portion of the tail states in the former case. If one measures the optical absorption at many temperatures and rigorously defines the temperature-independent convergence of the Urbach tails to define the indirect gap, the numbers become 9.1 eV for crystalline and 8.7 eV for amorphous silica.

Electromagnetic radiation above 10.4 eV, as well as ionizing radiation and electron bombardment, have long been known to introduce transient defects in both amorphous and crystalline silica. In amorphous (but not crystalline) silica, this transient defect is credited with being a precursor of many of the defects discussed in the previous chapter. Under such excitation, a 2.8 eV emission is observed. Its decay is exponential in crystalline silica and both non-exponential and blue-shifted with time in amorphous silica (this is characteristic of inhomogeneously broadened donor-acceptor pair emission). Figure 3-21 shows the transient optical absorption reported by Itoh for this defect. A 5.2 eV absorption peak with a 4.2 eV satellite peak are observed. It is remarkably similar for both amorphous and crystalline silica indicating that this state likely arises from the reorganization of bonds in the SiO_2 backbone common to silica in all its forms. This transient state has a triplet ODMR (Optically Detected Magnetic Resonance) signal shift an order of magnitude stronger than that observed for a recombining free electron and hole. The most important evidence comes from the observation that this transient state has a large volume change on the order of one SiO_2 molecular volume per defect.

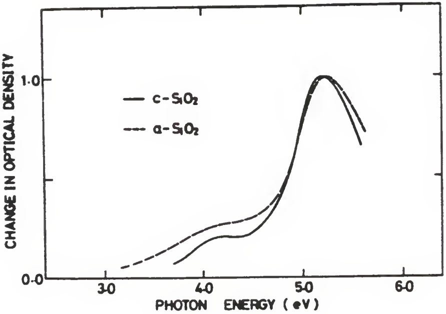

Figure 3-21: Transient optical absorption spectra of the defect believed to be the self-trapped exciton in crystalline and amorphous silica. Adapted from Ito89.

The Model for the Self-Trapped Exciton

The popular model to explain these observed properties is that of a self-trapped exciton in silica, usually abbreviated STE. This is actually a double exciton consisting of an oxygen vacancy with two extra electrons and an adjacent peroxy radical with two holes. Both the defect as a whole, as well as each site individually, have paired spins and are diamagnetic. The structure of this defect is shown in Figure 3-22. Note that in a SiO_2 crystal, the peroxy group must invade the adjacent interstitial site for room and this configuration makes the STE very similar to the close Frenkel pair defect in crystalline silica (and it can be considered a donor-acceptor pair in amorphous silica as well). Most authors simply call it the Frenkel defect, but Itoh is careful in pointing out that it is an isomer of the idealized Frenkel defect because the peroxy group occupies both the standard oxygen site and part of the adjacent vacancy site, giving a smaller vacancy-interstitial separation than in the classical Frenkel pair. The classical interstitially-bonded Frenkel defect for silica would have the extra oxygen simply inserted into the silica linkage in a non-resonant manner instead of as a closely bonded peroxy radical. Thus, it is more rigorous to represent the STE as $\equiv Si\bullet\ \bullet Si{-}O_2^{2+}{-}Si\equiv$ than as $\equiv Si\bullet\ \bullet Si{-}O^+{-}O^+{-}Si\equiv$. This distinction is not trivial, for reasons that will be addressed shortly.

The large Stokes shift between 10.4 eV excitation and 2.8 eV luminescence is attributed to the lattice relaxation necessary to break one Si-O bond and create the subsequent peroxy radical.

In another publication, Itoh makes several additional important points [Itoh88]. Evidence is building that the STE is common in insulating solids with strong electron-phonon coupling. Since SiO_2 is a "lone-pair" semiconductor with the

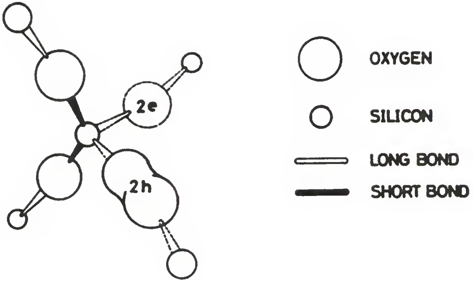

Figure 3-22: Proposed structure of the self-trapped exciton in silica consisting of an oxygen vacancy with two electrons and an adjacent peroxy radical with two holes. Adapted from Ito89.

valence band strongly associated with electrons at oxygen sites and the conduction band strongly associated with electrons at silicon sites, such coupling is unavoidable in silica. Strong experimental evidence of the STE exists for Y_2O_5 and Al_2O_3 as well. It would not be unreasonable to expect the STE to exist in all oxides.

Upon closer examination, Itoh found that the STE can decay through a completely intrinsic process and give the previously reported 2.8 eV luminescence as well as decay by charge transfer to other nearby defects through an extrinsic process resulting in 2.5 eV luminescence. The 5.2 eV transient absorption peak and the 4.2 eV satellite peak are not from separate absorption centers but are a superposition of two transitions of the same center. In an optical bleaching experiment, the fractional change in the optical density across the entire transient absorption spectrum of the STE was found to be completely independent of probing energies between 3.0 and 5.4 eV.

Due to the degree of polarization of the 2.8 eV intrinsic luminescence of the STE, Itoh was able to calculate that the STE is created by the breaking of one Si-O long bond followed by the oxygen entering a peroxy arrangement with the only other oxygen which is long-bonded to that same silicon atom. This is important because Robertson has challenged the model of the STE on the basis that 10.4 eV is not sufficient to break "three Si-O bonds" [Rob85]. It seems that Robertson is adhering to the "ball and stick" model of the peroxy ion being two oxygen atoms with a normal bond between them. It appears much more reasonable to the author that one Si-O long bond is broken and the free oxygen atom resonantly rearranges its electrons with the neighboring oxygen without ever breaking the bonds that the second oxygen atom shares with its silicon neighbors.

It is believed that the 5.2 eV transition results from one of the excess electrons at the vacancy site being promoted from a bonding to an anti-bonding orbital while the 4.2 eV transition results from one of the same electrons being physically transported to a higher orbital of the peroxy radical site, see Figure 3-23. The STE is metastable, which is probably due to the tetrahedral pseudo-bonding that occurs across the vacancy (the ground state of the STE has the two excess electrons in bonding orbitals of the vacancy and two holes in the anti-bonding orbitals of the peroxy radical). The STE decays with a time constant roughly on the order of milliseconds if left alone and nearly instantaneously if excited by either transition. The whole structure becomes unstable if one of the excess electrons cannot "see" the other across the vacancy or if the peroxy radical has even one electron in an anti-bonding orbital. Consequently, a single-exciton STE is never seen because there is no energetic advantage to its formation. The STE relaxes nearly all of the 10.4 eV used in its formation and is only about 2.8 eV in potential above the ground state. There is a significant metastable energy barrier between the STE and the ground state that can be overcome by energies in the range of 3.0 to 4.5 eV. However, the driving force to return to the ground state is not that large and this may explain why the STE readily transfers the offending electron to another defect in the extrinsic process, probably by propagating it along the silica backbone and possibly even accepting a lower energy replacement in the same manner. To occur with any likelihood, this charge transfer process would have to be very fast since the optical bleaching itself is known to be very fast.

The lifetime of the STE is about 1 ms [Hay84] in crystalline silica and about 10 μs [Tani88] in amorphous silica. The decay of the former is in the form of a stretched exponential or power law while the latter is exponential. Non-exponential

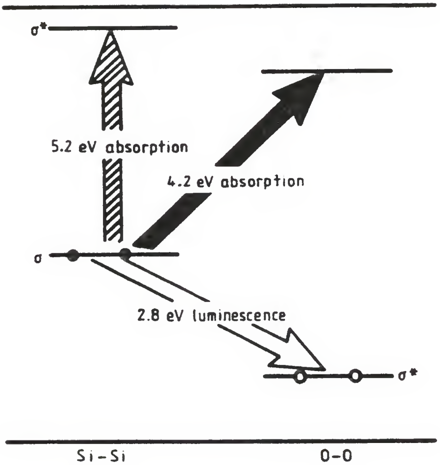

Figure 3-23: Ground state of the self-trapped exciton (STE) in silica with two electrons in bonding orbitals of the Si• •Si pseudo-bond and two holes in the anti-bonding orbitals of the peroxy radical along with proposed optical transitions:

2.8 eV emission from the intrinsic decay process of the STE to normal silica
5.2 eV absorption promoting a vacancy electron to an anti-bonding orbital
4.2 eV absorption transferring a vacancy electron to a higher orbital of the peroxy radical

Adapted from Ito88.

decay is usually observed in donor-acceptor pair luminescence when there is a distribution of pair separation distances. This also explains the observed blue shift with time seen in the PL of the a-SiO_2 STE. While the favorable bonding arrangement of the doubly charged STE (filled bonding orbitals in a pseudo-bond across the vacancy in a configuration some authors refer to as a "relaxed vacancy" and filled bonding orbitals at the peroxide with empty anti-bonding orbitals at both sites) makes this state nearly stable, the driving force for the destruction of the STE certainly comes from the very large strain it creates in the material. While one would expect this strain to be more severe in the crystalline material, the faster time constant of the amorphous case may be explained by the lower diffusivity of the oxygen in crystalline silica. Once the oxygen occupies an interstitial site, it must displace other lattice atoms to return to the vacancy site.

There are important points in three more papers, which involved Itoh, but with either Tanimura or Tanaka as primary authors. These are discussed in chronological order.

Tanimura et al. studied the formation of the STE when silica is exposed to electron bombardment and found the formation process was nonlinear with electron dose [Tani83]. This supports the idea that the singly ionized STE is unstable and that a two-step ionization process is necessary for the formation of the metastable STE. The current must be high enough that there is a significant likelihood of the same "mer" on the silica backbone being doubly ionized within the transient lifetime of the unstable singly ionized STE. In addition, the volume change of the STE was carefully measured and found to be at least one molecular volume and essentially the same for both crystalline and amorphous silica.

Tanaka et al. verified the volume change reported by Tanimura et al. and also discussed the likelihood of a STE explanation for transient absorption bands observed in As_2Se_3 [Tan85].

Finally, Tanimura et al. performed extensive experimental work on electron irradiated amorphous silica [Tani88]. The main transient absorption peak was found to be 5.3 eV for amorphous silica rather than the 5.2 eV reported for crystalline silica, while the satellite band remained at 4.2 eV in both materials, see Figure 3-24. The transient absorption of high purity silica as well as silica with high concentrations of -OH and Cl is identical indicating that this defect involves the backbone structure of SiO_2. A Gaussian deconvolution of the spectrum indicates the two absorption peaks are 5.30 eV with a full-width half-maximum (FWHM) of 0.78 eV and 4.20 eV with a FWHM of 1.16 eV.

Polished silica plates were placed on a 78 K cold finger and irradiated with a 2 MeV 20 ns electron pulse from a Febetron 707 accelerator creating electron-hole pairs in concentrations up to 2×10^{18} cm^{-3}. The time evolution of the PL intensity at 450 nm and the optical absorption at 250 nm were monitored following the electron pulse. Finally, a 308 nm laser pulse from a XeCl excimer laser was used to bleach the transient STE center. Figure 3-25 shows the resulting PL and transmission curves vs. time. t_e represents the electron pulse and t_l represents the laser pulse. The width of the laser pulse and the data sampling rate were not stated. The creation of centers at t_e and the destruction of centers at t_l are too fast for the instrument to clearly resolve. The destruction or bleaching of the center verifies that its excited state is unstable. It should be noted that these plates were only 1 cm thick, yet the material experienced a 70% reduction in the transmission of 250 nm UV light. The absorption

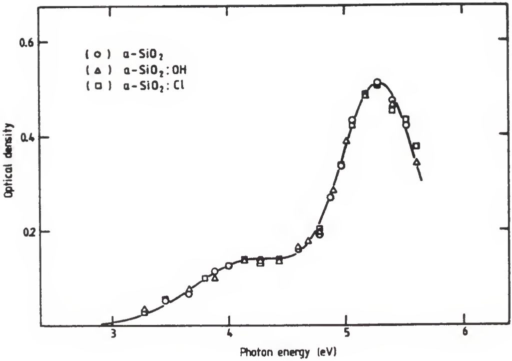

Figure 3-24: Transient optical absorption spectra of the self-trapped exciton in amorphous silica showing no difference among high-purity silica, -OH-rich silica, and Cl-rich silica. Peaks at:

5.30 eV with a FWHM of 0.78 eV

4.20 eV with a FWHM of 1.16 eV

Adapted from Tani88.

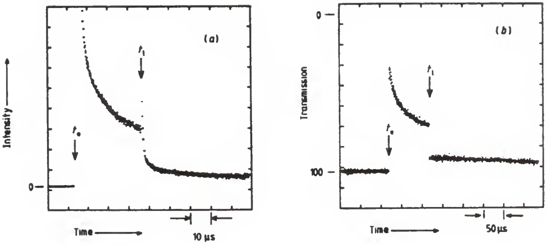

Figure 3-25: Decay of the self-trapped exciton (STE) in amorphous silica:

(a) PL intensity of decay emission (monitored at 450 nm)

(b) optical transmission of sample (monitored at 250 nm)

t_e denotes the 2 MeV electron pulse that creates the STEs while t_l denotes the 308 nm laser pulse that bleaches the STEs. Adapted from Tani88.

at the 5.3 eV (234 nm) peak would be about 20% stronger than it is at 250 nm. Clearly, the STE is a strong absorber of UV light.

Additional Evidence of the Nature of the Self-Trapped Exciton

A number of other sources offer some additional clues to the nature of the STE. Hayes performed OMDR measurements on crystalline quartz [Hay84]. In quartz, as well as amorphous silica, each oxygen atom is bound to two silicon atoms by one long bond (1.612 A) and one short-bond (1.607 A). Each silicon atom has two oxygen atoms connected by long bonds and two by short bonds. Hayes observed that long bonds are weaker and preferably broken. This is consistent with the structure presented by Itoh. A physical explanation of the difference in lifetimes for the STE in amorphous and crystalline silica has already been presented. However, Hayes attributes the 1 ms lifetime of the STE in its unexcited state in c-SiO_2 to his observation that the transition from the STE to the standard silica bonding configuration is spin-forbidden. If this explanation for the time constant is true (as opposed to the limited diffusivity argument previously proposed), one must make the argument that the 100x faster time constant in the amorphous case comes from some relaxation of the spin selection rules that is not seen in the crystalline case.

Silin discusses the transient defect in silica which he also attributes to the STE and describes how it can give rise to more traditional defects like the various E' centers, NBOHCs, and neutral peroxy bridges in amorphous silica [Sil80]. Careful reading of this paper indicates that Silin is actually discussing the singly-ionized version of the STE because of a specific reference to "an electron in an anti-bonding orbital" which makes the exciton unstable. This may be the critical difference between the mechanism that leads to defect formation and that which leads to the metastable doubly-ionized STE.

The Physics of Self-Trapping in Polar Solids

Some explanation of what exactly "self-trapping" means and why it occurs should be made. Mott and Davis are a good source for this but can get quite involved for the casual reader [Mot77]. In general, self-trapping occurs when an electron, hole, or exciton interacts with the lattice in such a way that it becomes distorted and the combined system has a lower energy than the free carrier. It is called self-trapping because the defect did not exist prior to being induced by the carrier; rather, the carrier created the defect to minimize the total energy of the system. Such a state is essentially a molecular polaron. The hindered-rotor problem and the Jahn-Teller effect from solid-state physics are analogues of self-trapping. Self-trapping occurs only when the lattice distortion is large enough to create a global minimum in the energy vs. coordination coordinate plot, see Figure 3-26 for an example. A local minimum is not sufficient for self-trapping at finite temperature as such metastable states are very shallow and free carriers can find their equilibrium position within a few lattice vibrations. Such thermalization is a femtosecond process [Bla94]. Strong interactions between the lattice and carriers occur in silica because it is a "lone-pair" insulator with a valence band made up of oxygen 2p-orbitals. This, combined with a reasonably large band-gap, guarantees that nearly every outer-shell electron in the solid is at an oxygen site. This strong polar nature of the lattice provides the needed carrier-phonon coupling. Self-trapping has been reported in many oxides including MgO, CaO, SrO, ZnO, BeO, and Al_2O_3.

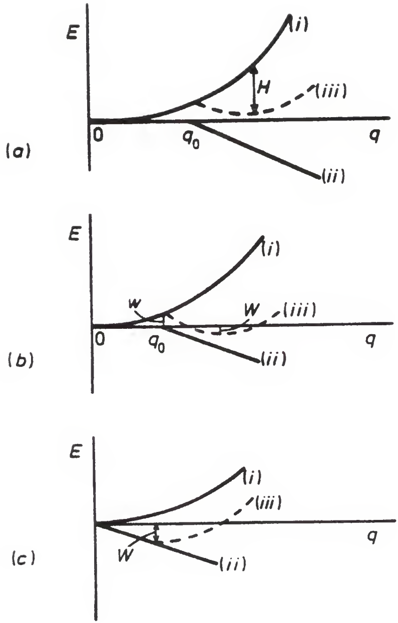

Figure 3-26: Theoretical self-trapping mechanism for a hole:
(i) denotes the elastic energy, **(ii)** denotes the electronic energy, and **(iii)** denotes the total energy.

(a) no polaron is formed

(b) a polaron is formed with trapping energy W

(c) the case of trapping by a pre-existing defect.

Adapted from Mot77.

The Polar Nature of Oxides and "Lone-Pair" Insulators

The domination of the valence band by oxygen in an oxide is explained in simple terms by Fowler [Fow86]. Taking SiO_2 as an example, each silicon atom contributes 4 valence electrons while each oxygen atom has 6 electrons in its outer shell. There are also two oxygen atoms for every silicon atom. This means that there are 12 valence electrons contributed by oxygen for every 4 contributed by silicon. Even if the bonding were covalent, the oxygen would contribute 75% of the total valence electrons. However, the Si-O bonding is highly ionic with the electrons favoring the oxygen. For this reason the valence band is almost totally dominated by electrons at oxygen sites.

In this same paper, Fowler also discusses the nature of the bonding across the oxygen vacancy in silica and supports the idea of a pseudo-bond bridging the vacancy:

> Even with the structural constraints imposed by the crystalline environment the silicons will approach to ≈2.5 Å [2.35 Å for amorphous] apart. . . . The suggestion that the O vacancy is better thought of as a Si-Si bond seems to be valid. [Fow86, 174]

In addition, Fowler discusses the STE in some detail. The paper is supportive of the position of Itoh, Tanimura, and Tanaka but does mention that some controversy exists on the subject. For example, based on the same evidence for the relaxation of the oxygen vacancy, Fowler points out that one would expect the oxygen vacancy associated with the STE to lead to a contraction and not an expansion as observed. The discussion closes with:

> Although no calculations have yet been reported which bear on the stability of this self-trapped exciton, it is reasonable to assume that the system has found the lowest energy atomic arrangement consistent

> with its being an excited electronic state; in a configuration-coordinate picture it is at the minimum of the excited-state curve. Apparently there are no low-energy crossovers to the ground-state configuration coordinate since radiative de-excitation occurs. [Fow86, 179]

Summary of the Properties of the STE

Mott has stated unambiguously that the coordination coordinate is a stress-related concept [Mot75]. Taking this into consideration, we can conclude that the STE is chemically and electronically stable, but is not favored elastically. This elastic constraint is relatively small in magnitude, as the chemical and electronic stability of the STE relaxes all but 2.8 eV of the 10.4 eV potential of the classical exciton.

The singly-ionized STE and the electronically excited STE are unstable. The excited STE decays either by returning to its own ground state by a fast charge transfer process or by the destruction of the STE itself (driven by the elastic strain). This charge transfer process has been observed and must be at least as fast as the destruction process to be observed at all.

The STE is formed spontaneously from hole-electron pairs in silica and can be formed by any process that provides the requisite 10.4 eV of energy needed to create the pair. The lifetime of the STE in amorphous silica is on the order of 10 μs.

A Thought Experiment Involving the STE

Rather than leave the reader in the dark for several chapters as to why the STE is important, the author believes that a small amount of argument foreshadowing the eventual conclusions of this study is appropriate at this point in the discussion. Consider the following thought experiment: What would happen if the elastic constraints of the silica matrix on the STE were somehow eliminated or even reversed? The STE would remain chemically and electronically stable (no net charge, no unpaired electrons, and no electrons in anti-bonding orbitals) but would no longer have the elastic driving force working against it. With this constraint removed, the metastable energy barrier between the ground state of the STE and normal silica would be at least 7.6 eV (10.4 eV - 2.8 eV) as the electronic and chemical portion of the relaxation are at least this large (the elastic contribution being negative). The excited state of the STE (4.2 eV or 5.3 eV above the ground state) would still be electronically and, especially, chemically unstable due to its anti-bonding nature, but would not be able to overcome the larger potential needed for the destruction of the STE in the absence of the elastic driving force. Under these conditions, the charge transfer mechanism, already significant, would become the dominant pathway for the de-excitation of the STE. The STE would remain as a very stable defect with strong UV absorption and provide energetic carriers to nearby defects.

There is actually some evidence supporting this idea in the literature. Edwards investigated the nature of the peroxy-radical defect in a-SiO_2 using a semi-empirical molecular-orbital computer program (MOPN) [Edw82]. The majority of the paper supports the idea of a peroxy-radical linkage as a precursor to the well-known defects in silica. However, the observation is made that the peroxy linkage is actually more stable than the single oxygen atom bridge when a great amount of disorder is present, specifically: large separations between silicon atoms or highly twisted silica tetrahedra.

Could a material possess so much disorder that unstrained STEs could actually exist? It is easy enough to make temporary STEs as any process that can generate electron-hole pairs will do. If these hole-electron pairs were generated in silica, which was nearly molten or sufficiently plastic to allow the surroundings to adjust to the volume of the STE, followed by a rapid quench within the lifetime of the STE (on the order of 10 μs), this might not only be possible, but likely.

General Review of Luminescence Processes

There are a number of general processes in materials that result in the emission of light (luminescence). The most commonly reported are shown in Figure 3-27. These are conduction band to acceptor transitions (a-i), donor to valence band transitions (a-ii), donor to acceptor transitions, or "pair emission" (a-iii), direct recombination from the conduction band to the valence band (may involve excitons or phonons) (b-i), direct recombination of "hot" carriers across the band-gap, or "avalanche emission" (b-ii), and finally, intraband transitions involving "hot" carriers, or "deceleration emission" (c). However, this is not a complete list. There are two additional types of radiative recombination processes that deserve consideration. These are processes that involve activator centers and isoelectronic centers.

Activator Centers

The author shall adopt the definition of an activator center from Henisch [Hen62]. An activator is a donor or acceptor defect that has such a large binding energy that its energetic location in the band-gap is close to the band-edge associated with the opposite carrier. A donor activator is located near the valence band edge and

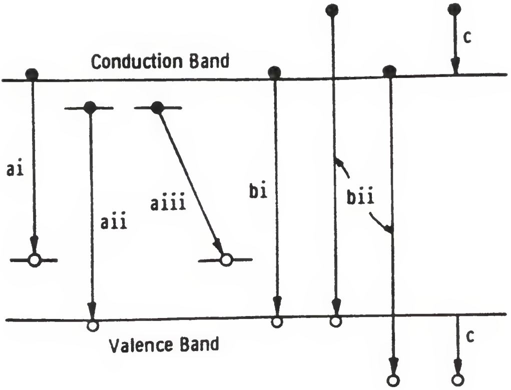

Figure 3-27: Commonly reported radiative recombination processes in materials, see text. Adapted from Ive66.

an acceptor activator is located near the conduction band edge. These defects defy the normal logic that donors always lie in the top half of the gap and acceptors in the lower half. These defects have a binding energy that is much higher than that predicted by only electronic considerations and is dominated by lattice energy (strain and chemistry) considerations. Figure 3-28 shows the locations of such activator centers and their ionization processes. Notice, that unlike the case of shallow donors or acceptors, the spontaneous ionization process can involve charge transfer from the opposite band (processes a-iii and b-iii). For reasons to be discussed, activators have huge carrier capture cross-sections and strong oscillator strengths for recombination. This class of impurities plays a very important role in luminescence, particularly in "activating" electroluminescence, hence the name "activator."

Unlike unionized donors or acceptors that can be ionized by a radiative transition, activators can be ionized by charge transfer from another defect or the matrix, and can serve as efficient charged recombination sites. This is depicted in Figure 3-29. Electron-hole pairs (from injected current in this depiction, but they may come from any process) recombine in the following manner: First, a hole is transferred to the unionized donor activator from the valence band, ionizing it in the process. Next, an electron recombines with the hole bound to the activator in a highly localized radiative process. The depiction in Figure 3-30 is even more rigorous as the process is inherently excitonic. The electron is actually transferred to an excited orbital of the charged activator, either from the conduction band or various intermediate trapping states. This transfer can be by either a multi-phonon relaxation process or tunneling from a trap state that happens to lie at a resonant energy. Both processes can be very fast. Once transferred, the bound exciton undergoes a radiative recombination. Of course, similar charge transfer processes can take place for the

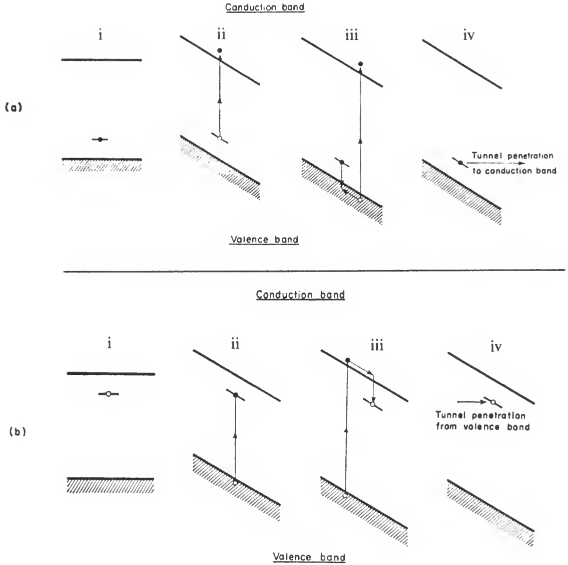

Figure 3-28: Activator centers and their ionization processes:

(a) a donor activator center

(b) an acceptor activator center

- **(i)** center in the ground state
- **(ii)** direct ionization
- **(iii)** ionization by charge transfer to or from a previously created hole (a) or electron (b)
- **(iv)** field ionization by tunneling

Adapted from Hen62.

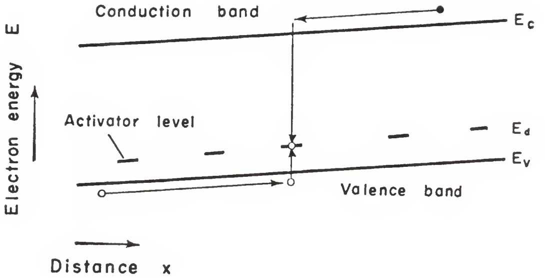

Figure 3-29: Carrier recombination at a donor activator center. The activator is ionized by the transfer of a hole from the valence band. The electron in the conduction band combines with the hole bound to the center. Adapted from Hen62.

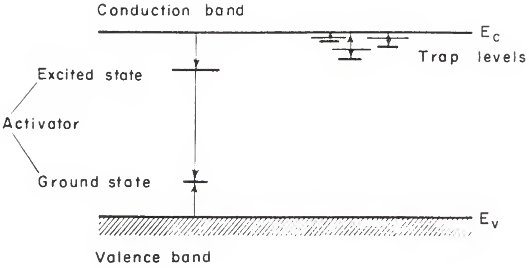

Figure 3-30: More rigorous depiction of carrier recombination at a donor activator center. The activator is ionized by the transfer of a hole from the valence band. The electron from the conduction band or various intermediate trapping states is transferred to an excited orbital of the charged activator by multi-phonon relaxation or tunneling. The bound exciton then undergoes a radiative recombination. Adapted from Hen62.

transfer of the initial hole, as well as for the electron and hole in the analogous case of an acceptor activator near the conduction band.

Isoelectronic Centers

Isoelectronic centers are defects with the same valence as the atoms they replace but act as trapping or recombination centers. Their significant binding energy is believed to come from differences in atomic size or electronegativity rather than coulomb interactions of valence electrons. Like activators, they have a large trapping cross-section for free carriers and, once ionized, readily form excitons by attracting a carrier of opposite charge. Isoelectronic centers were first reported in GaP in 1965 by Thomas et al. [Tho65]. They have been found to be particularly useful in the InP, $Ga_xIn_{1-x}P$ [Lor68] and $GaAs_{1-x}P_x$ [Gro71] semiconductor systems. For most applications, nitrogen has been found to be a particularly effective isoelectronic center.

Practical Considerations

Activator centers, isoelectronic centers, and more conventional "deep" donors or acceptors have several advantages over their shallow counterparts for enhancing the luminescence of both direct and indirect-gap semiconductors.

At first glance, direct-gap semiconductors appear to offer the best potential for luminescent devices with their fundamentally high likelihood of carrier recombination across the direct gap. However, the low Stokes shift of this very same direct gap can result in a substantial reabsorption problem in practical devices. This problem can be exacerbated by concentration or strain gradients in ternary or quaternary systems, which cause band-gap gradients. Luminescence from deep states introduces a large enough Stokes shift to the emission to eliminate the problem of reabsorption. In addition, the recombination efficiency of even direct-gap semiconductors can benefit from such centers as their carrier capture cross-sections compete favorably with non-radiative mechanisms.

Indirect-gap semiconductors are normally considered to be poor candidates for phosphors because the low probabilities of phonon-induced recombination. However, indirect-gap materials are often the only practical choices with band-gaps large enough to host green or blue radiative transitions. In such indirect systems, activator centers and isoelectronic centers induce enough localization in their trapped carriers so as to relax the momentum selection rules and create significant luminescence. This is not speculative theory but is seen in many real phosphors in practical use today.

There is another fundamental issue which plagues both direct and indirect-gap materials, but is particularly problematic for indirect-gap materials. This is the problem of non-radiative Auger deexcitation. In the Auger process, the energy of a recombining electron-hole pair is not released as light, but as the kinetic energy of a second electron. Due to its rest mass, the electron carries more momentum than a photon of the same energy and the Auger process can dominate when there is a substantial difference in momentum between electrons and holes, as is the case with indirect-gap materials. The Auger process requires the presence of a "bystander" electron and is more likely the higher the free-carrier concentration. It is for this reason that p^+-p-n-n^+ or even p-i-n diodes are often used as light-emitting diodes (LEDs) to minimize the carrier concentration in the active region. However, in the case of center-activated luminescence, defects must be present in the active region in substantial quantities. This is where the isoelectronic center is of great advantage because it is neutral and does not contribute to the free carrier concentration. Nitrogen-activated indirect-gap semiconductors dominate the blue LED market today. Because so much lattice energy is associated with activator and isoelectronic centers, their crystal solubility is limited. This places an upper limit on the efficiency of such systems.

Theoretical Considerations

Dean studied isoelectronic traps and deep bound states and found that they have similar properties despite the lower binding energies of the isoelectronic centers. Both states have strong phonon cooperation (electron-phonon coupling) and large carrier capture cross-sections [Dea70].

In an isoelectronic trap, which is initially neutral, the whole of the binding energy between the trap and the carrier is due to interactions with the free carrier wavefunction in the vicinity of the impurity atom and not from electrostatic forces. Lattice vibrations have a strong effect on the energy of the state and this causes the strong electron-phonon coupling. This can be considered in a different way. It is well known that an electron bound to a square well, even weakly, possesses sharply changing wavefunction gradients at the boundaries. Such large gradients are responsible for the observed strong wave-vector-independent phonon coupling. Figure 3-31 shows the radial dependance of the wavefunction of an electron with an effective mass of 0.35 m_o trapped by a square potential well with a width of 2 Å and a barrier height of only 10 meV. The trapping is stronger than that from a conventional donor with an electrostatic binding energy of 100 meV. Also, the electrostatic case does not exhibit the sharp gradient at the boundary. Transitions with strong phonon

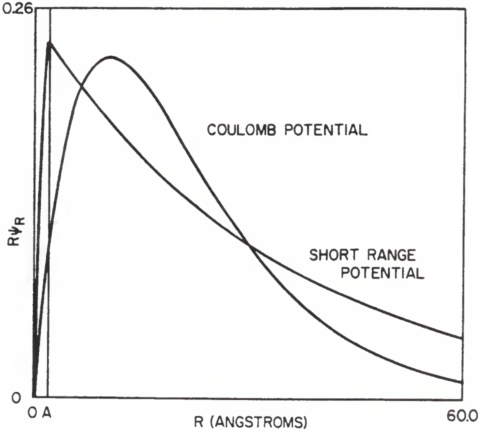

Figure 3-31: The radial dependence of the wave function of an electron with an effective mass of 0.35 m_o trapped by a square potential well with a width of 2 Å and a barrier height of 10 meV compared to that of the same electron trapped by a conventional donor with an electrostatic binding energy of 100 meV. Adapted from Dea70.

coupling are associated with broad (inhomogeneously broadened) bell-shaped emission bands, as in the case of the F center is alkali halides [Fow68].

The large capture cross-section seen in these traps also comes from the short-range potential. The anomalously high electron scattering cross-section of the deuteron, a weakly bound proton and neutron, is a classical example of this phenomenon.

If the majority of the binding energy of a deep donor or acceptor is derived from lattice potential, the trap will behave in a very similar manner to an isoelectronic trap. According to Dean, the carrier-phonon coupling will be strong if the defect binding energy is roughly 5 times as great as that predicted from the "effective-mass energy" of an ideal donor or acceptor according to Faulkner's theory [Fau69]. The deep donor oxygen and deep acceptor silicon in GaP are excellent examples of deep states that offer efficient radiative recombination.

According to Bube, a center that captures electrons with a binding energy E_b will act as a recombination center below a critical temperature, T_c, and act as a charge trap above that temperature [Bub60]. The relationship is given by: $T_c = E_b \ln(N_c \upsilon \sigma_c / 2\beta)/k$, where N_c is the density of states in the conduction band and β^{-1} is the lifetime of the radiative recombination process. If the carrier-phonon coupling is strong, the exciton can shed its excess momentum through a multi-phonon cascade, which is virtually instantaneous. Even for isoelectronic traps with shallow binding energies, the recombination rate is so high that the critical temperature is above room temperature. Deep states, particular activator centers, which are very deep, have both a high binding energy and strong lattice coupling. T_c is very high for such states.

Aggregation of Defects

Due to the large lattice energy of isoelectronic traps and activator centers as well as conventional deep donors and acceptors, these impurities have limited solid solubility. There is a strong tendency for such defects to minimize their total interfacial energy by forming clusters that act as one electronic state. A donor and acceptor may become nearest neighbors and become a neutral isoelectronic center. The ZnO center [Ber76] and CdO center [Dea70] in GaP, as well as the CuGa center in ZnS [Dea70] are examples of this. Some activator states are comprised of three or more nearest neighbor impurities. Dean presents several examples of radiative transitions involving multiple defects, see Figure 3-32. Fig 3-32a shows charge transfer from a donor to an isoelectronic center. Figure 3-32b shows the same process when the center is a donor-acceptor pair ("triade" emission). Figure 3-32c shows both an electron transferred from a donor and hole transferred from an acceptor to an isoelectronic center. Figure 3-32d shows the same process when the center is a donor-acceptor pair ("trapezoidal dipair" emission). The strong phonon-coupling of such states make charge transfer likely and a variety of transitions can take place when multiple defects are present.

As previously mentioned, nitrogen is used as an isoelectronic center in GaP. GaP is an indirect-gap semiconductor with an energy gap of 2.26 eV. When nitrogen is added, greatly enhanced luminescence is observed at 2.18 eV (570 nm). However, when the doping concentration of N exceeds 10^{19} cm^{-3}, the emission shifts to 590 nm (2.10 eV) due to the formation of N-N nearest neighbor pairs [Wil89]. The formation of these pairs is nonlinear with N doping concentration and occurs above a threshold level. The intensity of the green band of sp-Si and the bands of several other spark-

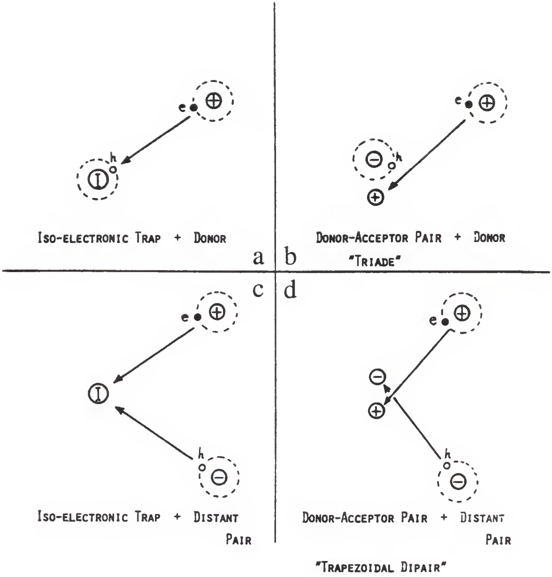
e
h
I
Iso-electronic Trap + Donor
e
h
Donor-Acceptor Pair + Donor
"Triade"
a
b
c
d
e
I
h
Iso-electronic Trap + Distant Pair
e
h
Donor-Acceptor Pair + Distant Pair
"Trapezoidal Dipair"

Figure 3-32: Radiative transitions involving multiple defects, see text. Adapted from Dea70.

processed materials will be shown to have an exponential dependence on the nitrogen concentration of the gas ambient during processing.

Conclusions

These various luminescent processes and their properties were presented in this section and the previous section as a primer for the reader so that the PL mechanisms of sp-Si can be better understood. As the properties of sp-Si and other spark-processed materials are explored and reported in the experimental chapters of this work, the reader should keep the behavior of deep centers and the STE in mind. This knowledge will be used to construct a proposed model for the states or molecular species responsible for the PL of sp-Si in Chapter 10. This model will address all of the experimental results and observations.

CHAPTER 4
MATERIALS, METHODS, AND EQUIPMENT

Materials

The vast majority of the experiments reported in this work used the same batch of silicon wafers from Wacker-Chemitronic. These were p-type B-doped <100> wafers with a concentration range of 3.8 - 5.5 x 10^{15} cm^{-3} and a resistivity range from 2.5 - 4.0 Ω cm. These were standard 4" (10 cm) wafers but were unusually thick (625 mm). For the vast majority of experimental work, the wafers were diced into 0.400" x 0.300" (1 cm x 3/4 cm) chips. The thickness of these chips gave them significant durability during handling and made sparking completely through the sample very unlikely, even for prolonged processing durations. Other materials used in this study were highly pure and will be discussed on a case-by-case basis.

The gases used in this study were all ultra-high purity (UHP) with the exception of carbon dioxide, which was instrument grade. Grade 5.0 UHP oxygen and grade 4.4 UHP nitrogen were used.

De-ionized (DI) water and electronic grade solvents including methanol, acetone, and trichloroethane (TCE) were used exclusively. A standard aqueous MOS etching solution consisting of a 40% concentration of 6 parts NH_4F and 1 part HF as well as Micro-90 brand electronic grade soap were also used.

Methods

Sample Preparation and Cleaning

A large number of samples were prepared for spark-processing including semiconductors, semi-metals, and metals. For each material, the most appropriate choice of a wafer dicing machine, diamond band-saw, or slow-cutting carbide wheel saw was used to cut the samples. Some ductile materials were available as wire and these were pounded flat with a hammer before polishing. Materials, which were not flat, were polished on a standard metallurgical polishing wheel. Small or irregularly shaped samples were attached to electrically conductive holders with silver-bearing paint. These holders were often highly doped silicon chips or copper (pre-1982) pennies, which had been cleaned with the same procedure as the samples.

All samples were cleaned by the same general procedure. The samples were cleaned in a heated ultrasonic cleaner in 15 minute steps. These steps included DI water and electronic grade soap, DI water, TCE (when necessary for degreasing), DI water, acetone, DI water, and methanol. The samples were then placed in a teflon dish containing a 50%/50% mixture of MOS enchant and methanol (to prevent bubble formation, which gives an uneven etch) for a time that depended on the etch rate of the material oxide in question (about 15 minutes for Si). This was followed by a rinse in DI water, and another 15 minutes in the ultrasonic cleaner with DI water, followed by 15 minutes with methanol. The samples were then dried by pressing them lightly between clean-room grade towels.

Spark-Processing of Samples

Power supply for spark-processing

As discussed in Chapter 2, the equipment and methods were improved and refined during the course of this study. Three general phases of this development were defined as Stage I, Stage II, and Stage III.

Stage I spark-processing involved the use of a Tesla coil, high voltage DC supply, or the pulsed high voltage supply from the flyback coil of a CRT (referred to as monitor-sparking). In the case of a DC supply, the frequency of the free-running spark gap is a function of the geometry of the gap and the breakdown potential of the gas ambient. Spark gaps, which exhibit negative differential resistance, have been used as oscillators for many years even before the invention of semiconductor devices or even vacuum tubes. The capacitance of the gap, as well as any stray capacitance in the system, is charged up by the supply until the dielectric breakdown voltage of the gas is achieved. The current of electrons moving toward the anode ionizes the gas molecules in the gap and these ions are in turn accelerated toward the cathode. When the gap is in breakdown the resistance drops dramatically, quickly draining off charge. This resets the system to a non-conducting state as the power supply charges it back up again. There is no control over the frequency of sparks or the duration (pulse width) of each spark event. The pulsed supplies (Tesla coil or monitor) may or may not operate as a free-running gap, depending on whether the gap geometry and gas ambient allow breakdown to occur for every voltage pulse. In this ideal case, the frequency is fixed but the pulse width is not controlled. All of these power supplies used in Stage I are essentially fixed voltage supplies that supply an unregulated current. The current depends on a number of other factors including the physical gap parameters, the gas ambient, and the conductivity of the sample. It is impossible to isolate the production variables with this kind of a supply as any change in material, gases, or tip geometry changes the spark current.

Stage II involved the use of a custom high voltage pulse generator manufactured by North Star Research Corporation in Albuquerque, New Mexico. It used a tetrode tube to switch the spark current on and off. Power was supplied by a model 830-33 1.5 kW variable 30 kV supply from Hypotronics. Because of the 4-pole arrangement of a tetrode tube, the acceleration of electrons within the tube is provided by the field between cathode and the screen and not between the cathode and the anode, as in a triode device. The tetrode tube's current gain is relatively insensitive to the floating voltage on the anode. The tube provides a square pulse of fixed current with a regulated pulse width at a regulated repetition rate while automatically adjusting its voltage gain and power dissipation to do so. The resonant frequency of the gap, its negative differential resistance characteristics, and the stray capacitance of the system can be ignored as the tube essentially "force feeds" a series of precise current pulses to the sample. In this stage, the various experimental parameters could be isolated from the spark current, which is a very important parameter in and of itself.

The equipment proved to be very unreliable in Stage II. A positive current is required for spark processing, but vacuum tubes switch electrons, which are negative charge carriers. Initially the anode of the tube was grounded and the cathode floated at high voltage. All of the control electronics had voltages that were referenced to the cathode and were floating at high voltage. This caused severe noise problems. Furthermore, all the electronics needed to be isolated from ground. While this might work in the dry air of New Mexico, it did not work in the damp air of Florida. The system evolved from Stage II to Stage III in a frustrating and prolonged series of repairs and redesigns, mostly by the author. The reliability problem was solved by redesigning the machine as a negative pulse generator and inverting the output with a large pulse coil. This allowed the cathode of the tube to be grounded and the grid and screen power supplies and control electronics to all be referenced to ground. This kept the system working. Making sure it worked correctly was another issue altogether.

To avoid interference, the system was initially triggered using fiber optics. However, the fiber optic detector in the system has no hysteresis and was susceptible to noise. This caused a retriggering problem creating a series of pulses for every intended pulse. This was replaced by a system that used a pulse coil to trigger the pulse generator. The electromagnetic and power line noise created by the device caused retriggering in the function generator used to control the pulses. The initial solution was to place the spark generator and the control circuits in different rooms across a hallway and use lots of power line filtering. The problem was finally solved by using an inexpensive non-triggerable sine-wave generator in conjunction with an adjustable pulse generator built by the author. This generator used extensive filtering of the power line and signal input as well as shielding and cleaned up the signal with Schmidt triggers at every stage.

At some point, a radio frequency oscillation problem (known as Barkhousen oscillation) resulted from a change in the secondary electron characteristics of the tube as it aged. The grid and screen bypass capacitances had to be adjusted by trial and error until operation was stable again. Stage III is defined as the point when all of these problems were solved and, in addition, a method of measuring the exact time-average spark current was developed.

The spark current is monitored as a function of time by a non-contact model 2878 current monitor from Pearson Electronics. This device measures current by inductively coupling the differential signal of the current and reintegrating it. The time-resolution is 2 ns and the signal droop is insignificant at the pulse widths the machine is capable of producing. Since the current monitor has no power supply, the time-average voltage at its output must be zero. Thus, the mean current being measured is referenced to the zero voltage level. Since the machine produces unipolar current pulses, the baseline of the measured signal from the current monitor will drop below ground by an amount proportional to the time-average current. Thus, 2 A, 1 μs pulses with a frequency of 10 kHz (1% duty), will produce a negative deflection in the signal baseline representative of the mean current of 20 mA. A device to accurately measure this negative deflection was also constructed by the author.

The gain of the tetrode tube is set by a variable DC power supply (known as the grid power supply) and a variable resistor (known as the grid current limiter). These determine the current gain of the tube and are known collectively as the current controls. For the convenience of the colleagues of the author, the power supply voltage at the anode of the tube and the settings of the current controls (in percentage of maximum) used in a particular experiment may be listed in the experimental chapters. These settings determine the spark current, which is the scientifically interesting value, and are listed only for the benefit of those who will be using the equipment built by the author.

Chamber for spark-processing

Stage II and Stage III spark-processing were conducted in a processing chamber built by the author. This chamber is a vacuum/pressure vessel with a capacity of approximately 5 liters. It has a 12-position sample holder attached to a rotary/linear magnetic linkage, and a sample loading hatch with a glass window. The vessel can be pumped down, baked-out, and back-filled with UHP gases numerous times to reduce contamination. Spark-processing can be performed at a fraction of an atmosphere to over 2 atmospheres (absolute). A model 902058 combination Pirani and diaphragm gauge from Kurt J. Lesker Co. is attached to the chamber. The Pirani gauge is used to measure vacuum and the diaphram gauge is used to measure absolute pressures from approximately 2 mbar to 2 bar. The diaphragm gauge reads true gas pressure independent of the chemistry of the gas and, in conjunction with needle valves, can be used to set the partial pressures of various gases to within +/- 1 mbar. A mechanical gauge is also provided for safety purposes and displays pressure in inches of mercury for vacuum and in psi above atmosphere. The chamber has a safe operating pressure of 25 psi (1.7 bar) above atmosphere. The system includes a modular anode tip holder that can accept various materials or wire of various diameters. This holder is electrically isolated and mounted to a linear micrometer stage that can be used to set the spark gap distance to within +/- 2.5 μm. In the early part of Stage II, this chamber was evacuated with an oil-mechanical pump with an oil vapor trap and a cryosorption pump. In the later part of Stage II, these two pumps were replaced by a turbo-molecular drag pump backed by two diaphragm pumps (Danielson Tribodyn model TD100-120). In Stage III, the author built a miniature water-cooled two-filament titanium sublimation pump to fit the small chamber. This was used in addition to the diaphragm/turbo pumps.

In Stage III, a typical pump-down procedure involves evacuating and back-filling the chamber with UHP gasses approximately 10 times followed by 24 hours of pumping to pressures lower than 10^{-3} μbar (10^{-6} torr) with 15 hours of baking. The titanium sublimation pump is usually run twice (using both filaments) during such a pump-down. If spark-processing in pure nitrogen is desired, the pumpdown is approximately 4 days, with three 15 hour bake-outs, and the sublimation pump is run at least 6 times. Unless otherwise stated, the total pressure of the various gases used during spark-processing is 1 bar (approximately 1 atm).

Characterization of Samples

Room temperature photoluminescence (PL)

The majority of photoluminescent spectroscopy in this work was conducted at room temperature and under continuous-wave excitation (CWPL). Excitation was provided by a 325 nm He-Cd laser. The sidebands of the laser as well as cavity light were greatly reduced by a band-pass filter placed at the exit of the laser. Stray laser light was blocked by an iris. An adjustable aluminum-on-quartz neutral density filter mounted to a linear stage was used to control the beam power. A quartz slide mounted at a 45° angle to the beam directed a small fraction of the beam power to a laser power meter for in-situ monitoring. The beam diameter was approximately 2 mm and it could be focused onto the sample with a quartz lens (0.5 mm dia.) or used unfocused. Samples were mounted to an adjustable XYZ stage using double-sided tape. Light from the samples was collected by a 1" (25 mm) quartz lens with a 5 cm focal length and refocused into the entrance slit of an Instruments SA, Inc. HR-320 scanning grating monochromator at the proper acceptance angle by a similar quartz lens having a 10 cm focal length. A long-pass filter with a 50% cutoff wavelength of 350 nm could be placed in front of the entrance slit to eliminate scattered laser light from the detector. Gratings of various blaze wavelengths could be used in the monochromator (see Appendix B). The light intensity was measured by a Peltier-cooled Hamamatsu R943-02 photomultiplier tube (PMT) with a GaAs detector. The tube was run in single photon counting mode with a preamplifier/discriminator. The PL system is shown schematically in Figure 4-1.

As discussed in Chapter 2, Stage III involved the implementation of means to prevent nonlinearities in the PL system resulting from chromatic aberrations and scattering/diffraction at small slit openings. This finally allowed good calibration curves to be made for the PL system which can be applied to Stage III measurements with great confidence and to Stage I/II measurements with a fair degree of confidence. Details are discussed in Appendix B.

In order to assign the peak locations of PL bands in an objective manner, these determineations were made by a computerized algorithm. A computer program which implements this algorithm is listed in Appendix C (filename: peak finder.bas).

High temperature photoluminescence

High temperature PL measurements were conducted by the author on sp-Si and a number of other materials. Low temperature PL of sp-Si had been adequately explored by Ludwig and was not repeated by the author (see Chapter 3). The author constructed a stainless steel sample stage containing a cartridge heater from Omegalux and a thermocouple. It was mounted to the XYZ stage using a ceramic insulator. The heater was capable of reaching temperatures as high as 700 °C. The stage was inclined slightly and the samples rested on a small ledge.

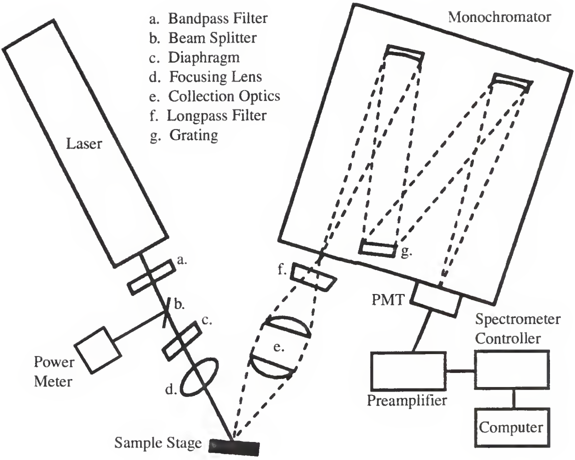

Figure 4-1: Schematic representation of the PL spectrometer used in this study.

Time-resolved photoluminescence

Time resolved photoluminescent spectroscopy (TRPL) was conducted by the author at the University of Rochester's Center for Photo-induced Charge Transfer in Rochester, New York. A pulsed 1064 nm Nd:YAG laser was frequency doubled to 532 nm by a heated nonlinear crystal and used to synchronously pump a 600 nm dye laser. This laser was in turn doubled to 300 nm by a room temperature crystal and used to excite the samples. The final pulse width of the excitation source was under 3 ps. The emitted light was wavelength-resolved by a monochromator and detected with a fast charge plate detector. A single photon counting technique in conjunction with a multi-channel analyzer was used to measure the decay characteristics of the luminescence.

Photoluminescent excitation (PLE)

Photoluminescent excitation measurements of samples produced by the author were conducted at Hewlett Packard (now Agilent) in Palo Alto, California by Dr. Regina Müller-Mach. While the exact equipment used is unknown to the author, the technique involves measuring the PL output intensity of a sample at a fixed wavelength while varying the excitation wavelength. It is similar in principle to an optical absorption measurement, except that it isolates the absorption mechanisms that lead to luminescence while ignoring all other optical losses.

Scanning-electron microscopy (SEM)

A Jeol JSM-35CF scanning electron microscope was used to produce images of fresh fracture surfaces of uncoated sp-Si samples.

Secondary-ion mass spectroscopy (SIMS)

Secondary Ion Mass Spectroscopy was performed by Maggie Lambers on samples produced by the author and Jeliazko Polihronov using a Physical Electronics Model 6600 SIMS. This technique measures the mass/charge ratio of sputtered particles and can be used to give a profile of composition vs. depth.

CHAPTER 5
RESULTS: PROCESSING PARAMETERS OF SPARK-PROCESSED SILICON

Electrical, Temporal, and Physical Processing Parameters

As discussed in Chapter 3, spark-processed silicon (sp-Si) exhibits two photoluminescent (PL) bands under 325 nm laser excitation. These are referred to as the UV/blue and green bands. The UV/blue band has a peak intensity near 372 nm when measured in radiometric units, 373 nm in quantum units, and 548 in photopic units (Figure 5-1). The green band has peaks near 531 nm, 542 nm, and 548 nm, respectively (Figure 5-2). When the radiometric intensities of these bands are plotted as a function of photon energy rather than wavelength (Figure 5-3), the green band appears symmetrical and Gaussian in form while the UV/blue peak appears slightly lopsided and truncated in the direction of higher photon energies. It appears that 325 nm (3.82 eV) radiation is sufficient to excite the entire green band but may only excite a longer wavelength tail of the true UV/blue band.

The results of a number of experiments designed to elucidate the influence of the major non-chemical processing parameters on the peak intensities and locations of the two PL bands of sp-Si are presented in this section.

Processing Current

It was realized in Stage I that the strength of a particular high voltage power supply has a major influence on the properties of the silicon that was spark-processed with that particular source. There was no adequate way to measure and control the

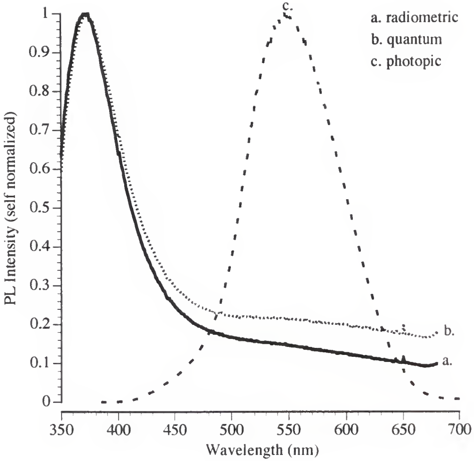

Figure 5-1: Typical PL spectra of UV/blue sp-Si under 325 nm excitation in radiometric units (a.), quantum units (b.), and photopic units (c.). Peaks are at 372 nm, 373 nm, and 548 nm, respectively.

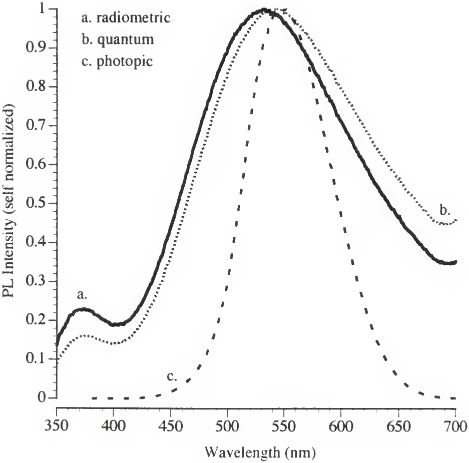

Figure 5-2: Typical PL spectra of green sp-Si under 325 nm excitation in radiometric units (a.), quantum units (b.), and photopic units (c.). Peaks are at 531 nm, 542 nm, and 548 nm, respectively.

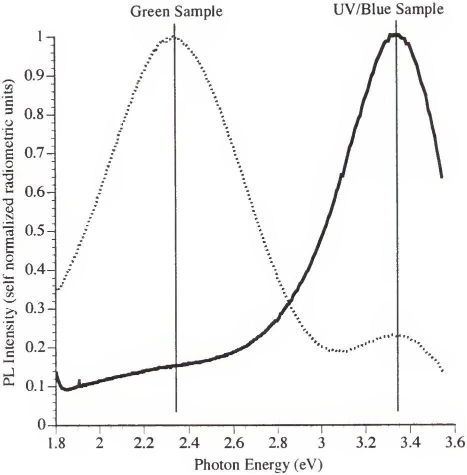

Figure 5-3: Self-normalized radiometric PL spectra of UV/blue (solid line) and green (dashed line) with photon energy as the X-axis instead of wavelength. The non-symmetric shape of the UV/blue band indicates that the luminescence may be from the tail of higher energy state that is not fully excited by 325 nm radiation.

intensity of the spark. This situation changed substantially in Stage II when the spark current was controlled by the current gain of a tetrode tube and was affected much less by the variation in other processing variables. However, the lack of the ability to accurately measure the current quantitatively, as would be needed to elucidate the role of current, was the primary impetus for the development of the equipment as it stands in Stage III. This, in turn, lead to the ability to compensate for the small current variations that still occurred when other parameters were changed. The majority of definitive experiments to determine the effects of temporal, physical, electrical, and chemical parameters became possible at this point. The largest impact of the current experiments that follow was to determine the current range that creates both strong UV/blue and green peaks at standard conditions. This allowed the informed choice of a standard current value for other experiments, such that both peaks were clearly represented in the parameter space.

Experimental procedure

Twelve samples were prepared to determine the effect of current on the PL of sp-Si. Standard 1 cm x 3/4 cm chips were cleaned and etched according to the standard protocol and placed in the clean processing chamber. Following the standard pumping and baking procedure, the chamber was back-filled with a mixture of 700 mbar of UHP N_2 and 300 mbar of UHP O_2 before processing each sample. A 0.25 mm diameter tungsten electrode was used with a gap distance of 0.50 mm. Based on subjective experience with spark processing and preliminary work in Stage II, target values for the average processing current of 10 mA, 20 mA, 40 mA, and 60 mA were chosen. It was decided to make three samples at each value. The pulse width was 1.0 μs with a 10.0 kHz repetition rate. The total processing duration was

15.00 minutes. To achieve this range of currents, power supply voltages between 2.76 kV and 10.20 kV were used. The full range of grid voltage supply and grid current limiter settings were used as well. It proved difficult to achieve more than 55 mA under these conditions and this was substituted for 60 mA as the highest current value.

For each sample, the time-average current was recorded. The samples looked similar to the eye with the spark processed area appearing somewhat larger for the higher currents. The porous region was similar in color except for the highest current samples, which appeared blackened.

The samples were measured in the standard PL setup using both a focused and unfocused beam. One of the highest current samples was accidentally broken and was excluded from the measurements. This left 11 samples, 3 at approximately 10 mA, 3 at approximately 20 mA, 3 at approximately 40 mA, and 2 at approximately 55 mA. The raw spectra were calibrated and converted to radiometric intensity vs. wavelength.

Experimental results

A 3-D overview of the unfocused beam data is shown in Figure 5-4. The focused beam data had a much higher randomness and, while they did not contradict the unfocused beam data, it was much harder to see the trends due to the highly anisotropic nature of spark-processed material. As a result of this observation, only unfocused beams were used in subsequent experiments.

The samples exhibited the standard UV/blue and green peaks. The un-deconvoluted peak locations and intensities were determined using the standard computerized algorithm. The peak locations are shown as a function of processing

PL of Sp-Si vs. Processing Current

Substrate Material:	Silicon
Atmosphere:	70% N_2 30% O_2
Electrode Material:	Tungsten 0.25 mm dia.
Electrode Gap:	0.50 mm
Frequency:	10.0 kHz
Pulse Width:	1.0 μs
Average Current:	**variable**
Processing Time:	15 minutes

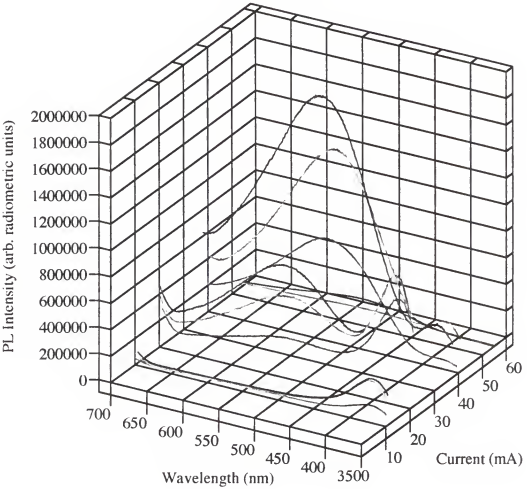

Figure 5-4: 3-D overview of the PL spectra of sp-Si as a function of the average processing current. There are three samples for each approximate current value except for 55 mA where there are only two.

current in Figure 5-5. The locations of both the UV/blue and green peaks varied somewhat as the current varied. This variation was fairly linear as shown in the figure. These shifts of the apparent peaks of about 5 - 10 nm total are consistent with the sample PL becoming more green and less blue as current is increased. Both peaks are consequently shifted slightly to longer wavelengths due to the slight overlap of these broad luminescent bands. There is no indication that the underlying energy levels of each state are shifted with changing current.

The intensities of these peaks are shown as a function of processing current in Figure 5-6. The absolute intensities of the UV/blue and green peaks increase between 10 mA and 20 mA. The intensity of the green peak continues to increase between 20 mA and 40 mA while the UV/blue peak decreases substantially. Between 40 mA and 55 mA, both peaks continue to decrease by more than an order of magnitude. If we divide the intensities of each sample by the processing current and plot this against current, we achieve a sort of "efficiency factor" (Figure 5-7). Since the processing time is the same for each sample, the current is proportional to the total processing charge to which the sample is exposed. Thus, for a certain amount of processing, we compare how efficiently a given current gives rise to both UV/blue and green luminescence. With this analysis, one can see that a current of 20 mA is somewhat more efficient in creating UV/blue PL than 10 mA, but the efficiency falls of by an order of magnitude by 40 mA and nearly two more orders of magnitude by 55 mA. For green PL, the efficiency rises substantially between 10 mA and 20 mA, remains similar between 20 mA and 40 mA, and declines substantially between 40 mA and 55 mA.

Location of UV/Blue and Green Peaks as a Function of Processing Current

Substrate Material: Silicon
Atmosphere: 70% N_2 30% O_2
Electrode Material: Tungsten 0.25 mm dia.
Electrode Gap: 0.50 mm
Frequency: 10.0 kHz
Pulse Width: 1.0 μs
Average Current: **variable**
Processing Time: 15 minutes

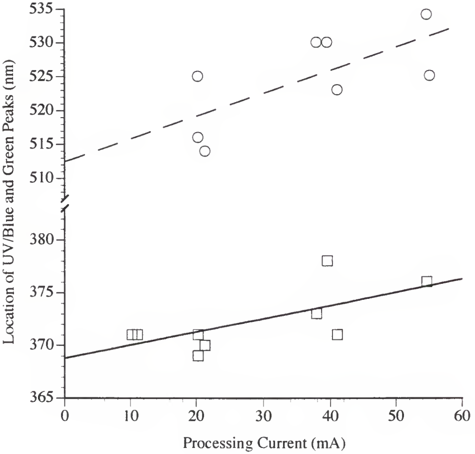

Figure 5-5: Peak locations of the PL bands of sp-Si as a function of the average processing current. Linear fits are shown for both bands. No clear green peak is exhibited by the 10 mA samples. No clear UV/blue peak is exhibited by one of the 55 mA samples. In addition, some overlap of data points occurs.

Intensity of UV/Blue and Green Peaks as a Function of Processing Current

Substrate Material:	Silicon
Atmosphere:	70% N_2 30% O_2
Electrode Material:	Tungsten 0.25 mm dia.
Electrode Gap:	0.50 mm
Frequency:	10.0 kHz
Pulse Width:	1.0 μs
Average Current:	**variable**
Processing Time:	15 minutes

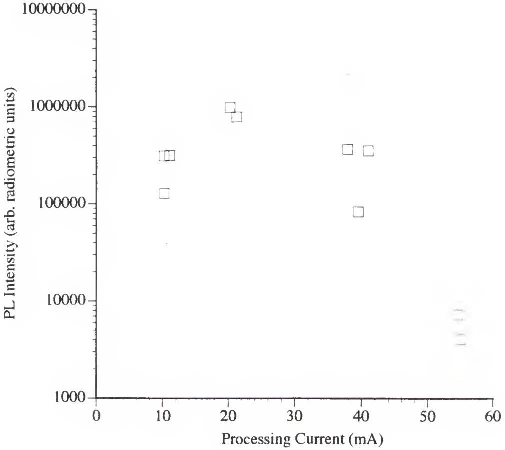

Figure 5-6: Peak intensities of the PL bands of sp-Si as a function of the average processing current. Unresolvable peaks were assigned as 372 nm and 525 nm. Some overlap of data points occurs.

Intensity of UV/Blue and Green Peaks per Unit of Processing Current as a Function of Processing Current

Substrate Material:	Silicon
Atmosphere:	70% N_2 30% O_2
Electrode Material:	Tungsten 0.25 mm dia.
Electrode Gap:	0.50 mm
Frequency:	10.0 kHz
Pulse Width:	1.0 μs
Average Current:	**variable**
Processing Time:	15 minutes

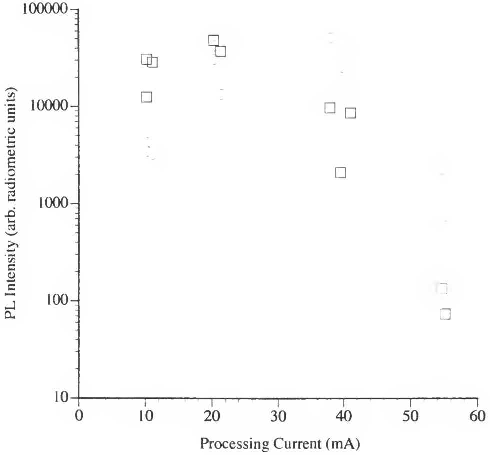

Figure 5-7: Peak intensities of the PL bands of sp-Si normalized to processing current as a function of the average processing current (see text). Unresolvable peaks were assigned as 372 nm and 525 nm. Some overlap of data points occurs.

The ratio of the peak intensity of the green band to the peak intensity of the UV/blue band can be plotted against processing current (Figure 5-8) and is found to increase exponentially with current.

Discussion of current results

The average spark current has a very strong influence on the intensity and color of the PL of sp-Si. It can be said that current is a dominant variable. All previous experiments, which did not control current variations as other processing parameters were changed, are questionable at this point. Two general trends are seen. Initially, the PL of both bands increases with current. This is easily explained as a larger current results in a greater amount of processed material. However, the PL intensity decreases above about 20 mA for the UV/blue band and above about 40 mA for the green band. The influence here is probably thermal. Above a certain temperature, the conditions are less favorable for the formation of the defects or molecules that give rise to the luminescence. The fact the green favors a higher current than the blue is consistent with the general trend in the literature of the green peak dominating at higher processing temperatures. Somewhere between 40 mA and 55 mA, the PL intensity decreases rapidly. Samples processed at these high currents appear blackened and significantly different to the eye.

These results allow one to create a sample with a desired PL spectrum. It is now evident that unless one wants to virtually exclude one color of PL from a sample, spark-processing for the purpose of creating strongly luminescing material is best confined to currents between about 20 mA and 40 mA. It is uncanny how well the color ratio data fits an exponential relationship with current. This color ratio can be adjusted over a range of nearly two orders of magnitude. The expected color of a

Ratio of Green Peak PL Intensity to UV/Blue Peak Intensity as a Function of Processing Current

Substrate Material: Silicon
Atmosphere: 70% N_2 30% O_2
Electrode Material: Tungsten 0.25 mm dia.
Electrode Gap: 0.50 mm
Frequency: 10.0 kHz
Pulse Width: 1.0 μs
Average Current: **variable**
Processing Time: 15 minutes

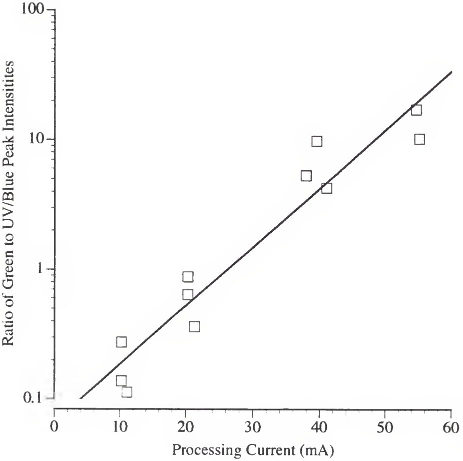

Figure 5-8: Ratio of the peak intensity of the green band of sp-Si to the peak intensity of the UV/blue band as a function of the average processing current. Exponential fit is shown. Unresolvable peaks were assigned as 372 nm and 525 nm.

sample can be selected with a known processing current. Interpolating from the data, a 1:1 ratio occurs, on average, with a current of approximately 26 mA. During the course of the experimental phase of this work, the 1:1 ratio appeared to occur at 21 mA based on preliminary calibration curves for the PL system that have since been refined. Accordingly, 20.0 mA was used as a "standard" current for further experiments. A standard current at which both strong UV/blue and green bands occur is desirable so that the most knowledge may be gained from a finite number of experiments.

Following the current experiments were three experiments in which the pulse width, repetition frequency, and both pulse width and repetition frequency were varied while maintaining an average current of 20.0 mA. In the first two experiments, the intensity of the spark pulses was allowed to change to maintain the constant average current (variable pulse width with fixed frequency or variable frequency with fixed pulse width). In the third, the pulse width was used as the independent variable. The current gain of the tube was not adjusted but the frequency was adjusted to maintain the average current. This left the pulse intensity approximately constant and the frequency roughly inversely proportional to the pulse width. These choices of variables allows the influence of these important but interrelated parameters to be fully explored and may give some incite into the thermal and kinetic processes involved in spark-processing as well as allow one to differentiate between the two. All three experiments will be presented before the results will be discussed.

Pulse Width with Fixed Frequency

Following the current experiments, the first electrical/temporal parameter to be explored was the pulse width. In these experiments, the frequency of pulses was held constant and the width of each pulse was changed as the independent variable. The average current was also held constant. This necessitated that the instantaneous intensity of the pulses change in inverse proportion to the pulse width. For example, 1 μs pulses averaging 2 A repeating at 10 kHz give an average current of 20 mA. For 0.5 μs pulses to give an average current of 20 mA, the instantaneous current of the pulses would have to be 4 A.

Experimental procedure

Eighteen samples were prepared to determine the effect of the pulse width on the PL of sp-Si. Standard 1 cm x 3/4 cm chips were cleaned and etched according to the standard protocol and placed in the clean processing chamber. Following the standard pumping and baking procedure, the chamber was back-filled with a mixture of 700 mbar of UHP N_2 and 300 mbar of UHP O_2 before processing each sample. A 0.25 mm diameter tungsten electrode was used with a gap distance of 0.50 mm. The time-average processing current was fixed at 20.0 mA and the repetition rate was set at 10.0 kHz. The shortest pulse width capable of maintaining a spark was found to be approximately 175 ns. For very long pulses, the spark intensity must be quite low to maintain a given average current and there is a limit to how low the intensity may be in order to maintain a spark across the gap. Under the chosen conditions, pulses as long as 5.0 μs could be maintained. Accordingly, two samples were made at each of the following pulse widths: 175 ns, 250 ns, 0.50 μs, 1.0 μs, 1.5 μs, 2.0 μs, 2.5 μs, 3.5 μs, and 5.0 μs. The total processing duration was 15.00 minutes. Near the end of the

15 minutes, the two 5.0 μs samples were being sparked somewhat intermittently as the low-intensity spark was having difficulty penetrating the accumulated porous region. To achieve this range of pulse widths, power supply voltages between 3.22 kV and 11.76 kV were used. The full range of grid voltage supply and grid current limiter settings were used as well.

The samples corresponding to pulse widths from 0.50 μs to 2.0 μs looked similar to the eye with the spark-processed region similar in size, texture, and color. The 175 ns and 250 ns samples had a slightly larger porous region and the central white region was tan in color and poorly defined. The 3.5 μs and 5.0 μs samples had a very large irregular porous region with a large central region. The central region was yellow in color and the entire 5.0 μs sample was covered in a yellow powder. The 2.5 μs sample was slightly larger than the 2.0 μs sample and the central region had a slight yellow tint. The author speculates that a significant quantity of tungsten oxide or tungsten/silicon compounds may be formed at very large pulse widths. As discussed in Chapter 3, tungsten has been ruled out as contributing to either PL band of sp-Si.

The samples were measured in the standard PL setup using an unfocused beam. The raw spectra were calibrated and converted to radiometric intensity vs. wavelength.

Experimental results

A 3-D overview of the data is shown in Figure 5-9. The samples exhibited the standard UV/blue and green peaks. The un-deconvoluted peak locations and intensities were determined using the standard computerized algorithm. The peak locations are shown as a function of pulse width in Figure 5-10. The locations of

PL of Sp-Si vs. Pulse Width

Substrate Material:	Silicon
Atmosphere:	70% N_2 30% O_2
Electrode Material:	Tungsten 0.25 mm dia.
Electrode Gap:	0.50 mm
Frequency:	10.0 kHz
Pulse Width:	**variable**
Average Current:	20 mA
Processing Time:	15 minutes

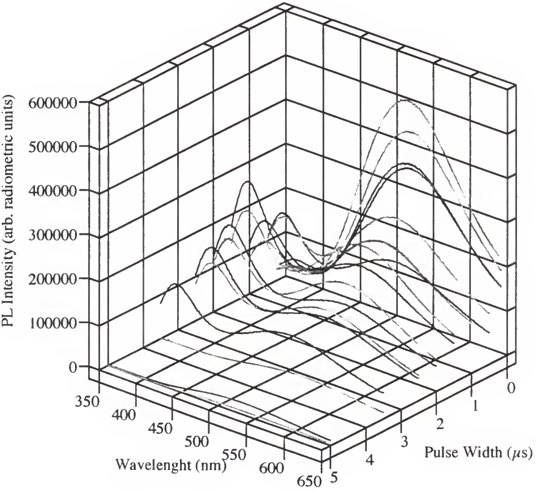

Figure 5-9: 3-D overview of the PL spectra of sp-Si as a function of pulse width. There are three samples for each pulse width.

Location of UV/Blue and Green Peaks as a Function of Pulse Width

Substrate Material: Silicon
Atmosphere: 70% N_2 30% O_2
Electrode Material: Tungsten 0.25 mm dia.
Electrode Gap: 0.50 mm
Frequency: 10.0 kHz
Pulse Width: **variable**
Average Current: 20 mA
Processing Time: 15 minutes

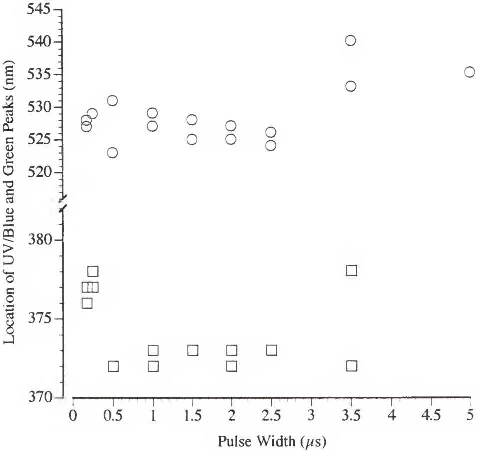

Figure 5-10: Peak locations of the PL bands of sp-Si as a function of pulse width. The 5 μs samples did not exhibit a UV/blue peak. There are two samples for each pulse width. Overlap may cause them to appear as one.

both the UV/blue and green peaks changed very little as the pulse width varied. The intensities of these peaks are shown as a function of pulse width in Figure 5-11. The intensity of the UV/blue band is low at both extremes of the pulse width range and quite intense over the entire range from 0.50 μs to 2.5 μs. It appears to be at a maximum near 1.5 μs. The intensity of the green peak is maximized at the shortest pulse widths and decreases rapidly with increasing pulse width. This trend is well-fit by an exponential function shown in the figure.

The ratio of the peak intensity of the green band to the peak intensity of the UV/blue band can be plotted against pulse width, see Figure 5-12. This ratio is near 1:1 for pulse widths from 0.50 μs to 2.5 μs and becomes very large at very short and very long pulse widths. At short pulse widths, the green is very strong. While the green is weak at the longest pulse widths, the blue is much weaker still.

Frequency with Fixed Pulse Width

The role of the repetition frequency of pulses was explored in this set of experiments. The pulse width and average current were held constant. Just as in the last set of experiments, the instantaneous intensity of the pulses was a dependent variable.

Experimental procedure

Twelve samples were prepared to determine the effect of frequency on the PL of sp-Si. Standard 1 cm x 3/4 cm chips were cleaned and etched according to the standard protocol and placed in the clean processing chamber. Following the standard pumping and baking procedure, the chamber was back-filled with a mixture of 700 mbar of UHP N_2 and 300 mbar of UHP O_2 before processing each sample. A

Intensity of UV/Blue and Green Peaks as a Function of Pulse Width

Substrate Material:	Silicon
Atmosphere:	70% N_2 30% O_2
Electrode Material:	Tungsten 0.25 mm dia.
Electrode Gap:	0.50 mm
Frequency:	10.0 kHz
Pulse Width:	**variable**
Average Current:	20 mA
Processing Time:	15 minutes

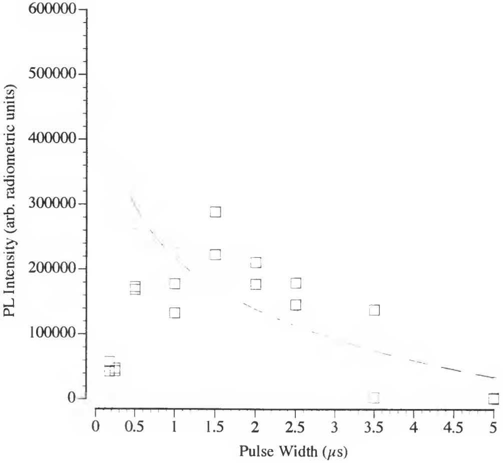

Figure 5-11: Peak intensities of the PL bands of sp-Si as a function of pulse width. An exponential fit is shown for the green band. Unresolvable peaks were assigned as 373 nm. There are two samples for each pulse width. Overlap may cause them to appear as one.

Ratio of Green Peak PL Intensity to UV/Blue Peak Intensity as a Function of Pulse Width

Substrate Material: Silicon
Atmosphere: 70% N_2 30% O_2
Electrode Material: Tungsten 0.25 mm dia.
Electrode Gap: 0.50 mm
Frequency: 10.0 kHz
Pulse Width: **variable**
Average Current: 20 mA
Processing Time: 15 minutes

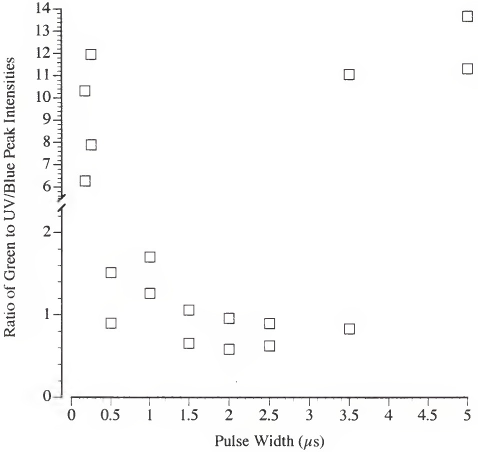

Figure 5-12: Ratio of the peak intensity of the green band of sp-Si to the peak intensity of the UV/blue band as a function of pulse width. There are two samples for each pulse width. Unresolvable peaks were assigned as 373 nm.

0.25 mm diameter tungsten electrode was used with a gap distance of 0.50 mm. The time-average processing current was fixed at 20.0 mA and the pulse width was set at 1.0 μs. Two samples were prepared at each the following target frequency values: 2.50 kHz, 5.00 kHz, 10.0 kHz, 15.0 kHz, 20.0 kHz, and 25.0 kHz. While the frequency can be measured accurately to many significant digits, limited selectivity and a slight drift of the function generator sets a practical limit of about three significant digits. The total processing duration was 15.00 minutes. This set of experiments was very taxing on the system, particularly at low frequencies. To achieve this range of frequencies, power supply voltages between 3.93 kV and 18.14 kV were used. The full range of the grid voltage supply and grid current limiter settings were used as well. While the system was designed to operate at power supply voltages of 25 kV or higher, some internal arcing occurred due to high ambient humidity and repairs had to be made. After the repairs, a dehumidifier was moved into the laboratory to allow this series of experiments to be completed.

The samples corresponding to frequencies from 10.0 kHz to 25 kHz looked similar to the eye with the spark-processed region similar in size, texture, and color. The 2.50 kHz and 5.00 kHz samples had a smaller, and less defined central region which was more tan than white, and a larger somewhat irregularly shaped brownish region. The halo of loose white material that often surrounds the porous region was unusually thick on these two samples.

The samples were measured in the standard PL setup using an unfocused beam. The raw spectra were calibrated and converted to radiometric intensity vs. wavelength.

Experimental results

A 3-D overview of the data is shown in Figure 5-13. The samples exhibited the standard UV/blue and green peaks. The un-deconvoluted peak locations and intensities were determined using the standard computerized algorithm. The peak locations are shown as a function of frequency in Figure 5-14. The locations of both the UV/blue and green peaks changed very little as the frequency varied. The intensities of these peaks are shown as a function of frequency in Figure 5-15. The intensity of the UV/blue and green bands is quite high for all frequencies measured except 2.50 kHz, where it is still significant. The intensity of the UV/blue band appears to be at a maximum near 10 kHz, while the intensity of the green band appears to be at a maximum near 15 kHz.

The ratio of the peak intensity of the green band to the peak intensity of the UV/blue band can be plotted against frequency, see Figure 5-16. The trend looks rather odd and discontinuous but is consistent with the description of the previous figure. At 10 kHz and below, the peak intensities of the two bands are similar. Above 10 kHz, the UV/blue peak has reached its maximum and is already decreasing while the green peak continues to increase. The green peak does not begin to decrease until above 15 kHz and, while the UV/blue is also still decreasing, the green decreases at a faster rate. The jump in the ratio between 10 kHz and 15 kHz from about 1:1 to about 2:1 is a direct result of the 5 kHz separation between the optimal conditions for each band.

PL of Sp-Si vs. Frequency of Pulses

Substrate Material: Silicon
Atmosphere: 70% N_2 30% O_2
Electrode Material: Tungsten 0.25 mm dia.
Electrode Gap: 0.50 mm
Frequency: **variable**
Pulse Width: 1.0 μs
Average Current: 20 mA
Processing Time: 15 minutes

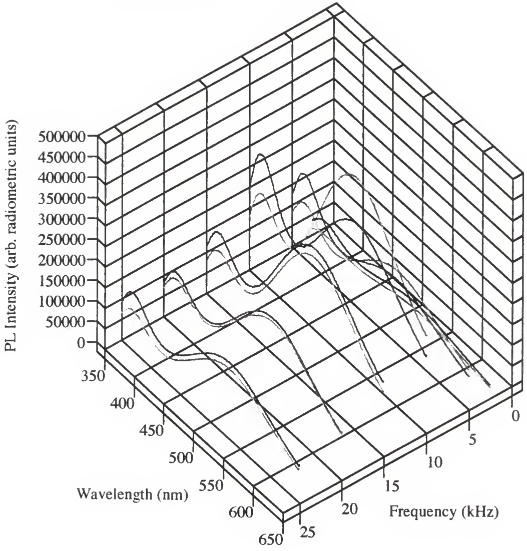

Figure 5-13: 3-D overview of the PL spectra of sp-Si as a function of the frequency of pulses. There are two samples for each approximate frequency.

Location of UV/Blue and Green Peaks as a Function of the Frequency of Pulses

Substrate Material:	Silicon
Atmosphere:	70% N_2 30% O_2
Electrode Material:	Tungsten 0.25 mm dia.
Electrode Gap:	0.50 mm
Frequency:	**variable**
Pulse Width:	1.0 μs
Average Current:	20 mA
Processing Time:	15 minutes

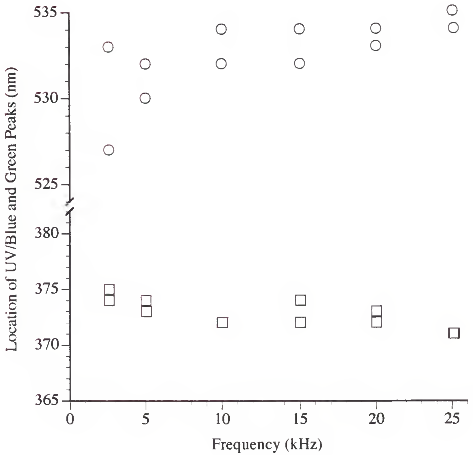

Figure 5-14: Peak locations of the PL bands of sp-Si as a function of the frequency of pulses. There are two samples for each approximate frequency. Overlap may cause them to appear as one.

Intensity of UV/Blue and Green Peaks as a Function of the Frequency of Pulses

Substrate Material:	Silicon
Atmosphere:	70% N_2 30% O_2
Electrode Material:	Tungsten 0.25 mm dia.
Electrode Gap:	0.50 mm
Frequency:	**variable**
Pulse Width:	1.0 μs
Average Current:	20 mA
Processing Time:	15 minutes

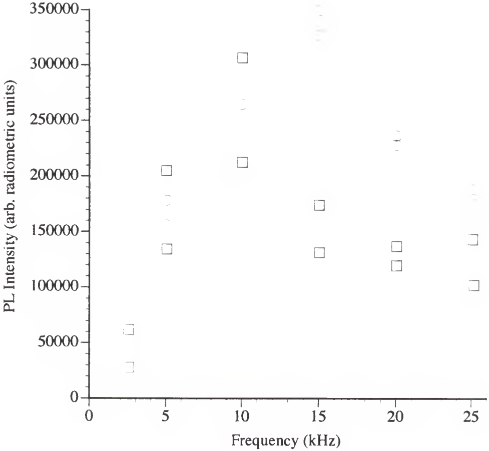

Figure 5-15: Peak intensities of the PL bands of sp-Si as a function of the frequency of pulses. There are two samples for each approximate frequency. Overlap may cause them to appear as one.

Ratio of Green Peak PL Intensity to UV/Blue Peak Intensity as a Function of the Frequency of Pulses

Substrate Material:	Silicon
Atmosphere:	70% N_2 30% O_2
Electrode Material:	Tungsten 0.25 mm dia.
Electrode Gap:	0.50 mm
Frequency:	**variable**
Pulse Width:	1.0 μs
Average Current:	20 mA
Processing Time:	15 minutes

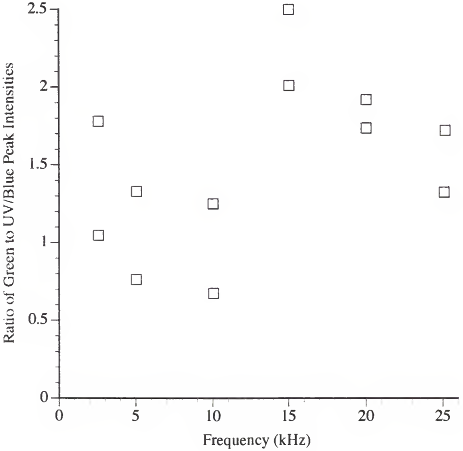

Figure 5-16: Ratio of the peak intensity of the green band of sp-Si to the peak intensity of the UV/blue band as a function of the frequency of pulses. There are two samples for each approximate frequency.

Variable Pulse Width and Frequency

In this set of experiments, the current gain controls were not adjusted as the pulse width was changed. Instead, the frequency was adjusted to maintain a constant current. The result of this is that the instantaneous spark intensity is essentially constant in contrast with the previous two sets of experiments.

Experimental procedure

Twenty samples were prepared to determine the effect of the pulse width with constant intensity on the PL of sp-Si. Standard 1 cm x 3/4 cm chips were cleaned and etched according to the standard protocol and placed in the clean processing chamber. Following the standard pumping and baking procedure, the chamber was back-filled with a mixture of 700 mbar of UHP N_2 and 300 mbar of UHP O_2 before processing each sample. A 0.25 mm diameter tungsten electrode was used with a gap distance of 0.50 mm. The time-average processing current was fixed at 20.0 mA. Two samples were made at each of the following pulse widths: 175 ns, 250 ns, 0.50 μs, 0.75 μs, 1.0 μs, 1.5 μs, 2.0 μs, 2.5 μs, 3.0 μs, and 4.0 μs. The current gain controls were set to give an instantaneous pulse intensity which resulted in an average current of 20.0 mA when the pulse width was 1 μs and the frequency was 10.0 kHz. As the pulse width was changed, only the frequency was adjusted to maintain the same average current. The total processing duration was 15.00 minutes. The power supply voltage was set to 5.50 kV for the entire series of samples and the grid voltage supply and grid current limiter settings were likewise fixed at 13% and 50%, respectively.

The samples corresponding to pulse widths from 0.50 μs to 4.0 μs all looked similar to the eye with the spark-processed region similar in size, texture, and color. The 175 ns and 250 ns samples had a slightly larger irregularly shaped porous region and the central white region was tan in color. These differences were less evident than in the case of the variable pulse width samples with fixed frequency. These two samples also exhibited a larger amount of loose white material around the porous region. In addition, the longest pulse width samples did not have the odd yellow color or irregular shape that occurred when the frequency was fixed. With the exception of very short pulse widths, it appears that when the duty ratio (pulse width/period) is similar, the size and appearance of the porous region is similar.

The samples were measured in the standard PL setup using an unfocused beam. The raw spectra were calibrated and converted to radiometric intensity vs. wavelength.

Experimental results

A 3-D overview of the data is shown in Figure 5-17. The samples exhibited the standard UV/blue and green peaks. Figure 5-18 shows the relationship between the pulse width and period (1/frequency) necessary to maintain a constant average current. The solid line represents the ideal case for perfectly square pulses. The deviation from this line occurs due to the fact that the pulses are not square but have a high initial current which then levels off for about 2 μs before falling again. This is consistent with the stages of the development of a spark as discussed in Chapter 3. Consequently, the true instantaneous intensity is significantly higher for the very short pulse widths, even when the current gain controls are not adjusted.

The un-deconvoluted peak locations and intensities were determined using the standard computerized algorithm. The peak locations are shown as a function of pulse width in Figure 5-19. The locations of both the UV/blue and green peaks changed very little as the pulse width varied. The intensities of these peaks are shown

PL of Sp-Si vs. Pulse Width (variable frequency)

Substrate Material:	Silicon
Atmosphere:	70% N_2 30% O_2
Electrode Material:	Tungsten 0.25 mm dia.
Electrode Gap:	0.50 mm
Frequency:	**variable (dependent variable)**
Pulse Width:	**variable (independent variable)**
Average Current:	20 mA
Processing Time:	15 minutes

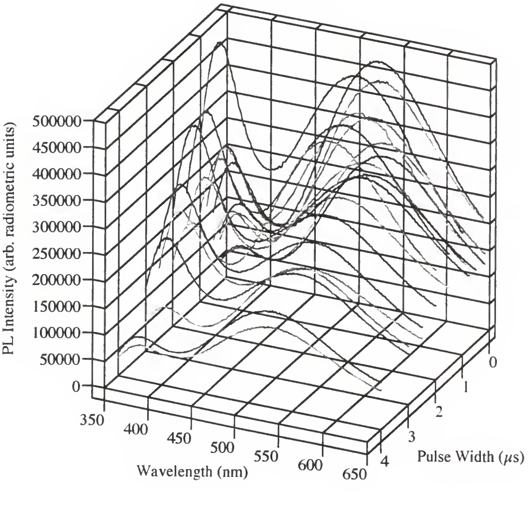

Figure 5-17: 3-D overview of the PL spectra of sp-Si as a function of pulse width with variable frequency (see text). There are two samples for each pulse width.

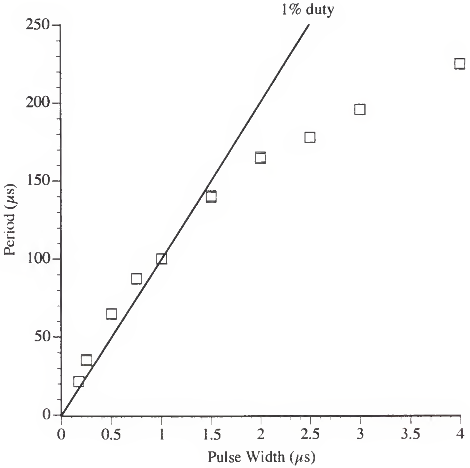

Figure 5-18: Relationship between pulse width and frequency necessary to maintain a constant average current without adjusting pulse intensity. The solid line represents the ideal relationship for square pulses using 1 ms pulses at 10 kHz as a reference (1% duty). There are two samples for each pulse width.

Location of UV/Blue and Green Peaks as a Function of Pulse Width (variable frequency)

Substrate Material:	Silicon
Atmosphere:	70% N_2 30% O_2
Electrode Material:	Tungsten 0.25 mm dia.
Electrode Gap:	0.50 mm
Frequency:	**variable (dependent variable)**
Pulse Width:	**variable (independent variable)**
Average Current:	20 mA
Processing Time:	15 minutes

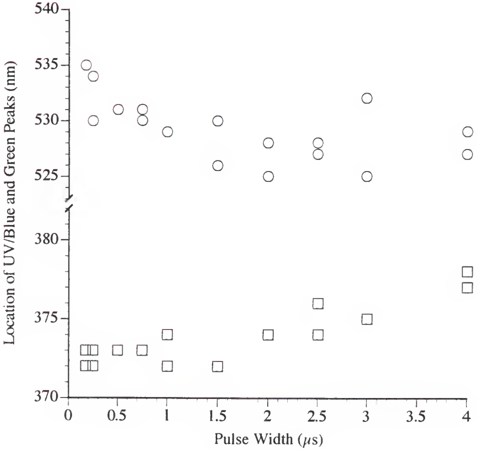

Figure 5-19: Peak locations of the PL bands of sp-Si as a function of pulse width with variable frequency (see text). There are two samples for each pulse width. Overlap may cause them to appear as one.

as a function of pulse width in Figure 5-20. The intensity of the UV/blue band is low at both extremes of the pulse width range and quite intense over the entire range from 0.50 μs to 2.5 μs. It appears to be at a maximum near 1 - 1.5 μs. The intensity of the green peak is maximized at the shortest pulse widths and decreases with increasing pulse width. This trend is fairly linear as shown in the figure. In Figure 5-21, the same data is plotted in terms of the period of pulses (1/frequency). The dotted lines in the figure represent the periods corresponding to 5 kHz, 10 kHz, and 20 kHz.

The ratio of the peak intensity of the green band to the peak intensity of the UV/blue band can be plotted against frequency and seen to obey a fairly linear relationship, see Figure 5-22.

Discussion of Pulse Width and Frequency Variations

The results of the last three experiments can be taken together to fully understand the influence of pulse width, frequency, and intensity (instantaneous current). When the pulse width is varied with a constant frequency, the UV/blue band was intense over a large pulse width range from 0.50 μs to 2.5 μs. It was greatest near 1.5 μs, see Figure 5-11. The green band was most intense at the shortest pulse width and decreased exponentially with increasing pulse width.

When the pulse width and frequency were both allowed to vary, the results were somewhat different, see Figure 5-20. The UV/blue band was also strong from 0.50 μs to 2.5 μs, only the peak occurred at a slightly shorter pulse width (between 1.0 μs and 1.5 μs). This is not unexpected because, in the former case, the intensity is higher for shorter pulses and the intensity was relatively constant in the later. The UV/blue intensity is known to decrease at high current and high temperature. The very fact that the results of these two experiments are so similar demonstrates that

Intensity of UV/Blue and Green Peaks as a Function of Pulse Width (variable frequency)

Substrate Material:	Silicon
Atmosphere:	70% N_2 30% O_2
Electrode Material:	Tungsten 0.25 mm dia.
Electrode Gap:	0.50 mm
Frequency:	**variable (dependent variable)**
Pulse Width:	**variable (independent variable)**
Average Current:	20 mA
Processing Time:	15 minutes

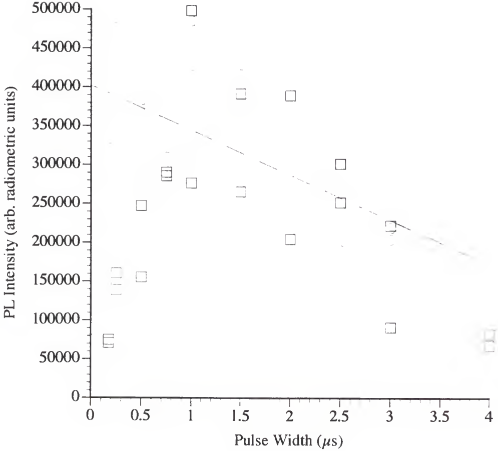

Figure 5-20: Peak intensities of the PL bands of sp-Si as a function of pulse width with variable frequency (see text). A linear fit is shown for the green band. There are two samples for each pulse width.

Intensity of UV/Blue and Green Peaks as a Function of Pulse Width (variable frequency) Plotted in terms of the Period of Pulses (1/f)

Substrate Material: Silicon
Atmosphere: 70% N_2 30% O_2
Electrode Material: Tungsten 0.25 mm dia.
Electrode Gap: 0.50 mm
Frequency: **variable (dependent variable)**
Pulse Width: **variable (independent variable)**
Average Current: 20 mA
Processing Time: 15 minutes

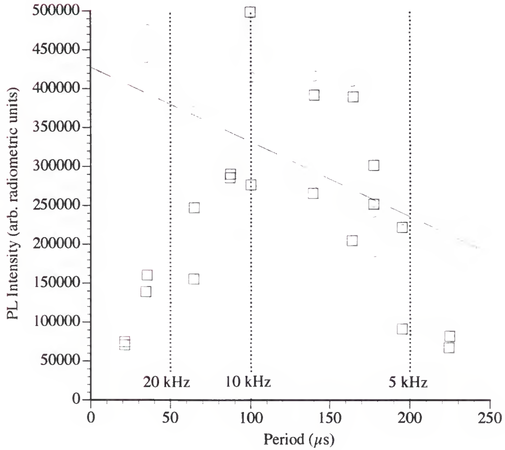

Figure 5-21: Peak intensities of the PL bands of sp-Si as a function of pulse width with variable frequency plotted in terms of the period of pulses (1/f), see text. A linear fit is shown for the green band. Dotted lines denote frequencies of 5 kHz, 10 kHz, and 20 kHz. There are two samples for each pulse width.

Ratio of Green Peak PL Intensity to UV/Blue Peak Intensity as a Function of Pulse Width (variable frequency) Plotted in terms of the Frequeny of Pulses

Substrate Material:	Silicon
Atmosphere:	70% N_2 30% O_2
Electrode Material:	Tungsten 0.25 mm dia.
Electrode Gap:	0.50 mm
Frequency:	**variable (dependent variable)**
Pulse Width:	**variable (independent variable)**
Average Current:	20 mA
Processing Time:	15 minutes

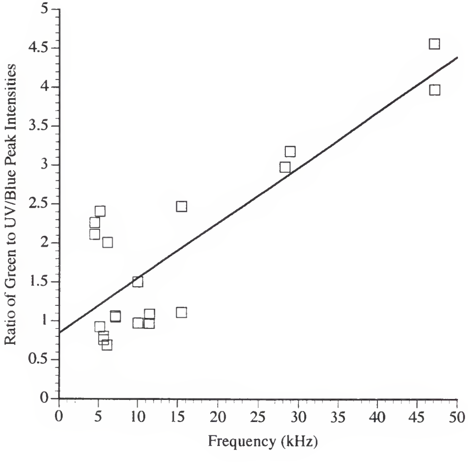

Figure 5-22: Ratio of the peak intensity of the green band of sp-Si to the peak intensity of the UV/blue band as a function of pulse width with variable frequency plotted in terms of the frequency of pulses (see text). A linear fit is shown. There are two samples for each pulse width. Overlap may cause them to appear as one.

independent of current or thermal considerations, there is a strong temporal factor involved. The defect or molecule responsible for the UV/blue PL prefers a certain time interval to form and the formation is less efficient if the pulse lasts for a shorter or longer period of time. This seems to imply that something is getting quenched in. This will be discussed again when all the experimental work has been presented.

The green band also prefers very short pulse widths when the intensity is held relatively constant, but the trend is not nearly as strong as when the shorter pulses are more intense. There is only a 2:1 ratio in intensity for the green between 175 ns and 4 μs pulse widths in the later case (Figure 5-20). It appears that temporal considerations are less important than intensity for the green band. In fact, as the pulses are not truly square, but are initially more intense, the entire observed trend may still be simply due to intensity variations. The high initial current when the spark begins quickly decreases and remains nearly constant for approximately 2 μs, as has been discussed. A closer examination of the data (Figure 5-20, green) shows that the intensity of the green peak does not change much between 0.5 μs and 2.0 μs. Instantaneous spark intensity is clearly the dominant factor for the green PL intensity. Pulse width may or may not play a role.

Frequency, being inversely proportional to the period between pulses, plays a role as well. In the variable frequency with fixed pulse width experiment, the UV/blue peak appears to prefer a frequency of 10 kHz, see Figure 5-15. The UV/blue intensity dies off fairly rapidly above 10 kHz despite the lower intensity of the pulses. This may seem counter intuitive given the blue peak's preference for lower currents, but probably represents a period of time between pulses necessary for the cooling-off or quenching previously suggested. At higher frequencies (shorter periods), the material may not have enough time to cool between pulses. When the instantaneous intensity is held constant, the UV/blue also prefers a frequency of approximately 10 kHz (Figure 5-21) indicating that this temporal dependence is dominant whether the intensity is held constant or not.

In the variable frequency with fixed pulse width experiment, the green peak appears to prefer a higher frequency of 15 kHz, despite the fact that the pulse intensity is lower at 15 kHz than at 10 kHz. The green continues to be stronger than the UV/blue at 20 kHz and 25 kHz despite decreasing pulse intensity. This is also counter intuitive. It appears that a higher instantaneous current only benefits the green band if it occurs on a time scale shorter than 1 µs. Despite the strong current-dependence, there appears to be a temporal factor for the green after all. In addition, the formation process for the UV/blue and green species may be competitive. It can be seen in Figure 5-15 that the green intensity peaks only after the UV/blue begins decreasing. This is the cause for the strange appearance of Figure 5-16. Competition between the two PL bands for excited carriers could explain this as well. In Chapter 8, direct evidence of competition between the UV/blue and green bands in sp-Si will be presented and this subject will be addressed again.

Now that the effects of current, frequency, and pulse width have been discussed, it is appropriate to revisit the literature on Stage I spark-processing. As discussed in Chapter 3, the pulse width when sparking with a VGA monitor has been claimed to be 10 or 20 ns [Lud96a]. These pulse widths were measured by connecting an oscilloscope across a resistor placed between the sample and ground. Such a setup is not impedance matched and the scope used was very susceptible to interference from the spark. The author has determined that the bulk of this interference is internal to the scope's video circuitry and does not scale to the horizontal sweep rate or the input voltage range.

Under controlled Stage III conditions, the author found it impossible to sustain sparks with widths under 175 ns. Even with the immense power of the Stage III equipment that overcomes the stray capacitance of the gap in less than 5 - 10 ns, any attempt to drive the spark gap with a pulse width shorter than 175 ns results in a loss of spark intensity, but not duration. As discussed in Chapter 3, the spark discharge phase lasts from 100 ns to 10 μs [Zha97]. The observed limit of 175 ns is on the shorter end of this range. The claimed 10 or 20 ns is significantly below this range.

According to Ludwig, the instantaneous current of the spark is approximately 45 amps. This determination was based, not only on this short pulse width, but also on the assumption that the capacitance of the spark gap is charged to the open circuit potential of the power supply (approximately 15 kV). No allowance was made for the breakdown potential of air, which is approximately 2,000 V/mm between polished spherical electrodes in dry air. The breakdown potential of a 1 mm gap between a narrow tip and a nano-porous surface in humid air is on the order of hundreds (not thousands) of volts. The power supply is heavily loaded when driving such a spark gap and its open circuit voltage is irreverent.

The vast majority of the author's samples appeared similar to the type of Stage I samples Ludwig was discussing. The author observed that the samples appeared blackened when the average spark current was 55 mA. The PL intensity was also very low for such samples. Using 55 mA as an upper limit for the average current and 175 ns as a lower limit for the pulse width, together with a 19 kHz repetition rate for monitor-sparking, the maximum possible instantaneous current is about 17 A.

While the author has never made a direct measurement of the instantaneous current of Stage I sparking, he suspects it is approximately 1 A based on subjective experience.

Processing Time

Several preliminary experiments were conducted in Stage I and Stage II to determine the effect of the duration of spark-processing on the luminescence of sp-Si. These were repeated with Stage III equipment and methods resulting in the clearest results, which are presented here. There are no significant contradictions between these final results and the preliminary measurements.

Experimental procedure

Standard 1 cm x 3/4 cm chips were cleaned and etched according to the standard protocol and placed in the clean processing chamber. Following the standard pumping and baking procedure, the chamber was back-filled with a mixture of 700 mbar of UHP N_2 and 300 mbar of UHP O_2 before processing each sample. A 0.25 mm diameter tungsten electrode was used with a gap height of 0.50 mm. Two samples were prepared at each of the following processing times: 1 min., 5 min., 10 min., 15 min., 20 min., 25 min., 30 min., and 60 min. The pulse width was 1.0 μs with a 10.0 kHz repetition rate. The time-averaged current was fixed at 20.0 mA (2 A pulses). To achieve this current, power supply voltages between 5.43 kV and 5.66 kV were used. The grid voltage supply was set from 10% to 12% of maximum, and the current limiter was set from 40% to 80% of maximum.

It was clear to the eye that the longer the duration of sparking the greater the amount of built-up porous material, with the diameter and height of the porous region also increasing.

The samples were measured in the standard PL setup using an unfocused beam. The laser power was monitored and found to vary by less than 1/2% throughout the measurements. The raw spectra were calibrated and converted to radiometric intensity vs. wavelength.

Experimental results

A 3-D overview of the data is shown in Figure 5-23. The samples exhibited the standard UV/blue and green peaks. The un-deconvoluted peak locations and intensities were determined using the standard computerized algorithm. The peak locations are shown as a function of processing time in Figure 5-24. The locations of both the UV/blue and green peaks varied little except for the UV/blue peaks of the 1 minute samples, which were small and poorly developed.

The peak intensities of these bands are shown as a function of processing time in Figure 5-25. For both peaks, the trend is generally linear from 1 to 30 minutes, but some saturation is evident by about 20 minutes. When the 60 minute data points are considered, the intensities are best fit by a logarithmic function. This saturation is more clearly shown by plotting the intensity per unit of processing time against processing time (Figure 5-26) resulting in a sort of "efficiency" factor. It can be seen that the intensity per unit of processing time decreases with longer processing time for both peaks. The trend of the UV/blue peak can be fit closely by an exponential fit, while the green peak is fit fairly well by a more slowly decreasing exponential.

The ratio of the peak intensity of the green band to the peak intensity of the UV/blue band can be plotted against processing time (Figure 5-27) and found to increase in a fairly linear fashion.

PL of Sp-Si vs. Processing Time

Substrate Material:	Silicon
Atmosphere:	70% N_2 30% O_2
Electrode Material:	Tungsten 0.25 mm dia.
Electrode Gap:	0.50 mm
Frequency:	10.0 kHz
Pulse Width:	1.0 μs
Average Current:	20 mA
Processing Time:	**variable**

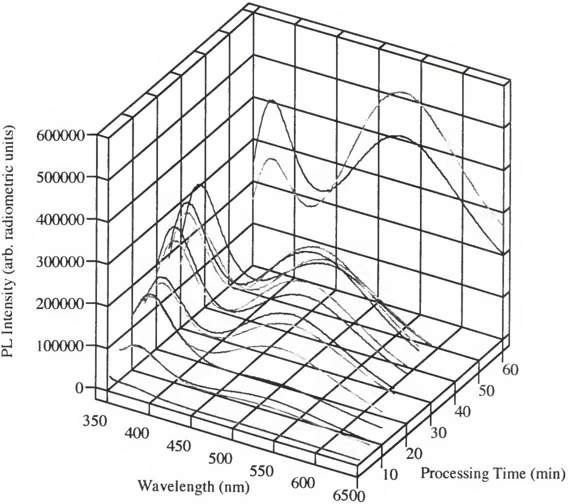

Figure 5-23: 3-D overview of the PL spectra of sp-Si as a function of processing time. There are two samples for each time value.

Location of UV/Blue and Green Peaks as a Function of Processing Time

Substrate Material:	Silicon
Atmosphere:	70% N_2 30% O_2
Electrode Material:	Tungsten 0.25 mm dia.
Electrode Gap:	0.50 mm
Frequency:	10.0 kHz
Pulse Width:	1.0 µs
Average Current:	20 mA
Processing Time:	**variable**

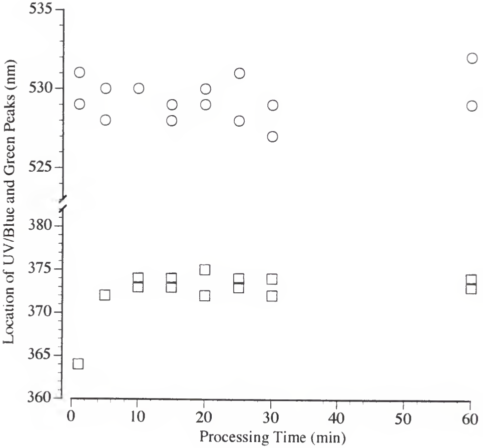

Figure 5-24: Peak locations of the PL bands of sp-Si as a function of processing time. All data points are in pairs. Overlap may cause them to appear as one.

Intensity of UV/Blue and Green Peaks as a Function of Processing Time

Substrate Material:	Silicon
Atmosphere:	70% N_2 30% O_2
Electrode Material:	Tungsten 0.25 mm dia.
Electrode Gap:	0.50 mm
Frequency:	10.0 kHz
Pulse Width:	1.0 μs
Average Current:	20 mA
Processing Time:	**variable**

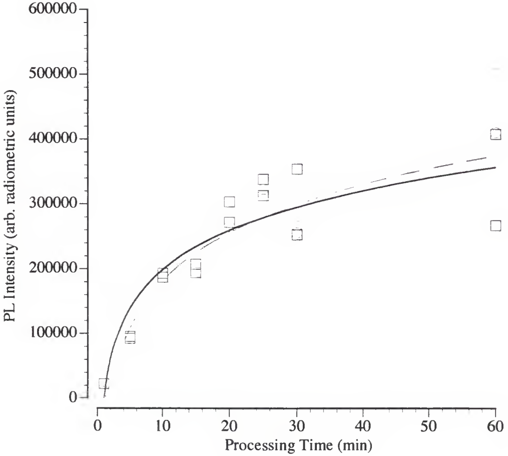

Figure 5-25: Peak intensities of the PL bands of sp-Si as a function of processing time. Logarithmic fits are shown for both bands. All data points are in pairs. Overlap may cause them to appear as one.

Intensity of UV/Blue and Green Peaks per Unit of Processing Time as a Function of Processing Time

Substrate Material: Silicon
Atmosphere: 70% N_2 30% O_2
Electrode Material: Tungsten 0.25 mm dia.
Electrode Gap: 0.50 mm
Frequency: 10.0 kHz
Pulse Width: 1.0 μs
Average Current: 20 mA
Processing Time: **variable**

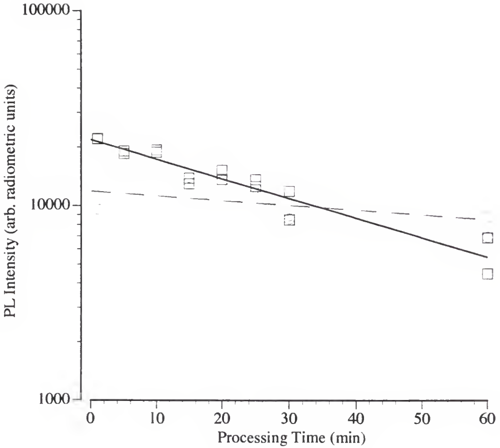

Figure 5-26: Peak intensities of the PL bands of sp-Si normalized to processing time as a function of processing time (see text). Exponential fits are shown for both bands. All data points are in pairs. Overlap may cause them to appear as one.

Ratio of Green Peak PL Intensity to UV/Blue Peak Intensity as a Function of Processing Time

Substrate Material:	Silicon
Atmosphere:	70% N_2 30% O_2
Electrode Material:	Tungsten 0.25 mm dia.
Electrode Gap:	0.50 mm
Frequency:	10.0 kHz
Pulse Width:	1.0 μs
Average Current:	20 mA
Processing Time:	**variable**

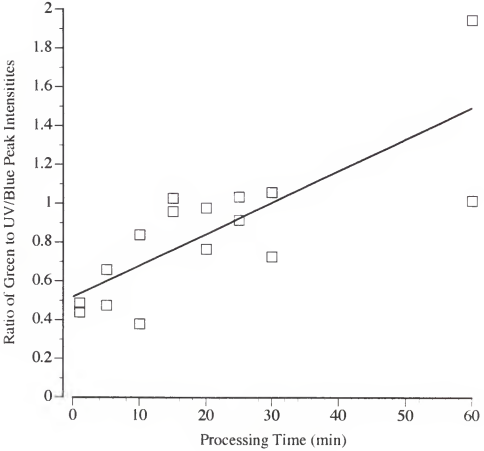

Figure 5-27: Ratio of the peak intensity of the green band of sp-Si to the peak intensity of the UV/blue band as a function of processing time. Linear fit is shown. All data points are in pairs.

Discussion of processing time results

The PL intensity of the sample increases with processing time. This trend is monotonic and less than linear although no clear saturation is seen. While a linear trend was previously reported (Figure 3-16), the conditions used in this study are more intense than Stage I monitor sparking. Furthermore, the trend observed here was fairly linear for the first 20 minutes or so. Thus, this experiment goes beyond the scope of the previous one and there is no direct contradiction.

The relative intensity of the green peak to that of the UV/blue peak was found to increase with processing time. This maybe due to reprocessing or annealing of porous material already formed. While the diameter of the spark-processed area increased with time, the spark could be seen to return to the center region from time to time regardless of how long the sample was processed.

Electrode Diameter

Stage III experiments were conducted to study the effect of the electrode diameter on the luminescence of sp-Si. Stage I experiments seemed to indicate that doubling the electrode diameter reduced the PL intensity by approximately 4 times. The more controlled Stage III measurements indicated different trends for the UV/blue and green peaks.

Experimental procedure

Standard 1 cm x 3/4 cm chips were cleaned and etched according to the standard protocol and placed in the clean processing chamber. Following the standard pumping and baking procedure, the chamber was back-filled with a mixture of 700 mbar of UHP N_2 and 300 mbar of UHP O_2 before processing each sample.

Four samples were prepared with tungsten anode electrodes of each of the following diameters: 0.25 mm, 0.50 mm, and 1.00 mm. A 0.10 mm wire proved to be too flexible to accurately set the gap distance and was consumed too rapidly for spark-processing of any significant duration. The pulse width was 1.0 μs with a 10.0 kHz repetition rate. Spark-processing was performed for 15.00 minutes duration. The time-averaged current was fixed at 20.0 mA (2 A pulses). To achieve this current, power supply voltages between 5.67 kV and 5.86 kV were used. The grid voltage supply was set from 10% to 14% of maximum, and the current limiter was set from 30% to 65% of maximum.

The samples were measured in the standard PL setup using an unfocused beam. These measurements were carried out in two sessions over two days. The laser power was monitored and found to vary by less than 1/2% throughout the measurements in each session. However, there was a 3% difference in laser power between sessions. The spectra for the second session were linearly adjusted for the power difference. The raw spectra were calibrated and converted to radiometric intensity vs. wavelength.

Experimental results

A 3-D overview of the data is shown in Figure 5-28. The samples exhibited the standard UV/blue and green peaks. The un-deconvoluted peak locations and intensities were determined using the standard computerized algorithm. The peak locations are shown as a function of electrode diameter in Figure 5-29. The mean peak locations of both the UV/blue and green bands varied little. However, there was a great deal of spread in the peak location of the relatively weak green bands of the 1.0 mm electrode samples. The intensities of the UV/blue peaks generally increase

PL of Sp-Si vs. Electrode Diameter

Substrate Material:	Silicon
Atmosphere:	70% N_2 30% O_2
Electrode Material:	Tungsten **variable dia.**
Electrode Gap:	0.50 mm
Frequency:	10.0 kHz
Pulse Width:	1.0 μs
Average Current:	20 mA
Processing Time:	15 minutes

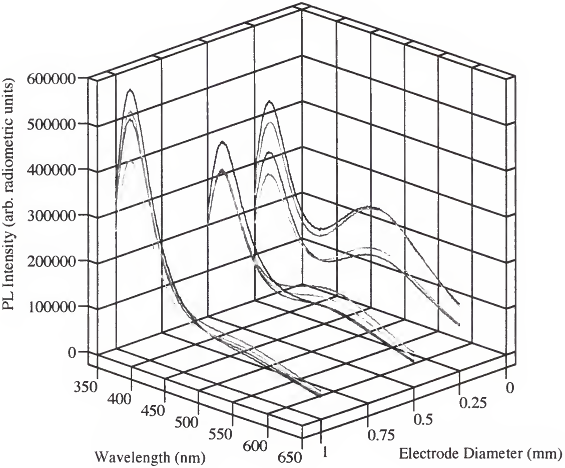

Figure 5-28: 3-D overview of the PL spectra of sp-Si as a function of electrode diameter. There are four samples for each diameter value.

Location of UV/Blue and Green Peaks as a Function of Electrode Diameter

Substrate Material:	Silicon
Atmosphere:	70% N_2 30% O_2
Electrode Material:	Tungsten **variable dia.**
Electrode Gap:	0.50 mm
Frequency:	10.0 kHz
Pulse Width:	1.0 μs
Average Current:	20 mA
Processing Time:	15 minutes

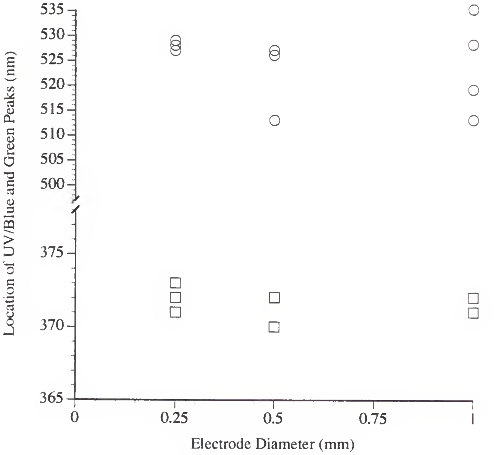

Figure 5-29: Peak locations of the PL bands of sp-Si as a function of electrode diameter. All data points are in groups of four. Overlap may cause them to appear as less than four.

and the intensities of the green peaks generally decrease as the electrode diameter increases (Figure 5-30). Both peaks have a lower intensity for all four 0.50 mm samples than would be expected if these trends were linear.

The ratio of the peak intensity of the green band to the peak intensity of the UV/blue band can be plotted against electrode diameter (Figure 5-31) and found to decrease in a fairly linear fashion. The 0.50 mm samples are slightly "bluer" than would be suggested by a linear fit, but the ratio shows less of a nonlinear deviation than either of the absolute intensities.

Discussion of electrode diameter results

There is no obvious reason why the samples sparked with the 0.50 mm diameter tungsten tip appeared to have a lower intensity than that suggested by the general trend of the data. However, the ratio of the intensity of the green peak to that of the UV/blue peak follows a clear linear trend, decreasing with increasing tip diameter. This is probably due to differences in local spark intensity. While there was only a small difference in the diameter of the spark processed area (the larger tips gave slightly larger sample diameters), there was likely a large difference in the volume of gas involved when the spark emanated from tips of different diameter. The increase in the intensity of the green peak with smaller tip diameters and the increase in the intensity of the blue peak with larger tip diameters are probably similar in origin to the trends discussed in Chapter 3. The green peak is always associated with more intense sparking or higher sample temperature during processing. The effects of spark-processing with tips of different diameters are also likely to be thermal in origin because the same spark current is heating a smaller volume of gas when the tip is smaller.

Ratio of Green Peak PL Intensity to UV/Blue Peak Intensity as a Function of Electrode Diameter

Substrate Material:	Silicon
Atmosphere:	70% N_2 30% O_2
Electrode Material:	Tungsten **variable dia.**
Electrode Gap:	0.50 mm
Frequency:	10.0 kHz
Pulse Width:	1.0 μs
Average Current:	20 mA
Processing Time:	15 minutes

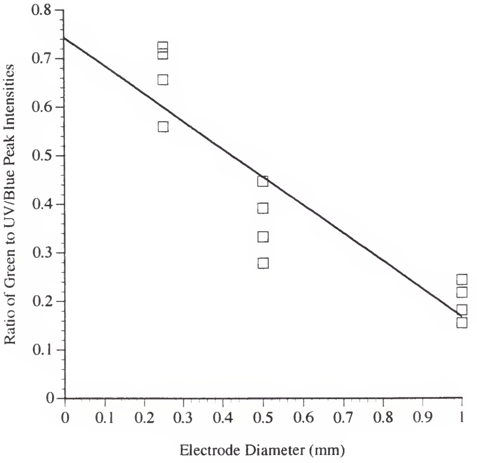

Figure 5-31: Ratio of the peak intensity of the green band of sp-Si to the peak intensity of the UV/blue band as a function of electrode diameter. Linear fit is shown. All data points are in groups of four.

Electrode Gap Distance

It has long been evident that the distance between the anode tip and the silicon substrate has a significant effect on spark-processing. This factor has usually been eliminated by selecting a fixed gap distance chosen on the basis of purely subjective observations and sticking with it. The importance of the gap distance was explored extensively in Stage III.

Experimental procedure

Standard 1 cm x 3/4 cm chips were cleaned and etched according to the standard protocol and placed in the clean processing chamber. Following the standard pumping and baking procedure, the chamber was back-filled with a mixture of 700 mbar of UHP N_2 and 300 mbar of UHP O_2 before processing each sample. A 0.25 mm diameter tungsten electrode was used. Three samples were prepared for the following electrode gaps: 0.20 mm, 0.30 mm, 0.40 mm, 0.50 mm, 0.60 mm, 0.70 mm and 0.80 mm. Two samples were made at 0.90 mm and 1.00 mm. Samples with 0.10 mm gaps proved to be impractical as the growing porous region fused with the tip within a few minutes of processing time. This appears to have occurred with one of the 0.20 mm samples as well. The pulse width was 1.0 μs with a 10.0 kHz repetition rate. Spark-processing was performed for 15.00 minutes duration. The time-averaged current was fixed at 20. mA (2 A pulses). To achieve this current, power supply voltages between 5.39 kV and 5.80 kV were used. The grid voltage supply was set from 10% to 16% of maximum, and the current limiter was set from 20% to 61% of maximum.

The samples were measured in the standard PL setup using an unfocused beam. These measurements were carried out in two sessions over two days. The laser power was monitored and found to vary by less than 1% between the two sessions.

Experimental results

A 3-D overview of the data is shown in Figure 5-32. The samples exhibited the standard UV/blue and green peaks. The un-deconvoluted peak locations and intensities were determined using the standard computerized algorithm. The peak locations are shown as a function of electrode gap in Figure 5-33. The mean locations of both the UV/blue and green peaks varied little. The peak location of the green band appears to trend slightly toward shorter wavelengths as gap distance increases. This is apparently due to the increase in the relative intensity of the UV/blue peak as the gap becomes larger. The intensities of the UV/blue peak and green peak are shown in Figure 5-34. While there is a lot of spread in the data, the average intensities of the UV/blue peaks increase in a linear manner with increasing gap distance while the intensities of the green peaks decrease in a linear manner. The sum of the two peak intensities is roughly constant over the entire range of gap distances.

The ratio of the peak intensity of the green band to the peak intensity of the UV/blue band can be plotted against electrode gap distance (Figure 5-35) and found to decrease exponentially.

Discussion of electrode gap distance results

The intensity of the UV/blue peak increases linearly with increasing gap distance while the intensity of the green peak decreases linearly. The amount of

PL of Sp-Si vs. Electrode Gap

Substrate Material:	Silicon
Atmosphere:	70% N_2 30% O_2
Electrode Material:	Tungsten 0.25 mm dia.
Electrode Gap:	**variable**
Frequency:	10.0 kHz
Pulse Width:	1.0 μs
Average Current:	20 mA
Processing Time:	15 minutes

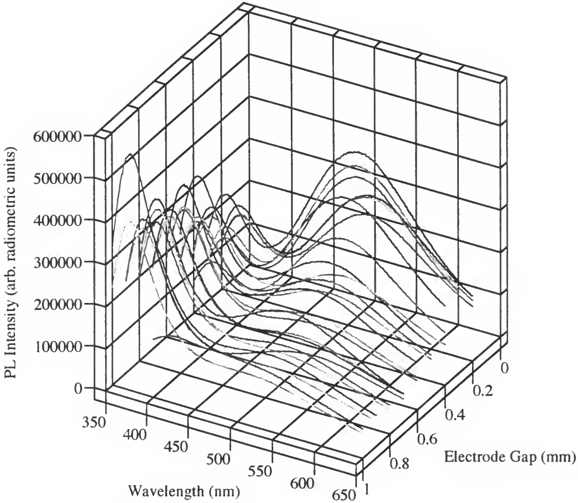

Figure 5-32: 3-D overview of the PL spectra of sp-Si as a function of electrode gap distance. There are three samples for each 0.10 mm increment from 0.20 mm to 0.80 mm and two samples at 0.90 mm and 1.00 mm.

Intensity of UV/Blue and Green Peaks as a Function of Electrode Diameter

Substrate Material:	Silicon
Atmosphere:	70% N_2 30% O_2
Electrode Material:	Tungsten **variable dia.**
Electrode Gap:	0.50 mm
Frequency:	10.0 kHz
Pulse Width:	1.0 µs
Average Current:	20 mA
Processing Time:	15 minutes

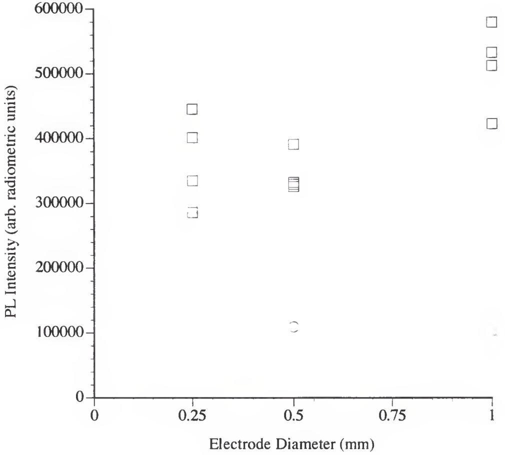

Figure 5-30: Peak intensities of the PL bands of sp-Si as a function of electrode diameter. All data points are in groups of four. Overlap may cause them to appear as less than four.

Location of UV/Blue and Green Peaks as a Function of Electrode Gap

Substrate Material:	Silicon
Atmosphere:	70% N_2 30% O_2
Electrode Material:	Tungsten 0.25 mm dia.
Electrode Gap:	**variable**
Frequency:	10.0 kHz
Pulse Width:	1.0 μs
Average Current:	20 mA
Processing Time:	15 minutes

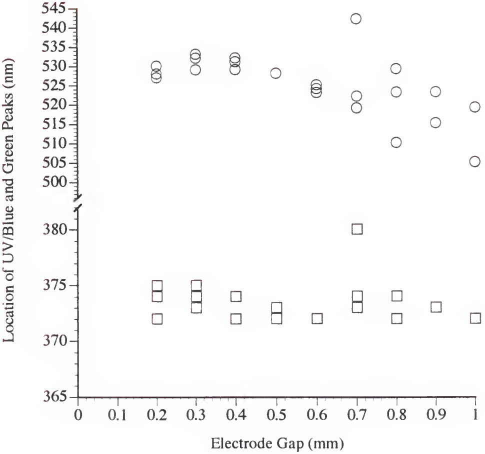

Figure 5-33: Peak locations of the PL bands of sp-Si as a function of electrode gap distance. There are three samples for each 0.10 mm increment from 0.20 mm to 0.80 mm and two samples at 0.90 mm and 1.00 mm. Overlap may cause them to appear as less.

Intensity of UV/Blue and Green Peaks as a Function of Electrode Gap

Substrate Material:	Silicon
Atmosphere:	70% N_2 30% O_2
Electrode Material:	Tungsten 0.25 mm dia.
Electrode Gap:	**variable**
Frequency:	10.0 kHz
Pulse Width:	1.0 µs
Average Current:	20 mA
Processing Time:	15 minutes

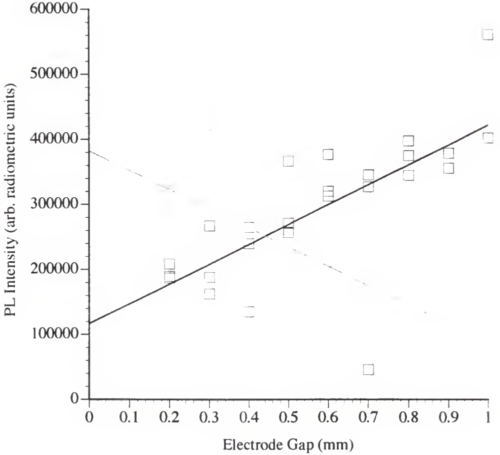

Figure 5-34: Peak intensities of the PL bands of sp-Si as a function of electrode gap distance. Linear fits are shown for both bands. There are three samples for each 0.10 mm increment from 0.20 mm to 0.80 mm and two samples at 0.90 mm and 1.00 mm. Overlap may cause them to appear as less.

Ratio of Green Peak PL Intensity to UV/Blue Peak Intensity as a Function of Electrode Gap

Substrate Material:	Silicon
Atmosphere:	70% N_2 30% O_2
Electrode Material:	Tungsten 0.25 mm dia.
Electrode Gap:	**variable**
Frequency:	10.0 kHz
Pulse Width:	1.0 μs
Average Current:	20 mA
Processing Time:	15 minutes

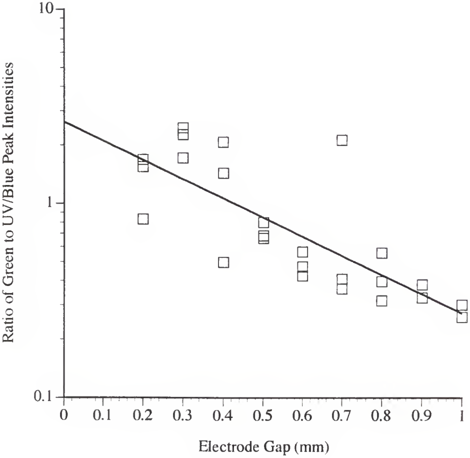

Figure 5-35: Ratio of the peak intensity of the green band of sp-Si to the peak intensity of the UV/blue band as a function of electrode gap distance. Exponential fit is shown. There are three samples for each 0.10 mm increment from 0.20 mm to 0.80 mm and two samples at 0.90 mm and 1.00 mm.

increase and decrease is essentially the same. Put another way, the sum of the peak intensities of both peaks is unchanged as the electrode gap distance is changed. The ratio of the intensity of the green peak over that of the UV/blue peak decreases with increasing gap distance in an exponential manner. This trend is even stronger than that seen with increasing electrode diameter in the previous section. Remarkably, the gap distance has no noticeable effect on the diameter of the processed region. This is true over the whole gap distance range of 0.20 to 1.00 mm. The larger the gap, the greater the volume of gas involved in the spark. It can be argued, as it was for tip diameter, that when the spark is confined to a smaller volume of gas, greater local heating occurs. In this case, this is the only explanation. as the diameter of the porous region itself does not change.

Tip Material

Tip material is included under physical parameters because, as discussed in Chapter 3, chemical contamination from the tip is not responsible for the PL bands. However, differences in peak intensity were attributed to the properties of the tip material, including corrosion resistance [Hum98]. While most refractory metals were tested in this paper and found to be inferior to tungsten. one promising candidate was not considered.

Rhenium is a dense yet ductile refractory metal with a melting point almost as high as tungsten. It has better high temperature spark erosion characteristics than tungsten and is commonly used to plate relay contacts for this very reason. Rhenium has good electrical conductivity, while tungsten is a fairly poor conductor compared to most metals. Furthermore, rhenium is available in significantly purer grades than tungsten because it can be drawn into wire as opposed to tungsten, which is prepared by powder metallurgy and retains significant porosity.

Samples were sparked with tungsten and rhenium anodes with a large spark gap (approximately 1 mm) for 15 minutes and 1 hour under Stage I conditions (monitor sparking). The rhenium was observed to oxidize much less than the tungsten. Rhenium oxide is a dense black powder, which adhered to the tip and was apparently non-conductive because it interfered with the spark and had to be scrapped off with a knife several times so that sparking could resume. The tungsten oxide had a tan color and tended to flake off the tip as it accumulated. It also did not appear to interfere with the spark. Tungsten oxide is known to have fairly good conductivity.

The 15 minute rhenium-tip and tungsten-tip samples all exhibited strong UV/blue PL bands. In each case, the peak intensity of the tungsten-tip samples was about twice that of the rhenium-tip samples. Only the 1 hour tungsten-tip sample exhibited a strong green PL peak. The differences must be due to a greater current from the same supply when tungsten is used.

When a small spark gap is used (approximately 0.3 mm) with a rhenium tip, a sample sparked for 1 hour has a PL intensity almost indistinguishable from one sparked for 15 minutes. The adherent oxide appears to form rapidly on the very tip of the wire. Subsequent sparking occurs between the side of the wire shaft and a larger area of the sample.

These observations, in addition to the previous work [Hum98], indicate that despite its fairly rapid oxidation, tungsten appears to be the best tip material for spark-processing.

Chemical Processing Parameters

Early in Stage I it was learned that the chemistry and pressure of the gas ambient were critical parameters. The literature is clear that both nitrogen and oxygen must be present for the UV/blue and green bands of sp-Si to exist. It was also evident to the naked eye that the spark intensity (corresponding to current) decreased as the ratio of N_2 to O_2 in the chamber was increased. Figure 3-15 is indicative of the early results obtained with fixed-voltage supplies. In the previous section, it was determined that current is a major processing parameter. Thus, the previous results were caused by a combination of the gas chemistry and the current variations. If the current were held constant, the results would likely be much different. Such experiments were carried out in Stage II and III and the latter are presented here.

Nitrogen Concentration

In preliminary Stage II experiments it became clear that very small amounts of oxygen present in the chamber had a substantial influence on the properties of the samples. With "pure" N_2, a noticeable difference in the diameter of the spark could be seen depending on whether the chamber had been pumped down for one day or four days prior to back-filling with UHP N_2. There was also a difference in the PL intensity of such samples. Also, if the native oxides were not etched from the samples, sample stage, and tip holder shortly before evacuation, the spark could be seen to start with a large diameter and evolve over the course of a few minutes to a smaller diameter as minute quantities of oxygen were liberated and made available to the spark. Oxygen appears to be ionized much more readily than nitrogen. Clearly, when fewer ions are available, the spark must occupy a larger volume to maintain the same current. Based on these observations, pure N_2 was rarely used as an experimental parameter and the reader should not equate the occurrence of PL in a sample sparked in "pure" N_2 with a process not involving oxygen. Oxygen appears to always be involved when PL is observed. This oxidation may occur from minute quantities of oxygen in the chamber or may occur instantly on the porous surface when the samples are removed from the chamber and exposed to air.

Experimental procedure

Eighteen samples were prepared to determine the effect of the N_2 concentration on the PL of sp-Si. Two samples were prepared for each of the following nitrogen concentrations: 10%, 20%, 30%, 50%, 60%, 70%, 80% and 90%. Standard 1 cm x 3/4 cm chips were cleaned and etched according to the standard protocol and placed in the clean processing chamber. Following the standard pumping and baking procedure, the chamber was back-filled with the desired partial pressure of UHP N_2. Following this, UHP O_2 was added until a total pressure of 1,000 mbar was reached. A 0.25 mm diameter tungsten electrode was used with a gap distance of 0.50 mm. The average spark current was fixed at 21.0 mA. The pulse width was 1.0 μs with a 10.0 kHz repetition rate. The total processing duration was 15.00 minutes. To achieve this range of currents, power supply voltages between 5.20 kV and 5.58 kV were used. The adjustment of the grid voltage supply varied from 20% to 24% and grid current limiter was held at 0% throughout these experiments.

It was soon evident that more data were needed at very high nitrogen concentrations and 10 more samples were produced, two at each of the following N_2 concentrations: 80%, 90%, 95%, 97%, and 99%. These samples were produced with power supply voltages near 5.6 kV and grid voltage supply and current limiter settings of approximately 10% and 50%, respectively. The overlap in nitrogen concentrations between the two experiments was deliberate so that the data could be corrected and directly compared.

Samples with nitrogen concentrations ranging from 70% to 99% were virtually indistinguishable to the eye. The sparked area was slightly larger for the 70% samples but by an amount so small that it would be questionable had the trend not continued below 70%. All had central regions that were tan in color with a well-defined perimeter. These central regions were surrounded by a brown ring with a sharply defined outer perimeter. Finally these brown areas were surrounded by a small "halo" of white power on the surface of the silicon. These samples looked just like standard sp-Si samples prepared in air. As the nitrogen concentration was decreased from 50% to 10%, there is a gradual trend toward larger central porous regions, smaller brown rings, and smaller and thinner halo regions. The central regions of the 10% and 20% nitrogen samples were poorly defined and were slightly darker in tint. In general, the total differences between the appearance of the samples were minor compared to that which occurred when temporal and electrical parameters were changed in other experiments. This lends credence to the observations that the material is predominantly an oxide regardless of the atmosphere and that nitrogen, while crucial for luminescence, is a minority constituent.

The samples were measured in the standard PL setup using an unfocused beam. The raw spectra were calibrated and converted to radiometric intensity vs. wavelength. The spectra of the second set of samples were multiplied by a correction factor based on the mean values of the green peak intensities of all eight 80% and 90% N_2 samples.

PL of Sp-Si vs. Nitrogen Concentration

Substrate Material:	Silicon
Atmosphere:	**N_2 and O_2 variable**
Electrode Material:	Tungsten 0.25 mm dia.
Electrode Gap:	0.50 mm
Frequency:	10.0 kHz
Pulse Width:	1.0 μs
Average Current:	21 mA
Processing Time:	15 minutes

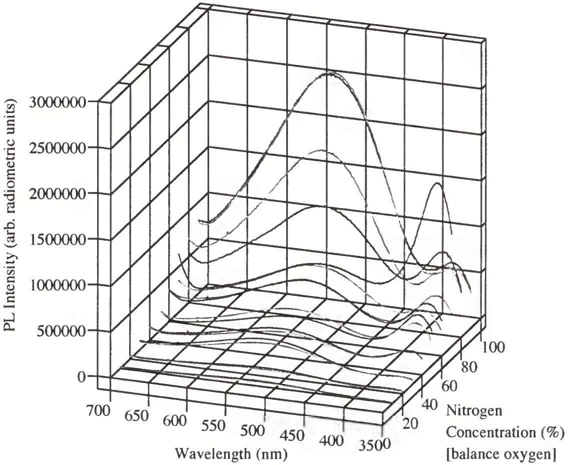

Figure 5-36: 3-D overview of the PL spectra of sp-Si as a function of the nitrogen concentration of the ambient (balance oxygen). There are two samples for each concentration increment.

Location of UV/Blue and Green Peaks as a Function of Nitrogen Concentration

Substrate Material:	Silicon
Atmosphere:	**N_2 and O_2 variable**
Electrode Material:	Tungsten 0.25 mm dia.
Electrode Gap:	0.50 mm
Frequency:	10.0 kHz
Pulse Width:	1.0 μs
Average Current:	21 mA
Processing Time:	15 minutes

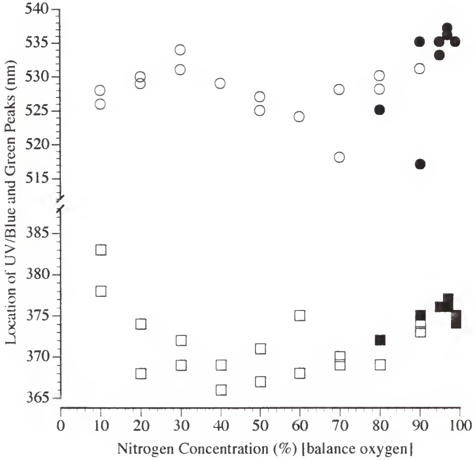

Figure 5-37: Peak locations of the PL bands of sp-Si as a function of the nitrogen concentration of the ambient. There are two samples for each concentration increment except at 80% N_2 and 90% N_2 at which there are four. Overlap may cause them to appear as less. Filled symbols represent the second set of samples, see text.

Intensity of UV/Blue and Green Peaks as a Function of Nitrogen Concentration

Substrate Material: Silicon
Atmosphere: **N_2 and O_2 variable**
Electrode Material: Tungsten 0.25 mm dia.
Electrode Gap: 0.50 mm
Frequency: 10.0 kHz
Pulse Width: 1.0 μs
Average Current: 21 mA
Processing Time: 15 minutes

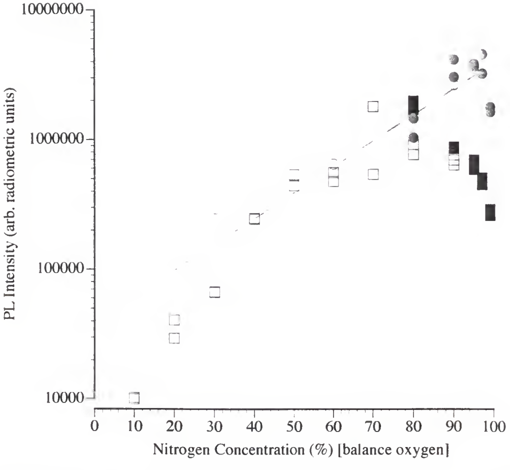

Figure 5-38: Peak intensities of the PL bands of sp-Si as a function of the nitrogen concentration of the ambient. There are two samples for each concentration increment except at 80% N_2 and 90% N_2 at which there are four. Overlap may cause them to appear as less. An exponential fit is shown for the green band of the first set of samples. Filled symbols represent the second set of samples, see text.

Ratio of Green Peak PL Intensity to UV/Blue Peak Intensity as a Function of Nitrogen Concentration

Substrate Material:	Silicon
Atmosphere:	**N_2 and O_2 variable**
Electrode Material:	Tungsten 0.25 mm dia.
Electrode Gap:	0.50 mm
Frequency:	10.0 kHz
Pulse Width:	1.0 µs
Average Current:	21 mA
Processing Time:	15 minutes

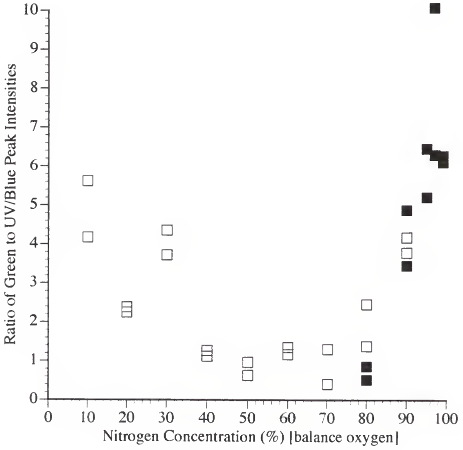

Figure 5-39: Ratio of the peak intensity of the green band of sp-Si to the peak intensity of the UV/blue band as a function of the nitrogen concentration of the ambient. There are two samples for each concentration increment except at 80% N_2 and 90% N_2 at which there are four. Filled symbols represent the second set of samples, see text.

Experimental results

A 3-D overview of the data for the first set of samples is shown in Figure 5-36. The samples exhibited the standard UV/blue and green peaks. The un-deconvoluted peak locations and intensities were determined using the standard computerized algorithm. The peak locations are shown as a function of nitrogen concentration in Figure 5-37. Both sets of samples are depicted in the figure, with the symbols for the first set unfilled and those corresponding to the second set filled. The locations of both the UV/blue and green peaks varied little across the entire concentration range.

The intensities of these peaks are shown as a function of nitrogen concentration in Figure 5-38. The absolute intensity of the UV/blue peak increases as the nitrogen concentration increases until around 70% to 80% N_2 at which point it saturates and then begins to decrease. The intensity of the green peak continues to increase reaching a maximum around 90% to 97% N_2 but can be seen to decrease significantly when 99% N_2 is reached. With the sole exception of the 99% N_2 samples, the green intensity data is closely fit by an exponential. The exponential fit shown in the figure was calculated from the first set of samples only.

The ratio of the peak intensity of the green band to the peak intensity of the UV/blue band can be plotted against nitrogen concentration, see Figure 5-39. The samples are significantly more green both at low nitrogen concentrations (below 40%) and at high nitrogen concentrations (above 80%). From 40% to 80% N_2, the ratio is around 1:1.

Discussion of nitrogen concentration results

The trend for the green peak is the easiest to explain. Nitrogen is obviously strongly involved in the green PL mechanism. The appearance of the samples indicates that there is plenty of oxygen available in the spark to form an oxide matrix but that very high concentrations of nitrogen make more nitrogen available for inclusion in sp-Si. A minority constituent can very significantly in relative abundance and still be a small part of the whole. Only at some point between 97% and 99% nitrogen, is oxygen so scarce that the formation of the porous oxide matrix itself is hindered and the PL is reduced somewhat. Finally, the nonlinear relationship between nitrogen concentration and PL intensity resembles the known case of nitrogen clustering into N_2 isoelectronic centers discussed in Chapter 3. While the luminescent species here may not be as simple as a N_2 center, it may involve the presence of more than one nitrogen atom per center. This analysis will be revisited in Chapter 7 after the role of nitrogen in spark-processed elements other than silicon has been explored.

Because the PL intensity of the UV/blue peak is maximized at much lower nitrogen concentrations than the green peak, it is somewhat more difficult to explain. While the center or chemical species responsible clearly involves nitrogen, oxygen may play a larger role in such a center. Another possibility is that the UV/blue and green mechanisms are competitive. This could be either competition for available nitrogen during the initial defect center formation at the time of processing (similar to that seen in N vs. N_2 isoelectronic centers) or competition over excited charge carriers during the PL measurement. This topic must be taken up later as well, not only until other elements are discussed, but also after time-resolved PL experiments have been presented. This is because it will be shown that the UV/blue and green PL processes are slower when both are present in the same sample than they are in samples that are either predominantly UV/blue or predominantly green.

Air Pressure

Initially, Stage I experiments were conducted in a partially evacuated glass tube containing air. As expected, no spark could be observed in vacuum. As the air pressure was increased, a glow discharge was seen that slowly developed into a cone of plasma. This plasma cone evolved into discrete spark events between 200 and 300 mbar pressure. Using an AM radio placed next to the chamber, the point at which sparking occurred could be detected by the sudden appearance of static on the radio. The "plasma-processed" samples had a very thin and uniform porous area and exhibited only weak blue PL.

These early experiments were followed up in Stage II using both air and pure gases. Pulses of 1.0 μs with a 10.0 kHz repetition rate were used and the samples were sparked for 15.00 minutes from a 0.25 mm diameter tungsten electrode. However, optimal values of the other processing parameters had not yet been established. These experiments were conducted with a fairly large 1.00 mm gap and voltage and grid control settings that were later learned to correspond to a fairly large current of about 35 mA.

Experimental procedure

In the first of these experiments, the cleaned and etched samples were placed in the chamber, which was evacuated and back-filled with normal air to the desired pressure. This experiment was never repeated because it was discovered that sparking in humid air in a closed chamber produced nitric acid that attacked a number of parts in the vacuum system.

Six samples were produced by sparking in air at the following pressures: 210 mbar, 324 mbar, 426 mbar, 607 mbar, 799 mbar, and 1,001 mbar.

Experimental results

A 3-D overview of the air pressure data is shown in Figure 5-40. All the samples exhibited one or both of the standard PL peaks except for the 210 mbar sample which exhibited neither and had a complicated peak structure in the 400 - 500 nm range consistent with known defects in silica as discussed in Chapter 3. As expected, this luminescence was very weak. The undeconvoluted peak locations and intensities were determined using the standard computerized algorithm. The peak location is shown as a function of air pressure in Figure 5-41. The 324 mbar sample exhibited no discernable green peak. Both undeconvoluted peaks were somewhat blue shifted with increasing air pressure. The PL peak intensities are shown as a function of air pressure in Figure 5-42. The 1 mm spark gap used for this experiment is too large to give substantial green PL. Here we see the PL initially increases rapidly as the pressure is increased and the trend appears to begin to saturate between 800 mbar and 1,000 mbar (approximately one atmosphere). The increase in the green PL is smaller but appears to show a similar saturation. The ratio of the peak intensity of the green peak to the peak intensity of the UV/blue peak is shown in Figure 5-43. The samples appear to be slightly more blue at higher pressures.

PL of Sp-Si vs. Air Pressure

Substrate Material:	Silicon
Atmosphere:	Air, **variable pressure**
Electrode Material:	Tungsten 0.25 mm dia.
Electrode Gap:	1.00 mm
Frequency:	10.0 kHz
Pulse Width:	1.0 μs
Average Current:	≈ 35 mA (Stage II)
Processing Time:	15 minutes

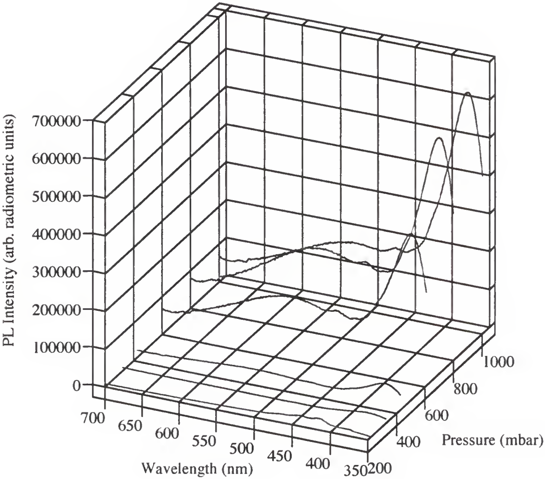

Figure 5-40: 3-D overview of the PL spectra of sp-Si as a function of the pressure of the air ambient.

Location of UV/Blue and Green Peaks as a Function of Air Pressure

Substrate Material:	Silicon
Atmosphere:	Air, **variable pressure**
Electrode Material:	Tungsten 0.25 mm dia.
Electrode Gap:	1.00 mm
Frequency:	10.0 kHz
Pulse Width:	1.0 μs
Average Current:	≈ 35 mA (Stage II)
Processing Time:	15 minutes

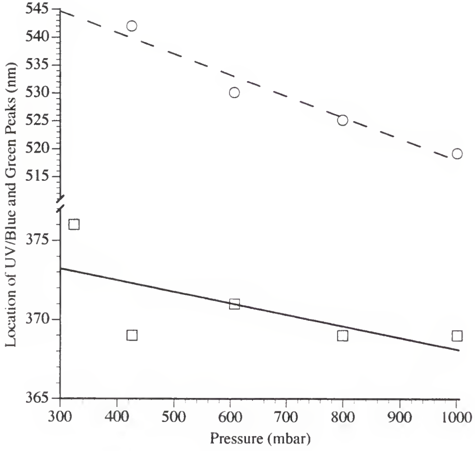

Figure 5-41: Peak locations of the PL bands of sp-Si as a function of the pressure of the air ambient. Linear fits are shown for both bands.

Intensity of UV/Blue and Green Peaks as a Function of Air Pressure

Substrate Material:	Silicon
Atmosphere:	Air, **variable pressure**
Electrode Material:	Tungsten 0.25 mm dia.
Electrode Gap:	1.00 mm
Frequency:	10.0 kHz
Pulse Width:	1.0 µs
Average Current:	≈ 35 mA (Stage II)
Processing Time:	15 minutes

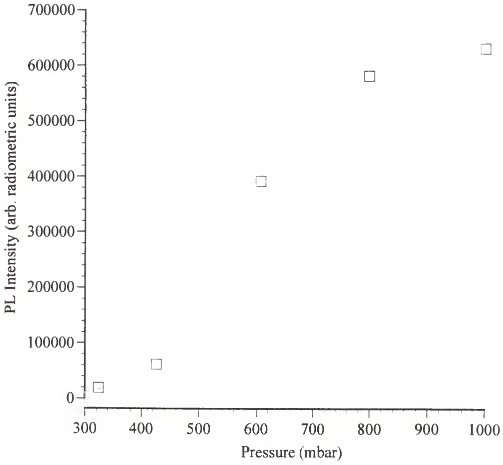

Figure 5-42: Peak intensities of the PL bands of sp-Si as a function of the pressure of the air ambient. The 324 mbar sample had no clear green peak, only a shoulder, and its intensity at 525 nm was substituted.

Ratio of UV/Blue and Green Peaks as a Function of Air Pressure

Substrate Material:	Silicon
Atmosphere:	Air, **variable pressure**
Electrode Material:	Tungsten 0.25 mm dia.
Electrode Gap:	1.00 mm
Frequency:	10.0 kHz
Pulse Width:	1.0 μs
Average Current:	≈ 35 mA (Stage II)
Processing Time:	15 minutes

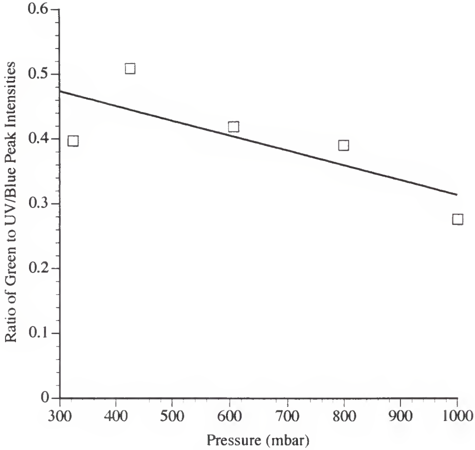

Figure 5-43: Ratio of the peak intensity of the green band of sp-Si to the peak intensity of the UV/blue band as a function of the pressure of the air ambient. The 324 mbar sample had no clear green peak, only a shoulder, and its intensity at 525 nm was substituted.

Discussion of air pressure results

There are not enough data points here to say anything definitive. The apparent trends might not be real. This experiment proved to be corrosive to the equipment and was repeated with a mixture of UHP N_2 and UHP O_2 rather than air.

Gas Pressure

The previous air pressure experiment was repeated using a mixture of 70% UHP N_2 and 30% UHP O_2 to roughly approximate the composition of air. All other conditions were the same.

Experimental procedure

One sample was processed at each of the following total pressures: 400 mbar, 599 mbar, 800 mbar, 1,001 mbar, 1,199 mbar, 1,400 mbar, 1,599 mbar, 1,800 mbar, and 1,998 mbar.

Experimental results

A 3-D overview of the gas pressure data is shown in Figure 5-44. Unfortunately, no green PL was discernable in these samples. Again, the large gap arbitrarily chosen for these experiments is to blame. The peak location of the UV/blue band is shown as a function of gas pressure in Figure 5-45. The peak location is essentially constant at all pressures (2 nm scatter). The intensity of the UV/blue peak is shown as a function of gas pressure in Figure 5-46. While there is a lot of scatter, the intensity appears to increase linearly with pressure.

PL of Sp-Si vs. Gas Pressure

Substrate Material:	Silicon
Atmosphere:	70% N_2 30% O_2, **variable pressure**
Electrode Material:	Tungsten 0.25 mm dia.
Electrode Gap:	1.00 mm
Frequency:	10.0 kHz
Pulse Width:	1.0 μs
Average Current:	≈ 35 mA (Stage II)
Processing Time:	15 minutes

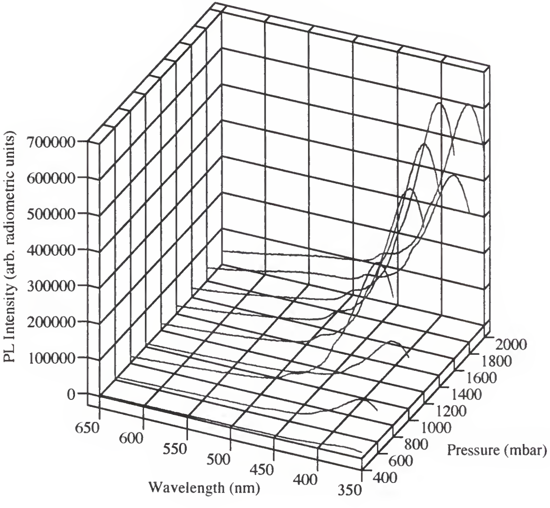

Figure 5-44: 3-D overview of the PL spectra of sp-Si as a function of the pressure of the gas ambient.

Location of the UV/Blue Peak as a Function of Gas Pressure

Substrate Material:	Silicon
Atmosphere:	70% N_2 30% O_2, **variable pressure**
Electrode Material:	Tungsten 0.25 mm dia.
Electrode Gap:	1.00 mm
Frequency:	10.0 kHz
Pulse Width:	1.0 μs
Average Current:	≈ 35 mA (Stage II)
Processing Time:	15 minutes

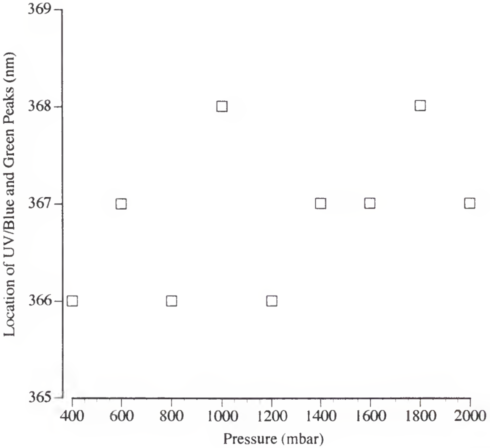

Figure 5-45: Peak location of the UV/blue PL band of sp-Si as a function of the pressure of the gas ambient.

Intensity of the UV/Blue Peak as a Function of Gas Pressure

Substrate Material:	Silicon
Atmosphere:	70% N_2 30% O_2, **variable pressure**
Electrode Material:	Tungsten 0.25 mm dia.
Electrode Gap:	1.00 mm
Frequency:	10.0 kHz
Pulse Width:	1.0 μs
Average Current:	≈ 35 mA (Stage II)
Processing Time:	15 minutes

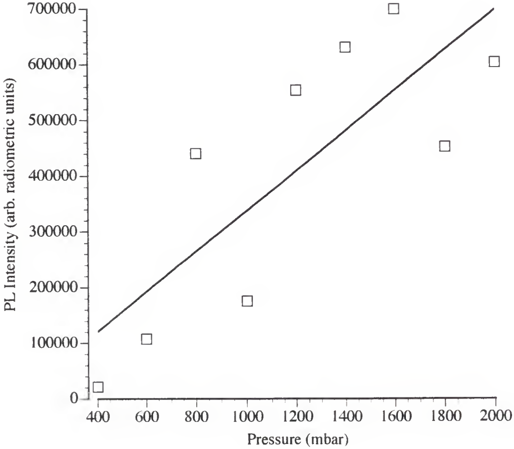

Figure 5-46: Peak intensity of the UV/blue PL band of sp-Si as a function of the pressure of the gas ambient. A linear fit is shown.

Discussion of gas pressure results

The only definitive conclusion that can be drawn from the gas pressure results taken together with the preceding air pressure results is that the peak locations of the two PL bands are not significantly dependent on pressure. The two experiments contradict one another as to whether the intensity increases with increasing pressure in a uniform manner or if saturation occurs. However, it can be stated that regardless of the exact relationship, the intensity of both PL bands increases at higher processing pressure. The large scatter seen in the data is typical of Stage II and earlier experiments where there was no fine control of the spark current.

The author is not satisfied with these results and believes that it would be worthwhile for a succeeding investigator to perform the gas pressure experiment using Stage III equipment. Samples should be sparked with a 0.50 mm gap at about 25 mA current at small increments from about 400 mbar to 2000 mbar with at least two samples at each pressure.

Pure Atmospheres

Samples were spark-processed using standard conditions in air (with the chamber open to prevent corrosion), pure nitrogen, and pure helium. In the latter two cases the chamber was pumped and baked for 4 days each time and back-filled with the selected UHP gas at least 10 times. A titanium sublimation pump was also run twice each day of the pump down to remove as much water and oxygen as possible. These samples were produced late in Stage II. The PL spectra were measured under identical conditions and are shown in Figure 5-47.

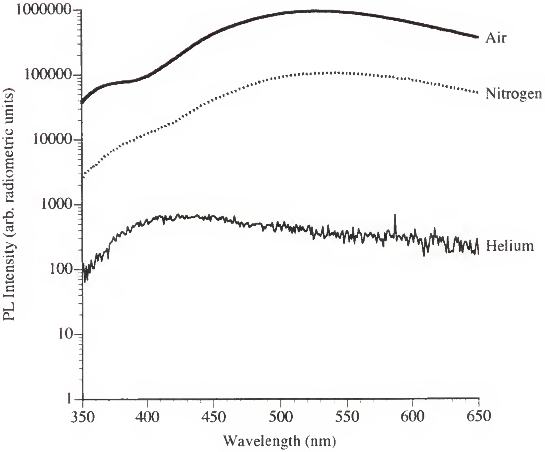

Figure 5-47: PL spectra of sp-Si samples produced in air, nitrogen, and helium ambients, see text.

In this logarithmic graph, the two peaks of the air-sparked sample are distinctly visible. It is interesting that when sparking in the purest nitrogen atmosphere obtainable, with a regulated current supply, the PL intensity of the green peak is almost exactly one order of magnitude lower than it is in the air-sparked sample. With a fixed voltage supply, this difference would have been several orders of magnitude. A shoulder at the location of the UV/blue peak is present but the intensity difference is larger. Both the significant green PL in a "pure" nitrogen-sparked sample and the apparently larger dependence of the UV/blue intensity on the presence of residual oxygen are consistent with the trends shown in Figure 5-38. However, this is completely inconsistent with the literature, which was based on fixed-voltage power supplies that did not maintain a constant current.

Helium is an inert gas and it is surprising that spark-processing occurred at all. The broad PL appears to peak around 425 nm and is over three orders of magnitude less intense that that of the air-sparked sample. This is consistent in location and intensity with the previous literature on sparking in pure O_2. This demonstrates that even trace oxygen (in the form of water) in the chamber can result in the production of an oxide material, as was suspected in the "pure" N_2 results.

Nitrogen and Carbon Dioxide

Several sp-Si samples have been produced by the author by spark-processing in a CO_2 atmosphere during Stage I. It was evident that the resulting PL differed from that of conventional air-sparked sp-Si. This deserved a closer look using Stage III equipment and procedures. As it was already known that nitrogen plays a crucial role in the PL of conventional sp-Si, an experiment was performed to examine the effects of sparking in pure CO_2 as well as mixtures of N_2 and CO_2. These results are reported in terms of N_2 concentration with the balance being CO_2, instead of O_2 as in previous experiments. It should be noted that due to the unavailability of UHP CO_2, instrument grade CO_2 was used instead.

Experimental procedure

Fourteen samples were prepared to determine the effect of the N_2 and CO_2 concentrations on the PL of sp-Si. Two samples were prepared for each of the following nitrogen concentrations: 10%, 30%, 50%, 70%, and 90%. In addition, 4 samples were prepared in pure CO_2 (0% N_2). Standard 1 cm x 3/4 cm chips were cleaned and etched according to the standard protocol and placed in the clean processing chamber. Following the standard pumping and baking procedure, the chamber was back-filled with the desired partial pressure of UHP N_2. Following this, CO_2 was added until a total pressure of 1,000 mbar was reached. A 0.25 mm diameter tungsten electrode was used with a gap distance of 0.50 mm. The average spark current was fixed at 21.0 mA. The pulse width was 1.0 μs with a 10.0 kHz repetition rate. The total processing duration was 15.00 minutes. To achieve this range of currents, power supply voltages between 5.37 kV and 5.70 kV were used. The adjustment of the grid voltage supply setting varied from 16% to 21% and the grid current limiter setting was held at 0% throughout the experiments.

Samples with nitrogen concentrations ranging from 10% to 90% were virtually indistinguishable to the eye. All had central regions that were tan in color with a well-defined parameter. These central regions were surrounded by a brown ring with a sharply defined outer perimeter. Unlike their N_2/O_2 counterparts, these samples do not have a halo of white powder. The 30% N_2 sample, and especially the 10% N_2 sample, have a hint of black in the central area, probably carbon soot. The

0% N_2 (100% CO_2) samples are similar in shape and form but are slightly larger. In addition, the central region has some black areas and the surrounding ring is a mixture of black and the usual brown. Again, the presence of carbon is the likely explanation.

The samples were measured in the standard PL setup using an unfocused beam. These measurements were carried out in two sessions over two days. The laser power was monitored and found to vary by less than 1/2% throughout the measurements in each session. However, there was a 4% difference in laser power between sessions. The spectra for the second session were linearly adjusted for the power difference. The raw spectra were calibrated and converted to radiometric intensity vs. wavelength.

Experimental results

A 3-D overview of the data is shown in Figure 5-48. The samples exhibited a broad green peak and some had a shoulder in the blue. The un-deconvoluted peak locations and intensities were determined using the standard computerized algorithm. The peak locations of the green band are shown as a function of nitrogen concentration in Figure 5-49. At 90% N_2, the peak location is near that which would be expected for conventional sp-Si, while it is at a significantly longer wavelength for lesser N_2 concentrations.

The intensities of these peaks are shown as a function of nitrogen concentration in Figure 5-50. With the exception of one 90% N_2 sample being significantly more intense than the other, the intensity is essentially constant from 10% N_2 through 90% N_2. This is in stark contrast to conventional sp-Si (Figure 5-38).

PL of Sp-Si vs. Nitrogen Concentration

Substrate Material:	Silicon
Atmosphere:	**N_2 and CO_2 variable**
Electrode Material:	Tungsten 0.25 mm dia.
Electrode Gap:	0.50 mm
Frequency:	10.0 kHz
Pulse Width:	1.0 µs
Average Current:	21 mA
Processing Time:	15 minutes

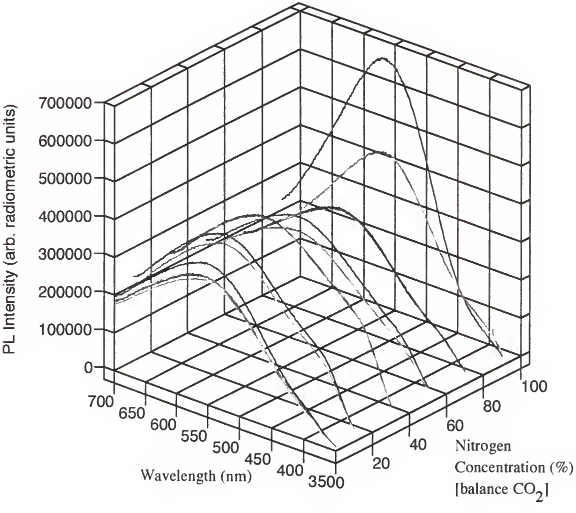

Figure 5-48: 3-D overview of the PL spectra of sp-Si as a function of the nitrogen concentration of the ambient (balance CO_2). There are two samples for each concentration increment, except at 0% N_2 where there are four.

Location of Green Peak as a Function of Nitrogen Concentration (balance CO_2)

Substrate Material:	Silicon
Atmosphere:	**N_2 and CO_2 variable**
Electrode Material:	Tungsten 0.25 mm dia.
Electrode Gap:	0.50 mm
Frequency:	10.0 kHz
Pulse Width:	1.0 μs
Average Current:	21 mA
Processing Time:	15 minutes

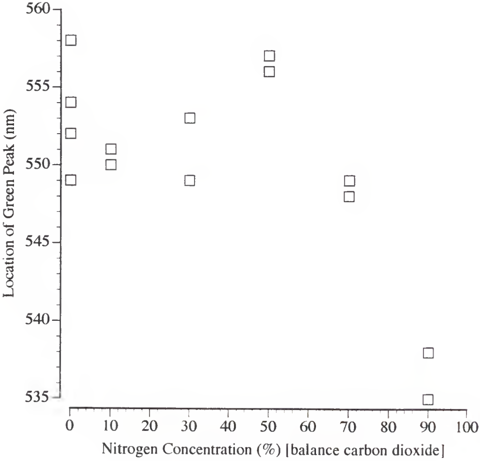

Figure 5-49: Peak location of the PL spectrum of sp-Si as a function of the nitrogen concentration of the ambient (balance CO_2). There are two samples for each concentration increment, except at 0% N_2 where there are four.

Intensity of Green Peak as a Function of Nitrogen Concentration (balance CO_2)

Substrate Material:	Silicon
Atmosphere:	**N_2 and CO_2 variable**
Electrode Material:	Tungsten 0.25 mm dia.
Electrode Gap:	0.50 mm
Frequency:	10.0 kHz
Pulse Width:	1.0 μs
Average Current:	21 mA
Processing Time:	15 minutes

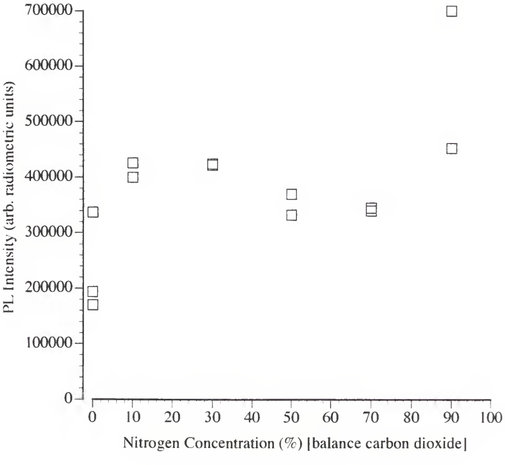

Figure 5-50: Peak intensity of the PL spectrum of sp-Si as a function of the nitrogen concentration of the ambient (balance CO_2). There are two samples for each concentration increment, except at 0% N_2 where there are four.

The 0% N_2 (100% CO_2) samples average about half as bright as those with some nitrogen.

Figure 5-51 shows the self-normalized spectra of three samples: 0% N_2 (pure CO_2), 30% N_2, and 90% N_2. The pure CO_2 sample has a green peak that is significantly broader in addition to being located at a longer wavelength. The green peak at other concentrations appears to be a superposition of two curves. The blue shoulder was that largest for the 30% N_2 samples.

The samples processed with significant amounts of CO_2 have a PL afterglow that is perceptible to the eye. This will be discussed when time resolved PL is presented in Chapter 8.

Discussion of nitrogen and carbon dioxide results

The PL of these samples appears to result from the superposition of three types of luminescence. The two bands seen in conventional sp-Si and an additional carbon-related broad green band near 555 nm. This band and the green nitrogen-related band must have a similar efficiency and dependence on concentration for the cumulative peak PL intensity to remain constant over such a large concentration range. While this might be a coincidence, it may also have a deeper underlying meaning. There may be a common absorption mechanism with charge transfer to more than one emission mechanism, neither of which is the efficiency-limiting step in the process. Evidence of charge transfer will be presented in Chapter 8

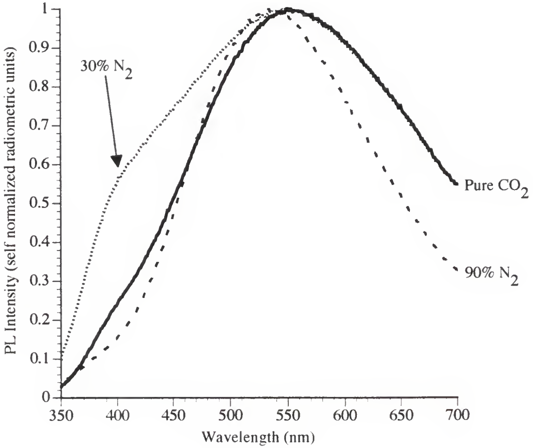

Figure 5-51: Self-normalized PL spectra of sp-Si in pure CO_2 (solid line), 30% N_2 (dotted line), and 90% N_2 (dashed line). The balance was CO_2.

CHAPTER 6
RESULTS: MICROSCOPY AND CHEMICAL SPECTROSCOPIES OF SPARK-PROCESSED SILICON

Scanning Electron Microscopy (SEM)

SEM micrographs were taken of a typical Stage I monitor sparked sample at the site of a fresh fracture through the center of the spark-processed region. The samples were not coated. Stage I monitor sparking is dramatically more similar to Stage II and III sparking than the early low-current Tesla coil sparking represented by the SEM micrographs in the literature. These images are of the cross-section of the wafer at the upper edge of the spark-processed region. Figure 6-1 shows the microstructure at 130 X magnification. The image is deliberately somewhat dark to bring out the limited contrast of the area of interest. A number of the channels or "worm holes" described in Chapter 3 are exposed by the fracture. The exposed sections are hundreds of micrometers in depth. They can also be seen to twist and turn rather than proceed straight through. The figure may be compared with Figure 3-4. The porous region of the monitor sparked sample is significantly thicker. The worm holes of the Tesla coil sparked sample are shorter, much straighter, and less convoluted than those of the monitor sparked sample. These winding paths are extraordinarily unlikely to have been created by single spark events as Ludwig suggests [Lud96a], but represent the cumulative erosion of the same channel around which the insulating matrix was built-up. The spark repeatedly strikes these preferred pathways depositing more and more material around them.

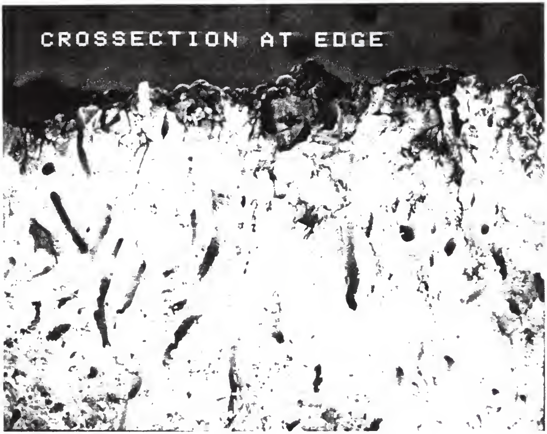

Figure 6-1: Cross-sectional SEM micrograph of a fresh fracture in sp-Si taken at the outer edge of the porous region with 130 X magnification.

Figure 6-2 shows a region of the same sample at 750 X magnification. Here the openings of the wormholes can be clearly seen as well as the porous material that has accumulated around them. This micrograph is also a cross-section, but in this particular region, the surface is slanted toward the viewer. It contains features similar to both the plan view of Figure 3-3a and the cross-section of Figure 3-3c. At this magnification the structure of the monitor-sparked samples is very similar to that of the Tesla coil-sparked samples. Cracking and porosity on a number of scales can be seen in Figure 6-2. In the lower portion, large sections with dimensions of tens of micrometers can be seen. On the surface surrounding the holes, there are highly fractured dendritic-like growths of redeposited material. The texture ranges from "cauliflower-like" over the majority of the figure, to "cactus-like" on the extreme left side, to "crystal-like" on the extreme right. In the cauliflower region, a preponderance of three-fold interfaces and 120° angles can be seen on several scales.

Figure 6-3 shows one of the smallest features in the cauliflower region of the previous figure at 20,000 X magnification. At this scale, the features appear to consist of balls made up of sections meeting at three-fold interfaces. Within these sections, smaller subdivisions can be seen. Again, 120° angles dominate the image on more than one scale. This hexagonal arrangement is strong evidence that surface tension plays a significant part in the formation of the porous material. Silicon vaporized by the spark and ejected by the shock wave may react with oxygen and nitrogen and condense into liquid droplets that quickly quench to solid form and fall to the surface only to be buried by the next layer of built-up porous material.

Figure 6-4 shows the top section of the ball located at the center of the previous figure. The magnification is 60,000 X. At this point charging effects in the SEM became severe and it was not possible to increase the magnification further.

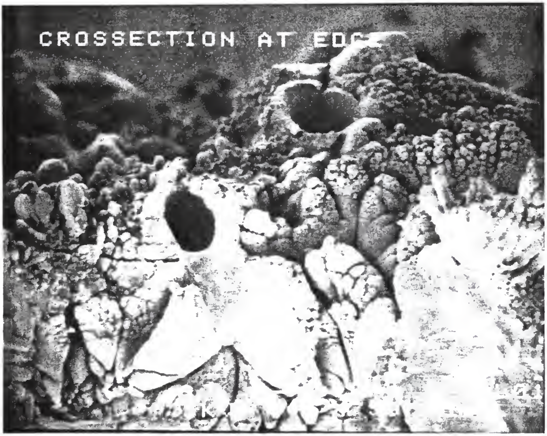

Figure 6-2: Cross-sectional SEM micrograph of a fresh fracture in sp-Si taken at the outer edge of the porous region with 750 X magnification.

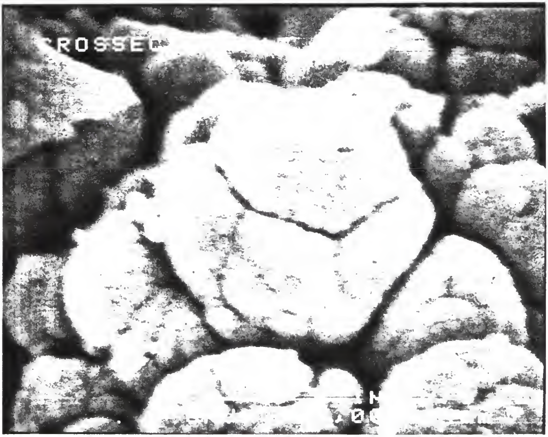

Figure 6-3: Cross-sectional SEM micrograph of a fresh fracture in sp-Si taken at the outer edge of the porous region with 20,000 X magnification.

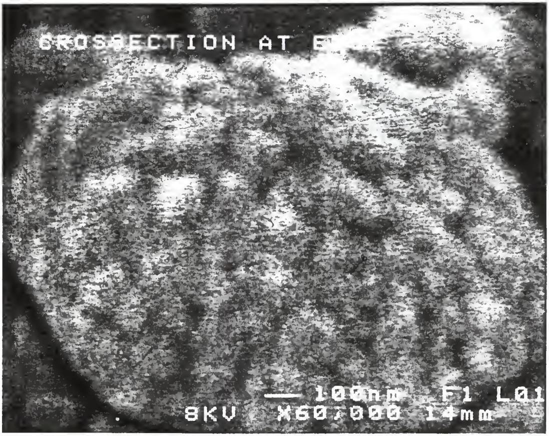

Figure 6-4: Cross-sectional SEM micrograph of a fresh fracture in sp-Si taken at the outer edge of the porous region with 60,000 X magnification.

However, if one looks carefully, subclusters as small as 50 nm can be seen mixed in among larger subclusters of 100 nm to 300 nm diameter. It is reasonable to assume that this trend continues into the nanometer scale.

Spark-processed silicon appears to have a fractal or fractal-like structure. No determination of a fractal dimension has been made, but size invariance is clearly seen in the figures. This is no doubt a characteristic of the growth mechanism of sp-Si.

Fourier Transform Infrared Spectroscopy (FTIR)

Three Stage II sp-Si samples were prepared: one sparked in humid air at atmospheric pressure, one sparked in UHP nitrogen (1,000 mbar) and one sparked in UHP oxygen (1,000 mbar). The chamber was pumped for a day and baked for about 3 hours for the pure oxygen sample. To prepare for the pure nitrogen sample, the chamber was pumped out for four days and there were several three-hour bake cycles. The pure nitrogen sample was done last and was the first measured in the FTIR spectrometer. The air and oxygen samples were stored under vacuum in a glass desiccator. The nitrogen sample was added to the desiccator immediately before the samples were transported to the FTIR spectrometer. The spark conditions were typical of Stage II (15 min, 7.5 kV, 50%/50% on the current gain controls, 10.0 kHz frequency, 1.0 μs pulse width, 0.50 mm spark gap, and 0.25 mm tip diameter). These condition were later known in Stage III to create an average current of about 35 mA and give a predominantly green sample in air or mixtures of nitrogen and oxygen approximating air.

The porous region of the pure nitrogen sample was certainly mostly silicon and silica. These experiments were preformed before the sublimation pump was installed on the chamber. As mentioned in Chapter 5, the author has noticed significant differences in the appearance of the spark between one-day and four-day pump downs when attempting to exclude oxygen. In addition, when sparking in UHP N_2, the spark changes appearance after a few minutes and it is likely that oxygen from adsorbed water and from the native oxide on the sample and stainless steel sample stage provides many of the ions present in the spark plasma. In addition, the rough porous surface of the nitrogen-sparked sample is certainly oxidized the moment the chamber door is opened.

Both transmission and diffuse reflection FTIR measurements were made. The transmission signal was very weak through the 625 μm thick chips with approximately 10^{15} cm^{-3} doping. The spectra of all three samples looked the same and appeared to represent organic contamination of the spectrometer. However, the diffuse reflection measurements were meaningful.

Figure 6-5 shows the FTIR signals of the three samples from 400 cm^{-1} to 4000 cm^{-1}. Transmission FTIR spectra from approximately 3000 to 4000 cm^{-1} and reflection spectra from 400 cm^{-1} to 100 cm^{-1} were previously reported [Hum95a]. The figure shows the same O-H Stretching modes reported by Hummel (Figure 3-7) as well as an H_2O-related signal, probably due to adsorbed water, in the range of 1400 - 1800 cm^{-1}. There was also a small signal attributed to adsorbed CO_2 near 2300 cm^{-1} for both the oxygen and nitrogen processed samples. The N_2-related signal reported by Hummel is also present for the oxygen and nitrogen samples but is strangely absent for the air-sparked sample. As would be expected, it is the strongest for the nitrogen-sparked sample.

Figure 6-6 shows the signals from 400 cm^{-1} to 1400 cm^{-1} in greater detail. In this range, the Si-O-Si stretching modes, two Si-O-Si bending modes, the O-Si-O

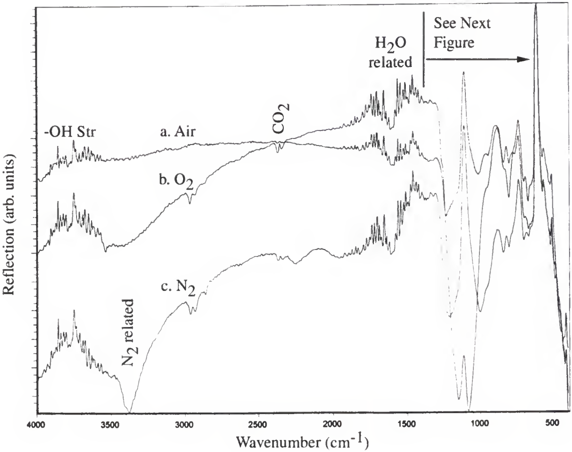

Figure 6-5: Diffuse reflection FTIR signals of silicon samples sparked in air (a.), UHP O_2 (b.), and UHP N_2 (c.), see text.

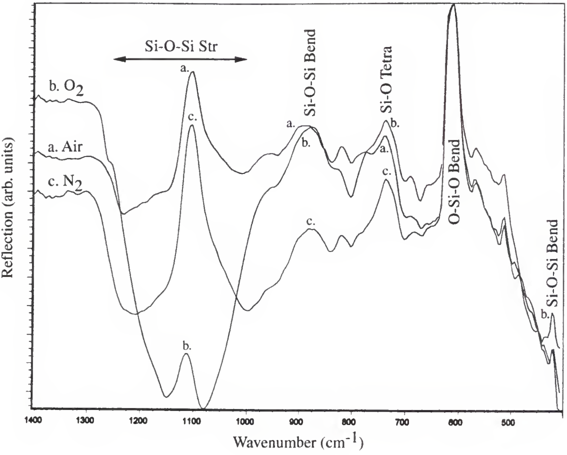

Figure 6-6: Diffuse reflection FTIR signals of silicon samples sparked in air (a.), UHP O_2 (b.), and UHP N_2 (c.). Detailed view of data from 400 cm^{-1} to 1400 cm^{-1}, see text.

bending mode, and the Si-O tetrahedral mode were the same as those reported by Hummel. The Si-O-Si stretching modes and both Si-O-Si bending modes were the strongest for the oxygen sample. The Si-O tetrahedral mode was roughly equal in intensity for the oxygen and air samples. The nitrogen sample has the weakest Si-O-Si bending mode near 870 cm^{-1} and the weakest Si-O tetrahedral mode. The only surprise here is the O-Si-O bending mode, which was very strong for all three samples. The Si-O-Si bending mode near 870 cm^{-1} as well as the Si-O tetrahedral mode and O-Si-O bending mode are much stronger than those seen by Hummel. This may be due to the higher sparking currents used in Stage II/III producing a greater amount of porous material and a greater degree of oxidation. Only the Si-O-Si bending mode near 450 cm^{-1} was more prominent in the previous work. These measurements were performed on different equipment and this may account for some of the differences.

No significant new peaks were observed that are not present in the literature. These results essentially confirm the previous results of Hummel et al. [Hum95a]. In particular, the various hydrogen-related modes commonly seen in porous silicon, but absent in the previous measurements of sp-Si, do not appear in these samples. The strongest N_2-related signal comes from the nitrogen-sparked sample and most of the strongest silica-related peaks belonged to the oxygen-sparked sample. These are both expected results. The strange lack of a strong N_2-related signal in the air-sparked sample is unexpected considering that air is mostly nitrogen. The author offers no explanation for this single inconsistency.

Secondary-Ion Mass Spectroscopy (SIMS)

Secondary-ion mass spectroscopy is a very useful technique with significant limitations. It is best suited to the investigation of depth profiles of minority constituents at dopent-level concentrations within a relatively uniform majority constituent. It is not well suited to the examination of constituents which are a significant portion of the whole or when the matrix changes properties with depth.

Normally, the SIMS signal for a minority constituent is calibrated at the surface of a sample using another type of direct measurement of concentration. The sputter and ionization yields are strongly dependent on the matrix material but, as the impurities are such a small part of the whole, they may change dramatically without changing the properties of the bulk.

SIMS is not particularly well suited to the study of sp-Si, which is porous, has several constituents in significant proportions, and may have large density variations with depth. It is not possible to assign an absolute concentration to a SIMS signal and it is not possible to establish a uniform etch rate. Nevertheless, as the majority of promising chemical spectroscopies available to the author had already been performed on sp-Si by his colleagues, there were few viable choices remaining for further investigation. Some meaningful trends can be seen from the data, but the reader should keep these substantial limitations in mind.

Four Stage II sp-Si samples were produced for SIMS measurements. These included two samples produced in pure N_2 and two in pure O_2. These were prepared and handled in the same manner as the FTIR samples of the previous section. In addition, two Stage I monitor-sparked samples were prepared by Jeliazko Polihronov (a member of the author's research group), one with flowing air and one with stagnant air (see Chapter 3). The SIMS measurements were performed by Margarida Lambers at the University of Florida's Microfabritec facility. The sputter source was a 205.00 to 210.00 nA 5.00 keV Cs^+ ion beam. The system is known to exhibit a significant oxygen background signal.

The raw counts as a function of sputter time are shown for these samples in Figures 6-7 through 6-12. The isotopes corresponding to each signal are shown to the right of the figures. Observed signals include O, Si, SiN, SiO, SiC, C, WO, and W. Due to the extreme sensitivity of the instrument to O and Si, the ^{30}Si and ^{18}O isotopes were measured to prevent saturation of the detector. The W signal was present in the pure O_2 samples but not the pure N_2 samples. This is attributed to increased oxidation of the tip in the oxygen atmosphere. The WO signal was present in the stagnant air sample but not the flowing air sample. Again, this is attributed to the increased heat and oxidation in the absence of spray cooling. The SiO signals followed the Si signals and the SiC signals followed the C signals, as would be expected.

The intensities of the O, SiN, and C signals were divided by the intensity of the Si signal for each sample and sputter time and corrected for isotope abundance to obtain atomic ratio profiles. These are plotted as a function of sputter time in Figures 6-13 through 6-18. These ratios are not (and cannot be) corrected for sputter yield, ionization yield, and instrumental sensitivity for different elements. However, several trends can be observed. The two Stage I samples are very similar. The sample produced in flowing air is completely uniform with constant amounts of O, SiN, and C, see Figure 6-13. The sample produced in stagnant air has uniform concentrations of O and C, but the concentration of SiN decreases substantially towards the surface, see Figure 6-14. There seems to be less nitrogen incorporated into the matrix near the

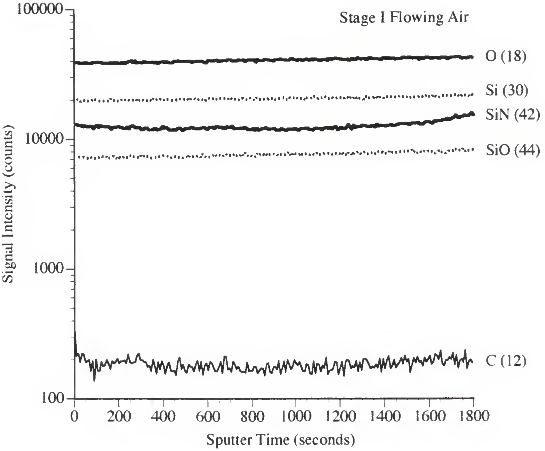

Figure 6-7: SIMS profile of a Stage I sample spark-processed in flowing air. The ion identity and atomic mass corresponding to each signal is shown on the right side of the figure, see text.

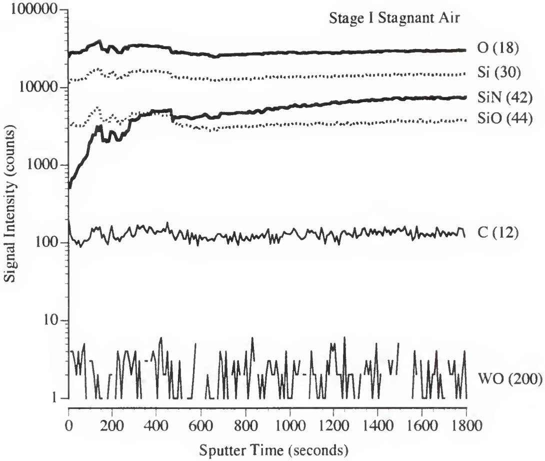

Figure 6-8: SIMS profile of a Stage I sample spark-processed in stagnant air. The ion identity and atomic mass corresponding to each signal is shown on the right side of the figure, see text.

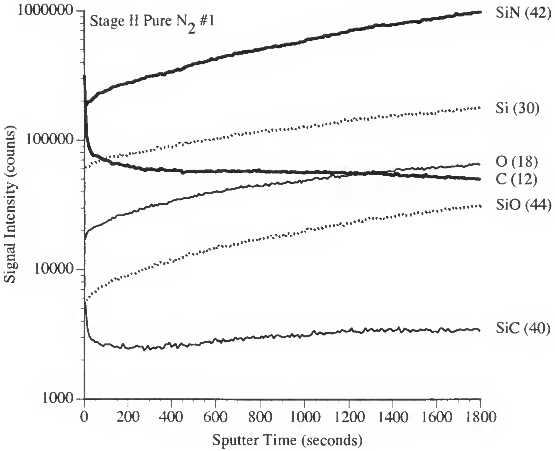

Figure 6-9: SIMS profile of the first Stage II sample spark-processed in pure N_2. The ion identity and atomic mass corresponding to each signal is shown on the right side of the figure, see text. For clarification: the O (18) signal is a thin line and the C (12) signal is a thick line.

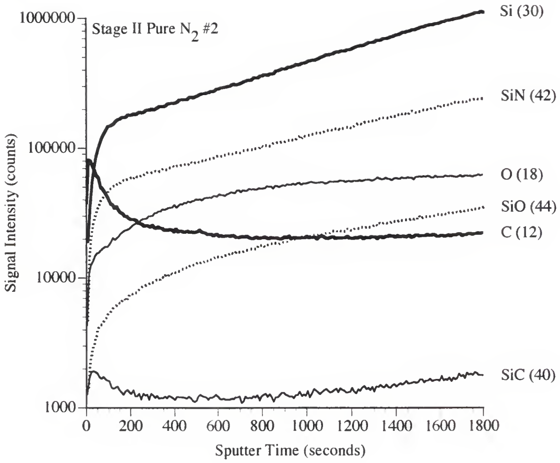

Figure 6-10: SIMS profile of the second Stage II sample spark-processed in pure N_2. The ion identity and atomic mass corresponding to each signal is shown on the right side of the figure, see text. For clarification: the SiO (44) signal is a dotted line and the C (12) signal is a thick line.

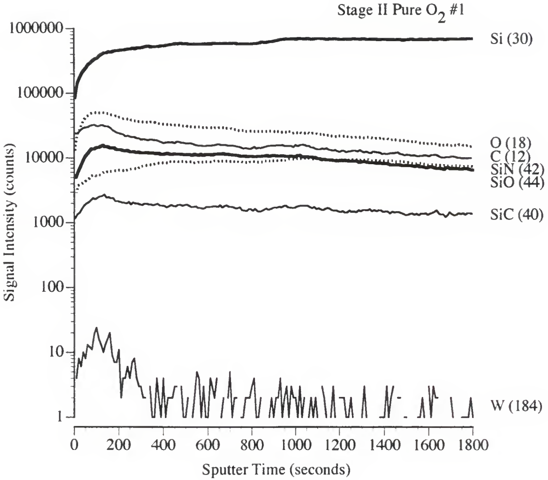

Figure 6-11: SIMS profile of the first Stage II sample spark-processed in pure O_2. The ion identity and atomic mass corresponding to each signal is shown on the right side of the figure, see text. For clarification: the SiN (42) signal is a dotted line and the SiO (44) signal is a thick line.

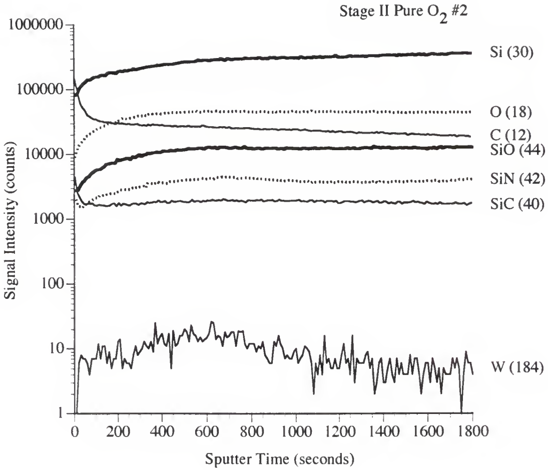

Figure 6-12: SIMS profile of the second Stage II sample spark-processed in pure O_2. The ion identity and atomic mass corresponding to each signal is shown on the right side of the figure, see text.

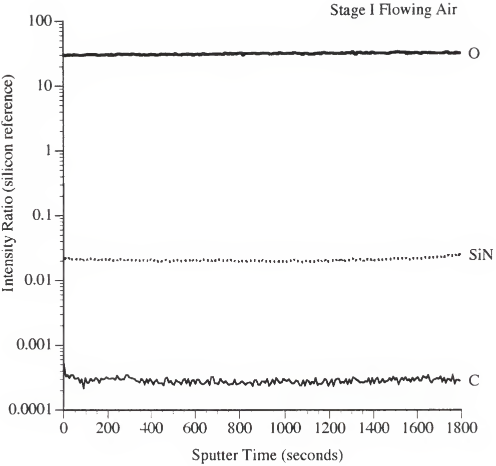

Figure 6-13: SIMS atomic ratio profile of the Stage I sample spark-processed in flowing air. The ion identity is shown on the right side of the figure. All signals are referenced to silicon and corrected for isotope abundance, see text.

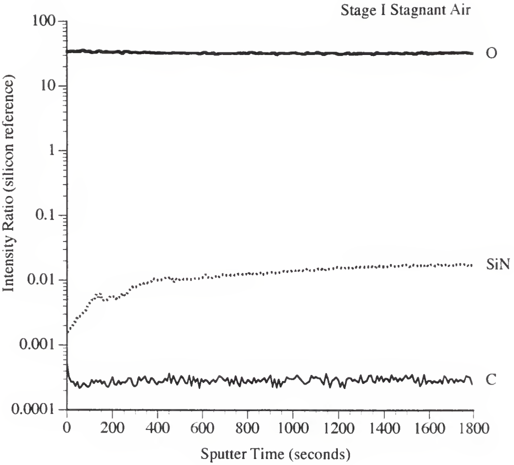

Figure 6-14: SIMS atomic ratio profile of the Stage I sample spark-processed in stagnant air. The ion identity is shown on the right side of the figure. All signals are referenced to silicon and corrected for isotope abundance, see text.

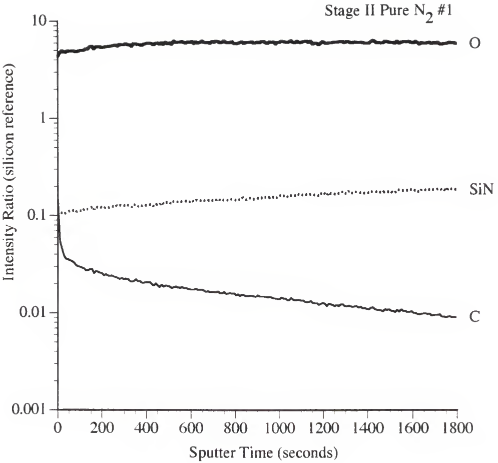

Figure 6-15: SIMS atomic ratio profile of the first Stage II sample spark-processed in pure N_2. The ion identity is shown on the right side of the figure. All signals are referenced to silicon and corrected for isotope abundance, see text.

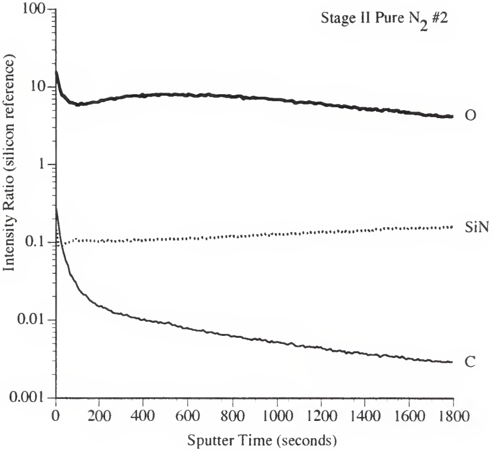

Figure 6-16: SIMS atomic ratio profile of the second Stage II sample spark-processed in pure N_2. The ion identity is shown on the right side of the figure. All signals are referenced to silicon and corrected for isotope abundance, see text.

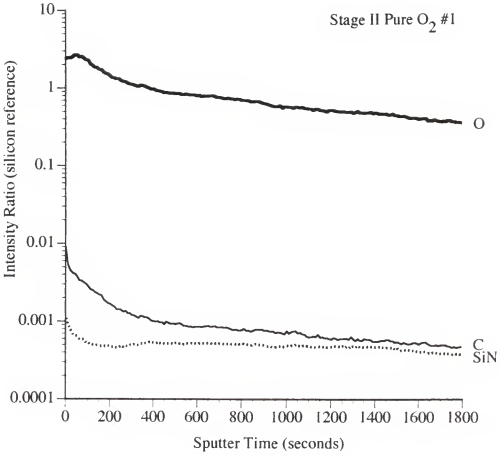

Figure 6-17: SIMS atomic ratio profile of the first Stage II sample spark-processed in pure O_2. The ion identity is shown on the right side of the figure. All signals are referenced to silicon and corrected for isotope abundance, see text.

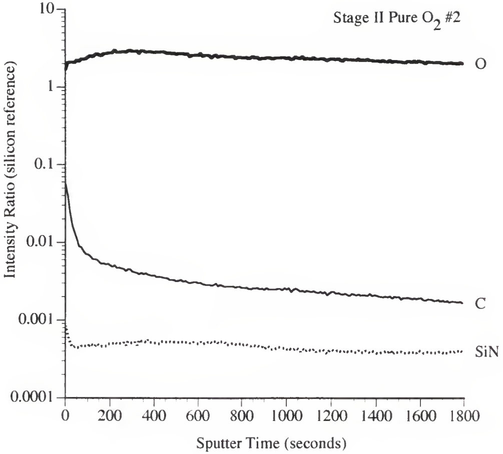

Figure 6-18: SIMS atomic ratio profile of the second Stage II sample spark-processed in pure O_2. The ion identity is shown on the right side of the figure. All signals are referenced to silicon and corrected for isotope abundance, see text.

surface. This is consistent with the increasing incorporation of nitrogen with depth observed in XPS measurements of a similar sample (Figure 3-6).

The two samples processed in nitrogen (Figures 6-15 and 6-16) are quite similar to one another. The nitrogen concentration (from SiN) is uniform, and the oxygen concentration also appears to be fairly uniform. These samples contain significant amounts of oxygen. The small change in the oxygen concentration of the second sample near the surface may indicate additional oxidation after the sample was removed from the chamber. The carbon concentration increases substantially toward the surface. The two samples produced in oxygen (Figures 6-17 and 6-18) are also similar to one another. The oxygen concentrations are fairly uniform, the nitrogen concentration are also fairly uniform and much lower than in the nitrogen-sparked samples. There may also be a small amount of adsorbed nitrogen near the surface indicated in these two figures. The carbon concentrations are similar to those of the nitrogen-sparked samples and also show a significant increase in the amount of carbon near the surface.

The most significant result of the SIMS measurements is the identification of the source of carbon contamination. In the samples sparked in air, the carbon is distributed evenly throughout the porous region. In the samples processed in UHP gases in the chamber, the carbon was concentrated near the surface. The carbon in sp-Si is clearly coming from the air. In the air sparked samples, the carbon contamination occurs continuously while the porous layer is created. In the samples produced in pure atmospheres, the carbon is coming from contact with air after the chamber is opened and the samples are exposed.

CHAPTER 7
RESULTS: OTHER SPARK-PROCESSED ELEMENTS

Preliminary Exploration

Early in Stage I it was decided that spark-processing should be attempted on materials other than silicon to see if photoluminescence after spark-processing is unique to silicon, unique to semiconductors, or a general property of elements. Accordingly, all the elemental semiconductors and semi-metals were spark-processed, as were a number of metals. Most of the materials were available on hand and many had hand-written labels claiming them to be 99.99% to 99.9999% pure. As this was a preliminary review with the intention of following up on promising materials, this was sufficient. There were later some indications that the aluminum used was not pure.

All samples were cleaned according to the standard protocol and etched if there appeared to be a significant native oxide. Many of them needed to be polished before cleaning to obtain a flat surface. Most of the samples were mounted to a holder with silver paint, which was allowed to dry for 24 hours before processing. The time of spark processing was subjective and varied from sample to sample depending on the rate at which an oxide was formed. Some materials had adherent oxides while others did not. Some materials experienced substantial melting or were eroded rapidly by the spark. Because many of these elements were highly toxic or had toxic oxides, all spark processing was performed in a fume hood.

After processing, the PL spectra of the samples were measured as were the native oxides of the same elements for the purpose of comparison.

Semiconductors

The elemental semiconductors are (in alphabetical order): boron (B) with a room temperature band gap of 1.55 eV, carbon (C) with a gap of 5.7 eV (as diamond), germanium (Ge) with a gap of 0.67 eV, selenium (Se) with a gap of 1.5 eV, silicon (Si) with a gap of 1.107 eV, tin (Sn) with a gap of 0.08 eV (as gray tin, which is stable below 286.4 K), and tellurium (Te) with a gap of 0.33 eV. Silicon has been previously discussed in great detail. Spark processing of a carbon (graphite) cathode (using spectroscopic grade electrodes) was performed with both a tungsten anode and a carbon anode. In the former case, a yellow powder was formed, primarily on the anode. This is believed to be tungsten carbide and is not of interest. In the latter case, the cathode electrode was consumed and the anode electrode was not, as was expected. It would not be an exaggeration to state that carbon has the least adherent oxide of any spark-processed material! Selenium has poor conductivity, a low melting point, and is highly flammable in air. Spark-processing of selenium proved to be dramatically unsuccessful. The remaining elements could all be spark-processed with no difficulty except for boron, which has such a low conductivity that it had to be heated on a hot plate to increase its intrinsic carrier concentration enough to allow spark-processing. Due to its fairly small band gap, this worked well.

The following paragraphs describe the PL of these various spark-processed elements in alphabetical order.

Spark-processed boron

Figure 7-1 shows the PL spectrum of sp-B under 325 nm excitation. Sp-B has a PL peak near 560 nm that is clearly not present in the native oxide (also shown in the figure). This luminescence is definitely due to the spark-processing.

Spark-processed germanium

The PL spectrum of sp-Ge is shown in Figure 7-2. A blue peak is seen near 410 nm. This peak is quite strong, comparable to that of sp-Si. A tail is present in the green. A green peak is not seen for this sample due to the specific processing conditions. However, a green peak was reported in the literature and will be discussed later in this chapter. The PL spectrum of the native oxide is also shown greatly magnified. The structure near 450 nm does not correspond to the peak seen in the spark-processed sample. Clearly spark-processing is responsible for the luminescence.

Spark-processed tin

The PL spectra of three sp-Sn samples are shown in Figure 7-3. The processing conditions were similar. Tin tended to melt forming a crater and the porous material did not adhere well to the substrate. Occasionally a small island of material managed to stick (often at the edge of the crater). The PL intensity was primarily influenced by the amount of material that happened to stick on a given sample. As can be seen from the figure, the peak wavelength varied from about 560 nm to 620 nm. This is a substantial variation.

Figure 7-4 shows the PL spectra of the native oxide of unsparked tin and that of sp-Sn in the center of the crater where the oxide was thin. Both have been

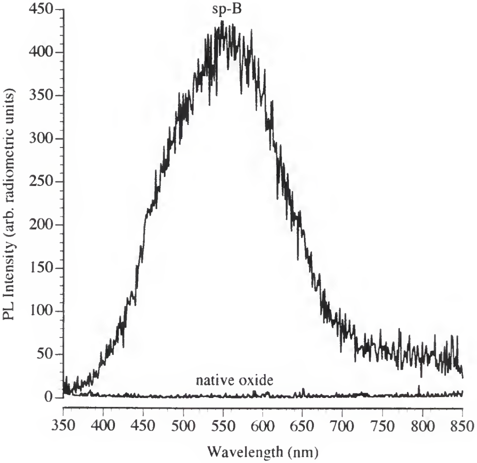

Figure 7-1: PL spectra of spark-processed boron and the native oxide of boron. $\lambda_{excitation} = 325$ nm.

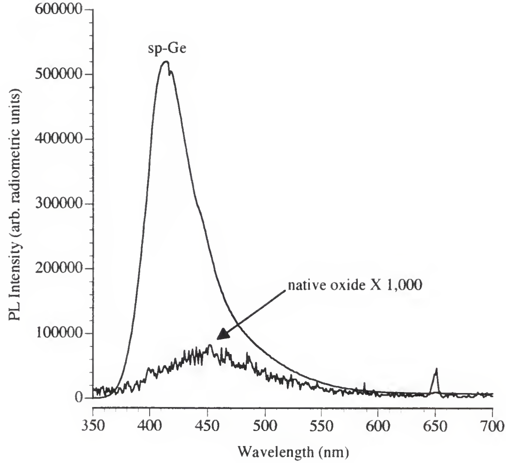

Figure 7-2: PL spectra of spark-processed germanium and the native oxide of germanium (multiplied by 1,000). $\lambda_{excitation} = 325$ nm.

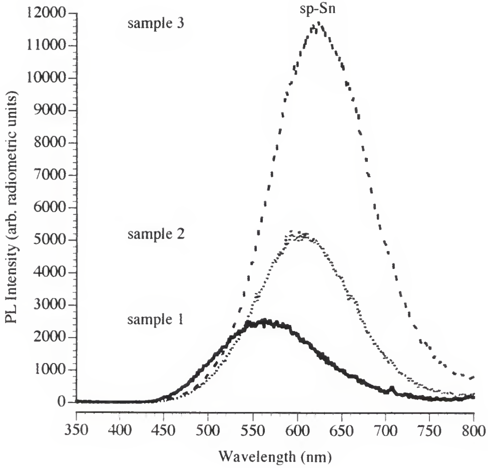

Figure 7-3: Three PL spectra of spark-processed tin, see text. $\lambda_{excitation} = 325$ nm.

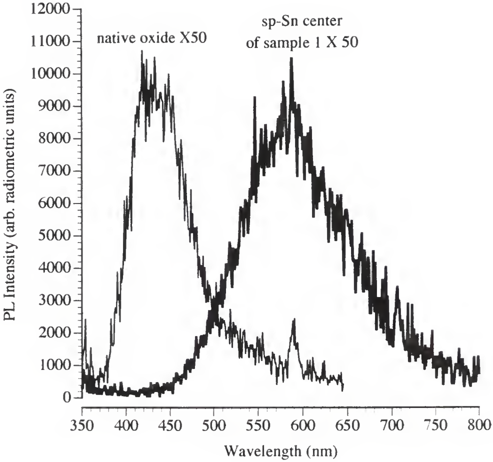

Figure 7-4: PL spectra of the native oxide of tin and the center of spark-processed tin sample 1, see text. This graph shares the same intensity axis with the previous figure. $\lambda_{excitation}$ = 325 nm.

multiplied by 50 and plotted on the same intensity axis as the previous figure. The PL of the native oxide occurs at a much shorter wavelength than that of the spark-processed samples. The sp-Sn sample spectra have no features at this wavelength indicating that the PL is created by the spark-processing. The large difference in intensity between the sp-Sn spectra in the two figures demonstrates that the luminescence observed is dependent on the quantity of material available to measure.

Sp-Sn differs significantly from sp-Si in that the peak wavelength is variable, not fixed. These two types of luminescence are not likely to be caused by a similar phenomenon.

Spark-processed tellurium

The PL spectrum of sp-Te can be seen in Figure 7-5. A broad green peak is observed at approximately 550 nm. Tellurium also tended to melt and the oxide was not adherent. The PL was rather strong despite the limited amount of material to measure. Also in the figure is the PL spectrum of the native oxide of tellurium multiplied by 100. This spectrum is featureless (the peak near 650 nm is a spurious second-order line of the laser caused by the grating). Again, the PL is definitely the result of the spark-processing.

While this was a promising material, tellurium and its oxides are highly toxic, much more so than arsenic. It is about as toxic as possible for a non-radioactive element. The decision was made not to work with it further.

Semi-Metals

The semi-metals are antimony, arsenic, and bismuth. These materials do not have a band gap, but such a small overlap of the valence and conduction bands that

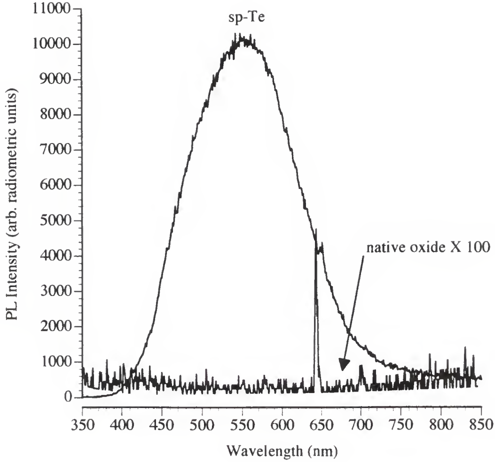

Figure 7-5: PL spectra of spark-processed tellurium and the native oxide of tellurium. $\lambda_{\text{excitation}} = 325$ nm.

they are often referred to as having a negative "gap". It is likely that such materials would be influenced by quantum confinement in a manner similar to semiconductors. These semi-metals will be discussed in alphabetical order.

Spark-processed antimony

The PL spectrum of sp-Sb is shown in Figure 7-6 (thick line). It has a peak intensity near 470 nm. Also included in the figure is the featureless spectrum of the native oxide (thin line) multiplied by 1,000 and the spectrum of the edge of the spark processed region (dotted line), which peaks at a different wavelength (approximately 570 nm). The main PL band also appears to have a shoulder in this region. As there is no PL in the native oxide, this luminescence is clearly the result of the spark-processing. Its intensity is significant but nowhere near as intense as that of sp-Si and sp-Ge.

Spark-processed arsenic

Several sp-As samples were prepared. Figure 7-7 shows the PL spectra of one such sample (thick line). It was noticed that when a sample was allowed to sit in air for two weeks, the PL peak wavelength was substantially blue-shifted and the peak intensity was dramatically increased. The author measured the same sample 14 days later under identical conditions and this is also shown in the figure (dotted line). This spectrum is over 100 times as intense and appears to be a superposition of two peaks. The spectrum of the native oxide of arsenic is also shown (thin line). The sp-As sample was also measured 28 days later but the PL equipment had been used for other measurements in the meantime and the intensities were not able to be compared directly. Figure 7-8 shows the self-normalized spectra of this first sample at 0 days (thick line), 14 days (dotted line), and 28 days (dashed line). Each one peaks at a

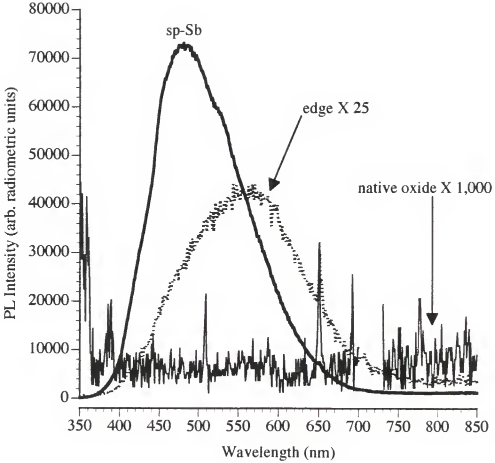

Figure 7-6: PL spectra of spark-processed antimony (thick line), the native oxide of antimony (thin line) multiplied by 1,000, and the edge of the spark-processed region (dotted line) multiplied by 25. $\lambda_{excitation}$ = 325 nm.

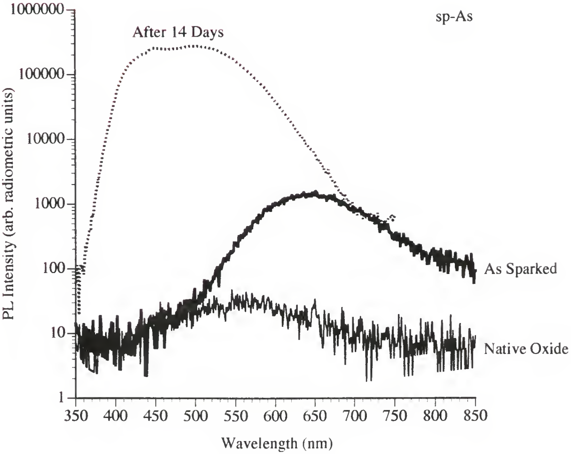

Figure 7-7: PL spectra of freshly a prepared spark-processed arsenic sample (thick line), the native oxide of arsenic (thin line), and the spark-processed sample after 14 days (dotted line), see text. $\lambda_{excitation} = 325$ nm.

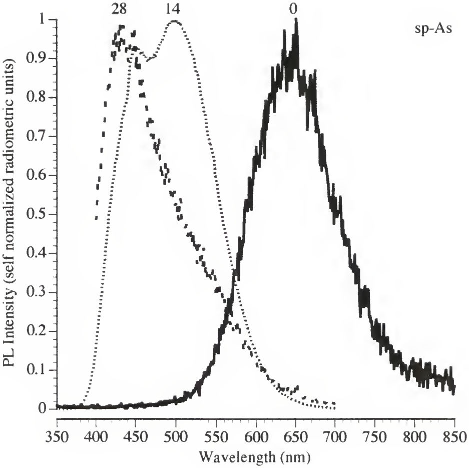

Figure 7-8: Self-normalized PL spectra of a freshly prepared sp-As sample (solid line), the same sample after 14 days (dotted line), and after 28 days (dashed line), see text. $\lambda_{excitation} = 325$ nm.

progressively shorter wavelength. The 28-day sample appears to consist of only the shorter-wavelength component of the two peaks comprising the spectrum of the 14 day sample. Is this shift continuous or are there three or more distinct states through which the luminescent species evolves? Another sp-As sample was produced to answer just this question.

Figure 7-9 shows the PL of a second sp-As sample that was left on the sample stage and measured periodically over a 10-day period with no adjustments to the PL system. Shown in this figure are the native oxide (thin line), sp-As as sparked (thick line), sp-As after 7 days (dotted line), after 8 days (dashed line), and after 10 days (alternating long and short dashes). It should be noted that the native oxide spectrum measured this time was essentially featureless. The 7, 8, and 10-day spectra become progressively more intense and peak at progressively shorter wavelengths. The last three spectra appear to converge with one another between 650 nm and 700 nm. These spectra all appear to have a red tail, which is an artifact of the grating. The grating used for this measurement has a 630 nm blaze wavelength and is actually more sensitive to the false second order of 350-400 nm light that occurs at 700-800 nm than it is to real 350-400 nm light. This is further exacerbated by the fact that the GaAs detector is insensitive near its band gap in the red and a large correction factor is used to correct for this. Since there is no way to differentiate between actual red light and blue light that is passed to the detector due to harmonic effects of the grating, this factor is erroneously applied to this blue light for which the detector is already highly sensitive. This does not occur with the as-sparked sample because it has no significant intensity in the blue. The author's experience in interpreting such spectra indicates that all four curves do in fact converge by 700 nm.

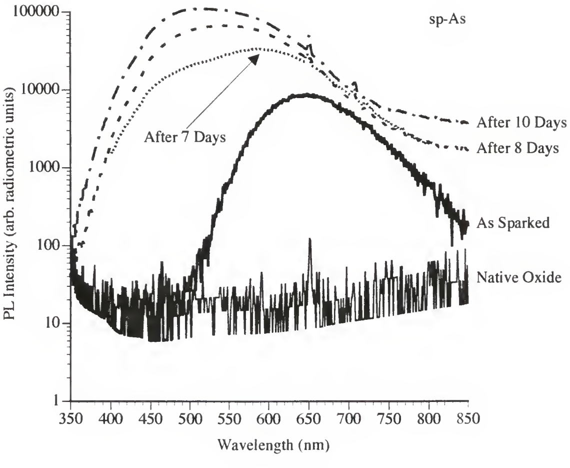

Figure 7-9: PL spectra of a freshly prepared spark-processed arsenic sample (thick line), the native oxide of arsenic (thin line), and the spark-processed sample after 7 (dotted line), 8 (dashed line), and 10 (alternating long and short dashes) days, see text. $\lambda_{excitation} = 325$ nm.

Figure 7-10 shows the same four sp-As spectra, this time self normalized and plotted on a linear intensity scale. The peak wavelength of the sample moves steadily to shorter wavelengths with increasing time. At 7 days, the sample appears to have a shoulder near the peak of the 10-day spectrum. However, this shoulder does not occur at the same wavelength as the shoulder on the 14-day spectrum of Figure 7-8. Also, the 10-day spectrum of Figure 7-10 is still at a somewhat longer wavelength than the 14-day spectrum in Figure 7-8. The 7, 8, 10, 14, and 28-day spectra all occur at unique wavelengths. This proves that the wavelength is changing continuously as the sample ages. The occasional appearance of a shoulder likely indicates that portions of the sample are evolving more rapidly than others.

Many of the arguments against the quantum size effect explanation of sp-Si do not apply to sp-As. In the case of sp-As, the peak locations are not fixed, and the shorter wavelength peaks are much more intense than the longer wavelength ones. This change in intensity is large and highly nonlinear as would be expected in a quantum dot where the oscillator strength increases with decreasing particle size. Furthermore, the remarkable convergence of the spectra seem to fit quantum theory as well because the population of quantum dots luminescing at a given wavelength would have the same oscillator strength.

These remarkable phenomena of sp-As were not initially clear as the continuous wavelength shift was obscured by anomalous sensitivity peaks in the grating near 410 and 450 nm. Such artifacts are common and are known as "ghosts". It was not until the Stage III calibrations were applied to the data after the experimental phase of this study was complete that this behavior was clear. The intensity of aged sp-As is very high, almost as high as that of Si and Ge. Spark-processed arsenic demands further study.

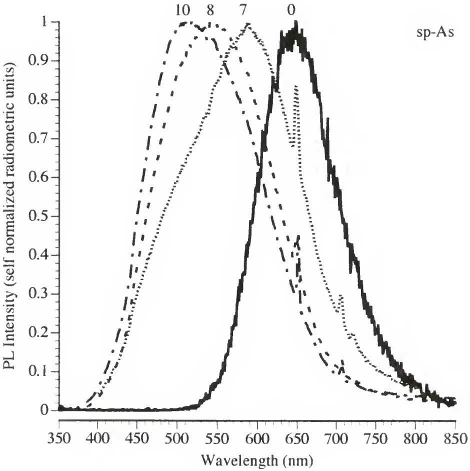

Figure 7-10: Self-normalized PL spectra of a freshly prepared spark-processed arsenic sample (solid line) and the spark-processed sample after 7 (dotted line), 8 (dashed line), and 10 (alternating long and short dashes) days, see text. $\lambda_{excitation} = 325$ nm.

Spark-processed bismuth

The PL spectrum of sp-Bi is shown in Figure 7-11 (thick line). Also shown is the spectrum of the native oxide multiplied by 1,000 (thin line). The PL of sp-Bi exhibits a two-peak structure with the main peak near 580 nm and a satellite peak near 490 nm. It is fairly intense, comparable to sp-Sb and stronger than sp-Sn or sp-Te. As the spectrum of the native oxide is featureless, the PL of sp-Bi clearly is the result of the spark processing.

Metals

For a time it seemed that PL as a result of spark-processing was characteristic of semiconductors and semi-metals (elements with a positive or very small negative band gap). This made a general quantum size effect explanation seem plausible. In addition, many of the initial spark-processed metals did not give significant luminescence. These included chromium (no PL), copper (no PL), iron (no PL), magnesium (no initial PL, laser exposure created PL and a color change in the oxide), and manganese (very weak PL near 475 nm in both sparked and native oxide). However, metals that gave significant PL upon spark processing were found. These include aluminum, nickel, tantalum, and zinc. These will be discussed in alphabetical order.

Spark-processed aluminum

The PL spectrum of sp-Al is shown in Figure 7-12 (thick line). It appears to have a two-peak structure with a broad peak near 590 nm and a complicated peak structure near 450 nm. The lower wavelength peak appears to occur at a similar

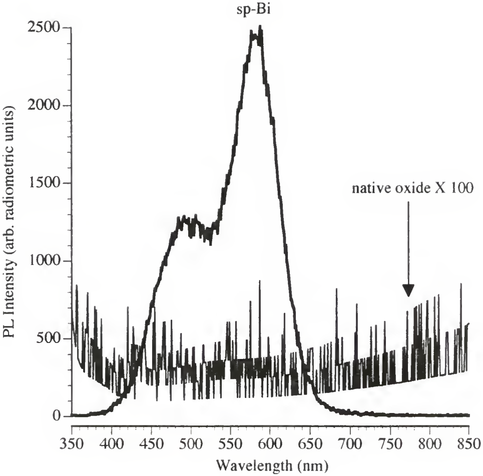

Figure 7-11: PL spectra of spark-processed bismuth (thick line) and the native oxide of bismuth (thin line) multiplied by 100. $\lambda_{excitation} = 325$ nm.

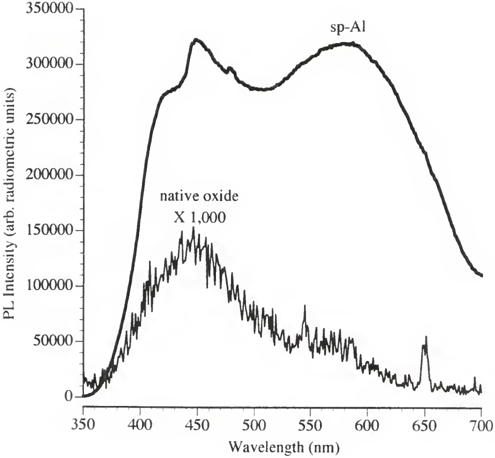

Figure 7-12: PL spectra of spark-processed aluminum (thick line) and the native oxide of aluminum (thin line) multiplied by 1,000. $\lambda_{excitation} = 325$ nm.

wavelength as the PL from the native oxide, shown multiplied by 1,000 in the figure (thin line). The longer wavelength peak appears to be unique to the spark-processed sample. Sp-Al was also produced under Stage II and III conditions and only the longer wavelength peak is seen (to be presented in the next two sections of this chapter). No structure is seen near 450 nm. The author suspects contamination. As previously mentioned, most of the materials used in this first survey of elements, particularly the metals, were available on hand and were not purchased by the author. Contamination is a real possibility. The intensity of sp-Al is quite large, almost as intense as sp-Si and sp-Ge.

Spark-processed nickel

The PL spectrum of sp-Ni is shown in Figure 7-13 (thick line), along with the spectrum of the native oxide (thin line). Substantial PL was visible in the sample, but, by the time the sample was aligned and this measurement was taken, the luminescence was apparently lost. The decision was made to look at nickel again in later experiments based on the initial observation of PL with the eye. The oxide material produced by spark-processing was not adherent to the substrate and likely flaked off during handling.

Spark-processed tantalum

The PL spectrum of sp-Ta is shown in Figure 7-14 (thick line). The spectrum of the native oxide multiplied by 250 is also shown (thin line). Sp-Ta appears to have a peak intensity near 630 nm. There is no such feature in the native oxide. The luminescence is unique to the spark-processed sample.

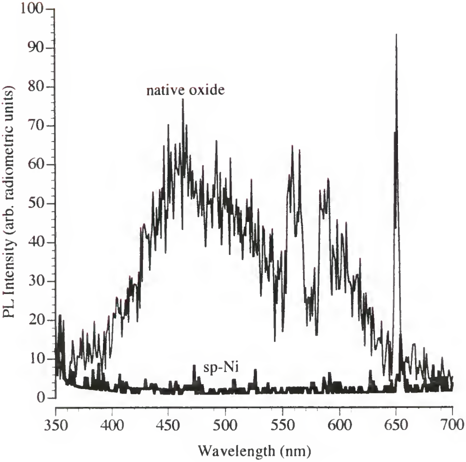

Figure 7-13: PL spectra of spark-processed nickel (thick line) and the native oxide of nickel (thin line). $\lambda_{excitation} = 325$ nm.

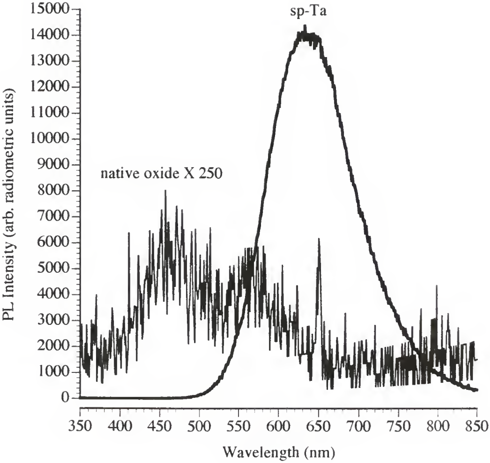

Figure 7-14: PL spectra of spark-processed tantalum (thick line) and the native oxide of tantalum (thin line) multiplied by 250. $\lambda_{\text{excitation}} = 325$ nm.

Spark-processed zinc

The PL spectrum of sp-Zn is shown in Figure 7-15 (solid line). The spectrum of the native oxide is also shown (dotted line). These spectra are easy to explain. Zinc oxide is a direct gap semiconductor with an band gap of about 3.3 eV. The sharp peak seen in this figure is the direct gap luminescence of ZnO. ZnO has a high concentration of non-stoichiometric defects and is known to have a large variety of optically active mid-gap states associated with various substitutional, vacancy, and interstitial defects [Van96, Pro95, Xu_96, Byl78, Ort97, Liu92]. The features seen from 550 to 750 nm are consistent with these, as is the peak of the native oxide centered near 580 nm.

The author was able to observe spectra similar to that of sp-Zn using thermal oxides grown on polished zinc surfaces. These later samples were much more intense than spark-processed samples. Chang has apparently discovered conditions for spark-processing which are very efficient at producing highly luminescent ZnO, but has come to the same conclusions with regard to the origin of the luminescence [Cha00b]. This reference discusses the nature of these various known defects in more detail than would be appropriate here. Sp-Zn is a material with a mundane explanation for its luminescence and is not of further interest for this study.

Additional Work with Selected Elements

It was noticed that the materials that gave substantial PL in the previous survey generally had a chemically stable oxide with a high heat of formation. Such strongly bonded oxides have an ionic character and were referred to as "lone-pair" oxides in Chapter 3. These oxides have a band gap wide enough to host states with

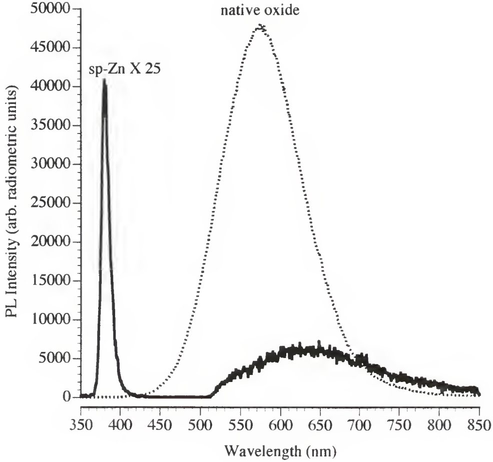

Figure 7-15: PL spectra of spark-processed zinc (thick line) multiplied by 25 and the native oxide of zinc (thin line). $\lambda_{excitation} = 325$ nm.

visible optical transitions. A list of all elements that have a high oxide heat of formation was made and these were individually evaluated as potential candidates for further investigation. Properties considered included toxicity, radioactivity, vapor pressure of the element or its oxides (so as not to contaminate the vacuum system), available purity, availability in the form of sheet or plate, and price. Two semiconductors (silicon and germanium) and several metals were chosen for further study. These metals were aluminum, nickel, and tantalum, as well as titanium, a metal not previously investigated.

The standard 10^{15} B-doped p-type Si wafers used elsewhere in this study were also used for this experiment. The germanium used was cut from a single crystal believed to be highly pure. The aluminum and nickel were both purported to be 99.999% pure, and the tantalum was labeled as 99.95% pureity. The titanium was highly pure "MARZ grade" wire, which was pounded flat with a hammer and polished, before cleaning and etching.

Due to the observation that the color of the PL of sp-Si is dependant on substrate temperature and that this could be influenced by the size of the heat sink under the sample during processing, all the samples spark-processed in this experiment were mounted to small pieces of copper-clad plastic printed circuit board material using conductive silver paint. The paint was allowed to dry for 24 hours under vacuum to remove any volatile compounds. The samples were secured to the stage by a small screws that electrically grounded the copper surface of the mounts, while the samples were thermally insulated from the stage. This allowed them to become very hot during processing.

The processing was performed in air with an open chamber using Stage II equipment. The power supply voltage was 7.5 kV, the pulse width was 1.0 μs, and the repetition rate was 10.0 kHz. The current gain controls were both set to the 50% position. These conditions were later shown in Stage III to produce an average current of approximately 35 mA. The spark time varied from sample to sample on a subjective basis such that the apparent amount of built up porous material was as equal as possible.

Semiconductors

The sp-Si sample had the typical appearance. Its self-normalized PL spectrum is shown in Figure 7-16 (solid line). The spectrum exhibits the standard green peak and a hint of the UV/blue band, as is typical for samples produced with a large current.

The sp-Ge sample appeared rough and anisotropic. A large central region of about 3 mm was surrounded by a thick region of gray/white powder. The spectra of two separate regions of the central area are shown in the same figure. These are labeled Ge (a), which is depicted by a dotted line and Ge (b), which is depicted by a dashed line. Both are self-normalized. The Ge (a) spectrum appears to have the 410 peak discussed in Chapter 3. The Ge (b) spectrum appears to peak near 470 nm and is consistent with the superposition of near-equal quantities of the 410 nm and 500 nm bands. The 500 nm peak was also discussed in Chapter 3.

Metals

The self-normalized PL spectra of the metals are shown in Figure 7-17. From left to right the spectra are sp-Ni with a maximum peak intensity near 510 nm (solid line), sp-Al with a peak near 580 nm (dotted line), sp-Ta with a peak near 650 nm

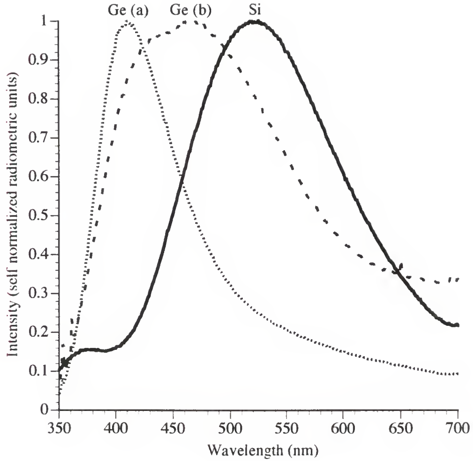

Figure 7-16: Self-normalized PL spectra of spark-processed silicon (solid line) and two regions of a spark-processed germanium sample (dotted and dashed lines), see text. $\lambda_{excitation} = 325$ nm.

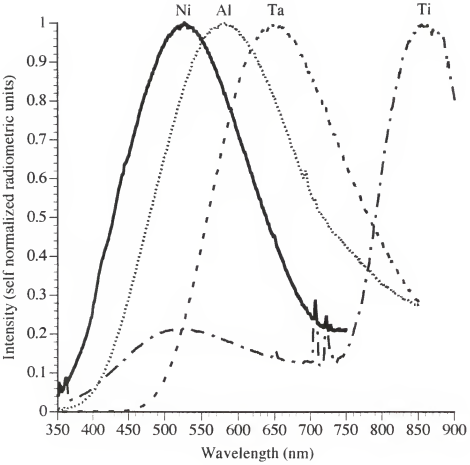

Figure 7-17: Self-normalized PL spectra of spark-processed nickel (solid line), spark-processed aluminum (dotted line), spark-processed tantalum (dashed line), and spark-processed titanium (alternating long and short dashes). $\lambda_{excitation} = 325$ nm.

(dashed line), and finally sp-Ti with a peak near 850 nm (alternating long and short dashes). In addition, sp-Ti has a broad satellite peak near 525 nm.

The appearance of the sp-Ni samples was similar to those of the previous section. The luminescent material consisted of a thin gray-white powder in and around a shallow crater eroded by the spark. Unlike the previous instance, there was no difficulty measuring the PL spectrum.

The sp-Al samples appeared similar to sp-Si samples in that the center of the porous region was raised above the substrate surface and was a light gray color. Furthermore, it was surrounded by a darker ring, as in the case of silicon. However, there was no halo region of powder around this ring. The PL of sp-Al in this section is in virtually the same location as the broad band seen in the previous measurements (Figure 7-12). The other structure seen near 450 nm in that figure is not present. It is also not present in any of the large number of sp-Al samples produced for the third section of this chapter. The conclusion must be drawn that this peak structure near 450 nm was the result of contamination. Possibly, the "pure" aluminum used in that case was actually an aluminum alloy.

The sp-Ta samples appeared to have a small yellowish raised porous region surrounded by a very thin dark ring. A large quantity of white powder was seen outside of this ring to a total diameter of about 5 mm. The PL spectrum of sp-Ta is essentially the same in this and the previous set of measurements. The small 20 nm discrepancy may be explained by the existence of chromatic aberrations in the PL system prior to Stage III. This was particularly a problem in the longer wavelength range of the visible spectrum.

The sp-Ti samples had a raised medium-gray porous region in the center, which was irregularly shaped. In one instance it was surrounded by a thin halo of fine white powder. Surrounding this was a "rainbow" pattern of oxidized Ti with the colors dependant on the thickness of the oxide. This was probably produced by the heat of the spark-processing causing standard surface oxidation of the surrounding metal. The PL spectrum of sp-Ti appeared to be blue to the eye. Upon closer examination, it was revealed that the visible portion was only a small part, and that the majority of the luminescence was in the near-IR. Because a cooled GaAs detector was used, and the correction factor becomes asymptotic after 900 nm, there may be doubts as to the exact location of this peak. However, there appears to be a definite decrease in the luminescence between 850 nm and 900 nm indicating that the real peak is near 850 nm.

Chemical Processing Parameters

After considering the results of Stage I and II work on other elements besides silicon, it appeared that germanium, aluminum, and tantalum were the most promising candidates for further study. Molybdenum was also included on this list because tantalum stock, mislabeled as molybdenum had been used in Stage I and II measurements. This was discovered and the erroneous results were not included in those sections of this Chapter. Had the properties of sp-Mo actually been screened in the previous two sets of experiments, it would not have been included in this section. Nevertheless, detailed Stage III work was performed on sp-Mo and is presented for the sake of completeness. In addition, nickel was included because there was some ambiguity with the previous results, as has been discussed. Nickel was not considered a good candidate. Titanium was a very promising candidate but was excluded because the author lacked access to a good infrared PL spectroscopy system, which would be needed to properly characterize sp-Ti. The author decided to leave the work on sp-Ti for his colleagues who were in the process of building an infrared system at the time this was being written.

Experimental

Germanium, aluminum, tantalum, molybdenum, and nickel were spark-processed under different mixtures of UHP N_2 and UHP O_2 under almost identical conditions to those used for silicon in Chapter 5 (Figures 5-36 through 5-39). The only difference was that an average current of 20.0 mA was used instead of 21.0 mA. Two samples of each element were spark-processed in gases of each of the following nitrogen concentrations: 0% (pure O_2), 10%, 30%, 50%, 70%, 90%, and 95%. In addition, two sp-Ge samples were prepared in 100% N_2.

Results and Discussion

Spark-processed germanium

The samples used in this experiment were diced from an undoped Ge wafer.

With the exception of the two sparked in 100% N_2, the sp-Ge samples all have a large quantity of white powder covering the entire sample. This powder is the same color on all samples and the amount of powder does not begin to diminish until 70% N_2 is reached. Even so, there is a significant amount of powder on the 95% N_2 sample. The porous region itself does not appear as homogeneous as in sp-Si samples, but it is circular with a well-defined darker border. This border is very thin and is constant in thickness but appears darker (almost black) in the 95% N_2 and 100% N_2 samples. The diameter of the central raised area decreases with increasing nitrogen concentration from about 3 mm at 0% N_2 to about 1 mm at 95% N_2. There is no ring around the porous region as in other elements. The 100% N_2 samples have eroded black craters containing a small amount of gray/brown porous material. This is sounded by a loose porous material, which varies from brown to almost white.

A 3-D overview of the PL of sp-Ge as a function of the nitrogen concentration of the ambient is shown in Figure 7-18. Sp-Ge exhibites two peaks near 413 nm (blue) and 510 nm (green), the latter only occurring at or above 95% N_2. At 90% N_2, a green shoulder is observed. The peak locations of the two PL bands of sp-Ge are shown in Figure 7-19. There is no significant variation except that the weak luminescence of the 100% N_2 samples occurs at approximately 520 nm, which may, or may not, be significant given the limited amount of data for the green band.

The undeconvoluted peak PL intensities of the two bands are shown in Figure 7-20. The intensity of the blue peak appears to increase with increasing nitrogen concentration until somewhere around 70% N_2, after which it decreases significantly. This is remarkably similar to the behavior of the UV/blue peak of sp-Si. However, this band has a significant intensity at 0% N_2 (pure O_2). This is in stark contrast to the behavior of both bands in the sp-Si and, as will be shown, the behavior of sp-Al and sp-Ta. Nevertheless, the presence of nitrogen increases the intensity of this peak by 6 or 7 times. The intensity of the green band at 90% N_2 was estimated from the shoulder simply by taking the intensity value at 500 nm. This band has a significant intensity at 90% N_2 and 95% N_2 but is much weaker at 100% N_2.

Figure 7-21 shows the self-normalized PL spectra of a 95% N_2 sample (solid line), a pure N_2 sample (dotted line), and a pure O_2 sample (dashed line). This figure demonstrates that the blue band is at the same location and has the same shape in pure O_2 or in mixtures of O_2 and N_2. This is true of all mixtures, not only the ones shown in the figure. The green band of the 95% N_2 sample occurs in a similar location as

PL of Sp-Ge vs. Nitrogen Concentration

Substrate Material:	Germanium
Atmosphere:	**N_2 and O_2 variable**
Electrode Material:	Tungsten 0.25 mm dia.
Electrode Gap:	0.50 mm
Frequency:	10.0 kHz
Pulse Width:	1.0 μs
Average Current:	20 mA
Processing Time:	15 minutes

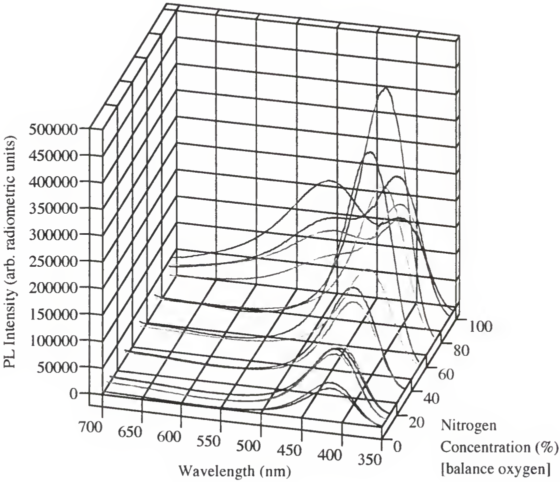

Figure 7-18: 3-D overview of the PL spectra of spark-processed germanium as a function of the nitrogen concentration of the ambient. $\lambda_{excitation} = 325$ nm.

Location of Blue and Green Peaks as a Function of Nitrogen Concentration

Substrate Material:	Germanium
Atmosphere:	**N_2 and O_2 variable**
Electrode Material:	Tungsten 0.25 mm dia.
Electrode Gap:	0.50 mm
Frequency:	10.0 kHz
Pulse Width:	1.0 ms
Average Current:	20 mA
Processing Time:	15 minutes

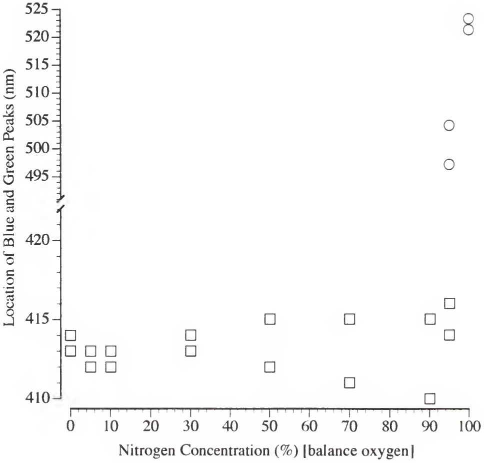

Figure 7-19: Peak locations of the blue and green PL bands of spark-processed germanium as a function of the nitrogen concentration of the ambient.

Intensity of Blue and Green Peaks as a Function of Nitrogen Concentration

Substrate Material:	Germanium
Atmosphere:	**N_2 and O_2 variable**
Electrode Material:	Tungsten 0.25 mm dia.
Electrode Gap:	0.50 mm
Frequency:	10.0 kHz
Pulse Width:	1.0 ms
Average Current:	20 mA
Processing Time:	15 minutes

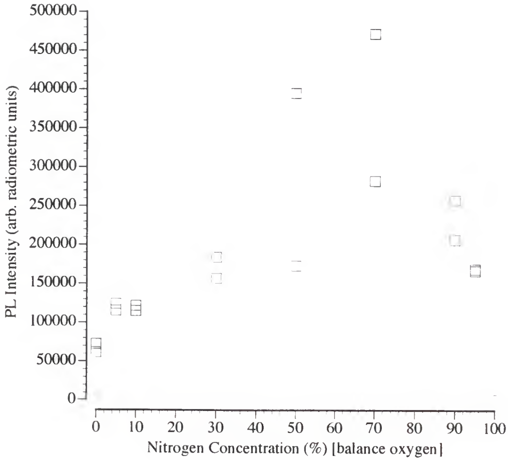

Figure 7-20: Undeconvoluted peak PL intensities of the blue and green bands of spark-processed germanium as a function of the nitrogen concentration of the ambient.

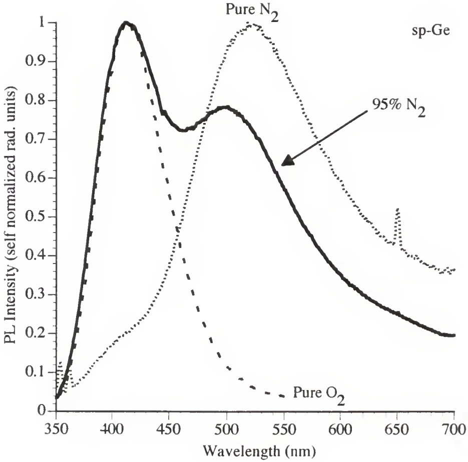

Figure 7-21: Self-normalized PL spectra of several spark-processed samples: 95% N_2 (solid line), pure N_2 (dotted line), and pure O_2 (dashed line).

that of the pure N_2 sample. The small difference in peak wavelength can be completely accounted for by the mathematical addition of the underlying green peak with the strong blue peak. This seems to indicate that the state involved may have a true emission peak near 520 nm, as was seen in the 100% N_2 samples.

It is reasonable to conclude, as in the case of silicon, that residual oxygen is responsible for the PL of the pure N_2 sample. The blue peak is also very weak in this sample as is the UV/blue peak of sp-Si processed in pure N_2.

Spark-processed aluminum

The samples used in this experiment were cut from 2.0 mm aluminum plate (Aldrich Chemical Co. lot # 09602JQ). This material is sold as 99.999% pure grade and has the following impurities: 2 ppm Fe and In, 1 ppm Ca, Co, and Ni, 0.7 ppm Cu, 0.5 ppm Ag, 0.2 ppm Mg, and 0.1 ppm Ba and V.

The spark-processed aluminum samples all have a similar appearance. A dark gray raised porous region is surrounded by a thick dark brown ring. This in turn is surrounded by a fine white halo of constant size. The size of the center region is fairly constant but the thickness of the ring decreases with increasing nitrogen concentration. At the time of writing, the halo regions appear identical as well. However, when the samples were fresh, and for some weeks afterward, the interface between the brown ring and the halo on the 0% N_2 and 5% N_2 samples had a deep blue color and exhibited blue PL.

A 3-D overview of the PL spectra of sp-Al as a function of the nitrogen concentration of the ambient is shown in Figure 7-22. Sp-Al exhibits a broad yellow peak near 570 nm. Note: monochromatic light at 570 nm is yellow in color. Due to the sensitivity of the eye and the width of the band, the PL appears to be greenish-

PL of Sp-Al vs. Nitrogen Concentration

Substrate Material:	Aluminum
Atmosphere:	**N_2 and O_2 variable**
Electrode Material:	Tungsten 0.25 mm dia.
Electrode Gap:	0.50 mm
Frequency:	10.0 kHz
Pulse Width:	1.0 ms
Average Current:	20 mA
Processing Time:	15 minutes

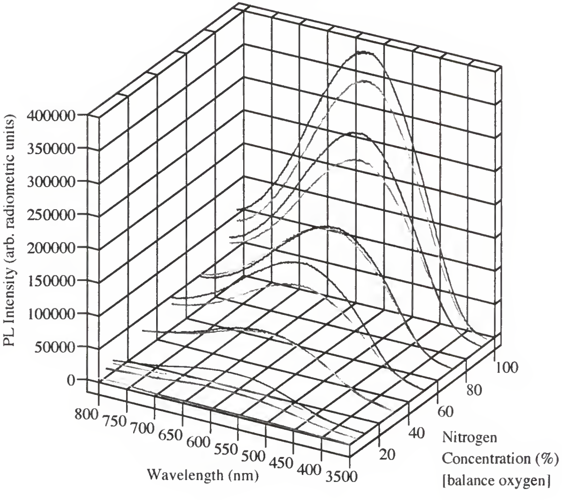

Figure 7-22: 3-D overview of the PL spectra of spark-processed aluminum as a function of the nitrogen concentration of the ambient. $\lambda_{excitation} = 325$ nm.

white to the observer. The peak location of the PL band of sp-Al is shown in Figure 7-23. The peak location of this band varies little. There is a slight blue-shift with increasing N_2 concentration (about 10 nm). Weak PL occurs in the 0% N_2 sample, but at a much longer wavelength above 640 nm.

The peak PL intensity of the yellow band of sp-Al is shown as a function of the nitrogen concentration of the ambient in Figure 7-24. As in the case of the green peak of sp-Si, the intensity increases exponentially with increasing nitrogen concentration. The PL from the 0% N_2 sample is much less intense and was not used in the calculation of the exponential fit shown in the graph.

Figure 7-25 shows the spectra of a 50% N_2 sample (solid line), a pure O_2 sp-Al sample multiplied by 25 times (dotted line), and the native oxide of Al multiplied by 25 times (dashed line). These were measured under identical conditions and may be compared with respect to both peak location and relative intensity. The native oxide has a main peak near 450 nm and a shoulder near 380 nm. In addition, there may be some structure between these wavelengths. The pure O_2 sample has a peak near 640 nm, a shoulder below 500 nm and a small feature near 380 nm, as in the native oxide. None of these occur at the same wavelength as the yellow peak of sp-Al.

The blue rings on the pure O_2 and 5% N_2 samples all have a slightly different peak location. The two furthest separated peaks are shown in Figure 7-26 (dotted and dashed lines). Again, the 50% N_2 sample is shown for comparison (solid line). The three spectra are self-normalized. The PL of the blue rings is similar to that of the native oxide from the previous figure. Again, they have no features in common with the main PL band of sp-Al.

Location of the PL Peak as a Function of Nitrogen Concentration

Substrate Material:	Aluminum
Atmosphere:	**N_2 and O_2 variable**
Electrode Material:	Tungsten 0.25 mm dia.
Electrode Gap:	0.50 mm
Frequency:	10.0 kHz
Pulse Width:	1.0 ms
Average Current:	20 mA
Processing Time:	15 minutes

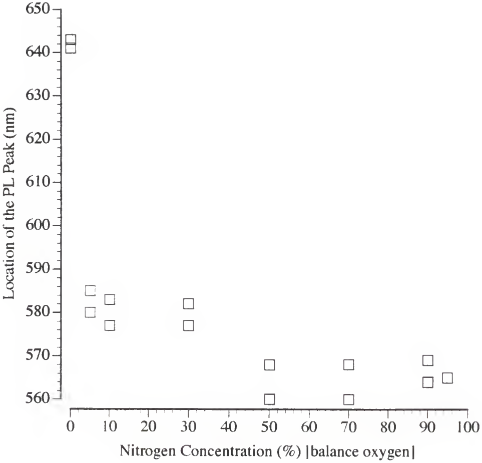

Figure 7-23: Peak location of the PL band of spark-processed aluminum as a function of the nitrogen concentration of the ambient.

Intensity of the PL Peak as a Function of Nitrogen Concentration

Substrate Material:	Aluminum
Atmosphere:	**N_2 and O_2 variable**
Electrode Material:	Tungsten 0.25 mm dia.
Electrode Gap:	0.50 mm
Frequency:	10.0 kHz
Pulse Width:	1.0 ms
Average Current:	20 mA
Processing Time:	15 minutes

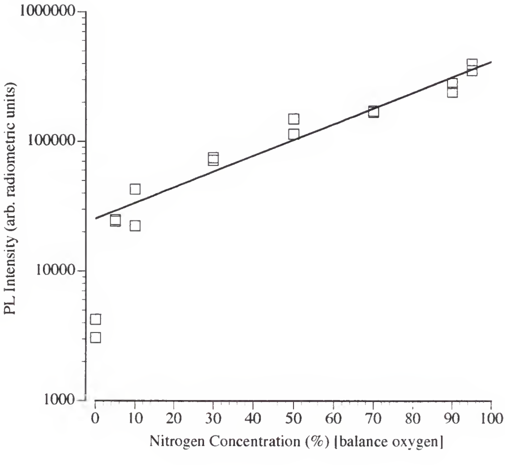

Figure 7-24: Peak intensity of the PL band of spark-processed aluminum as a function of the nitrogen concentration of the ambient. Exponential fit shown.

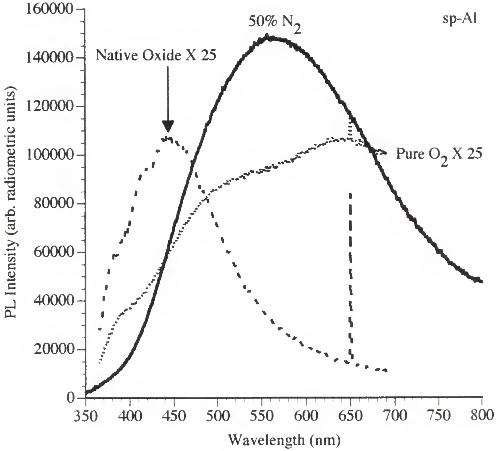

Figure 7-25: PL spectra of a 50% N_2 sp-Al sample (solid line), a pure O_2 sample (dotted line), and the native oxide (dashed line) multiplied by 25.

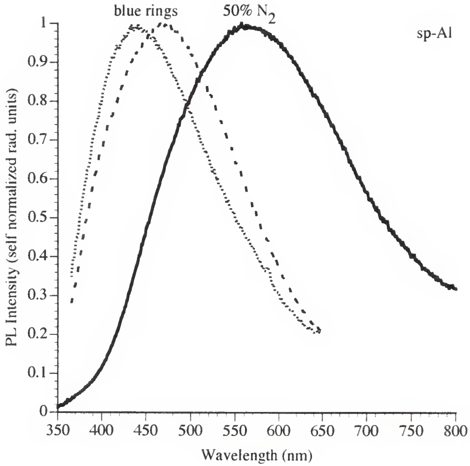

Figure 7-26: Self-normalized PL spectra of a 50% N_2 sp-Al sample (solid line) and the blue rings found on some samples (dotted and dashed lines), see text.

It is clear that the PL of sp-Al is unique and strongly nitrogen-related. The native oxide and the samples processed in pure O_2 have no features in common with this primary luminescence. This is identical to the case of sp-Si. In addition, the exponential dependence of intensity on nitrogen concentration occurs for both sp-Al and the green peak of sp-Si. The small (10 nm) shift in the PL band with increasing nitrogen concentration is probably the result of the peak becoming stronger and better defined relative to the background.

Spark-processed tantalum

The samples used in this experiment were cut from 1.0 mm tantalum plate (Aldrich Chemical Co. lot # 07510DS). This material is sold as 99.9+% pure grade and has the following impurities: 125 ppm Ni, 85 ppm Fe, 30 ppm Ca and Mn, 12 ppm Mo, and 3 ppm Zr. This lot is, in fact, 99.97% pure.

The centers of the sp-Ta samples show little variation across the nitrogen concentration range. The central porous region is slightly raised and has a metallic gray color. All samples have a light brown halo region that is slightly thicker and darker at high nitrogen concentration. Under 325 nm excitation, all the samples have a ring surrounding the center that emits blue light. This region does not appear distinct from the rest of the halo under normal light.

A 3-D overview of the PL spectra of sp-Ta as a function of the nitrogen concentration of the ambient is shown in Figure 7-27. The peak location of the PL band of sp-Ta is shown in Figure 7-28. Sp-Ta exhibits a red peak near 640 nm that appears to shift to slightly longer wavelengths with increasing nitrogen concentration. The pure O_2 sample exhibits a distinctly different peak location near 585 nm.

PL of Sp-Ta vs. Nitrogen Contentration

Substrate Material:	Tantalum
Atmosphere:	**N_2 and O_2 variable**
Electrode Material:	Tungsten 0.25 mm dia.
Electrode Gap:	0.50 mm
Frequency:	10.0 kHz
Pulse Width:	1.0 ms
Average Current:	20 mA
Processing Time:	15 minutes

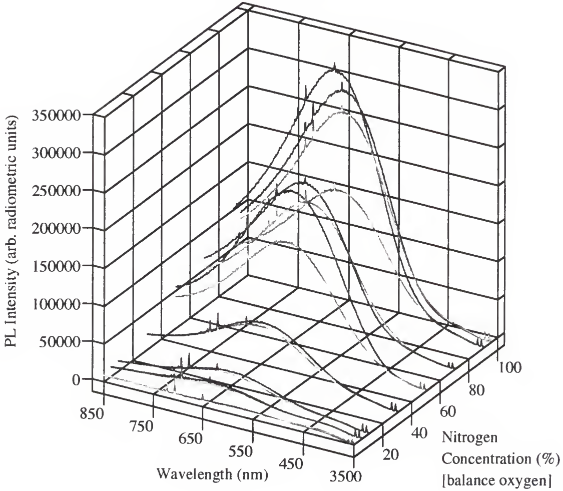

Figure 7-27: 3-D overview of the PL spectra of spark-processed tantalum as a function of the nitrogen concentration of the ambient. $\lambda_{excitation} = 325$ nm.

Location of the PL Peak as a Function of Nitrogen Concentration

Substrate Material:	Tantalum
Atmosphere:	**N_2 and O_2 variable**
Electrode Material:	Tungsten 0.25 mm dia.
Electrode Gap:	0.50 mm
Frequency:	10.0 kHz
Pulse Width:	1.0 ms
Average Current:	20 mA
Processing Time:	15 minutes

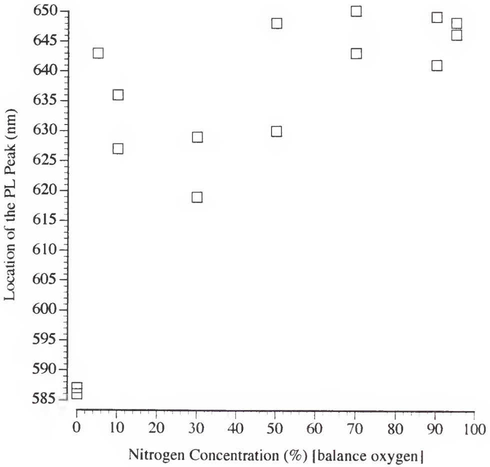

Figure 7-28: Peak location of the PL band of spark-processed tantalum as a function of the nitrogen concentration of the ambient.

The peak PL intensity of the red band of sp-Ta is shown as a function of the nitrogen concentration of the ambient in Figure 7-29. As in the case of the green peak of sp-Si and the yellow peak of sp-Al, the intensity follows an exponential relationship. In addition, as in the other two cases, the PL of the pure O_2 sample was significantly lower in intensity and was not used in the calculation of the exponential fit because it is distinct from the nitrogen-related luminescence.

Figure 7-30 shows the spectrum of a 50% N_2 sample (solid line), the spectrum of a pure O_2 sample multiplied by 10 times (dotted line), and the spectrum of the native oxide of tantalum multiplied by 10 times (dashed line). These samples are measured under identical conditions. In addition to the second-order laser line, some second-order plasma lines from the laser are visible near 700 nm and should be ignored by the reader. The native oxide has a peak near 425 nm. The pure O_2 sample has a shoulder at this wavelength and a broad peak near 580 nm. Both of these are distinct from the main PL band. The spectra of the various halo regions were measured and were found to resemble the native oxide. Figure 7-31 shows the PL spectra of the blue luminescing rings on a 50% N_2 sample (solid line), which is representative of the higher nitrogen concentration samples, and on a 10% N_2 sample (dotted line), which is representative of the lower nitrogen concentration samples. These were measured under the same conditions and may be compared directly in intensity with the data in the previous two figures. These rings have luminescence resembling either the native oxide or the pure O_2 sample in addition to a band near 700 nm. None of these features resembles the primary luminescence of sp-Ta.

It is clear that the PL of sp-Ta is unique and strongly nitrogen-related. The native oxide and the samples processed in pure O_2 have no features in common with this primary luminescence. This is identical to the case of sp-Si and sp-Al. In

Intensity of the PL Peak as a Function of Nitrogen Concentration

Substrate Material:	Tantalum
Atmosphere:	**N_2 and O_2 variable**
Electrode Material:	Tungsten 0.25 mm dia.
Electrode Gap:	0.50 mm
Frequency:	10.0 kHz
Pulse Width:	1.0 ms
Average Current:	20 mA
Processing Time:	15 minutes

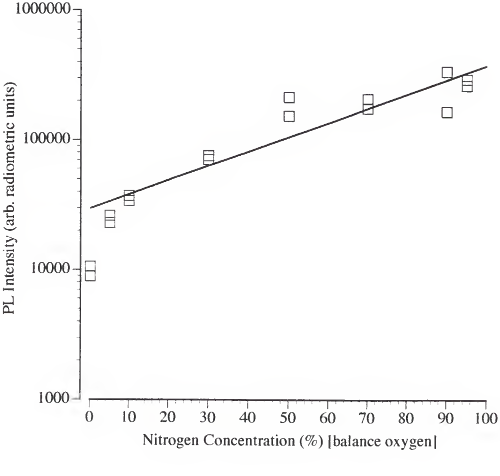

Figure 7-29: Peak intensity of the PL band of spark-processed tantalum as a function of the nitrogen concentration of the ambient. Exponential fit shown.

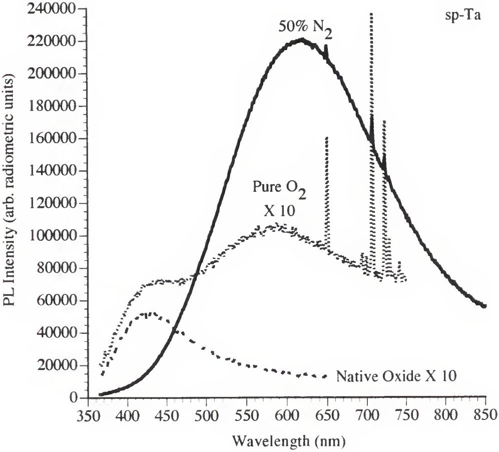

Figure 7-30: PL spectra of a 50% N_2 sp-Ta sample (solid line), a pure O_2 sample (dotted line) multiplied by 10, and the native oxide (dashed line) multiplied by 10.

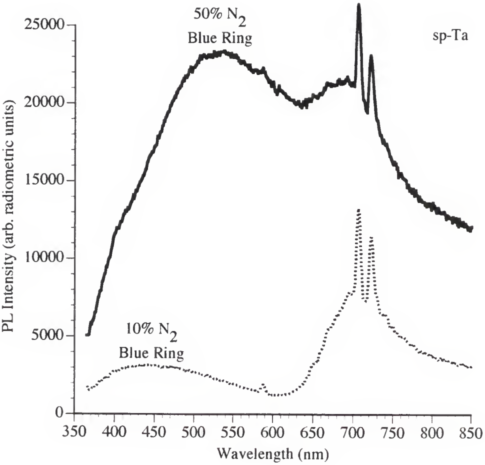

Figure 7-31: PL spectra of the blue-luminescing rings on two sp-Ta samples: 50% N_2 (solid line) and 10% N_2 (dotted line), see text.

addition, the exponential dependence of intensity on nitrogen concentration occurs for sp-Ta, as well as, sp-Al and the green peak of sp-Si. As in the cases of sp-Al, the small shift in the PL peak with increasing nitrogen concentration is probably the result of the band becoming stronger and better defined relative to the background. The shift is in the opposite directions for each element but always away from the location of the peak of the pure O_2 sample, as would be expected.

Spark-processed molybdenum

The samples used in this experiment were cut from 1.0 mm aluminum plate (Aldrich Chemical Co. lot # 03914MS). This material is sold as 99.9+% pure grade and has the following impurities: 430 ppm W, 15 ppm Ta, 7 ppm Ca, 4 ppm Fe and Mg, 0.2 ppm Mg, and 3 ppm Zr. This lot is, in fact, 99.95% pure.

The dependence of the PL of sp-Mo on nitrogen was investigated only due to the previous confusion with mislabeled tantalum stock. The PL was weak and not dependent on nitrogen, see Figures 7-32 through 7-34. As seen in Figure 7-35, the luminescence of sp-Mo is identical to that of the native oxide, only weaker.

The samples all had eroded craters in the center surround by white halos that turned an India blue after UV exposure.

Spark-processed nickel

The samples used in this experiment were cut from 1.0 mm nickel plate (Aldrich Chemical Co. lot # 17424MR). This material is sold as 99.98% pure grade and has the following impurities: 13 ppm Fe and Pd and 0.1 ppm Mg. This lot is, in fact, 99.997% pure.

The sp-Ni samples have an eroded center region surrounded by a fine white halo except for the pure O_2 samples, which have a black powder surrounding the

PL of Sp-Mo vs. Nitrogen Contentration

Substrate Material:	Molybdenum
Atmosphere:	**N_2 and O_2 variable**
Electrode Material:	Tungsten 0.25 mm dia.
Electrode Gap:	0.50 mm
Frequency:	10.0 kHz
Pulse Width:	1.0 ms
Average Current:	20 mA
Processing Time:	15 minutes

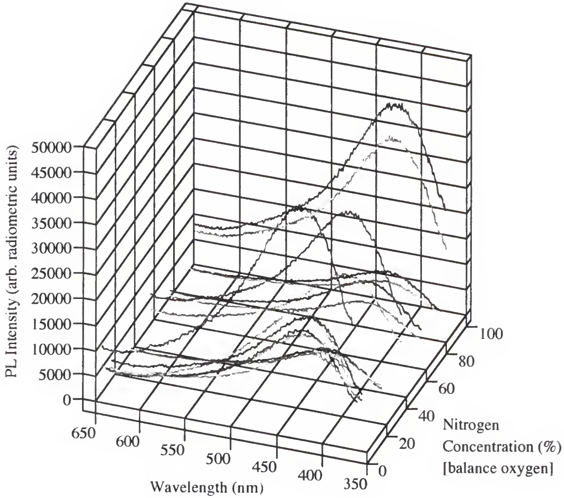

Figure 7-32: 3-D overview of the PL spectra of spark-processed molybdenum as a function of the nitrogen concentration of the ambient. $\lambda_{excitation} = 325$ nm.

Location of the PL Peak as a Function of Nitrogen Concentration

Substrate Material: Molybdenum
Atmosphere: **N_2 and O_2 variable**
Electrode Material: Tungsten 0.25 mm dia.
Electrode Gap: 0.50 mm
Frequency: 10.0 kHz
Pulse Width: 1.0 ms
Average Current: 20 mA
Processing Time: 15 minutes

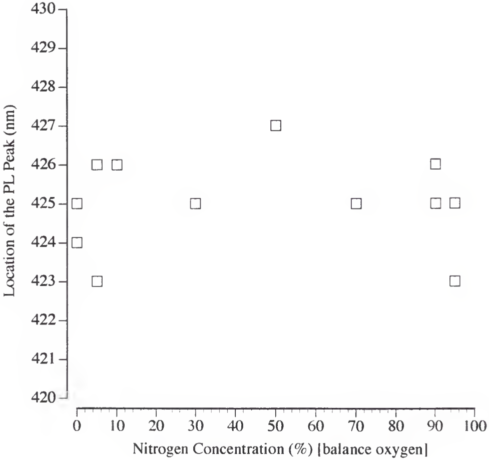

Figure 7-33: Peak location of the PL band of spark-processed molybdenum as a function of the nitrogen concentration of the ambient.

Intensity of the PL Peak as a Function of Nitrogen Concentration

Substrate Material:	Molybdenum
Atmosphere:	**N_2 and O_2 variable**
Electrode Material:	Tungsten 0.25 mm dia.
Electrode Gap:	0.50 mm
Frequency:	10.0 kHz
Pulse Width:	1.0 ms
Average Current:	20 mA
Processing Time:	15 minutes

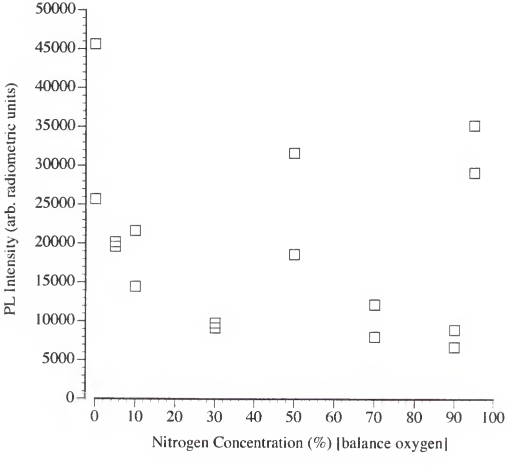

Figure 7-34: Peak intensity of the PL band of spark-processed molybdenum as a function of the nitrogen concentration of the ambient.

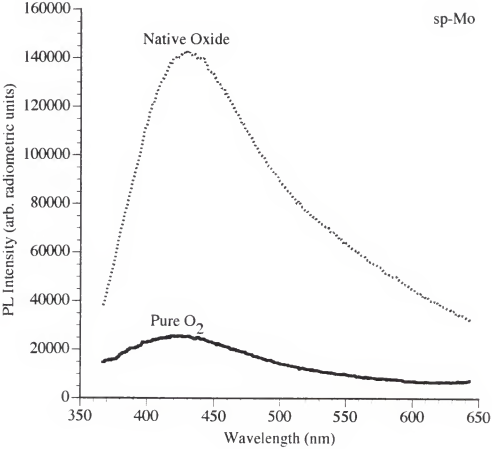

Figure 7-35: PL spectra of a pure O_2 sp-Mo sample (solid line) and the native oxide (dashed line).

center. In addition, the pure O_2 samples were covered with a fine flocculent black material resembling cotton candy. This crumbled immediately when the samples were moved, leaving no trace.

A 3-D overview of the sp-Ni spectra is shown in Figure 7-36. The PL from these samples in not nitrogen dependent and is centered just below 430 nm. Some of these samples have a dual peak and a maximum intensity near 435 nm, see Figure 7-37. The peak intensity has no correlation to the nitrogen concentration of the ambient, see Figure 7-38.

Figure 7-39 shows the PL spectrum of a 50% N_2 sample (solid line), the spectrum of the native oxide (dotted line), and the spectrum of the black powder on a pure O_2 sample (dashed line). The PL of the 50% N_2 samples is stronger than, but otherwise identical to, the spectrum of the black powder from the pure O_2 samples. In addition, the native oxide appears to have a shoulder at this wavelength and a broad structure between 450 nm and 550 nm.

As previously mentioned, Ni was only included in this set of experiments due to the ambiguity and contradiction in previous measurements. The 430 nm peak is substantially different than the previously reported 510 nm peak (Figure 7-17). It is also noticeably narrower. The author is sure of the purity of the Ni used in this final set of measurements. Because the PL was so weak this time, it is possible that an impurity in the previous Ni samples was responsible for the stronger luminescence reported. However, the weak PL of sp-Ni is clearly not nitrogen-related and, thus, is of little interest.

PL of Sp-Ni vs. Nitrogen Contentration

Substrate Material:	Nickel
Atmosphere:	**N_2 and O_2 variable**
Electrode Material:	Tungsten 0.25 mm dia.
Electrode Gap:	0.50 mm
Frequency:	10.0 kHz
Pulse Width:	1.0 ms
Average Current:	20 mA
Processing Time:	15 minutes

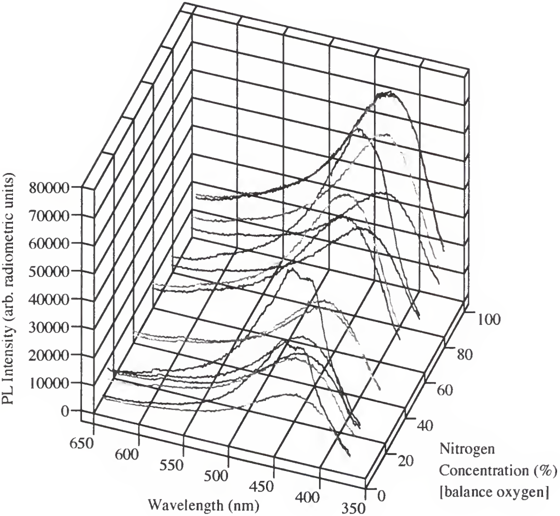

Figure 7-36: 3-D overview of the PL spectra of spark-processed nickel as a function of the nitrogen concentration of the ambient. $\lambda_{excitation} = 325$ nm.

Location of the PL Peak as a Function of Nitrogen Concentration

Substrate Material: Nickel
Atmosphere: **N_2 and O_2 variable**
Electrode Material: Tungsten 0.25 mm dia.
Electrode Gap: 0.50 mm
Frequency: 10.0 kHz
Pulse Width: 1.0 ms
Average Current: 20 mA
Processing Time: 15 minutes

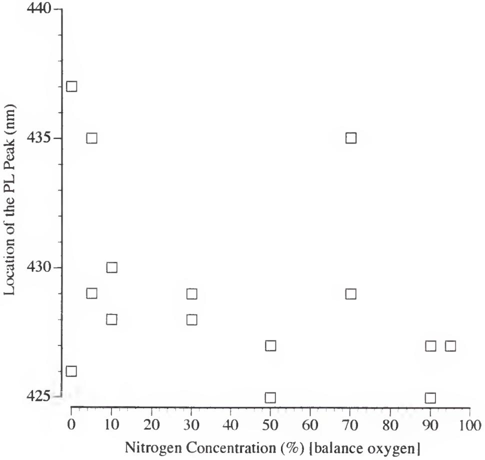

Figure 7-37: Peak location of the PL band of spark-processed nickel as a function of the nitrogen concentration of the ambient.

Intensity of the PL Peak as a Function of Nitrogen Concentration

Substrate Material:	Nickel
Atmosphere:	**N_2 and O_2 variable**
Electrode Material:	Tungsten 0.25 mm dia.
Electrode Gap:	0.50 mm
Frequency:	10.0 kHz
Pulse Width:	1.0 ms
Average Current:	20 mA
Processing Time:	15 minutes

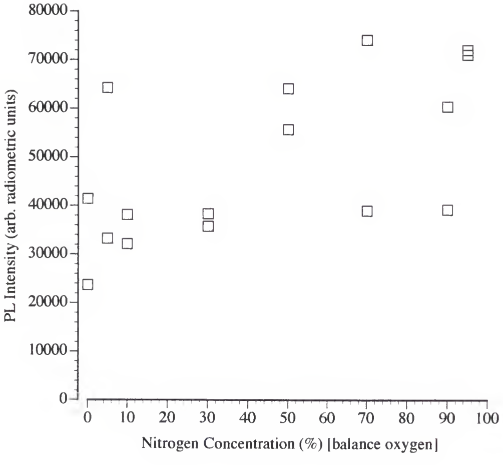

Figure 7-38: Peak intensity of the PL band of spark-processed nickel as a function of the nitrogen concentration of the ambient.

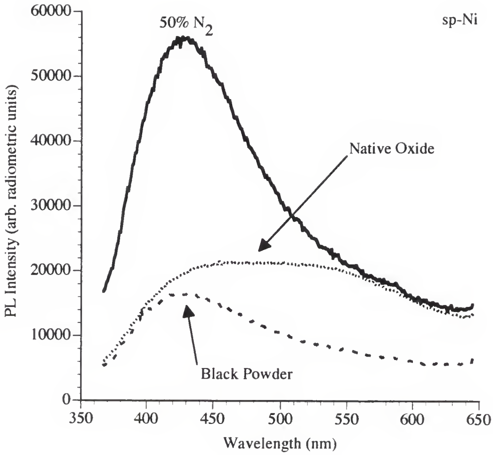

Figure 7-39: PL spectra of a 50% N_2 sp-Ni sample (solid line), the native oxide (dotted line), and the black powder found on pure O_2 sp-Ni samples (dashed line), see text.

Note on titanium

Titanium samples were cut, cleaned, and etched and left for a future researcher to spark-process once infrared PL capabilities become available. These were cut from 0.0625" (1.6 mm) titanium plate (Electronic Space Products International lot # D98353A1). This material is sold as 3N7 grade (99.97% pure) and has the following impurities: 100.0 ppm O and Fe, 70.0 ppm N, and 30.0 ppm C.

Summary

The results of this section in addition to the work on silicon in Chapter 5 reveal the existence of 6 strongly nitrogen-related peaks. It is remarkable that this behavior was seen in all the elements that were considered good candidates based on the criteria of strong PL after spark-processing, and adherent oxide, and a high oxide heat of formation. Many elements that met one or more of these criteria had to be excluded for one of the reasons discussed in the second section of this chapter. In most cases, toxicity was the main factor. It would not be surprising if many of these show the same relationship between PL and nitrogen concentration.

The 6 strongly nitrogen-related PL bands are: the UV/blue band of sp-Si, the green band of sp-Si, the blue band of sp-Ge, the green band of sp-Ge, the yellow band of sp-Al, and the red band of sp-Ta. Among all these bands, only the blue band of sp-Ge exists after spark-processing in pure oxygen. However, it is still strengthened dramatically by the presence of nitrogen. The UV/blue band of sp-Si and the blue band of sp-Ge are very similar in one respect. They both reach maximum intensities at nitrogen concentration of approximately 70 - 80% (similar to air). They both begin decreasing substantially before oxygen becomes scarce.

The green band of sp-Si, the yellow band of sp-Al, and the red band of sp-Ta all continue to increase in intensity to very high nitrogen concentrations. In the case of sp-Si, it was proven that this trend eventually reverses when oxygen becomes scarce (less than a couple percent). Al and Ta would probably follow the same trend based on observation of the spark itself and the fact that as the porous matrix appears to be an oxide in all cases. The green band of sp-Ge only exists at high nitrogen concentrations and appears to follow the same trend (higher at 95% than 90% but much lower again in "pure" N_2). It was not present at lower nitrogen concentrations, at least under the chosen processing conditions, so there was not enough data to mathematically fit the relationship. However, in the remaining bands (green band of sp-Si, yellow band of sp-Al, and red band of sp-Ta), there was plenty of data, which was seen to closely fit an increasing exponential in every case. Figure 7-40 shows the intensity vs. nitrogen concentration for these three bands. The green peak of sp-Si is shown in green, the yellow peak of sp-Al is shown in black (due to the poor contrast of yellow, especially for the microfilm reader), and the red peak of sp-Ta is shown in red. The intensity data was linearly scaled such that the average of the 50% samples for each element would be 1 on the graph.

The slopes of the sp-Al and sp-Ta intensity are very similar. Even the data points are remarkably similar. In both cases they lie slightly above the exponential trend at moderate nitrogen concentrations and slightly below it at the extremes. The green peak of sp-Si has a moderately steeper slope. This exponential constant could be reported in many ways. A characteristic value (the change in nitrogen concentration needed to increase the intensity by a factor of e), in percent per decade, or even percent per decibel. The most intuitively meaningful figure is probably the absolute change in nitrogen concentration (in percent of the total concentration)

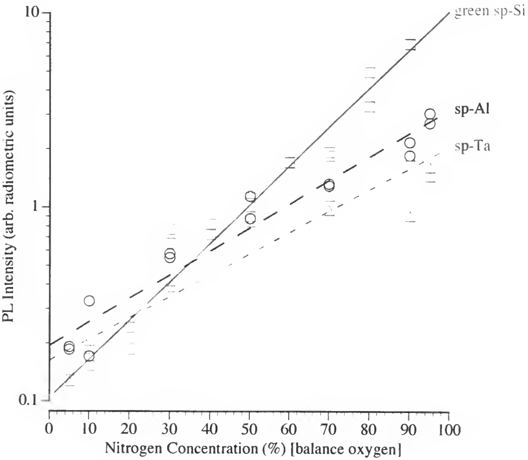

Figure 7-40: The relationship between the nitrogen concentration of the ambient and the peak PL intensity of the green band of sp-Si (green squares), the yellow band of sp-Al (black circles), and the red band of sp-Ta (red triangles). Exponential fits are shown for all three bands, see text.

necessary for the luminescence to double in intensity. This has the following values for each band: 15.2% for the green band of sp-Si, 25.0% for sp-Al, and 27.6% for sp-Ta.

It is interesting to note that the units of the slope are proportional to volume (1/concentration). However, this volume probably has no physical meaning as the concentration axis is actually in percent, not quantity per volume, and it is the concentration of the gas, not of the porous material (the relationship may not be linear), and finally, the intensity values are linear but arbitrary. What can be said definitively is that the dependence of the PL intensity on nitrogen concentration is exponential (highly nonlinear) and similar for all three elements. This is very strong evidence of a similar mechanism.

CHAPTER 8
RESULTS: OTHER LUMINESCENT SPECTROSCOPIES

Variable Excitation Power

The effects of varying the excitation power on the PL sp-Si was studied early in Stage I. The results were clear enough that these measurements did not need to be repeated in Stage II or III.

Spectral Shape vs. Power

Experimental procedure

Two monitor-sparked Stage I samples were selected from a batch of 15 samples. One had a very prominent UV/blue band and one had a very prominent green band. The former was prepared by directing a jet of cool air on the region being processed. The samples were mounted to the sample stage and illuminated with the focused attenuated bean from the 325 nm He-Cd laser. A variable gray filter was used to adjust the beam power in small increments from approximately 1/4 mW to over 15 mW (approximately 6 W/cm^2). For each sample, the PL spectrum was taken at each of these increments (roughly 8-10 spectra per sample). The slit openings were optimized for each sample to give a large number of counts and a good signal-to-noise ratio.

Results and analysis

The spectra of these samples were self normalized. For each sample, the spectra were found to have essentially the same spectral shape and peak location for each laser power measured. Figure 8-1 shows the spectral shape of the UV/blue sample for different laser powers. To avoid cluttering the figure, only the lowest, highest, and middle-most laser powers are shown. At very low powers, there appears to be a greater relative intensity at lower wavelengths and the peak is slightly red-shifted. The lower power spectra were taken with the entrance and exit slits of the monochromator fully open. The chromatic aberration problem associated with very large and very small slit openings was discovered and corrected between Stage II and III and was not known at this point. This is discussed in Appendix B. The lens separation distance was too large in Stage I and longer wavelengths were overemphasized at larger entrance-slit openings. This error is believed to be the sole cause of the discrepancy seen in this figure.

Figure 8-2 shows the spectral shape for the green sample for different laser powers. Again, only three powers are shown on the graph. The three self normalized curves completely overlap, as did the omitted curves. It is apparent that both PL bands of sp-Si have the same shape regardless of the power of the excitation beam.

Power Linearity of Sp-Si

Experimental procedure

The UV/blue and green peak intensities of more than a dozen samples were measured as a function of laser beam power. Roughly half these samples had predominantly UV/blue peaks and the balance were predominantly green.

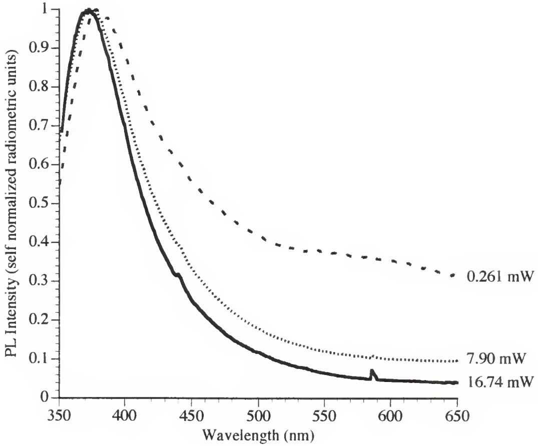

Figure 8-1: Self normalized PL spectra of a UV/blue Stage I sp-Si sample measured at several excitation powers, see text. $\lambda_{excitation} = 325$ nm.

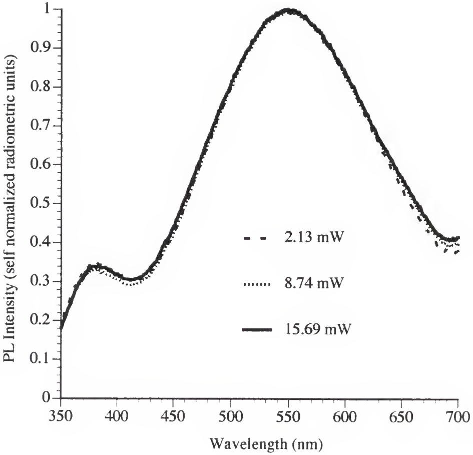

Figure 8-2: Self normalized PL spectra of a green Stage I sp-Si sample measured at several excitation powers, see text. $\lambda_{excitation} = 325$ nm.

Measurements were taken at the instrumental peak wavelengths of both types of samples. In Stage I with a 630 nm blaze-wavelength diffraction grating in the monochromator, the instrumental peak of the UV/blue band of sp-Si was approximately 410 nm. This is sufficiently close to the true peak so as to still represent the UV/blue band. As the calibration curve is flat in the middle of the visible range, the instrumental peak of the green band was very close to its actual location.

The focused beam of the 325 nm laser was used to illuminate the samples. The laser power was attenuated with a variable gray filter. Measurements of the UV/blue and green peak were made on more than a dozen samples. The peak intensity at a fixed wavelength was measured as the beam power was varied. While the slit openings were optimized between samples, they were kept constant for each sample. Data was gathered until the laser power reached it maximum of approximately 35 mW (14 W/cm^2 power density) or until the photomultiplier tube registered more than 500,000 counts per second, whichever came first.

Results and discussion

The resulting intensity vs. power curves were highly linear. Typical power response curves for UV/blue and green samples are shown in Figure 8-3. There is no sign of nonlinearities or saturation at high power nor threshold behavior at low power. There appears to be a small but non-trivial intercept at the intensity axis with zero laser power, but this is due to the fact that these were very early experiments conducted before there was a dedicated darkroom for the photoluminescence measurements. Some stray light was present. No spark-processed sample has ever shown any sign of luminescence without excitation.

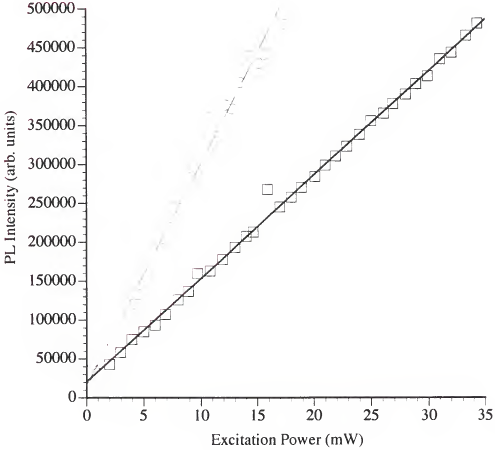

Figure 8-3: Peak PL intensities of UV/blue and green Stage I sp-Si samples as a function of excitation power, see text. Linear fits are shown.

High-Temperature Photoluminescent Spectroscopy

Understanding how the PL of any band changes with temperature is very important to understanding the nature of the state responsible. Whether the PL is thermally activated or thermally quenched and the degree of its stability is essential for establishing the identity of the luminescent process. In a series of Stage I experiments, the elevated-temperature peak PL intensity of sp-Si was compared to that of a number of different luminescent materials. Several clear differences were seen.

The work of Augustin and Ludwig was discussed in Chapter 3. These measurements were made under conditions similar to what the author defined as Stage I for his own work. It was clear from this that the PL of sp-Si is thermally quenched, not thermally activated, and that the interesting data lies above room temperature. Accordingly, the author conducted extensive PL measurements at higher temperatures under Stage III conditions but did not conduct low temperature measurements. The thermal behavior of these samples has both similarities to, and differences from, those prepared by monitor-sparking.

Stage I Measurements

Experimental procedure

The thermal quenching of the PL of a number of materials was compared in these experiments. The materials were placed on the hot stage described in Chapter 4 and the temperature was gradually increased from room temperature to as high as 750 K while the PL intensity at each sample's room-temperature instrumental peak was continuously monitored. In addition, the PL intensity was monitored as the sample was allowed to cool back down to room temperature. This allowed the degree of thermal quenching to be compared to the permanent degradation from combined annealing and UV exposure. The following samples and wavelengths were used: UV/blue sp-Si @ 404 nm, anodically etched PS @ 651 nm, thermal zinc oxide @ 379 nm (direct gap luminescence) and 508 nm (defect luminescence), boro-phospho-silicate glass (mostly SiO_2, 20% B_2O_3, and a small quantity of P_2O_5) damaged by 40 keV X-ray radiation @ 455 nm, spectroscopic grade silica powder @ 464 nm, and an unknown luminescing glass @ 420 nm.

Experimental results

Figures 8-4 and 8-6 show the thermal quenching behavior of these materials. Sp-Si is shown in both figures for comparison. The dotted lines show the PL intensities as the samples cooled. The color of each curve represents the approximate location of each sample's peak location in the visible spectrum. The temporary quenching and permanent degradation can be seen. Sp-Si and the direct luminescence of ZnO had no significant degradation, as is the case for the unknown glass. The X-ray damaged glass and the mid-gap defect luminescence from ZnO showed some degradation. PS was strongly degraded and the PL of the silica powder was completely destroyed.

For reference, Figures 8-5 and 8-7 show the initial room-temperature PL spectra of each of these samples. The use of color is the same as in the preceding figures. As these measurements were done early in Stage I, the Stage III calibration factors cannot be applied with great accuracy and this is reflected in the unusual shape of the UV/blue band of sp-Si, for example. Figures 8-8 and 8-9 show the ascending temperature data for each of these samples using the semi-empirical

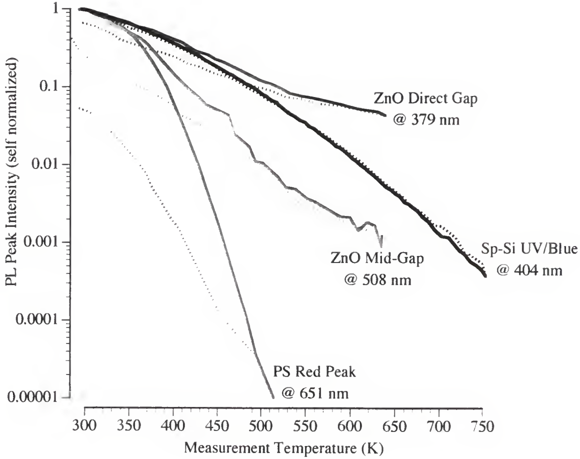

Figure 8-4: Peak PL intensities of several types of luminescing samples as a function of temperature. See text for details. Each sample was measured at its room-temperature instrumental peak. Solid and dotted lines represent increasing and decreasing temperatures, respectively.

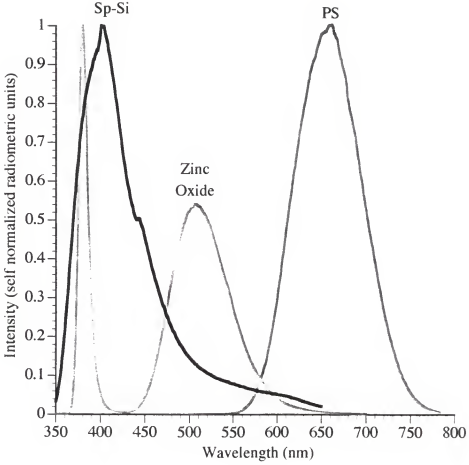

Figure 8-5: Self normalized room-temperature PL spectra of the samples from the previous figure (8-4). Color assignments are the same as in the previous figure.

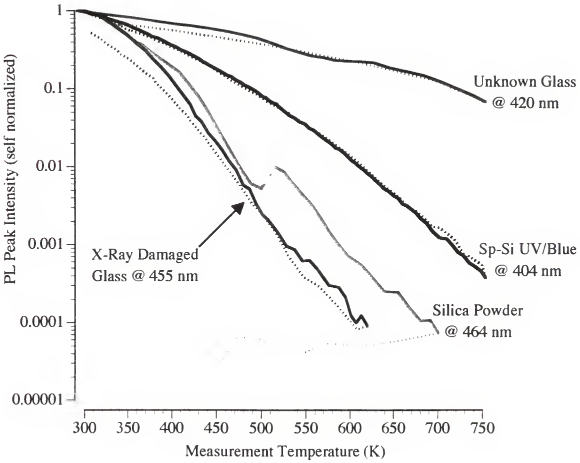

Figure 8-6: Peak PL intensities of several more types of luminescing samples as a function of temperature. Sp-Si is shown again for comparison. See text for details. Each sample was measured at its room-temperature instrumental peak. Solid and dotted lines represent increasing and decreasing temperatures, respectively.

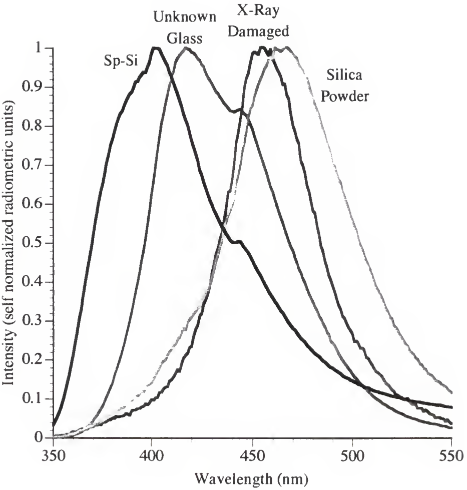

Figure 8-7: Self normalized room-temperature PL spectra of the samples from the previous figure (8-6). Color assignments are the same as in the previous figure.

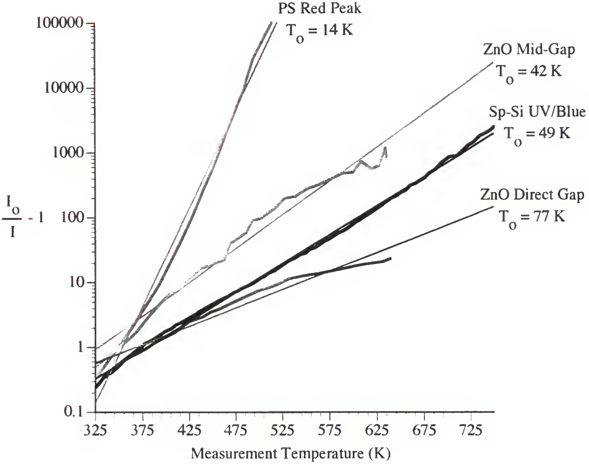

Figure 8-8: Plot of $[I_o/I(T)] - 1$ vs. temperature for the samples represented in Figure 8-4. Characteristic temperatures are shown (see text).

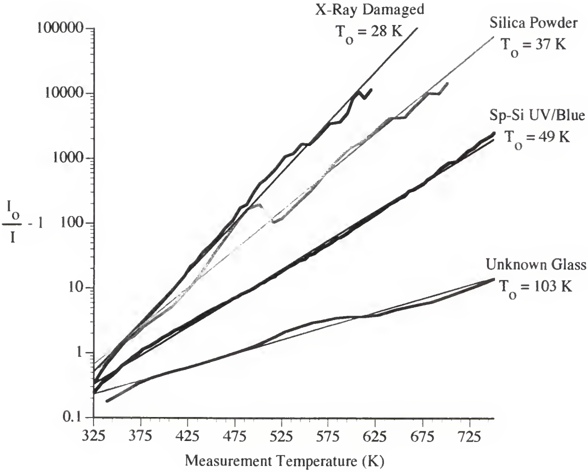

Figure 8-9: Plot of $[I_o/I(T)] - 1$ vs. temperature for the samples represented in Figure 8-6. Characteristic temperatures are shown (see text).

method of Collins as discussed in Chapter 3 [Col80]. Here $I_o/I - 1$ is plotted against temperature. Exponential fits and the corresponding characteristic disorder temperatures (T_o) are shown in the figures.

Analysis and discussion

The mid-gap PL from ZnO is associated with point defects, many of which are non-stoichiometric. It is not surprising that these defects are eliminated by annealing the thin thermal oxide layer in air. Non-stoichiometric defects (oxygen vacancies) are also believed to be responsible for the PL from the silica powder. Given the large surface to volume ratio of the powder it is not surprising that the luminescence was completely destroyed by annealing. The temporary increase of the PL seen near 525 K may be related to surface passivation by "naked" silanol groups as described in Chapter 3 and seen in Figures 3-13 and 3-14. The PL from PS is known to originate from a thin surface layer. PS sustained significant permanent annealing damage as well. Little can be said about the unknown glass except that it is much more resistant to thermal attenuation than the materials known to exhibit defect-related luminescence. Its PL probably originates from a stable impurity. The direct-gap PL of ZnO is chemically stable and exhibits a similar resilience. The PL of the X-ray damaged glass is almost certainly related to point defects created by ionizing radiation. It follows the thermal quenching trend of the silica powder, but is not irreversibly annealed. This is probably due to the low surface area to volume ratio, in contrast to the case of the silica powder. The attenuation of the UV/blue PL of sp-Si appears to be completely reversible. This is consistent with the literature on the annealing of sp-Si.

The characteristic disorder temperature, T_o, for the UV/blue band of 49 K is lower than those reported by Ludwig. However, 14 K is also low compared to the literature for PS. The fact that the intensity at a fixed wavelength was used instead of the integrated intensity (or even the true peak intensity) may account for this difference. The value of T_o for UV/blue sp-Si is about 51% higher than the average of the values for the silica powder and the X-ray damaged glass. Both are due to deep states in amorphous silica (the glass is almost 80% silica). The mid-gap PL of ZnO also comes from a deep state in an amorphous oxide. If this is included, T_o for UV/blue sp-Si is about 38% higher than the average of these three similar systems. As discussed in Chapter 3, T_o is a measure of the inhomogeneous ligand-field broadening of the state responsible for the PL. It is proportional to the amount of disorder in the material. These values indicate that sp-Si has about a 40% greater disorder than conventional amorphous oxides.

Stage III Measurements

Experimental procedure

PL spectra were taken of three Stage III samples at a variety of temperatures. These three samples were selected from the batch produced for the processing current experiments presented in Chapter 5. Strong UV/blue, green, and hybrid samples were chosen. Each sample was placed on the hot stage and PL spectra were taken under the same conditions at a variety of temperatures between room temperature and almost 800 K. The slits were optimized for the peak intensity of the room-temperature spectrum of each individual sample.

Experimental results

The PL spectra for each sample are shown in Figures 8-10 through 8-12. The PL intensity decreases with increasing temperature for all three samples. The curves in the figures are shown with alternating solid and dotted lines for clarity and the corresponding measurement temperatures are indicated on the right side of the figures. Figure 8-13 shows the peak location of the PL bands of these samples as a function of the measurement temperature. Blue squares represent the UV/blue band and green circles represent the green band. The symbols representing the bands of the UV/blue and green samples are unfilled while those representing the bands of the hybrid sample are filled. Black circles represent the green band that appears in UV/blue samples only at elevated temperatures. A linear fit is shown in the figure for the UV/blue band of the UV/blue sample. A thermal blue shift is seen for the green band of sp-Si similar to that reported by Ludwig, but it is seen to saturate before 600 K. A definite blue shift is also seen for the UV/blue band. This is in disagreement with the lack of a shift reported by Ludwig.

Figure 8-14 shows the peak PL intensities of the UV/blue and green band of the same samples using the same symbol conventions. All the intensities have been self normalized to 1 at room temperature. The decrease in intensity with increasing temperature is nonlinear and larger for the green than the UV/blue. The peak intensity of the UV/blue band of the hybrid sample is less rapidly quenched and its decrease appears to be almost linear. Figure 8-15 shows a plot of $I_o/I - 1$ for the UV/blue band of the UV/blue sample and the green band of the green sample as a function of measurement temperature using the methodology of Collins. Because the peak locations and shapes change, integrated intensities were used in the calculations. Exponential fits and characteristic disorder temperatures (T_o) are shown in the figure.

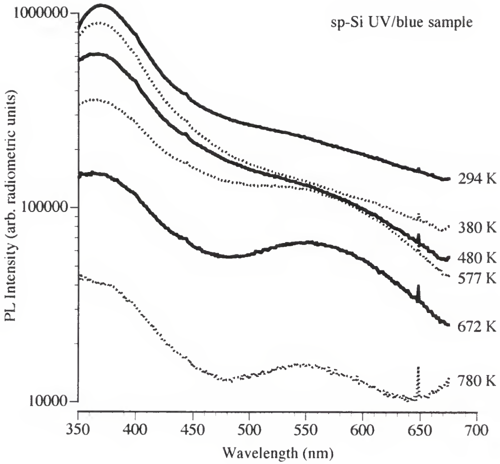

Figure 8-10: PL spectra of a Stage III UV/blue sp-Si sample as a function of measurement temperature, see text.

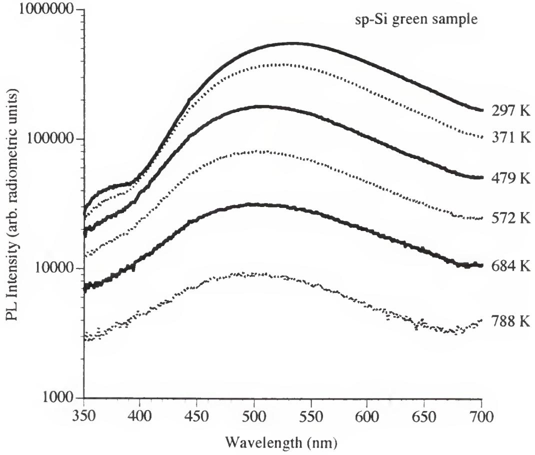

Figure 8-11: PL spectra of a Stage III green sp-Si sample as a function of measurement temperature, see text.

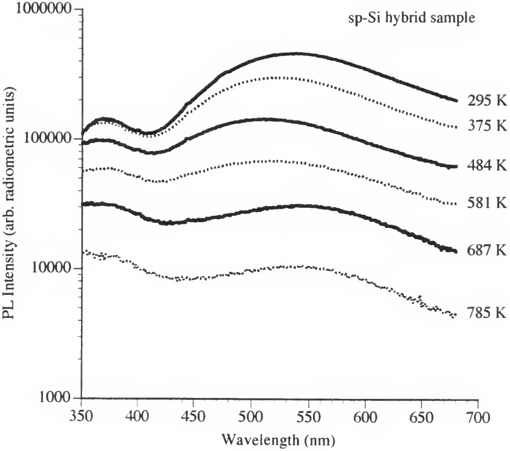

Figure 8-12: PL spectra of a Stage III hybrid sp-Si sample as a function of measurement temperature.

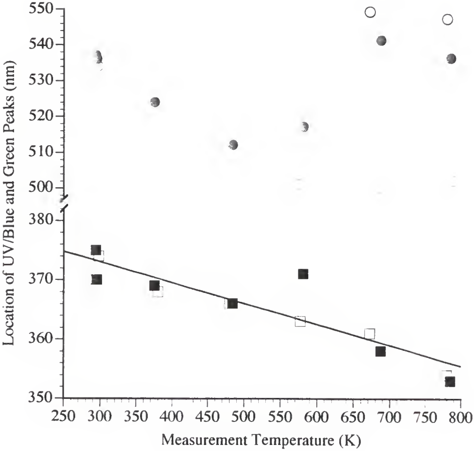

Figure 8-13: Peak locations of the PL bands of the sp-Si samples represented in the previous three figures plotted as a function of temperature. Blue squares represent the UV/blue band and green circles represent the green band. Filled symbols represent the peaks of the hybrid sample, while unfilled symbols represent either the UV/blue of green sample. Black circles represent the green peak seen in the UV/blue sample at high temperature. A linear fit is shown for the UV/blue band of the UV/blue sample.

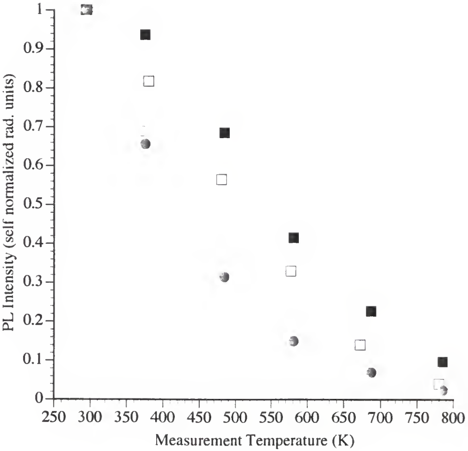

Figure 8-14: Peak intensities of the UV/blue and green PL bands of the samples from Figures 8-10 through 8-12 plotted as a function of measurement temperature. All peak intensities are self normalized to 1 at room temperature.

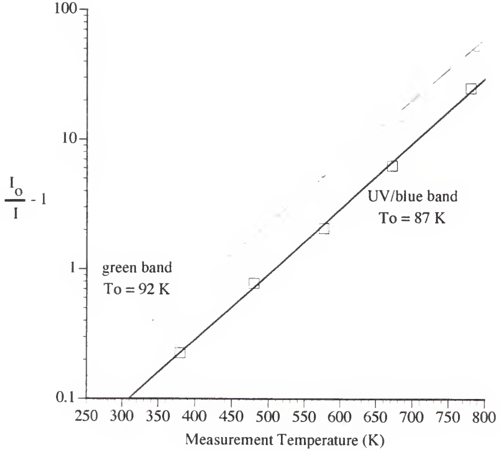

Figure 8-15: Plot of $|I_o/I(T)| - 1$ vs. temperature for the UV/blue band of the UV/blue sample and the green band of the green sample. Characteristic temperatures are shown (see text).

The values of 87 K for the UV/blue band and 92 K for the green band are within the range reported by Ludwig but, more significantly, are almost equal. Figure 8-16 shows the same $I_o/I - 1$ factor plotted as a function of inverse temperature. It can be seen from the data that, unlike the Stage I samples measured by Augustin and Ludwig, the activation energies are still increasing well past room temperature. Even at temperatures in the 700-800 K range, their values have not yet converged on their ideal limit. However, a lower limit for the activation energy, E_a, can be determined by fitting only the two highest-temperature data points of each band. These values are 573 meV for the UV/blue and 560 meV for the green band. Not only are these much higher than those reported by Ludwig, they are also nearly identical to one another.

Analysis and discussion

These measurements confirm the blue shift in the green band observed by Ludwig (Figure 3-10a). This shift appears to exist between 21 K and 500 K. Above 550 K, the peak emission wavelength is constant (Figure 8-13). This saturation could not have been observed by Ludwig or Augustin as their measurements stopped at about 450 K. At high temperatures, a green band was seen in the UV/blue sample. This occurred near 550 nm. The same peak was observed by Ludwig at the highest temperature measured (456 K). This luminescence is probably present all the time but only resolvable at high temperatures when the UV/blue peak is severely attenuated. Between 500 K and 650 K, the green peak of the hybrid samples appears to evolve from that of the standard green band to the special high-temperate green band. This is only resolvable when the green peak is severely attenuated, as well.

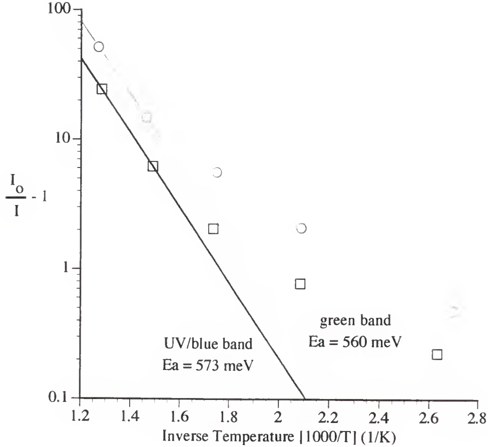

Figure 8-16: Plot of $[I_o/I(T)] - 1$ vs. inverse temperature for the same PL bands depicted in the previous figure (8-15). Thermal activation energies increase with temperature but have not yet approached a limit at the temperatures measured. Exponential fits and their corresponding activation energies are shown for the highest two data points for each sample. See text for details.

The clear linear blue shift in the UV/blue band of the UV/blue and hybrid samples seen in Figure 8-13 is not in agreement with the complete lack of a shift reported by Ludwig. There are two possible explanations. The first is that this relatively small shift cannot be seen without careful calibration of the PL system, such as that performed by the author. The other explanation is that the trend is so small that it could only be made clear over a large range of measurement temperatures. The linear fit made for the UV/blue sample also fits the hybrid sample data closely.

Between 20 K and room temperature, the UV/blue band of sp-Si and the blue band of sp-Ge were both observed to change more than the corresponding green peaks. The author observed that the change is greater for the green band of sp-Si above room temperature (Figure 8-14). The changes are nonlinear and there is not necessarily any conflict in these observations. It is more significant that the data are well fit by a Collins-type plot (Figure 8-15). The characteristic disorder temperatures, T_o, are well within the range reported by Ludwig and are essentially equal. This would not be unexpected if the excited state which gives rise to both PL bands were the same.

Plotting this same I_o/I - 1 factor as a function of inverse temperature results in continuously increasing activation energies as was described by Ludwig. However, these energies did not approach constant values near room temperature as previously reported. This may be due to differences between the author's Stage III samples and Ludwig's and Augustin's Stage I-like monitor-sparked samples. The author's samples appear to be much more stable. The conservative estimates of the activation energies were also essentially equal, which would be consistent with a single absorption mechanism for both PL bands. Using the same assumptions used by Ludwig to estimate the exciton radius, these higher values for the activation energies indicate a carrier localization distance of about 6.7 Å in silica. The density of amorphous silica is dependent on the preparation conditions, but is usually between 2.4 and 2.8 g cm^{-3}. It has been reported to be as high as 4.35 g cm^{-3} for silica exposed to shock waves. These densities correspond to molecular spacings of about 3.4 Å and 2.8 Å, respectively. For comparison, the distance between the long-bonded and short-bonded oxygen sites within one SiO_2 molecule is approximately 2.6 Å.

Photoluminescent Excitation Spectroscopy (PLE)

Experimental Procedure

Four samples were prepared for PLE measurements. These were two UV/blue and two green samples. The samples were prepared in a mixture of 700 mbar N_2 and 300 mbar O_2 using a 0.25 nm tungsten anode with a 0.50 mm gap, a 10.0 kHz repetition rate, and a 1.0 μs pulse width. The UV/blue samples were processed with currents of 11.3 mA and 11.6 mA and the green samples were processed with currents of 35.7 mA and 36.2 mA. The PL spectra of these four samples, which were measured under identical conditions, are shown in Figure 8-17. With 325 nm excitation, they had radiometric peaks of 371 nm and 532 nm, respectively. The samples were send to Dr. Regina Müller-Mach at Hewlett Packard (now Agilent Technology) for PLE measurements. While it has long been suspected that 325 nm light is not sufficient to fully excite the UV/blue band, the eventual result that the PL peak of the UV/blue band is blue shifted 1 nm for every 1 nm blue shift of the excitation source was completely unexpected. This band represents a "moving target" for conventional PLE measurements where emission is monitored at a single

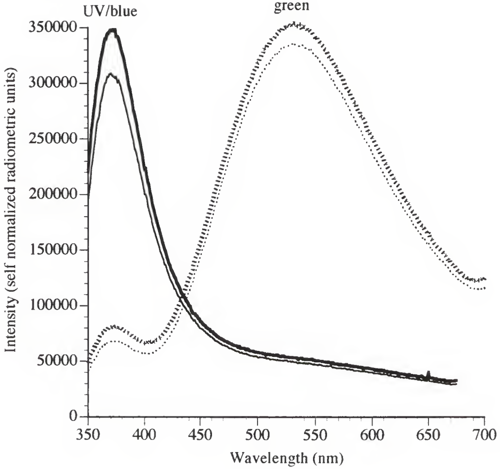

Figure 8-17: PL spectra of two UV/blue and two green samples used for PLE measurements. These sample were measured under identical conditions. The thick and thin solid lines represent the UV/blue samples and the thick and thin dotted lines represent the green samples.

wavelength. The PLE measurements of the UV/blue band cannot be interpreted at this time. However, the results for the green band are meaningful. In addition, conventional PL measurements were taken at a variety of excitation wavelengths.

Results

PL at different excitation wavelengths

The conventional PL measurements are discussed first. Figure 8-18 shows the PL spectra of the UV/blue band of a UV/blue sample measured at different excitation wavelengths. The thick line represents 250 nm excitation, the thin line represents 260 nm excitation, and the dotted line represents 288 nm excitation. The emission band is observed to increase in intensity and more toward shorter wavelengths as the excitation wavelength decreases. Figure 8-19 shows the PL spectra of the two green samples at a variety of excitation wavelengths. The thick blue line represents the second sample with 251 nm excitation, the thin blue line represents the first and second samples with 253 nm excitation (the curves overlap, so only one is shown). The thick green line represents the first sample with 282 nm excitation and the thin green line represents the second sample with 290 nm excitation. The thin red line represents the overlapping spectra of both samples with 300 nm excitation. Both the green band and UV/blue band of the green samples is seen to increase in strength and more toward shorter wavelengths as the excitation wavelength decreases.

Figure 8-20 shows the peak locations of the UV/blue and green bands of sp-Si as a function of the excitation wavelength. These data were derived from the spectra in the previous two figures. The unfilled blue squares and green circles represent the peak locations of the UV/blue and green bands of the UV/blue and green samples,

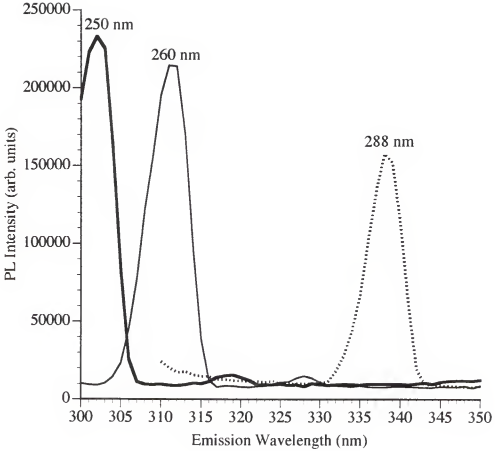

Figure 8-18: PL spectra of a UV/blue sample as a function of the excitation wavelength. The thick, thin, and dotted lines represent 250 nm, 260 nm, and 288 nm excitation, respectively.

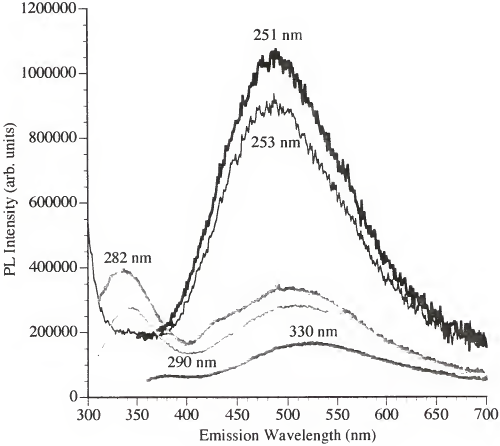

Figure 8-19: PL spectra of two green samples as a function of the excitation wavelength. The thick blue line represents the second sample with 251 nm excitation, the thin blue line represents the first and second samples with 253 nm excitation (they overlap), the thick green line represents the first sample with 282 nm excitation, the thin green line represents the second sample with 290 nm excitation, and, finally, the red line represents both samples with 330 nm excitation (overlap).

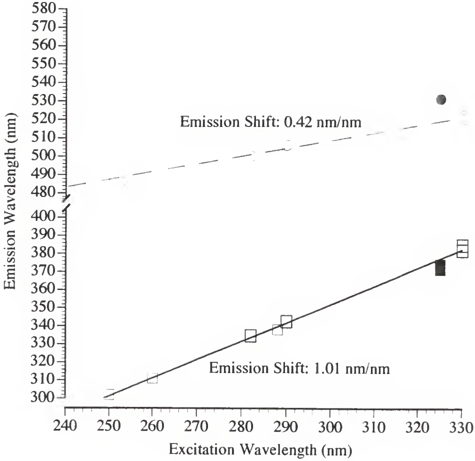

Figure 8-20: Peak locations of the UV/blue and green bands of sp-Si as a function of the excitation wavelength. Blue squares represent the UV/blue band of the UV/blue samples and green circles represent the green band of the green samples. Black squares represent the UV/blue band of the green samples and the filled symbols represent the typical peak locations for "in house" measurements with 325 nm excitation. The small deviation is attributed to calibration differences. Linear fits are shown for the peak locations of both bands of all four samples.

respectively. The black squares represent the peak locations of the UV/blue band of the green samples, and the filled symbols represent the peak locations of both bands as measured by the author. Linear fits are shown for both the green bands of the green samples and the UV/blue bands of all the samples. The "in house" points lie near these lines and differences in calibration are almost certainly the reason for the small difference. The emission peak of the UV/blue band is blue-shifted 1.01 nm/nm and the peak of the green band is blue-shifted 0.42 nm/nm. These trends are linear.

PLE of the green band

PLE spectra were taken for the green bands of both the green samples and the UV/blue samples. The latter were very noisy and had the same general form as the former. They are not shown. Figure 8-21 shows the data for the green band of the green samples. Emission intensity is plotted against the photon energy of the excitation source. The thick line represents the intensity of both samples monitored at 480 nm, 482 nm, and 485 nm (they all overlap), and the thin line represents the intensity of both samples monitored at 520 nm. These nearly overlap and only one is shown. Figure 8-22 shows the PLE spectrum for the green band of green sp-Si with 482 nm excitation (thick line) along with the remarkable fit from a simple model for the absorption of a disordered ligand field-broadened self-trapped exciton (STE). The details of this model are discussed in detail in the following discussion subsection.

Analysis and Discussion

For both peaks, the emission energy is higher the higher the excitation energy. The fact that this trend is so strong for the UV/blue made it impossible to determine the excitation band that leads to the UV/blue PL. However, the PLE spectrum of the

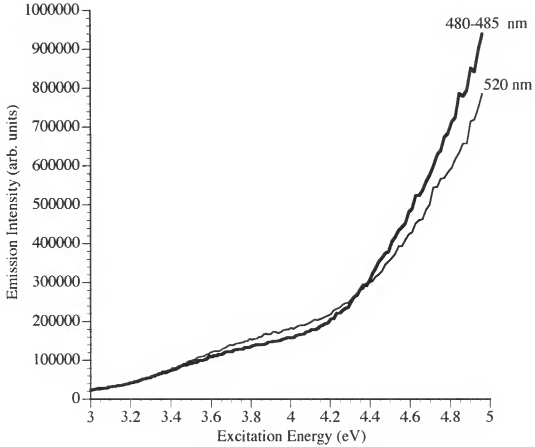

Figure 8-21: Excitation (PLE) spectra for the green band of the green samples of sp-Si as a function of the excitation (photon) energy. The thick line represents the intensity of both samples monitored at 480 nm, 482 nm, and 485 nm (they overlap) and the thin line represents the intensity of both samples monitored at with 520 nm (near overlap).

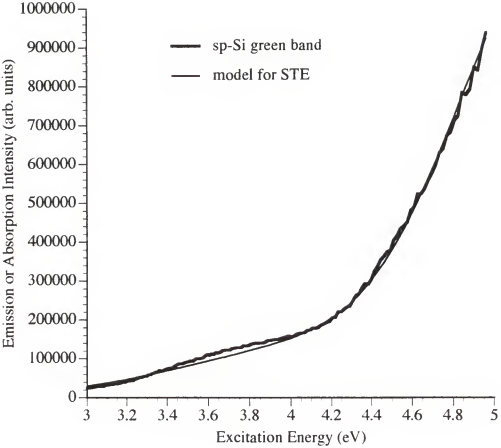

Figure 8-22: Excitation spectrum of the green band of green sp-Si with 482 nm excitation (thick line) and a model for the absorption spectrum of an inhomogeneously broadened self-trapped exciton in silica (thin line). See text for details.

absorption mechanism that leads to the green emission is evident. The lack of a result for the UV/blue band is not evidence of separate mechanisms for the two bands; it is just a lack of evidence. Given the shift of both peaks, a PLE-like spectrum constructed from the true peak or integrated intensities of numerous PL scans made at small excitation wavelength increments would be appropriate for any future investigations in this area. There is a consistent intensity increase seen in both Figures 8-18 and 8-19 as the excitation energy is increased, but it would take many such PL measurements to construct a PLE-like spectrum.

It can be seen from Figure 8-21 that excitation energies near 4 eV are slightly more efficient in producing 520 nm emission, while excitation energies closer to 5 eV are more efficient in producing 480 nm emission. This is the reason for the blue shift observed in the green band, as well as the larger shift of the UV/blue band. The higher the excitation energy, the more likely that carrier will find a higher-energy emission mechanism. In materials with inhomogeneously broadened bands, this is evidence of a charge transfer mechanism that behaves in a resonant manner. Differences in and energy levels and density-of-states distribution widths for different states may result in different shifts for the two bands.

The fit of the PLE spectrum shown in Figure 8-22 was generated by a simple parametric model with three degrees of freedom. It is based on the absorption bands for the STE in normal silica as reported by Tanimura (5.30 eV with a FWHM of 0.78 eV and 4.20 with a FWHM of 1.16 eV). The locations of these bands were fixed and were not parameters. The bands were treated as simple Gaussian curves. The three parameters were the widths of each of the two bands and the relative contribution of the two bands. The latter value is fairly arbitrary due to the wavelength dependence seen in Figure 8-21. The parameters were adjusted one at a time in a cyclic manner until the least-mean-square deviation between the model and the measured spectrum was minimized. The result of this fit are bands at 5.30 eV with a FWHM of 1.10 eV and 4.20 eV with a FWHM of 1.62 eV. These fitted bands are 41% and 40% broader than the observed bands for the STE in normal amorphous silica, which is remarkable because there was no linkage between the two width parameters used in the model. Mathematically, they were completely independent variables. The fact that they are both 40% greater than the STE in normal amorphous silica must be due to the constraints of the physical system as it is not inherent in the model. The measured PLE spectrum matches a theoretical STE with a 40% greater inhomogeneous ligand-field broadening than the measured STE in normal amorphous silica. In the Stage I thermal measurements presented above, the characteristic disorder temperature, T_o, for UV/blue sp-Si was observed to about 40% larger than the averages of those for deep states in three amorphous thermal oxides.

Time-Resolved Photoluminescent Spectroscopy (TRPL)

Spark-Processed Silicon

Experimental procedure

Six sp-Si samples were prepared for time-resolved PL measurements under standard conditions (a mixture of 700 mbar N_2 and 300 mbar O_2 using a 0.25 nm tungsten anode with a 0.50 mm gap, a 10.0 kHz repetition rate, and a 1.0 μs pulse width). These included two UV/blue samples prepared with currents of 10.0 mA, two green samples prepared with currents of 35.0 mA, and two hybrid samples prepared with currents of 21.0 mA. The samples were vacuum sealed after removal from the chamber until they could be measured. In addition, the 4 samples used for the previous PLE measurements were also used. The PLE measurements had not yet been fully analyzed at this point and it was assumed that the emission with 300 nm excitation would be similar to that with 325 nm excitation. The PL peaks are sufficiently broad that this assumption is valid. The time decay of these samples was measured at 370 nm and 540 nm. Due to the presence of intense 532 nm laser light used to create the 300 nm excitation source, the green band was not measured at this exact wavelength. All TRPL signals were recorded with a multi-channel analyzer at two time scales: 5 ps per channel and 89 ps per channel. Following the measurements, all 10 samples were annealed in flowing UHP nitrogen gas. The samples were placed in the furnace and the temperature was ramped up to 900 °C at a rate of 200 °C per hour. They were held at 900 °C for two hours and allowed to furnace cool to near room temperature before being removed. The time decay of the luminescence was again measured after annealing.

Analysis and results

In most cases, the majority of the luminescence appeared to occur on a very short sub-10 ps time scale. There was also significant luminescence at longer time scales. While the intensity was quit low, the duration was in the nanosecond range and accounted for a significant portion of the total time-integrated luminescence. It became clear that the luminescence fell naturally into three time scales. These are defined as primary, secondary, and tail luminescence. The primary and secondary decay were in the form of simple exponentials and were calculated from the 5 ps/channel data using proprietary software from Edinburgh Analytical Instruments, the manufacturer of the multichannel analyzer used to capture the data. Calculating a sub-10 ps time constant accurately when the time resolution of the equipment is 5 ps and the laser pulse width is approximately 3 ps is quite involved. In addition, the data on this time scale contain numerous artifacts resulting from multiple reflections of light within the instrument. Finally, an additional complication occurs due to extending ringing of the excitation laser pulse. The software compares the data file for the decay of the luminescence at the wavelength of interest to the signal of the 300 nm laser light also scattered off the same sample. A fit is made for the data file as a whole using a Marquardt alpha matrix. The software calculates the exponential lifetimes for the luminescence as well as their relative integrated contribution to the total luminescence. This software was used to identify the characteristics of the primary and secondary luminescence. The tail luminescence had lifetimes on the order of 10 ns and was often a simple exponential decay. However, it sometimes took the form of a stretched exponential. The analysis of the tail lifetimes is fairly straightforward. Initially, the period of time over which the remaining luminescence dropped to a value of e^{-1} times its initial value was used. This worked well when the tail was exponential in form but not well when it was a stretched exponential. Finally a standard method was adopted that involved integrating the entire tail and determining what the time constant of an exponential function with the same initial intensity would have to be in order to give the same integrated luminescence. This "exponential form factor" gave results with a much smaller distribution by taking into account the whole of the tail, not just its beginning.

The average primary lifetimes of the UV/blue and green bands of UV/blue, green, and hybrid samples, both before and after annealing, are shown in Figure 8-23. The corresponding average secondary lifetimes are shown in Figure 8-24 and the corresponding average tail lifetimes are shown in Figure 8-25. Figures 8-26 shows the average contributions of the primary, secondary, and tail PL of the UV/blue band

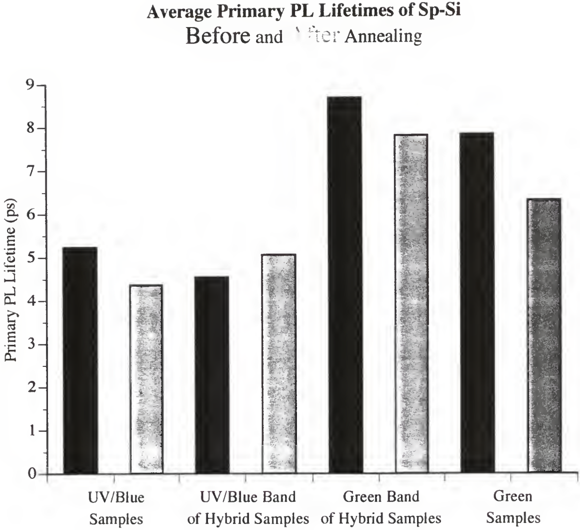

Figure 8-23: Average exponential lifetimes of the primary PL processes in several sp-Si samples. Black and gray bars indicate before and after annealing, respectively.

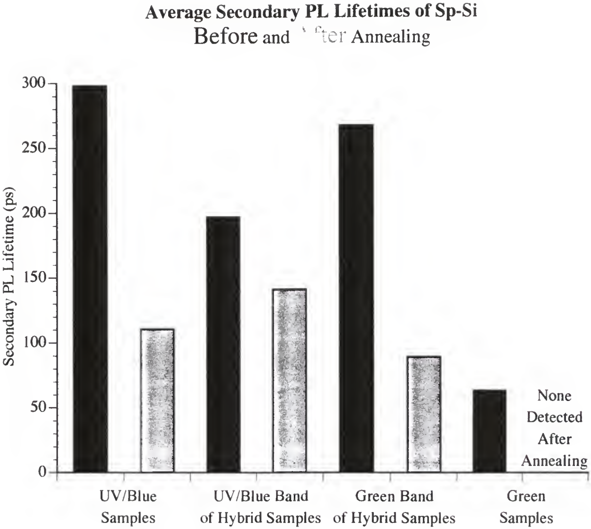

Figure 8-24: Average exponential lifetimes of the secondary PL processes in several sp-Si samples. Black and gray bars indicate before and after annealing, respectively.

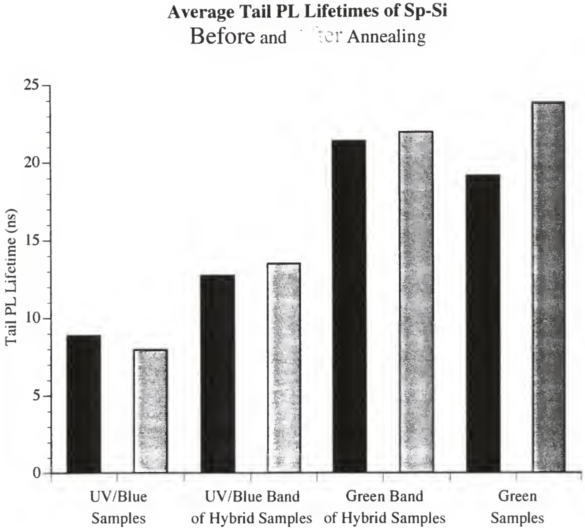

Figure 8-25: Average exponential lifetimes of the tail PL process in several sp-Si samples. Black and gray bars indicate before and after annealing, respectively.

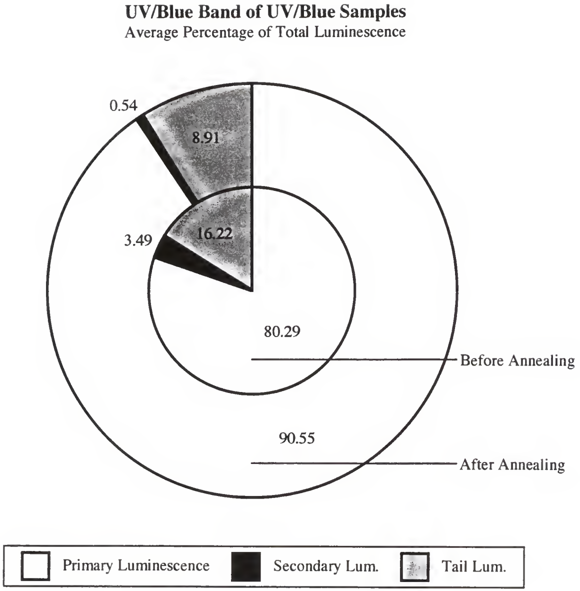

Figure 8-26: Average contribution of primary, secondary, and tail PL processes for the UV/blue band of a UV/blue sample measured both before and after annealing. White, black, and gray indicate primary, secondary, and tail contributions, respectively. Numerical percentages are indicated on the figure.

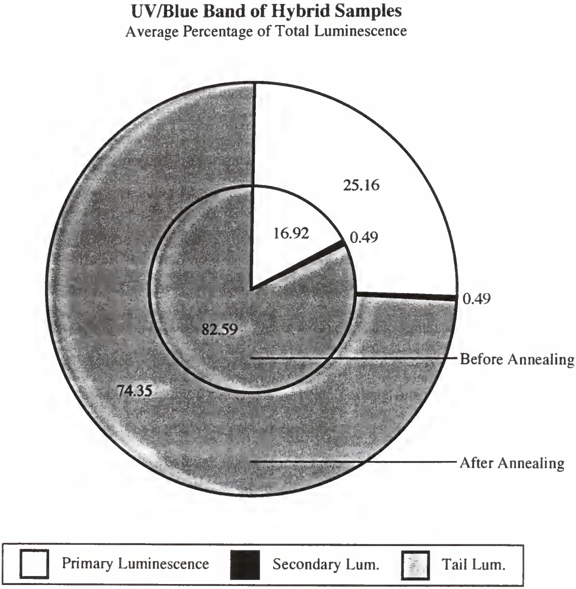

Figure 8-27: Average contribution of primary, secondary, and tail PL processes for the UV/blue band of a hybrid sample measured both before and after annealing. White, black, and gray indicate primary, secondary, and tail contributions, respectively. Numerical percentages are indicated on the figure.

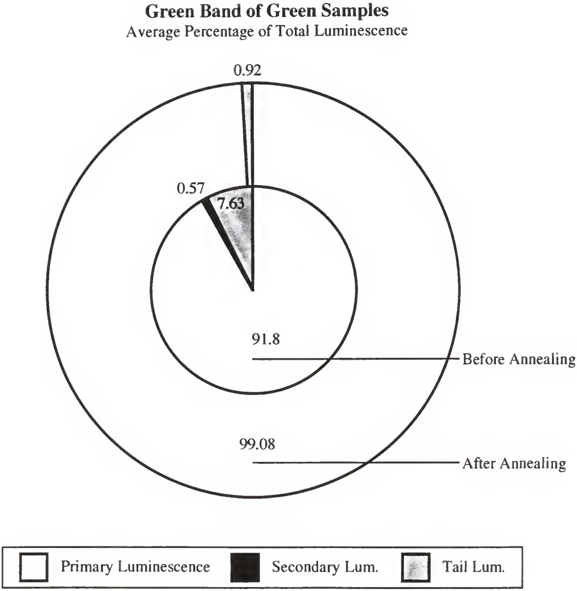

Figure 8-28: Average contribution of primary, secondary, and tail PL processes for the green band of a green sample measured both before and after annealing. White, black, and gray indicate primary, secondary, and tail contributions, respectively. Numerical percentages are indicated on the figure.

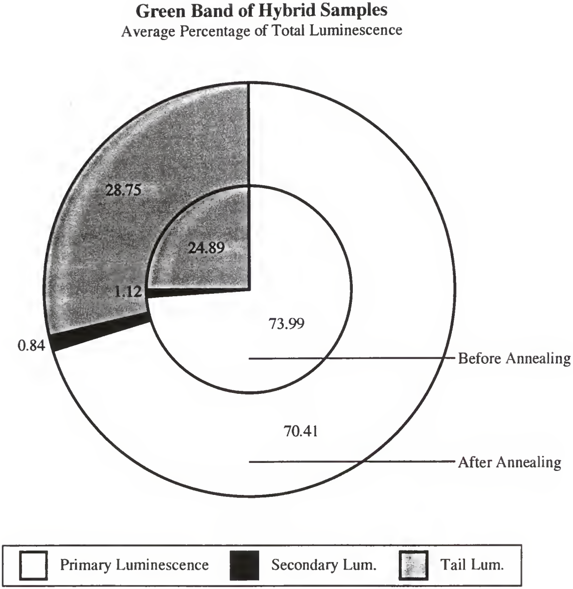

Figure 8-29: Average contribution of primary, secondary, and tail PL processes for the green band of a hybrid sample measured both before and after annealing. White, black, and gray indicate primary, secondary, and tail contributions, respectively. Numerical percentages are indicated on the figure.

of the UV/blue sample to the total luminescence. The inner circle represents the luminescence before annealing and the outer ring represents the luminescence after annealing. White, black, and gray areas on the figure represent the contributions of the primary, secondary, and tail processes. Numerical percentages are also indicated on the figure. Figures 8-27 through 8-29 indicate the corresponding averages for the UV/blue band of hybrid samples, the green band of green samples, and the green band of hybrid samples, respectively.

Discussion of time-resolved results

The primary time constants for the UV/blue bands of both the UV/blue and hybrid samples are constantly near 5 ps. The green bands for the green and hybrid samples have primary time constants that are consistently near 8 ps. These time constants are not significantly affected by annealing. The secondary time constants vary greatly from 50 - 300 ps with no apparent correlation to the color of the luminescence. These time constants are greatly reduced by annealing. The tail time constants are in the range of 9 - 12 ns for the UV/blue bands and 19 - 21 ns for the green bands. These are not significantly affected by annealing.

The proportions are very interesting. For the UV/blue band of the UV/blue samples, the secondary process accounts for about 4% of the luminescence and this contribution is reduced by 85% after annealing. The tail accounts for about 16% of the PL and annealing cuts this in half. The UV/blue band of the hybrid sample is much different. Secondary processes account for about 1/2% of the PL and are unaffected by annealing. The tail accounts for 83% of the PL and is cut by 10% by annealing. The differences are stunning. The vast majority of the UV/blue PL occurs on the sub-10 picosecond time scale when only the blue band is present. When the green band is also exhibited by the same sample, they vast majority of the UV/blue PL occurs on the 10 nanosecond time scale.

The green band is fairly similar. For the green band of the green samples, the secondary process accounts for about 1/2% of the PL. This is eliminated by annealing. The tail accounts for about 8% of the PL and this is cut by almost 90% with annealing. However, for the green band of the hybrid sample, the secondary process accounts for about 1% of the PL (reduced by 25% by annealing) and the tail process accounts for about 29% of the PL (reduced by almost 15% by annealing). While the primary luminescence is still dominant for the green band, the presence of the UV/blue band appears to almost quadruple the relative tail contribution of the green PL. When both PL bands are strong in a sample, the overall speed of both is substantially reduced.

Remarkably, there is no change in the peak locations or spectral shapes of either band when both are present. It is highly unlikely that six distinct PL mechanisms spanning over three orders of magnitude of time constants, yet all having similar efficiency, could be responsible for the same two types of emission. There appears to be one unique radiative mechanism for each band. The secondary and tail contributions must originate from carriers being temporarily intercepted by shorter and longer-lived traps, respectively. These traps eventually empty into the primary radiative pathway. The shorter lived traps appear somewhat less stable and more susceptible to annealing, as would be expected. The emission wavelength and efficiency is determined by the primary mechanism, while the apparent time constant is determined by the emptying of these traps, which becomes the rate limiting step.

The apparent speed of the radiative process might actually be closer to the fastest of the true speed of the radiative process or the speed of the non-radiative process. The former appears to be the case here. If the latter were true, one would expect an initially low efficiency with a large increase in the PL intensity and an increase in the apparent time constant of the primary PL process with annealing and passivation of competing non-radiative mechanisms. The intensity changes little and the primary lifetime is actually slightly reduced with annealing. For the PL to be both very fast and intense, the emission mechanism itself must be very fast. The primary PL processes are, in fact, as fast as they appear to be.

Spark-Processed Germanium

TRPL measurements were conducted on the sp-Ge samples used in Chapter 7. These were processed in mixtures of UHP N_2 and UHP O_2 ranging from pure O_2 to 95% N_2. The primary, secondary, and tail PL lifetimes are shown in Figure 8-30 as a function of the nitrogen concentration of the processing ambient. Blue squares, green circles, and red triangles indicate the primary, secondary, and tail PL, respectively. Unfilled symbols represent the blue band and filled symbols represent the green band. There are no strong trends seen in the data. There may be somewhat longer primary and shorter secondary and tail time constants for nitrogen concentrations near 50%, but it does not stand out.

Figure 8-31 shows the relative contributions of the primary, secondary, and tail PL processes for sp-Ge as a function of nitrogen concentration. The color assignments are the same as in the previous figure. Note the split vertical axis. There are no strong trends in the data with the exception of one 50% N_2 sample with a very large secondary contribution and a correspondingly smaller primary contribution. In general, there appears to be a somewhat smaller primary contribution below 70% nitrogen and a smaller secondary contribution at and above 70%.

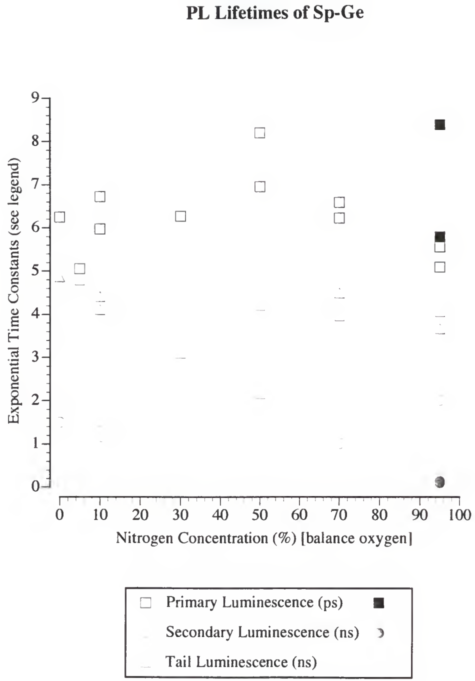

Figure 8-30: Exponential lifetimes of the primary, secondary, and tail PL processes for spark-processed germanium as a function of nitrogen concentration. Blue squares, green circles, and red triangles indicate the primary, secondary, and tail PL, respectively. Unfilled symbols represent the blue band and filled symbols represent the green band.

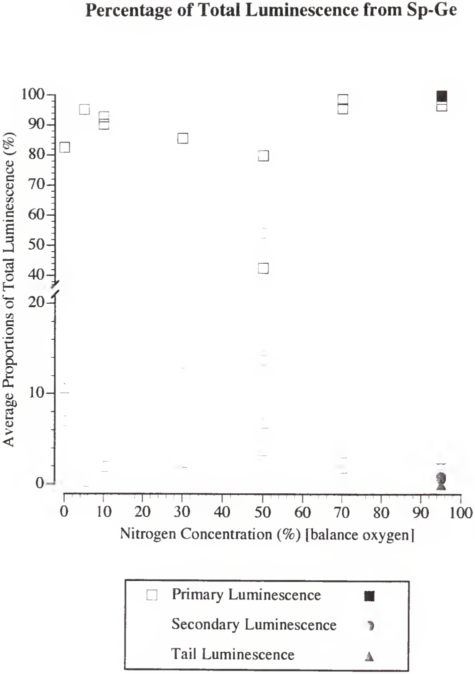

Figure 8-31: Contributions of the primary, secondary, and tail PL processes for spark-processed germanium as a function of nitrogen concentration. Blue squares, green circles, and red triangles indicate the primary, secondary, and tail PL, respectively. Unfilled symbols represent the blue band and filled symbols represent the green band. Note the split vertical axis.

These measurements have not revealed any major trends. While the intensity is strongly affected, the temporal characteristics of the blue PL band appear to be similar regardless of nitrogen concentration. There are only data available for the green peak at 95% N_2, so no comparisons can be made except to note that the green peak has time constants and contributions similar to those of the blue peak.

Several Spark-Processed Elements

Experimental procedure and results

TRPL measurements were performed on a number of spark-processed elements. The heated Stage II samples from the second section of Chapter 7 were used. The PL from these samples was compared to the UV/blue band of the stage III UV/blue sp-Si samples, the green band of the Stage III green sp-Si samples, the blue band of the 70% N_2 Stage III sp-Ge samples, and the green band of the 95% N_2 Stage III sp-Ge samples. In all cases when multiple samples were available, the average lifetimes and contributions were used.

Figure 8-32 shows the primary PL lifetimes for several spark-processed elements. Included in the figure are the UV/blue band of sp-Si, the green band of sp-Si, the blue band of sp-Ge, the green band of sp-Ge, the yellow band of sp-Al (measured at 580 nm), the red band of sp-Ta (@ 650 nm), the blue band of sp-Ti (@ 520 nm), the IR band of sp-Ti (@ 860 nm), and the blue band of sp-Ni (@ 530 nm). In hindsight, the measurements on sp-Ni may have been taken too close to the frequency-doubled 532 nm peak of the 1064 nm Nd:YAG laser used in these experiments (see Chapter 4). The data for sp-Ni may not be accurate. The colors used in this figure correspond to the approximate location of the peaks of the various

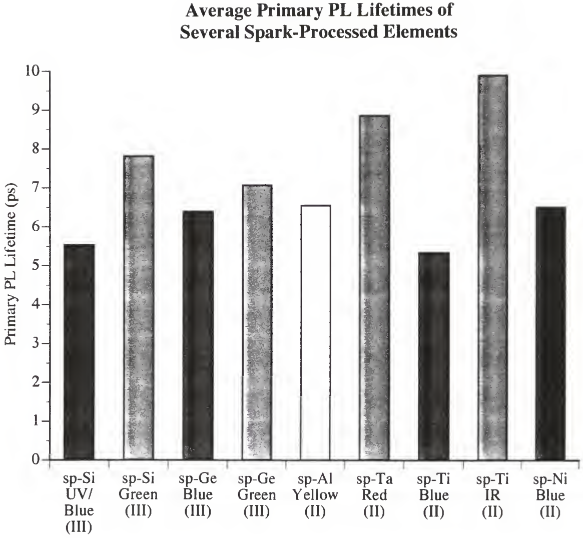

Figure 8-32: Average exponential lifetimes of the primary PL processes for several spark-processed elements. Colors indicate the approximate location of the PL peak of each sample on the visible spectrum. See text for details.

PL bands on the visible spectrum. The generation of samples (Stage II or III) is indicated on the figure. The corresponding lifetimes of the secondary and tail PL processes are shown in Figures 8-33 and 8-34, respectively.

Figure 8-35 shows the average contributions of the PL bands indicted in the previous three figures. The primary, secondary, and tail contributions are indicated by white, black, and gray regions on the figure. The vertical axis starts at 75%. Figure 8-36 shows all three PL lifetimes for both bands of the Stage III and heated Stage II sp-Ge samples. The shading assignments are the same as in the previous figure. Note the split vertical. Figure 8-37 shows the average contributions of the PL bands of both the Stage III and heated Stage II sp-Ge samples. The shading assignments are the same as in the previous two figures.

Analysis and discussion

Of the 9 bands presented in this section, 6 have been shown to be nitrogen-related (5 require nitrogen to exist at all), one has been shown to be unrelated to nitrogen (sp-Ni), and the nitrogen dependence of two are unknown (both belonging sp-Ti). The measurements on sp-Ni are suspect because they were measured at a wavelength close to 532 nm, which was used to pump the dye laser (see Chapter 4 for a description of the TRPL system).

The primary PL time constants for the many bands have little variation, all being between 5 and 10 ps. There is even less spread among those bands known to be nitrogen related. However, this is not the case with the secondary and tail time constants. The secondary lifetimes varied from 60 to 1,000 ps and the tail lifetimes varied from 4 to 19 ns. In addition, there is a significant distribution in the relative proportions of their contributions on these various time scales. The tail processes

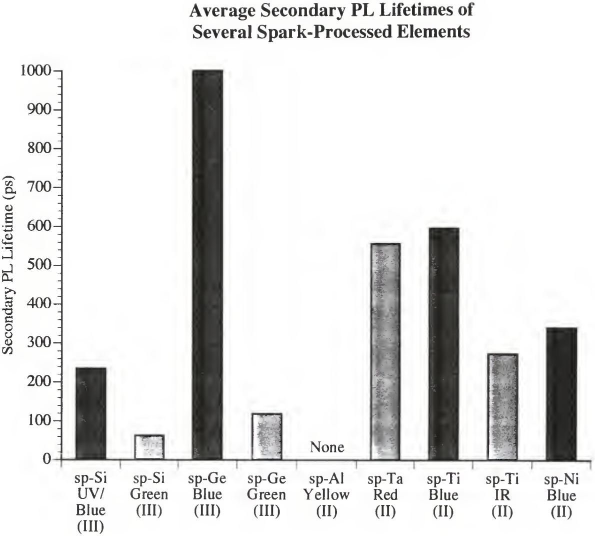

Figure 8-33: Average exponential lifetimes of the secondary PL processes for several spark-processed elements. Colors indicate the approximate location of the PL peak of each sample on the visible spectrum. See text for details.

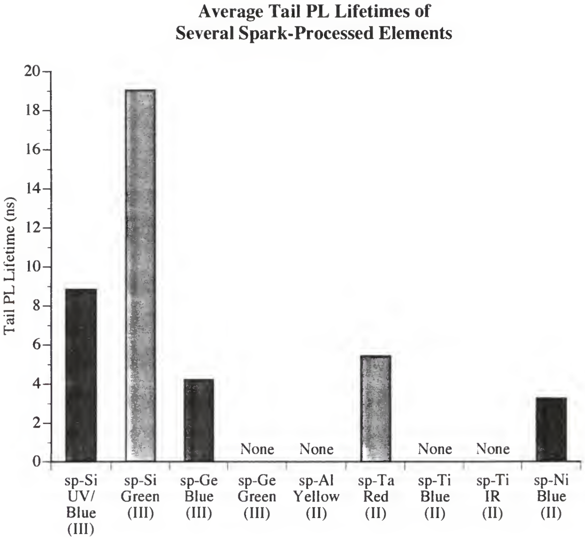

Figure 8-34: Average exponential lifetimes of the tail PL processes for several spark-processed elements. Colors indicate the approximate location of the PL peak of each sample on the visible spectrum. See text for details.

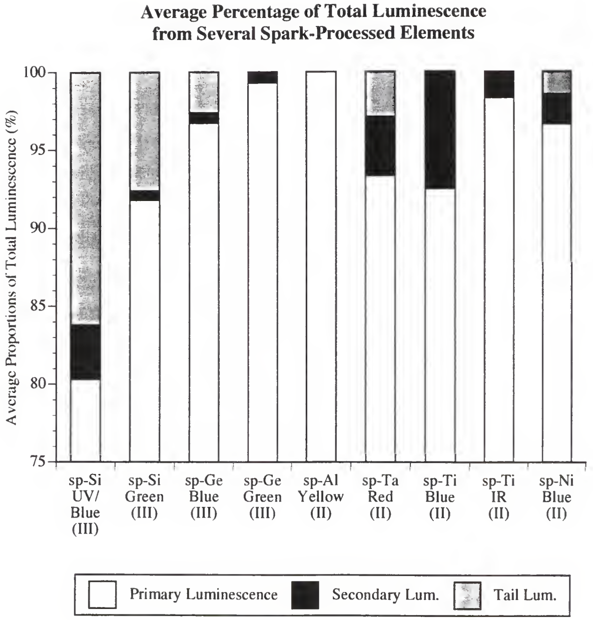

Figure 8-35: Average contributions of the primary, secondary, and tail PL processes for several spark-processed elements. White, black, and gray indicate the primary, secondary, and tail contributions, respectively. The vertical axis starts at 75%. See text for details.

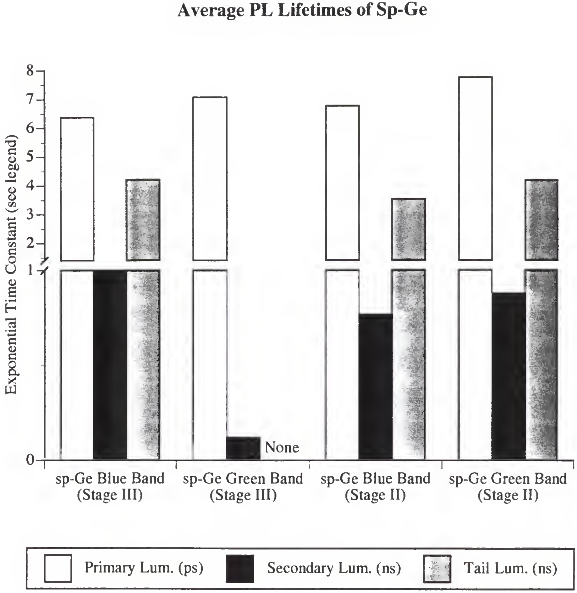

Figure 8-36: Average exponential lifetimes of the primary, secondary, and tail PL processes for Stage II and III spark-processed germanium. White, black, and gray indicate the primary, secondary, and tail lifetimes, respectively. Note the split vertical axis. See text for details.

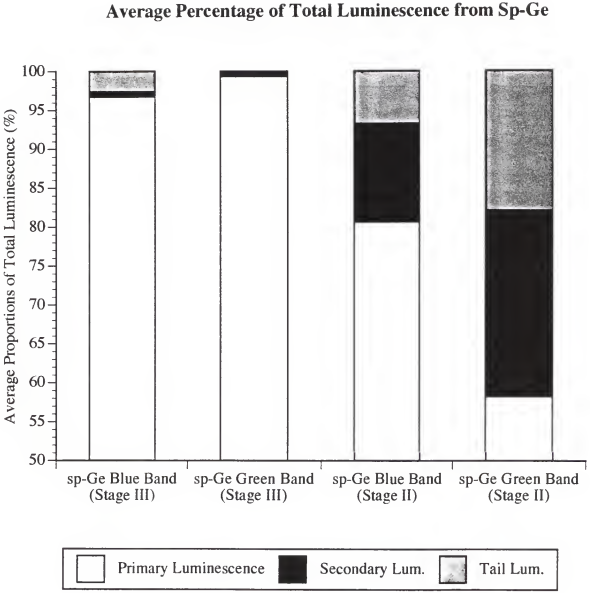

Figure 8-37: Average contributions of the primary, secondary, and tail PL processes for Stage II and III spark-processed germanium. White, black, and gray indicate the primary, secondary, and tail contributions, respectively. The vertical axis starts at 50%. See text for details.

contribute from 0% to 16% of the total PL for the various bands with a large amount of variation. These observations are consistent with a model based on similar emission mechanisms among these bands that have similar time constants but different wavelengths due to the chemical differences of the oxides. The large variation of time constants and contributions of the secondary and tail processes (previously attributed to short and long-lived traps) is expected, as such traps would be distinct from the primary PL mechanisms and material dependent.

While the time constants were similar for Stage III and heated Stage II sp-Ge samples, there was a large variation in their relative contributions to the total PL depending on how the samples were processed. The previous results for sp-Si also show large variations in the relative contributions as well as the secondary and tail, but not primary, lifetimes as a processing parameter (current) was changed. These observations are also consistent with such a model.

Spark-Processed Silicon Produced with Carbon Dioxide

Experimental procedure

TRPL measurements were conducted on sp-Si samples produced in mixtures of N_2 and CO_2 (see Chapter 5). The 100% CO_2 samples and 30% N_2/70% CO_2 samples from Chapter 5 were used. The former were measured at 550 nm and the latter were measured at 370 nm, 500 nm, and 600 nm. In addition, the visible afterglow of the pure CO_2 samples was measured at 0.2 second increments on the standard PL system used throughout this study for continuous-wave PL.

Experimental results

Figure 8-38 shows the lifetimes of the primary, secondary, and tail PL processes in sp-Si(N_2:CO_2). These contributions are indicated on the figure by white, black, and gray regions, respectively. Note the split vertical axis. Figure 8-39 indicates the relative contributions of these processes to the total luminescence. Figure 8-40 shows the overlapping intensity vs. time data for the afterglow of both pure CO_2 samples measured at 525 nm. The data from each sample were self normalized to 1 for continuous excitation. The afterglow at 0.2 seconds is seen to be more than 0.5% as intense as the continuous-wave PL and decays with lifetimes of 404 ms and 1.77 s. These are shown on the figure by thin and thick lines, respectively. Finally, Figure 8-41 shows the self normalized spectra of green sp-Si (thick line), a freshly produced sp-Si(CO_2) sample (thin line), and the same sample measured at a later date (dotted line). The bulk of the TRPL work was conducted several months after the samples were produced and the afterglow and final PL measurements yet another 6 months after this. It is unclear when the blue shift of the CO_2 samples occurred and whether it is a significant repeatable observation.

Analysis and discussion

The peak of the carbon-related band in the pure CO_2 samples was initially located near 550 nm and this wavelength was used to analyze the temporal behavior of the PL. The 30% N_2 (70% CO_2) sample combined this band with the standard green band, and a shoulder contributed by the UV/blue band (see Chapter 5). This sample was measured at 370 nm, 500 nm, and 600 nm. It was hoped that the 500 nm measurements would be more representative of the nitrogen-related green band and that the 600 nm measurements would be more representative of the carbon-related

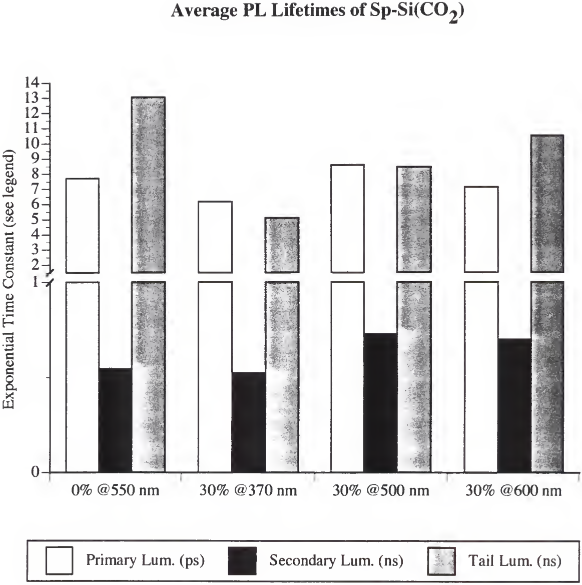

Figure 8-38: Average exponential lifetimes of the primary, secondary, and tail PL processes for spark-processed silicon processed in CO_2 or mixtures of N_2 and CO_2. White, black, and gray indicate the primary, secondary, and tail lifetimes, respectively. Nitrogen concentrations and measurement wavelengths are indicated on the figure. Note the split vertical axis. See text for details.

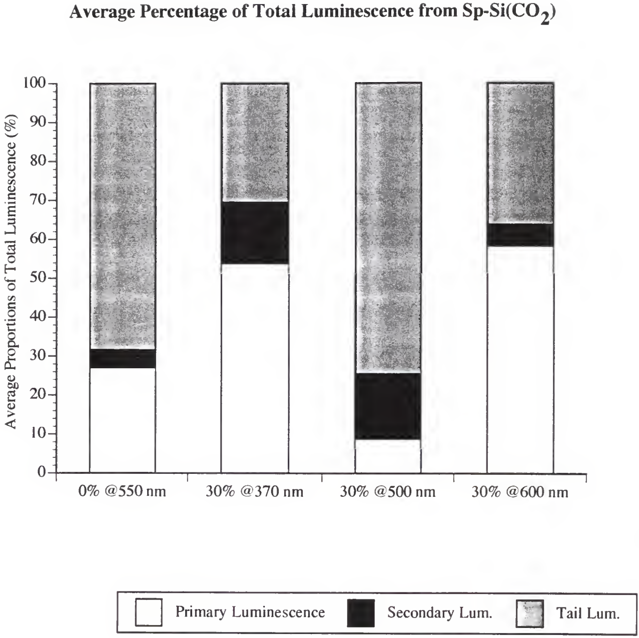

Figure 8-39: Average contributions of the primary, secondary, and tail PL for spark-processed silicon processed in CO_2 or mixtures of N_2 and CO_2. White, black, and gray indicate the primary, secondary, and tail contributions, respectively. Nitrogen concentrations and measurement wavelengths are indicated on the figure. See text for details.

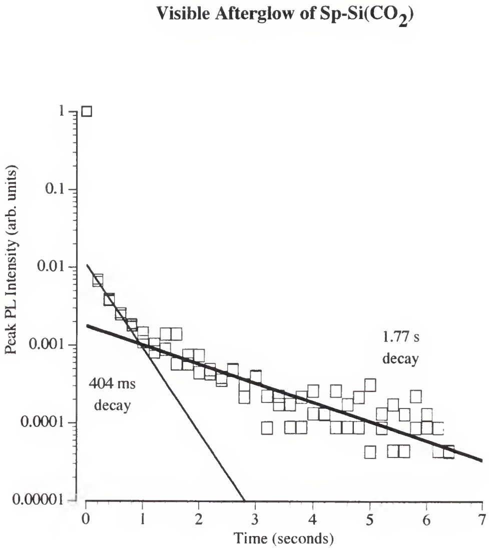

Figure 8-40: Decay of the visible afterglow of spark-processed silicon produced in CO_2. Calculated lifetimes are indicated on the figure. See text for details.

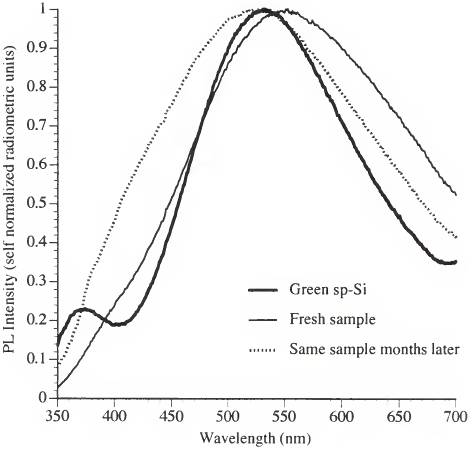

Figure 8-41: Self normalized PL spectra of green sp-Si (thick line), freshly prepared sp-Si(CO_2) (thin line), and the same sample measured several months later (dotted line). See text for details.

green band. This is in doubt given the apparent blue shift of the carbon-related band with time. The opposite appears to be true. Using the contributions of the pure CO_2 samples as a guide, we see that the majority of luminescence comes from tail processes. Actually, there was substantial afterglow on a time scale much longer than could be measured by the instrument. The contributions of the mixed gas sample at 600 nm most closely resemble this. Even when more than one band is present, such a large tail contribution is unexpected for the conventional nitrogen-related green band. The 600 nm contributions are much more similar to the green band of a hybrid sample as previously discussed. The blue shift of the carbon-related band is not well characterized, having been observed only once, but is appears to have occurred before the time resolved measurements were performed. The measurements of the mixed gas sample at 370 nm represent both the UV/blue band and a significant contribution from the broad carbon-related green band. Over half the PL occurs on the picosecond scale, which is somewhat intermediate between what has been observed from conventional UV/blue and hybrid samples. This is difficult to interpret, but is probably more related to the UV/blue band than the carbon-related green band.

While the relative contributions vary greatly, there is surprisingly little variation in the time constants observed at all wavelengths. The time constants at 370 nm were somewhat shorter as would be expected giving the contribution of the UV/blue band. The other time constants are similar to those of the conventional green band of sp-Si. The carbon-related green band appears to be similar to the nitrogen-related green band as far as the primary process is concerned, but there also appear to be carbon-related traps introduced when spark processing is conducted in carboniferous gasses. These traps appear to also effect the nitrogen-related luminescence.

The time resolved measurements were not able to resolve contributions on very large time scales. The tail was observed to have two components close to half a second and 2 seconds. There may very well be undiscovered contributions in the large range between nanoseconds and milliseconds. The time-integrated contribution of these very long lived components is huge and accounts for the overwhelming majority of the luminescence. It is about 200 times less intense than the continuous-wave PL but lasts 100,000,000 times as long as even the tail processes. These components may be due to very long-lived traps as well, but there is not enough evidence to determine this.

CHAPTER 9
RESULTS: MISCELLANEOUS

A number of qualitative observations were made which have not yet been presented. In addition, the results of some interesting experiments can be presented quite succinctly, without the need for figures. Finally, there were some "negative" or scientifically uninteresting results. These are all presented in this chapter in no particular order under the headings of useful results, interesting results, and uninteresting results.

Useful Results

Quantum Efficiency

As discussed in Chapter 3, quantum efficiencies for the PL of sp-Si of 5 to 10% have been claimed based on side-by-side comparisons of sp-Si with PS samples provided by other researchers. This approach assumes that the claimed quantum efficiencies for PS are correct. The first direct measurement of the quantum efficiency was performed on a predominantly green sample (70% N_2, 1.0 μs, 10 kHz, 40 mA). Spark-processing in 95% to 97% N_2 is known to create a green sample almost 5 times as bright as a typical sample, see Figure 5-38. In addition, annealing at high temperatures may further double or triple the luminescence. Also, samples sparked in dry gases may not have the benefit of -OH surface saturation in closed pores as discussed for humid air-sparked samples in Chapter 3.

The sample was placed on the sample stage but the collection optics were used to focus the gathered light on a calibrated wide-spectrum light power meter rather than the entrance slit of the monochromator. The power of the gathered light was measured with and without the long-pass filter to determine how much visible light was emitted from the silicon and how much UV light was being diffusely scattered off the sample. Both numbers were multiplied by a constant to account for the difference between the light-gathering solid angle of the optics and the whole hemisphere of emission. In addition, each number was divided by 0.96 for each air-to-glass or glass-to-air interface in the collection optics between the sample and the point of calibration. Finally, the power of the beam at the sample and the spectral reflection of the beam leaving the sample were measured with the power meter. The power efficiency was determined by dividing the emitted power by the beam power less the power of the spectral and diffuse reflections of the beam. The power efficiency was then converted to quantum efficiency.

After careful alignment and optimization, the low-end limit of the external quantum efficiency was determined to be approximately 1/3%. Any error in the measurements would make the optical alignment less than ideal, so the true value may be slightly higher but not lower. This may be as high as 1 or 2% for the brightest samples, possibly more with annealing or boiling. Based on geometric considerations alone, at least half of the emitted light does not leave the sample. Due to the scattering properties of porous materials, and the fact that the matrix is silicon-rich, most of the luminescence probably never escapes. The internal quantum efficiency could be very high. This is consistent with the interpretation of the time-resolved results in Chapter 8. As high currents and high nitrogen concentrations were never combined in an experiment, the author is only comfortable estimating external quantum efficiencies of about 1% for the brightest green-luminescing sp-Si samples, at this point in time. It would be worthwhile to attempt to maximize the luminescence of green and UV/blue samples under optimal conditions and redo these measurements, particularly with better-suited instruments (such as an integrating sphere).

This result does not validate the 5 to 10% figure in the literature, because the typical samples produced using Stage-II or III methods are much brighter than those produced by monitor sparking. These older numbers can only be overestimates. The origin of the error is probably an exaggeration of the claimed efficiencies of the PS samples to which sp-Si was compared.

Stark-Effect

A fine 0.10 mm wire was suspended horizontally approximately 0.25 mm from the surface of a Stage I monitor-sparked sample. The wire was centered over the sample and insulated from the substrate. The substrate was grounded and the wire was connected to a high voltage power supply. This non-contact method was used because heating from an injected current might be confused with field quenching in some types of systems. The sample was mounted on the PL stage in such a way that a focused 325 nm excitation beam struck the area under the wire at a small angle from the surface. The collection optics of the PL system were likewise focused on the area of the sample directly under the wire, but from the other side. The UV/blue peak PL intensity was monitored continuously as the voltage between the sample and the wire was slowly increased. There was no change in the intensity from zero volts to the breakdown potential of air (approximately 2,000 V/mm). Had a Stark-effect been present, there certainly would have been a decrease in the PL as discussed in Chapter

3. The lack of any Stark-effect quenching casts doubt on a quantum confinement model.

Influence of Ethanol

One well-known property of porous silicon (PS), is the effect that ethanol has on the PL. Very small concentrations of ethanol vapors are known to destroy the luminescent properties of conventional red-luminescing PS. This is attributed to the modification of surface states essential for the luminescence. In contrast, ethanol vapors have no visible effect on sp-Si. However, sp-Si soaked in ethanol experiences a reversible loss of about one third of the UV/blue PL intensity. When the ethanol evaporates, the PL completely recovers. This lends support to the hypothesis that the PL of sp-Si is a bulk, not surface, phenomenon.

PL in Different Ambients

A Stage II sample prepared under fairly standard conditions (7.5 kV, 10 kHz, 1.0 μs, 1.00 mm gap, and approximately 35 mA) was placed in a vacuum chamber having a quartz window. The PL spectrum was measured in air, UHP N_2, UHP O_2, vacuum, and air again. The samples were exposed to vacuum for several minutes between each gas as the chamber was evacuated and back-filled. No substantial difference could be observed in the peak intensity, peak location, or shape of the PL spectrum. Exposure to vacuum or the nature of the ambient present during the PL measurement appears to have no influence on the resulting PL. This is further evidence that the PL of sp-Si is insensitive to surface chemistry.

Interesting Results

Oxides of Nitrogen

As previously mentioned, spark processing in humid air in a closed chamber creates nitric acid, which attacks the chamber. Sparking in mixtures of UHP N_2 and UHP O_2 without moisture creates a dark brown gas in the chamber. This increases with increasing processing time and is most prominent at near equal ratios of N_2 and O_2. This gas has a very strong odor. Once noticed, provisions were made to pump the gas to a fume hood before opening the chamber.

The known oxides of nitrogen are: nitrous oxide (N_2O) or "laughing gas", which is stable, relatively non-toxic, and clear, nitric oxide (NO), which is unstable, toxic, and clear, nitrogen dioxide (NO_2), which is unstable, toxic, and brown, dinitrogen pentoxide (N_2O_5), which is unstable, toxic, and red, and nitrogen trioxide (NO_3), which is stable, harmless, and blue. Nitric oxide and nitrogen dioxide have historically been produced by electric sparks. The former is formed first and additional ionization produces the latter. Dinitrogen pentoxide is produced by the spontaneous dimerization of nitrogen dioxide.

The author believes that the dark brown gas visible in the chamber is a mixture of nitrogen dioxide and dinitrogen pentoxide. By necessity, nitric oxide must also be present. This is essentially smog. These compounds are visible in ppm concentrations and, thus, are probably not present in high enough concentrations to substantially alter the chemistry of spark-processing compared to the non-enclosed process.

Transmission Measurements

There has been some attention given to optical gain by diffuse scattering in random or porous media. This phenomenon is known as super radiance and is characterized by a nonlinear emission intensity vs. excitation power curve (this was seen to be linear for sp-Si in Chapter 8) and the onset of semi-transparency at the threshold excitation power for gain. The porous material from a Stage I monitor-sparked sample was scraped from a sample and placed on a glass slide in a very thin layer. The transmitted light was checked for nonlinearities with power variations for both 325 nm (10 W/cm) light and 488 nm (1.6 kW/cm) light, but none were found. There is no evidence of super radiance in sp-Si.

Uninteresting Results

Laser Ablation and Redeposition

The author performed some work on electroluminescence (EL) of sp-Si and this is covered in Appendix A. One of the major impediments to the creation of a practical EL device is the porous and anisotropic nature of the matrix itself. Several attempts were made to transfer the matrix material onto a substrate to form a thin film. A pulsed CO_2 laser was used to ablate the surface of a Stage II monitor-sparked sample under vacuum. A good plume of ejected material could be observed. The material refused to "stick" to a clean silicon substrate, with and without the native oxide, as well as a clean silica (quartz) substrate. The available chamber was not equipped to heat or cool the target and no further attempts were made.

Inert Gases

It was suspected that the addition of an inert gas to the spark chamber might modify the properties of the spark, such as the impact velocity of ions. It was hoped that a less porous and more uniform surface modification might be possible. Before adding oxygen to the mixture, a large amount of work was done with mixtures of nitrogen and helium or argon. The only clear result was that the weak PL of the material produced is similar to that of the green band of conventional sp-Si, but it is unstable. In some cases the intensity increased with laser and air exposure and in others it decreased. Both are believed to be due to a sub-optimal amount of oxidation in the porous material. The PL was either unstable when there was not enough of a protective oxide layer or, as the samples continued to oxidize when exposed to air, it became more intense.

The large amount of data and graphs produced are not interesting enough to warrant inclusion in this work. The experiments with oxygen, nitrogen, and an inert gas were never performed due to the lack of insight gained from these preliminary experiments.

CHAPTER 10
FURTHER DISCUSSION

Final Word on Quantum Dots

At first glance, it appeared that the oxygen-incorporated quantum dot model proposed by Filonov [Fil98] might be able to explain some of the behavior of the UV/blue band of sp-Si. As discussed in Chapter 3, Filonov modeled the optical properties of a symmetrical and energetically favorable silicon quantum dot; specifically the hydrogen terminated 14-Si cluster ($Si_{14}H_{24}$). The addition of bridging oxygen atoms to the structure resulted in a red-shift of the optical absorption and emission energies of the quantum dot. The Stokes shift of these $Si_{14}H_{24}O_x$ quantum dots was nearly constant. It appeared that the dependence of the peak emission energy of UV/blue sp-Si on the excitation energy might be explained by a distribution of these structures.

Filonov's calculations indicated that the structure could not accommodate more than 10 oxygen atoms and still behave like a silicon quantum dot. The relationship between the excitation and emission energies of this model is shown in Figure 10-1a (represented by a thick line). The molecular formulae of the extreme limits of this model corresponding to $Si_{14}H_{24}$ and $Si_{14}O_{10}H_{24}$ are also indicated on the figure as circles. The empirical emission vs. excitation data for the UV/blue band of sp-Si is also shown in Figure 10-1a (squares and a thin line). The two lines lie very close to one another. However, the trend for the UV/blue goes well beyond the limits of the quantum dot model in the higher energy direction and could be extended in the

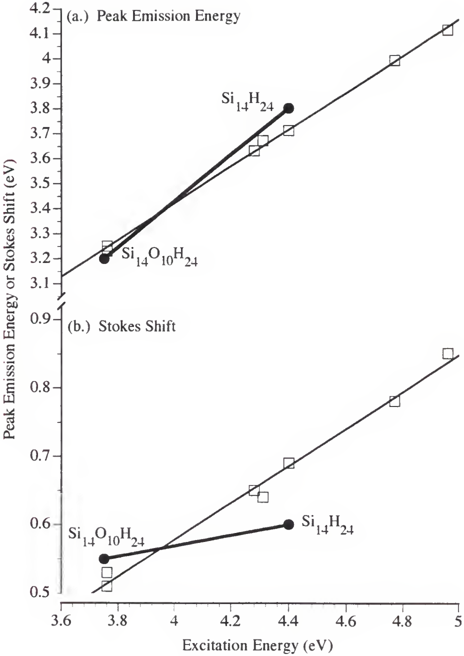

Figure 10-1: Comparison of the peak emission energy (a.) and Stokes shift (b.) of the UV/blue band of sp-Si (squares and thin lines) and the oxygen-incorporated quantum dot model of Filonov (circles and thick lines) as a function of excitation energy. The molecular formulae of the extreme limits of the model are indicated. The model cannot account for the UV/blue band of sp-Si, see text.

lower energy direction had those measurements been taken. While the 14-Si structure cannot account for this entire range, could a superposition of different quantum dots do so?

According to Filonov, the nearly constant Stokes shift is a consequence of a quantum dot's ability to physically relax because Coulomb interactions are not screened as in the bulk material. In the absence of strain, the majority of the Stokes shift of a quantum dot derives from the binding energy of the quantum confined exciton. This is a general principle, which should apply to other configurations besides Si_{14}. The Stokes shifts of the model and the UV/blue band of sp-Si are shown in Figure 10-1b. Here the differences between the two are clearly visible. The UV/blue band of sp-Si does not exhibit a near constant Stokes shift, but has a proportional Stokes shift of more that 1/4 eV per eV. This is evidence that the PL center interacts strongly with the lattice (or amorphous matrix) and is not consistent with a quantum dot interpretation.

The literature discussed in Chapter 3 indicates that room-temperature Stark effect quenching should occur in quantum systems. The total lack of Stark effect quenching described in Chapter 9 and the variable Stokes shift described above are substantial additions to the body of evidence against a quantum confinement interpretation of the PL of sp-Si.

Integrating Results from Multiple Chapters

Overview

Further discussion is necessary at this point to draw conclusions based on information presented in more than one chapter. This is not a summary as issues that have been previously determined are not included. Pertinent facts, quotations, results, inferences, and conclusions of the literature review and experimental chapters are summarized in the list below and indexed for the convenience of the reader. Reference citations have been made in the individual chapters and are not repeated here.

3a.) The line emission of Eu is broadened into a 200 nm wide band in sp-Si:Eu due to inhomogeneous broadening from the disordered ligand-field. This indicates that a distribution of states is not needed to explain the broad bands of sp-Si.

3b.) A partially reversible magnetic field quenching effect has been observed for the UV/blue peak of sp-Si but not the green peak. This is evidence that different states are involved.

3c.) Hsu observed the formation of nanoscale TiC:Ti particles produced by spark erosion of Ti in an organic solvent. Particles 5-50 nm in diameter were attributed to a vapor-phase reaction followed by rapid solidification, while 5-20 μm particles were attributed to solidification from the liquid phase.

3d.) Transitions with strong carrier-phonon coupling are associated with inhomogeneously broadened emission bands.

3e.) Self-trapping is expected to occur in all highly polar compounds, including most oxides, due to their strong carrier-phonon coupling. It has been observed in MgO, CaO, SrO, ZnO, BeO, and Al_2O_3.

3f.) The self-trapped exciton (STE) is associated with a large strain-inducing volume change of about one SiO_2 molecular volume per defect.

3g.) The majority of the volume change of the STE is due to its peroxy-radical linkage. Molecular-orbital calculations by Edwards indicate that this configuration is more stable than the single oxygen atom bridge in highly disordered silica.

3h.) The STE is known to transfer charge to other defects in silica.

3i.) The lifetime of the strained STE in amorphous SiO_2 is approximately 10 μs.

3j.) The STE in amorphous silica has two absorption bands at 5.30 eV and 4.20 eV with full-width half-maximum (FWHM) values of 0.78 eV and 1.16 eV, respectively. The STE is a very strong absorber of UV light.

3k.) The STE is metastable. It is chemically and electronically stable but is not favored elastically.

3l.) It was postulated that plastic (near-molten) silica could accommodate a STE without strain. If the silica were rapidly quenched within the lifetime of the STE, the driving force for the destruction of the STE could be eliminated or even reversed. The "frozen" STE would have a metastable energy barrier of at least 7.6 eV. Excitation by 4.2 or 5.3 eV radiation would not be sufficient to overcome this barrier. The charge transfer mechanism, already present, would become the dominant pathway for the return of the STE to its ground state.

3m.) Deep donors or acceptors with the majority of their binding energy coming from lattice, not electrostatic, potentials exhibit strong phonon coupling and very large capture cross sections.

3n.) Deep states act as traps or recombination centers depending on the lifetime of the radiative process. The carrier-phonon coupling is stronger for deeper states. This decreases the lifetime by allowing the excited state to shed excess momentum through a multi-phonon cascade. Such thermalization is a femtosecond process. In general, shallow states are more likely to act as traps and deep states as recombination centers.

3o.) The formation of N-N pair luminescing centers in GaP has been observed to have a nonlinear dependence on nitrogen concentration.

3p.) Very complicated processes involving four or more defects are routinely observed in luminescent materials. Such clusters have lower potential energies than isolated centers. In addition, charge transfer among defects is commonly observed.

5a.) Independent of current or thermal considerations, the UV/blue PL of sp-Si has a strong temporal dependence. It is optimized when the pulse width is in the range of 1.0 - 1.5 μs and the period is approximately 100 μs (10 kHz frequency).

5b.) The instantaneous spark intensity is the dominant factor for the green PL of sp-Si, although it appears that temporal factors are also significant. This is the PL intensity is most influenced by that portion of the current that occurs on a timescale of less than 1 μs. Also, the PL appears to be maximized when the period is approximately 67 μs (15 kHz frequency).

5c.) The fact that the conditions favorable for the formation of the green band of sp-Si result in a decrease in the intensity of the UV/blue band may indicate that the two processes are competitive. This might involve competition for available nitrogen during spark-processing or competition over excited charge carriers during the PL measurement.

5d.) Sp-Si produced in carbon dioxide exhibits a broad green PL band that exhibits at a different peak wavelength than the green band of conventional sp-Si. This band and the two nitrogen-related bands all have similar intensities. This may be the result of a common absorption mechanism combined with charge transfer to more than one emission mechanism, none of which are the efficiency-limiting step.

6a.) The microstructure of sp-Si is dominated by three-fold interfaces and 120° angles. This hexagonal structure is strong evidence that surface tension plays a significant part in the formation of the porous material.

7a.) Materials that exhibit substantial PL after spark processing generally have a chemically stable oxide with a high heat of formation. These materials have strong bonds with an ionic character and band-gaps wide enough to host states with visible optical transitions.

7b.) The blue band of sp-Ge is similar to the UV/blue band of sp-Si as they both reach a maximum intensity in the vicinity of 70% – 80% N_2. Both bands begin decreasing in intensity long before oxygen becomes scarce in the processing ambient. These two bands differ in that the green band of sp-Gi exists without the presence of nitrogen in the processing ambient. However, the addition of nitrogen increases the intensity of this band 6 or 7 times.

7c.) With the conditions used to produce sp-Ge, the green band exists only at very high nitrogen concentrations. However, it looses intensity when oxygen becomes scarce as do the green band of sp-Si and the bands of sp-Al and sp-Ta.

7d.) The peak PL intensity of the green band of sp-Si, as well as the bands of sp-Al and sp-Ta, have an exponential (highly nonlinear) dependence on the nitrogen concentration of the ambient present during spark-processing. The exponential constants are similar for these three bands. This is strong evidence of a common mechanism.

8a.) Stage I thermal measurements indicate that the UV/blue band of sp-Si has about a 40% greater disorder from inhomogeneous ligand-field broadening than three deep states in conventional amorphous oxides.

8b.) Near equal characteristic disorder temperatures for the UV/blue and green bands of sp-Si indicate equivalent amounts of ligand-field broadening.

8c.) Near equal activation energies for thermal quenching above half of an electron-volt for both the UV/blue and green bands of sp-Si indicate a spatial carrier localization for the excited state of less than 7 angstroms. This is on the order of the molecular size of amorphous SiO_2.

8d.) The thermal behavior of the UV/blue band of sp-Si is similar to that of the blue band of sp-Ge. The thermal behavior of the green band of sp-Si is similar to that of the green band of sp-Ge.

8e.) Both the UV/blue and green bands of sp-Si increase in intensity and shift towards shorter wavelengths as the excitation wavelength decreases. These trends are very linear with different slopes for each band. The intensity increase for the UV/blue band is larger than for the green.

8f.) The excitation spectra of the green band of sp-Si was found to be closely matched by model of a STE with a 40% greater disorder from inhomogeneous ligand-field broadening than the STE in normal amorphous silica.

8g.) The PL of sp-Si and other elements naturally falls into three timescales. These include primary luminescence in the range of 5-10 ps, a small secondary contribution on the order of 1 ns, and a "tail" contribution on the order of 10 ns. The secondary and tail contributions are attributed to shorter and longer-lived traps, respectively.

8h.) In sp-Si, when both PL bands are strong in the same sample, the contribution of the tail luminescence increases dramatically.

8i.) All six bands of sp-Si, sp-Ge, sp-Al, and sp-Ta, which have been shown to be highly nitrogen-related, have primary PL processes with similar time constants. The time constants and contributions of the secondary and tail PL vary greatly, as would be expected of traps in different oxides.

8j.) The primary PL processes of the nitrogen and carbon-related green bands in sp-Si are similar in lifetime, intensity, and dependence on nitrogen or carbon concentration. In addition, the addition of carbon appears to create much longer-lived traps that modify the temporal behavior of all three bands.

Analysis

Evidence of melting

SEM images of sp-Si indicate the role of surface tension in the formation of the matrix (6a.). Evidence of a rapidly quenched liquid phase was also found by Hsu during spark erosion of titanium (3c.). There is compelling evidence that at some point in the formation of spark-processed materials, the oxide matrix is molten. The most likely time for this would be during the spark pulse, as very high local temperatures would be required.

Absorption mechanism

It was observed in Chapter 8 that the PLE spectrum for the green band of sp-Si is closely matched by a model for a self-trapped exciton (STE) in silica broadened an additional 40% by an inhomogeneous ligand field (8f. and 3j.) Attempts to obtain meaningful PLE spectra of the UV/blue band were unsuccessful for reasons discussed in Chapter 8. Other measurements revealed that the characteristic disorder temperature of the UV/blue band of sp-Si was about 40% greater than those of the inhomogeneous ligand-field broadened deep centers in conventionally formed oxides (8a.). In fact, the near equal characteristic disorder temperatures for both bands in sp-Si indicate similar amounts of ligand-field broadening (8b.). Since the characteristic temperature is a measurement of how the excited state is thermally depopulated, the implication is that the excited state, which leads to both species of PL, is the same and that it is similar to the STE in silica.

The STE consists of a reorganization of the bonds of the silica backbone associated with a strain-inducing volume change on the order of one silica molecular volume per defect (3f.). Near equal values for the activation energies of thermal quenching above half an electron-volt for the both bands of sp-Si indicate carrier localization of the excited state within 7 Å (8c.) This is on the order of the molecular size of silica, which is also the scale of the STE. The normal STE is silica is a metastable state, which is chemically and electronically stable but not favored elastically (3k.). It was postulated that a STE formed in molten or near-molten silica would not experience strain, as the plastic matrix would simply adjust to the volume change (3l.). If the molten material were rapidly quenched within the lifetime of the STE, a stable version of the STE may be formed. Theoretical work by Edwards indicates that the part of the STE responsible for the large volume change, specifically the peroxy-radical linkage, would actually be more stable than the single oxygen atom bridge in highly disordered silica (3g.) Certainly, sp-Si appears to be highly disordered (3a., 8a., and 8b.)

Are the observed temporal factors for the creation of the PL bands of sp-Si consistent with the lifetime of the STE? The answer is clearly yes. The reported 10 μs lifetime of the STE in amorphous silica is about one order of magnitude longer than the preferred pulse width, and about one order of magnitude shorter than the preferred period, for the formation of both bands (3i., 5a, and 5b.). If the duration of the electrical discharge were substantially longer than 1 μs, the molten material may not be able to cool enough to solidify within the lifetime of a STE formed by the same electrical discharge. In addition, if the period between pulses were not substantially longer than the lifetime of the STE, the temperature may not fall enough before the next discharge, resulting is a higher baseline temperature, which may not offer sufficient quenching. It has been observed that current occurring at a longer timescale than 1 μs has little effect on the PL intensity and that PL intensity decreases rapidly at higher-than-optimal frequencies.

Emission mechanisms

Several properties of the emission mechanisms of the PL bands of sp-Si are known. The two nitrogen-related bands, as well as the carbon-related band, have a number of similarities and differences. They all have similar primary PL lifetimes on the sub-10 ps scale (8g.), similar efficiencies (5d.), and are all broad bands. These are characteristic traits of deep defect centers, also known as activator centers (3d., 3m., and 3n.).

There are also several differences between the two nitrogen-related bands. This indicates that these are not the result of two emission levels of the same center, but originate from different centers. The magnetic behavior (3b.), the degree of nitrogen dependence, and the effect of annealing differ between the two bands. In addition, the optimal processing parameters differ for the two bands.

The UV/blue emission band apparently originates from an unknown nitrogen-related defect, which may be as simple as an atomic nitrogen center. The exponential dependence of the green band on the nitrogen concentration is reminiscent of the nonlinear threshold-like formation of the N-N nearest neighbor pair center in GaP (3o.). The formation of such defect clusters is common (3p.) and would explain the strong nonlinear nitrogen dependence of the green band. In addition, the increase in the intensity of the green band with very high annealing temperatures, which is accompanied by a small decrease in the UV/blue emission, and the observation that high processing temperatures favor the green band at the expense of the UV/blue band (3q.) can both be explained by the increased diffusivity of nitrogen in silica at greatly elevated temperatures (in excess of 800 °C). The formation of nitrogen pairs or clusters would certainly deplete the population of simpler nitrogen centers. There is no way of knowing the exact nature of this center, but the evidence indicates the involvement of two or more nitrogen atoms per center.

Charge transfer

The excited STE has a propensity to engage in charge transfer in order to return to its ground state (3h.) There is evidence of charge transfer in sp-Si by both direct processes and through intermediate traps (8g.). When both PL bands are present, charge transfer to traps is more likely (8h.) Each species of PL center apparently decreases the carrier capture cross section of the other, possibly due to a dipole-dipole interaction. Whatever the mechanism, the likelihood that the carrier will find its way to a trap state increases by default.

There is also evidence that this charge transfer is a resonant process. The large increase in the intensity of the UV/blue band as the excitation wavelength is decreased (Figures 8-18 and 8-19) indicates that excitation of the main 5.3 eV band of the STE (or its low energy tail) is more likely to result in UV/blue emission than excitation of the 4.2 eV satellite band. In fact, samples that exhibit primarily green PL with 325 nm (3.82 eV) excitation, become primarily blue as the excitation wavelength is decreased toward 250 nm (4.96 eV). It can be surmised that the excited state of the UV/blue center lies at an energy in the silica band-gap closer to the 5.3 eV level of the STE and that the green center lies at an energy closer to the 4.2

eV level of the STE. In addition, there is also evidence of resonant behavior within each PL band. Not only do both peaks increase in intensity and shift towards shorter wavelengths as the excitation wavelength is decreases (8e.) but the converse is also true. When the emission is measured at a higher energy, the higher energy portion of the PLE spectrum becomes more intense, see Figure 8-21. The different proportions of the shifts seen for the two bands (Figure 8-20) likely arise from the different FWHF of the two absorption bands of the PLE and the much higher absorption of the 5.3 eV band compared to the 4.2 eV band.

The proposed model

The following model is consistant with all of the observed properties of the UV/blue and green bands. As the STE is an alteration of the bonding of the silica background, the ground state of the STE would lie near the valence band edge. The energy separation is approximately 2.8 eV for the normal metastable STE and would be less for a strain-relieved STE. Two nitrogen-related donor activator centers have ground states that lie within a few eV of the valence band edge. The exact nature of these centers is unknown, but the center for the green band has more than one nitrogen atom per center, as was previously discussed. When an electron is promoted to one of the anti-bonding levels of the STE by absorption, the hole in the valence band is free to move about the silica backbone and is transferred to one of these centers, either directly or by way of a trap. The excess electron in the anti-bonding orbital of the STE is transferred to a higher energy level of the ionized center due to the inherently high capture cross section of activator centers, which is further enhanced by Coulomb attraction. The electron and hole recombine radiatively at the activator center emitting either UV/blue or green light, depending on which center happened to be involved.

Applicability to other elements

How well does this model fit the observed PL from other spark-processed elements? To answer this question we should discuss both the absorption (STE) and emission (deep nitrogen-related center) portions of the model separately.

Self-trapping is expected to occur in all highly polar compounds, including most oxides, due to their strong carrier-phonon coupling. It has been observed in several common oxides (3e.). It is a general observation that materials, which exhibit substantial PL after spark-processing, generally have high oxide heats of formation, indicative of strong ionic bonds (7a.). In the absence of PLE measurements of other spark-processed materials, all that can be said is that an absorption mechanism based on self-trapping is possible and plausible. Interestingly, these materials with strong ionic bonds also have band-gaps wide enough to host states with visible optical transitions, which brings us to the second part of the model (emission mechanisms).

The strong candidate elements (based on the criteria outlined in Chapter 7) all exhibited PL bands that were strongly nitrogen related. The primary time constants of these bands were very similar (8g., 8i.). These time-resolved data also support the concept of charge transfer. The fact that the non nitrogen-related band of sp-Ni is also very fast may be evidence that the center involved also has a small spatial extent and a high degree of carrier-phonon coupling (also reflected by its spectral width) despite its different origin. There were concerns about the accuracy of the measurements on sp-Ni for reasons discussed in Chapter 8. The existence of a carbon-related center in sp-Si (8j.) with a primary lifetime and efficiency similar to those of the nitrogen-related centers indicates that the charge transfer process is flexible and can stimulate a variety of emission centers. The extrinsic decay process of the conventional metastable silica STE described in Chapter 3, with its characteristic 2.5 eV (500 nm) emission, is another example of this flexibility.

The green bands of sp-Si and sp-Ge (7c.) and the bands of sp-Al and sp-Ta (7d.) have several properties in common including a nonlinear dependence on nitrogen concentration (numerically similar in the case of sp-Si, sp-Al, and sp-Ta) and a preference for very high nitrogen concentrations. The thermal behavior of both the green bands of sp-Si and sp-Ge, as well as their UV/blue and blue bands are very similar. The relationship between intensity and nitrogen concentration is also very similar for the UV/blue and blue bands of these two materials. This includes both the optimal N_2 concentration and the decrease at very high N_2 concentration (7b.). The only significant difference is that the blue band of sp-Ge does exist, to some extent, without the addition of nitrogen to the processing ambient. There is not enough information to completely understand this, but it appears that there is a defect center in sp-Ge, which can be made much more efficient with the addition of nitrogen without experiencing a significant change in the energy of its optical transition. The identical spectral shape is not unexpected as band width is dominated by ligand-field broadening in these highly disordered spark-processed materials. In this instance, nitrogen may be passivating non-radiative pathways, as it has been known to do (see Chapter 3).

All the evidence points to the possibility and plausibility that the proposed model for the PL bands of sp-Si has analogues for other spark-processed materials, with respect to both absorption and emission mechanisms.

CHAPTER 11
SUMMARY AND CONCLUSIONS

This study was undertaken in order to better understand the nature of spark-processed silicon (sp-Si) and its luminescent properties. This endeavor consisted of two main thrusts: correlating the properties of sp-Si to the conditions under which it was produced, and attempting to glean an understanding of the mechanisms responsible for the luminescence of sp-Si. Both of these goals have been met. The major results and conclusions are listed below:

1.) Sp-Si consists of a porous silicon-rich silica matrix with embedded silicon nanoparticles. These nanoparticles are not responsible for the observed PL.

2.) The microstructure of sp-Si is dominated by three-fold interfaces and 120° angles on several scales. These are attributed to surface tension effects resulting from rapid melting and resolidification. Clusters as small as 50 nm in diameter have been observed.

3.) Sp-Si exhibits two intense PL bands with peaks near 372 nm and 531 nm when excited by 325 nm laser light. These are known as the UV/blue and green bands, respectively.

4.) Existing literature on defects in silica cannot account for the PL bands of sp-Si.

5.) The PL of sp-Si is stable against degradation by UV light exposure, thermal annealing, and HF etching.

6.) The intensities of both PL bands of sp-Si increase linearly with the intensity of the excitation source for all power densities measured (up to approximately 14 W/cm^2). In addition, the spectral shape does not change with excitation power.

7.) The ratio of the peak intensity of the green band to the peak intensity of the UV/blue band increases exponentially with current. This effect is believed to be largely thermal in origin with higher processing temperatures favoring the formation of the green band.

8.) Both oxygen and nitrogen must be present in the processing ambient for sp-Si to exhibit the UV/blue and green PL bands.

9.) The intensity of both PL bands in sp-Si is strongly dependent on the presence of nitrogen in the processing ambient. The intensity of the UV/blue peak increases with increasing nitrogen concentration until approximately 70% to 80% N_2 at which point it saturates and begins to decrease. The intensity of the green peak increases exponentially with increasing nitrogen concentration until oxygen becomes scarce in the range of 97% to 99% N_2.

10.) Every elemental semiconductor and semi-metal (with the exception of selenium, which is too flammable to spark-process) exhibits PL as a result of spark-processing, as do a number of metals.

11.) In addition to the two PL bands of sp-Si, two PL bands of sp-Ge and PL bands of sp-Al and sp-Ta have all been shown to be strongly nitrogen-related. Among these, only the blue band of sp-Ge exists in the absence of nitrogen. However, the addition of nitrogen increases the intensity of this band by 6 or 7 times. Both the UV/blue band of sp-Si and the blue band of sp-Ge reach maximum intensities in the vicinity of 70% to 80% N_2, long before oxygen becomes scarce. As is the case for the green band of sp-Si, the bands of sp-Al and sp-Ta increase exponentially in intensity with increasing nitrogen concentration until very high concentrations are reached (above 95% N_2). The exponential constants for these three bands are similar and this is attributed to the existence of similar PL mechanisms.

12.) Both PL bands of sp-Si are thermally quenched and blue-shifted with increasing temperature above 20 K. The blue shift of the green peak saturates above 600 K.

13.) The activation energies for thermal quenching continue to increase well above room temperature approaching values in excess of half and electron-volt.

14.) Both PL bands in sp-Si increase in intensity and are blue-shifted when the excitation wavelength is decreased. These shifts are linear.

15.) The primary PL lifetimes of sp-Si are consistently near 5 ps for the VU/blue band and 8 ps for the green band. For every spark-processed element measured, the primary PL lifetimes are in the range of 5 to 10 ps.

16.) External quantum efficiencies of approximately 1% are obtainable for the brightest green samples produced in this study. Simultaneous optimization of several processing parameters may result in efficiencies of several percent.

17.) The strong UV absorption of sp-Si is attributed to a stable strain-relieved version of the self-trapped exciton (STE) in silica created by the rapid melting and solidification during spark-processing.

18.) The STE is believed to return to its ground state by transferring charge to nearby defect centers. This charge transfer is observed for the conventional STE in silica.

19.) The emission mechanisms are attributed to nitrogen-related deep defect centers for the UV/blue band of sp-Si and more complicated deep defects containing two or more nitrogen atoms per center for the green band.

20.) Analogues of these absorption and emission mechanisms are believed to exist in many of the other spark-processed elements, particularly those shown to have nitrogen-related PL.

CHAPTER 12
FUTURE WORK

While the major goals of this study have been realized, there are a number of loose ends. Foremost among these is the remarkable behavior of sp-As, which appears to be different than most other spark-processed materials. Unlike the PL of sp-Si, the PL of sp-As may very well be amenable to a quantum confinement explanation. Despite the extreme toxicity of the oxides of arsenic, further investigation may be worthwhile.

The microstructure of sp-Si should be more fully characterized. The apparent size invariance of the microstructure implies a fractal geometry. A direct measurement of the fractal dimension should be made. The effects of changes in the processing parameters on the microstructure of sp-Si should also be investigated.

A PLE-like spectrum for both the UV/blue and green bands of sp-Si should be constructed from numerous PL measurements taken at small wavelength increments. These should include, if possible, measurements well above 5.3 eV. This could verify that the STE is the common absorption mechanism for both bands of sp-Si. This analysis should also be conducted on other spark-processed materials to determine if the STE is a general absorption mechanism in these oxides as well. Other methods of producing strain-relieved stable STEs without spark-processing might be possible. One idea is the use of electron beam or vacuum UV irradiation during the rapid solidification of silica. The propensity of the STE to transfer charge to other defects might be combined with luminescent states other than those present in sp-Si. Finally, the theory could be tested by attempting to bleach the STE with UV radiation in excess of 7.6 eV.

More accurate efficiency measurements should be conducted with equipment appropriate for such determinations. Combinations of the many processing parameters explored in this study should be investigated to maximize the efficiency of both PL bands.

More time-resolved PL work should be done at different temperatures. This could verify the charge transfer and trapping explanation of the three timescales observed for the PL of spark-processed materials. The influence of processing pressure on the formation of sp-Si needs to be reinvestigated using Stage III methods. The IR PL of sp-Ti should be investigated and the behavior of sp-Si(CO_2) should be verified. The minor inconsistency regarding the lack of a N-related FTIR signal from sp-Si(N_2) should also be resolved.

Finally, Stage III methods should be used to properly measure the current and pulse width of Stage I monitor-sparking so that the large amount of previous literature can be better understood in light of the results of this study.

APPENDIX A
ELECTROLUMINESCENCE AND PHOTOCONDUCTIVITY

A significant amount of work was conducted on electroluminescence (EL) of sp-Si with mixed results. No efficient long-lasting EL devices were produced. Much more interesting results were obtained while studying the photoconductivity of sp-Si.

Electroluminescence

Direct-Current Electroluminescent Devices

Electrical potentials of several hundred volts were applied to the Stage I sp-Si samples between the silicon substrate (the cathode) and a thin tungsten wire pressed to the center of porous region (the anode). Most samples exhibited an intense violet luminescence with potentials between 550 and 580 V. The current varied from about 0.9 mA to 2.0 mA, depending on the sample. Chang was simultaneously performing similar experiments on sp-Si samples with a thin (50 nm) gold layer, while the author used uncoated samples [Cha94]. The results were similar. Figure A-1 shows the EL spectrum of sp-Si (b) compared to the emission of a low-pressure N_2 plasma (a) [Cha94, Koz93]. This EL spectrum was measured by the author on an uncoated bare sample with a 1.0 mA current.

Due to the similarity between the EL of sp-Si and the line spectrum of N_2 plasma, a similar EL device was constructed in a bell jar. The violet EL was initially observed with air in the chamber. When the air was evacuated with a mechanical vacuum pump, the EL disappeared. When the jar was filled with He, the EL was red

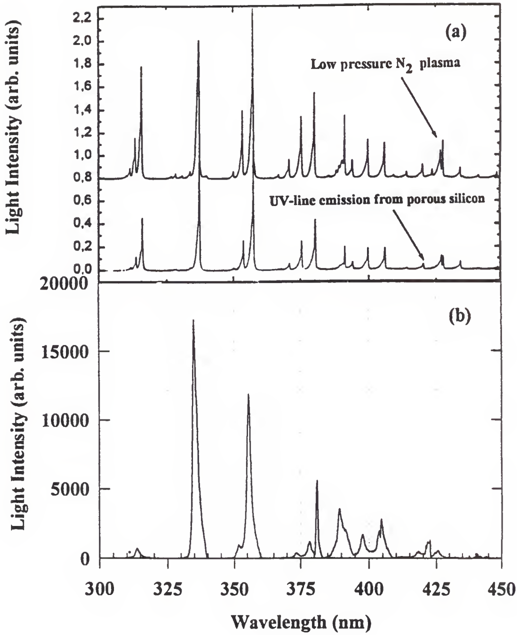

Figure A-1: Comparison of two emission sources:

(a) The emission spectrum of low-pressure N_2 plasma. Adapted from Koz93.

(b) The EL emission spectrum of sp-Si with DC excitation, see text. Figure adapted from Cha94 with permission (originally based on measurements by the author.)

in color. This disappeared with evacuation and, when the sample was again exposed to air, the violet EL returned. The EL was attributed to the creation of ions of the ambient gas due to local field enhancement from the nanoscale features. The devices were not particularly stable and lasted for only a few minutes.

The author tried to improve the devices by coating sp-Si samples with indium or gallium followed by a 20 hour anneal at 900 °C. The indium appeared to oxidize on the surface. The gallium diffused throughout the sample, filling pores with metal in the process. The EL occurred in the gallium-treated samples at potentials as low as 50 V.

Frame et al. created microdischarge cavities in silicon and observed intense visible and UV radiation when an electrical potential was applied in the presence of Ne or N_2 gas [Fra97]. This is the same general phenomenon as that observed by Chang and the author.

Thin-Film AC EL Devices

Thirty-six thin-film EL devices were prepared by sparking three different silicon wafers under different conditions. Each wafer was spark-processed at twelve different locations on its surface. Sparking was done with a stream of cool air directed on the area being processed, in stagnant air, and in stagnant air with the wafer heated to 350 °C. Spark times of 15, 30, 60, and 120 minutes were used for each condition on each wafer. The Si wafers were p-type $3.8 - 5.5 \times 10^{15}$ cm^{-3} B-doped <100> 625 μm thick, n-type $2.0 - 4.0 \times 10^{12}$ cm^{-3} Ph-doped <111> 400 μm thick, and n-type 1.6×10^{19} cm^{-3} As-doped <111> 350 μm thick. The heated samples were prepared first to avoid annealing the other samples.

The wafers were sent to Planar Systems in Beaverton, Oregon and coated with a 2 μm siliconoxynitride dielectric film covered by a conductive transparent indium-tin oxide (ITO) film. Upon their return, the samples were diced with a diamond band saw and tested for short circuits. Bottom contacts were prepared with indium and top contacts were prepared with conductive silver-bearing paint. The samples were excited with a variable 1,000 V 60 Hz sinusoidal power supply. Faint green EL started between 600 - 800 V for most samples and occurred about 5 - 10 V short of the breakdown potential. The luminescence did not last for more than a few minutes at a time. It was so faint that only half the people asked to observe it in a darkroom were able to see it. It was noticed that those who could see it were generally younger than those who could not. As the EL did not last long enough to allow sample alignment, no spectrum could be taken. The author speculates that a field-emission current of hot electrons flows among the nanoscale features. While this current may be enhanced by field-line concentration at these nanoscale features, it is probably related to solid state "tunneluminecence" (low-voltage cathodoluminescence), which has been observed for almost 40 years [Hil63]. The high capacitance of these thin film devices is believed to be the main cause of their inefficiency.

Thick Dielectric Oil AC EL Devices

With the assistance of Dr. Walco at Sandia National Laboratory, the author prepared several thick (low capacitance) devices. These consisted of a polished aluminum back contact coated with a potassium silicate insulting layer. Powder prepared by grinding the porous region of several sp-Si samples was placed on top of the silicate layer and covered with a dielectric oil (several different oils were used). The top contact was a glass slide covered with a thin film of ITO, with the ITO side facing the oil. The low capacitance of these thick devices allowed them to be driven at high frequency. A simple 10 kV 10 - 20 kHz power supply was used to excite the samples. The supply used feedback to drive the devices at their resonant frequencies. Blue, green, and red EL were observed to come from the sp-Si grains. This luminescence also occurred just below the onset of breakdown but, as the oil devices "healed" themselves after breakdown, it was easy to fine tune the potential to obtain significant luminescence. The author demonstrated this technique to Shidong Yu who prepared several similar samples, which were measured by the author. Figure A-2 shows the EL spectrum of one such sample (a) and the spectrum of the cathodoluminescence (CL) of sp-Si (b), which exhibits the same emission bands. This CL spectrum in not unique to sp-Si but occurs in all silica. Again, the EL is believed to originate from a hot-electron field emission current. However, the EL is a property of the silica component of sp-Si and is not related to the PL discussed in this work.

Photoconductivity

The author discovered a unique photoconductive effect in sp-Si. This is fully documented in the following reference:

> Stora, M. E. and Hummel, R. E., "Novel photoconductive effect in spark-processed silicon with metal contacts", *Materials Science and Engineering B* **69-70**, 188 (2000).
>
> The abstract of this paper is reproduced below:
>
> Spark-processed silicon (sp-Si) has been shown to display strong photoluminescence in the UV/blue and green spectral ranges. Furthermore, ferromagnetic behavior, electroluminescence, and cathodoluminescence have been reported. The present contribution reports on a novel photoconductive effect, which has been observed in

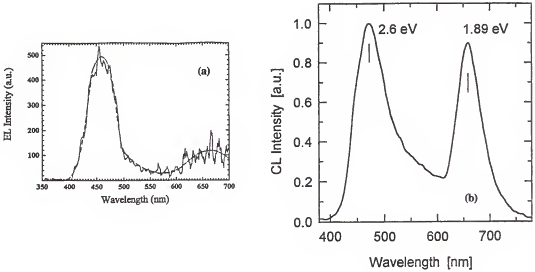

Figure A-2: Comparison of the EL and CL of sp-Si:

(a) Emission spectrum of a dielectric oil-based sp-Si EL device.

(b) CL emission spectrum of sp-Si.

Adapted from Hum01 with permission.

> a simple device made from sp-Si. A symmetric device consisting of two metal contacts on sp-Si increases its electrical conductivity dramatically when the junction of the sp-Si and the anode contact is illuminated with UV or visible light. However, its conductivity decreases when the sp-Si/cathode contact junction is illuminated. The magnitude of both effects is proportional to the intensity of the light source, and is dependent on the wavelength of the light. There is no significant change in conductivity when the bulk of the sp-Si is illuminated. This behavior is unique and strikingly different than existing devices such as p-n, p-i-n, and Schottky diodes, as well as photoconductive devices, which all show an increase in conductivity in both directions when illuminated.

The author proposed conducive mini-bands within the band gap of the amorphous matrix. This is not unprecedented. Papers by Dean [Dea70] and Mott, Davis, and Street [Mot75] support the existence of such mini-bands in disordered materials. It has since occurred to the author that a photovoltaic effect might be responsible for this behavior rather than the mechanism purposed in the paper. This should be investigated.

APPENDIX B
CALIBRATION OF THE PL SYSTEM

This appendix is intended to serve two purposes. Primarily, it is meant to be a set of instructions for the present colleagues of the author (and future members of the same research group) to follow to recalibrate the photoluminescence (PL) system used in this study should new equipment be added or major changes be made. Secondly, it is meant to be of benefit to others interested in research involving PL measurements as a general guide to some of the issues that may arise.

The equipment used to measure PL is discussed in detail in Chapter 4.

Calibration Issues

There are three major calibration issues that need to be addressed. These are the transmission of the optics, the characteristics of the grating, and the response of the detector. Using a known source, such as a quartz-tungsten-halogen (QTH) lamp, the second and third can be treated together as a "black box" as their properties are relatively constant and need only to be measured. It is the optics that are the cause of several complications. These complications fall into two areas: scattering or diffraction of light at very small slit openings, and chromatic aberrations coming from the light-gathering optics.

The problem with small slit openings is especially important, because QTH lamps are particularly bright, many orders of magnitude brighter than the types of samples usually encountered. Turning down the brightness of the QTH lamp is not an option if sufficient light in the blue and near UV is desired. If the calibration is not good for a whole range of slit openings, it is not useful. If a slit opening is smaller than the wavelength of light, that light will be scattered back from the slit. If the slit opening is on the order of the wavelength of light, diffraction will occur which can cause unpredictable transmission in the rest of the system. These problems were encountered in the course of this work. For the equipment in question, the apparent PL spectrum of a QTH lamp was unaffected for entrance slits at or larger than position #6 and for exit slits at or larger than position #17. For slits smaller than these, the sensitivity of the instrument is lower at longer wavelengths. Even at a fixed wavelength, the response of the inner slit is highly nonlinear. The outer slit has a fairly linear response above position #100 and the response below this is closely matched by a simple cubic relationship. In general, it is inadvisable to compare different samples measured at different slit openings.

Subsequently, the author discovered that the peak location of a spectrum changed with the size of the entrance slit. While investigating this, it was discovered that a similar thing happened depending on the sampling wavelength used to first align the sample and focus the optics. These were both found to be caused by chromatic aberrations in the lenses that collimate the light from the sample and focus it into the entrance slit of the monochromator at the appropriate acceptance angle.

At one point before the author began the bulk of his work, achromatic lenses had been used on the system. These were apparently replaced with quartz lenses when it became apparent that the near-UV transmittance of these lenses was very poor. After the chromatic aberration problem was recognized, the author considered the use of achromatic lenses. Air-gap quartz/LiF lenses designed for UV work are prohibitively expensive, so the original lenses were considered. The factory verified that the glasses used were not good in the UV, but that the main culprit was the epoxy used to join the two lens halves. The absorption of the epoxy might have been acceptable in the range of interest, except that an UV-activated hardener had been added. The author separated the lenses by soaking them in acetone for a couple of days, and attempted to put them together with no epoxy, and clamp them into the lens holders. Both humidity and dust were a problem, so the lenses were combined in a rapidly flowing stream of N_2. The curvatures of the lenses were so close that they seemed to bond to each other and required some force to separate. Unfortunately, the tolerances were so close that circular Fresnel patterns appeared. At this point, the author became aware of a better solution: when two non-achromatic lenses made from the same material are separated by a distance equal to the mean of their focal lengths, the chromatic aberrations of each lens are cancelled out [Möl88]. It was then verified that when these two lenses (10 cm and 5 cm focal lengths) were separated by 7.5 cm (center-to-center), the problems described above disappeared. The author constructed a fixture that allowed the first and second lenses to be moved together with a constant separation distance while determining the optimal location for the second lens. This lens was then secured in place by a set screw. Small adjustments in the position of the first lens can be made with a micrometer screw attached to the fixture. The center position of the screw is about 14 turns counter clockwise form all the way in, and this is used at the reference position. This setup keeps the separation distance between the lenses sufficiently close to the "achromatic condition". Most sample alignment must now be done with the sample stage and relative positions of the laser and monochromator, but once a good alignment is achieved, only tiny corrections are necessary for all samples of the same approximate thickness.

Measurements

The first step in calibrating the PL system is to select the configuration to be calibrated (the choice of gratings and filters). The second step is to measure the spectrum of a QTH lamp over the desired wavelength range. Several previous attempts to calibrate the system by the author and others were flawed because QTH lamps of very high wattage (often in housings with back reflectors that altered the spectrum) were used and were placed some distance away from the light gathering optics. To get a good calibration spectrum, a bare bulb at the exact sample position must be used. This necessitates a very low wattage bulb. The author used model 6318 10 W QTH bulbs from Oriel (3200 K color temperature) for these calibration measurements as well as a LAMBDA Model LT-802 regulated power supply set at 6.00 V. When the power supply was adequately warmed up, the supply potential varied by about +/- 0.01 V.

New bulbs should be burned-in for about 25 hours to stabilize. To prevent filament shock, the voltage should be ramped up and down over the course of a couple of minutes. Safety glasses with polymer lenses should be used when working with high-temp QTH bulbs since the near-UV output is significant.

After estimating the peak wavelength of the bulb's spectrum, set the monochromator at this wavelength and close all the slits completely. Slowly open the slits until some counts are present. For the time being, ignore the smallest allowed slit positions, as you will be working with one wavelength only. You will eventually put an iris between the bulb and the first lens, but if this is done before the optics are aligned, they will not be aligned correctly. Align the bulb and optics to maximize counts. You can use a strip of white paper to verify that the beam is indeed collimated between the first and second lens. You should also be able to see the image of the filament focused on the nearly closed entrance slit. Make sure you are imaging the filament on the entrance slit. Imaging the surface of the quartz bulb on the entrance slit will result in a local, but not global, maximum in counts. In addition, make sure that the center of the filament is imaged on the center of the slit, as there are small, but significant, differences in the temperature between the center and outer areas of a helical coil filament [Gib61].

Once the bulb is aligned, place a tiny iris between the lamp and the first lens. This iris must be perfectly aligned with the optical axis of the lens fixture and the bulb. This iris will allow you to open the entrance and exit slits of the monochromator to at least the minimum values. Determine the peak instrumental wavelength of the QTH bulb, set the counts at this wavelength to something near, but not over, saturation, and take your calibration spectrum. A long integration time of several seconds per data point is recommended. The author took spectra with the 330 nm and 630 nm blaze-wavelength gratings with the UV filter in place (since this is how the system is usually used) and additional spectra at short wavelengths with and without the filter using only the 330 nm blaze-wavelength grating (because it is somewhat more efficient at these wavelengths). From all these spectra, the author was able to create calibrations for the 330 nm grating with and without filter, and the 630 nm grating with and without filter. In addition, the author desired that the calibration for the two gratings be consistent with one another (equal calibrated counts for the same sample at any wavelength regardless of which grating is used). In order to do this, the author carefully measured the intensity at 480 nm (exactly halfway between 330 nm and 630 nm) with one grating in the system, carefully swapped gratings, and took a measurement with the other grating under the exact same conditions. Since the second grating could not be wavelength calibrated until after the measurement was taken, the second measurement was actually a small scan from about 470-490 nm. After the second grating was wavelength calibrated (using diffuse 325 nm laser radiation and finding the second-order line), the actual intensity at 480 nm was interpolated from the scan. The resulting sensitivity ratio for the two gratings was used to normalize the two calibration curves to one another.

Analysis

Once the spectra are gathered, the final step in generating the calibration curves is to analyze the data. The QTH bulb is not a true blackbody emitter. It is not even a good "graybody" emitter. Its spectral emissivity varies significantly in the visible range. See Larrabee for a detailed discussion of the spectral emissivity of tungsten [Lar59]. At 2800 K (the highest filament temperature for which the author could find good wavelength tabulated data), the emissivity varies from about 0.40 at 800 nm to about 0.46 at 400 nm [Dev54, Pre63]. This is a 15% difference, which must be taken into account. Most of the good data on the behavior of QTH bulbs are quite dated. Apparently, this subject was only an interesting area of scientific inquiry when such bulbs were new. Some early papers may state that the halogen gas in the bulb (usually iodine) absorbs a significant amount of light at some visible wavelengths [Stu64]. This is no longer true as much lower concentrations of halogen are used in modern bulbs.

The color temperature of the bulb should be measured carefully using a good spectrometer. The author used a Pritchard PR 880 from Photo Research. The average of several spectrometer readings was used. A pyrometer was not able to duplicate the results of the spectrometer with a sufficient degree of precision. The spectrometer will give a reading close to that of the hottest center part of the filament, which produces the most light. The actual temperature is best determined by looking up the color temperature vs. actual temperature on a published table [Lev68]. With the correct temperature, Planck's formula can be used to calculate the spectrum of the lamp [Dev54]. The other constants in the formula besides wavelength and temperature can be ignored, as relative, not absolute, brightness is all that is needed. Next, the spectrum obtained from Planck's formula is multiplied by the emissivity model (a linear interpolation for wavelengths between tabulated data is sufficient) to get the actual spectrum of the QTH bulb. The calibration factor at any given wavelength is just the number by which the measured spectrum must be multiplied in order to obtain the actual calculated spectrum. This is easily done on a spreadsheet program. The only potential pitfall here is that of units. Planck's formula generates radiometric units (units of power). If you are interested in quantum units (number of photons), you must multiply by wavelength. If you are interested in photopic (photometric) units, you must multiply the radiometric units by the International Standard Eye. In any case, the calibration is that curve, which when multiplied by the instrumental counts, gives the desired spectrum for the QTH bulb.

Results for the Equipment Used in this Study

The ratio of the instrumental intensities of the QTH bulb as measured with the 330 nm diffraction grating with and without the long-pass UV filter was used to calculate the transmission curve of the filter. Part of this curve is shown in Figure B-1. This curve does not saturate until well after 500 nm and, even at that point, about 4% of the light is reflected by the filter.

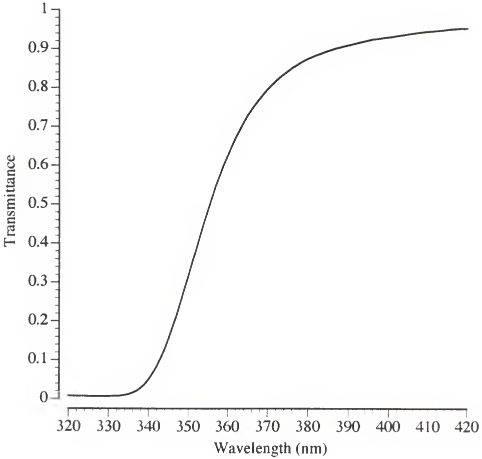

Figure B-1: Transmittance of long-pass filter used in PL system to eliminate 325 nm laser light. The curve does not saturate until well after 500 nm.

The calibration curves for the two gratings using radiometric units are shown in Figure B-2. The curves are normalized to 1 for the most efficient wavelength with the most efficient grating. The usable range of the gratings is defined as that range over which the correction factors change by less than one order of magnitude. In addition, the 330 nm blaze-wavelength grating experiences a large second-order discontinuity near 660 nm, limiting its useful range. The useful ranges were found to be about 345 - 660 nm for the 330 nm blaze-wavelength grating and 350 - 885 nm for the 630 nm blaze-wavelength grating. These calculations indicate that the 630 nm blaze-wavelength grating is the most useful one for the entire range of wavelengths. The real limitations of the system are the detector response limit near 890 nm and the limit imposed by the filter near 340 nm. The correction curve becomes asymptotic at both extremes. The differences between the two gratings near the lower limit are not significant compared to the filter. Only the 630 nm blaze-wavelength grating gives meaningful results all the way to the upper limit. As a rule of thumb, a diffraction grating can be expected to perform well in a wavelength range equivalent to 2/3 of the blaze wavelength to 5/3 of the blaze wavelength. Accordingly, the PL system used in this study would be best matched by a grating with a blaze-wavelength equal to about 525 nm. However, the 630 nm one works sufficiently well.

Figure B-3 shows the calibration curves for the 630 nm blaze-wavelength diffraction grating with the filter present using both radiometric and quantum units. Figure B-4 shows the same curves for the system without the filter. Clearly, if the filter is not needed to block 325 nm laser light (as in the case of measuring EL), the effective range of the system can be extended much further into the UV. In such a case, the reader would be advised to do the complete calibration measurements over the entire range without the filter, rather than with the filter as the author has done.

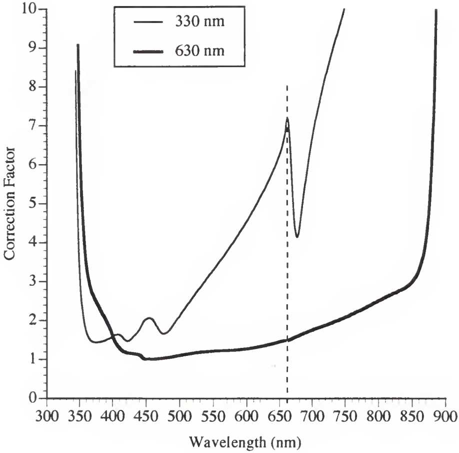

Figure B-2: Calibration curves for the 330 nm and 630 nm blaze-wavelength diffraction gratings with Filter using Radiometric units. The curves are normalized to 1 for the most efficient wavelength with the most efficient grating. The usable range is defined as that range over which the correction factors change by less than one order of magnitude. The 330 nm blaze-wavelength grating experiences a large second-order discontinuity near 660 nm (dotted line) limiting its useful range. Approximate useful ranges are:

330 nm blaze-wavelength grating: 345-660 nm
630 nm blaze-wavelength grating: 350-885 nm

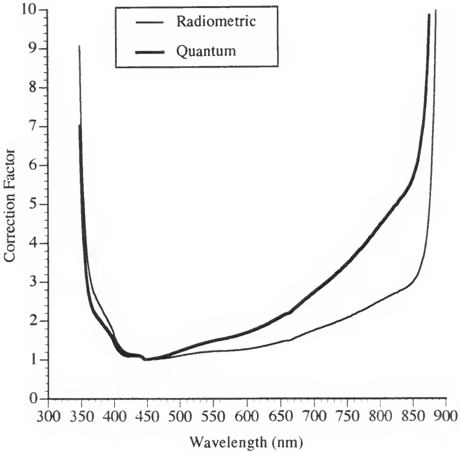

Figure B-3: Calibration curves for the 630 nm blaze-wavelength diffraction grating with Filter using Radiometric and Quantum units.

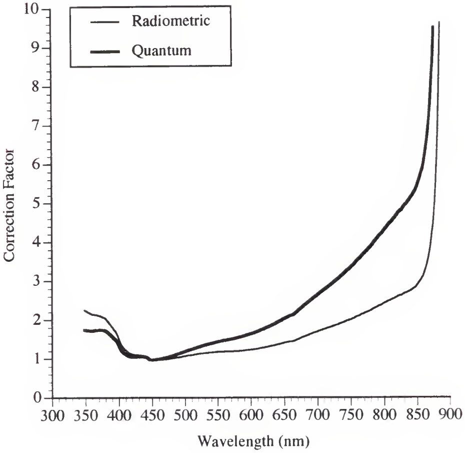

Figure B-4: Calibration curves for the 630 nm blaze-wavelength diffraction grating without filter using Radiometric and Quantum units.

Finally, Figure B-5 shows the calibration curve for the system with the filter present using photopic (photometric) units. It is normalized to 1 at 555 nm, as is the International Standard Eye [Ber76].

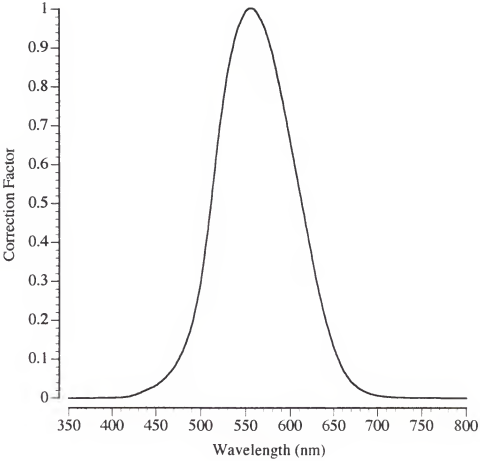

Figure B-5: Calibration curve for the 630 nm blaze-wavelength diffraction grating with filter using Photoptic (Photometric) units. The curve is normalized to 1 at 555 nm.

APPENDIX C
COMPUTER PROGRAMS

The author wrote a number of computer programs to help analyze large quantities of data. The programs are presented with a short description before each one.

These programs were written in Chipmunk BASIC v3.5.2b1 for the Apple Power Macintosh © Copyright 1997 by Ronald H. Nicholson, Jr. (rhn@nicholson.com), which is available at http://www.nicholson/rhn/basic/. This language was chosen because it is freeware, supports all traditional BASIC commands, is very fast (written in PowerPC native code), and has an efficient implementation of strings, arrays, and file I/O.

Programs to Analyze CWPL Data Files

These programs are used to manipulate data files created with ISA Spectralink software. These programs were used to analyze continuous-wave PL data files for this study.

Filename: fileconvert.bas

This program converts PC/DOS text files in the ISA Spectralink format to tab delimited Mac text files with wavelength and intensity in columns.

```
10 on error goto 240
20 clear
30 window 25,25,100,25
40 cls : print : print "Quick Spectrum Converter by
Michael E. Stora." : print
```

```
50 print "This program converts a Spectrum ASCII file
into two columns of tab-delimited text"
60 on error goto 240
70 input "Enter the file name of the file you wish to
convert (.txt): ",filename$
80 print : print "Converted filename will be:
";filename$+"-c.txt"
90 open filename$+".txt" for input as #1 : open
filename$+"-c.txt" for output as #2
100 input #1,a$
110 input #1,start
120 input #1,length
130 dim wavelength(length-1) : dim intensity(length-1)
140 input #1,a$
150 if a$ <> "-999.999" then goto 140
160 for i = 0 to length-1
170 wavelength(i) = start+i : input #1,intensity(i)
180 print #2,wavelength(i),intensity(i)
190 a$ = str$(wavelength(i))+" "+str$(intensity(i))
200 next i
210 close #1 : close #2
220 print : print "File Conversion Finished!" : print
230 end
240 call "beep",1 : print : print "That file does not
exist." : print : goto 60
```

Filename: multi-convert.bas

This program is based on fileconvert.bas but can automatically convert numerous sequentially numbered files at once.

```
50 cls : print : print "Quick Multi-Spectrum Converter by
Michael E. Stora." : print
100 print "This program converts sequentialy numbered
Spectrum ASCII files into two columns of tab-delimited
text"
200 input "Enter the file name prefix of the file you
wish to convert (###.txt): ",filename$
210 input "Enter the number of the first file in the
series: ",low%
220 input "Enter the number of the last file in the
series: ",high%
230 for file = low% to high%
250 print : print "Converted filename will be:
";filename$+str$(file)+"-c.txt"
```

```
300 open filename$+str$(file)+".txt" for input as #1 :
open filename$+str$(file)+"-c.txt" for output as #2
400 input #1,a$
500 input #1,dummy$ : input #1,a$ : start = val(a$)
600 input #1,dummy$ : input #1,a$ : length = val(a$)
650 dim wavelength(length-1) : dim intensity(length-1)
700 input #1,dummy$ : input #1,a$
800 if a$ <> "-999.999" then goto 700
900 for i = 0 to length-1
1000 wavelength(i) = start+i : input #1,dummy$ : input
#1,a$ : intensity(i) = val(a$)
1050 print #2,str$(wavelength(i)),str$(intensity(i))
1055 a$ = str$(wavelength(i))+" "+str$(intensity(i))
1100 next i
1200 close #1 : close #2
1250 next file
1300 print : print "File Conversions Finished!" : print
1400 end
```

Filename: calibrate.bas

This program, along with a tab-delimited text data file (calfile.txt) implements the PL spectrum calibrations described in Appendix B. The file calfile.txt contains the calibration data for radiometric, quantum, and photopic units with and without the UV long-pass filter. It would take approximately 30 pages to list this data here. Because the calibration is particular to the hardware used by the author, there is no point to do so.

```
10 print : print "Please wait.  Loading calibration data
. . .";
100 dim calibration(1000,6)
200 open "calfile.txt" for input as #1
300 for i = 300 to 1000
350 input #1,a$
400 for j = 0 to 6
500 calibration(i,j) = val(field$(a$,j+1,chr$(9)))
600 next j
700 next i
800 close #1
900 print "  Done."
1000 print : print "This program will apply the
calibration factors to a spectrum for the various"
```

```
1010 print "gratings, units of measure, and filter."
1020 print : input "Please enter the filename (-c.txt
assumed) or Q to quit: ",filein$
1025 if filein$ = "q" or filein$ = "Q" then bye
1030 fileout$ = filein$+"-c(" : filein$ = filein$+"-
c.txt"
1040 print "The output file will be named:
";fileout$;"xxx).txt"
1050 print : print "Please enter the conditions of the
measurement:" : print
1060 print "Visable or UV grating (V,U)? Default is
Visable: "; : get grating$
1070 if grating$ = "U" or grating$ = "u" then grating = 1
: goto 2000
1080 if grating$ = chr$(13) or grating$ = "V" or grating$
= "v" then grating = 2 : goto 2000
1090 print chr$(7);"That entry is invalid!" : print :
goto 1060
2000 print
2005 print : print "Was the 350 nm filter used (F,Y/N)?
Default is Filter: "; : get filter$
2010 if filter$ = "Y" or filter$ = "y" or filter$ = "F"
or filter$ = "f" then filter = 1 : goto 2500
2015 if filter$ = chr$(13) then filter = 1 : goto 2500
2020 if filter$ = "N" or filter$ = "n" then filter = 0 :
goto 2500
2030 print chr$(7);"That entry is invalid!" : goto 2005
2500 print
2505 print : print "Would you like the coversion done in
Radiometric, Quantum, or Photopic units?"
2510 print "Default is Radiometric: "; : get units$
2520 if units$ = chr$(13) or units$ = "R" or units$ = "r"
then units = 1 : goto 2600
2530 if units$ = "Q" or units$ = "q" then units = 2 :
goto 2600
2540 if units$ = "P" or units$ = "p" then units = 3 :
goto 2600
2550 print chr$(7);"That entry is invalid!" : goto 2505
2600 print : print : print "Conversion begining . . . ";
2610 calcol = grating*3+units-3
2620 if grating = 1 then suf$ = "U"
2630 if grating = 2 then suf$ = "V"
2640 if filter = 0 then suf$ = suf$+"N"
2650 if filter = 1 then suf$ = suf$+"F"
2660 if units = 1 then suf$ = suf$+"R).txt"
2670 if units = 2 then suf$ = suf$+"Q).txt"
```

```
2680 if units = 3 then suf$ = suf$+"P).txt"
2690 fileout$ = fileout$+suf$
3000 open filein$ for input as #1
3100 open fileout$ for output as #2
3200 input #1,a$
3300 if a$ = "" then 4000
3400 wavelength = val(field$(a$,1,chr$(9)))
3500 intensity = val(field$(a$,2,chr$(9)))
3600 wave% = int(wavelength+0.5)
3700 calintensity =
intensity*calibration(wave%,calcol)*(calibration(wave%,0)
^(1-filter))
3800 print #2,str$(wavelength),str$(calintensity)
3900 goto 3200
4000 close #1 : close #2
4100 print "Done.";chr$(7)
4200 print : print "Filename was saved as: ";fileout$ :
goto 1020
```

Filename: multiply spectrum.bas

This program allows all the intensity data in a PL spectrum to be multiplied by an inputted constant.

```
100 input "Enter name of file to multiplied by a
constant: ";filein$
200  input "Enter the constant to multiply by: ";con
300 fileout$ = filein$+"-multiplied"
400 print "Output file will be named: ";fileout$
1000 open filein$ for input as #1 : open fileout$ for
output as #2
1200 input #1,a$
1300 if a$ = "" then goto 1700
1400 wavelength = val(field$(a$,1,chr$(9)))
1500 intensity = val(field$(a$,2,chr$(9)))
1550 print #2,str$(wavelength),str$(intensity*con)
1600 goto 1200
1700 close #1 : close #2
4500 print "Finshed!";chr$(7) : print
```

Filename: normalize.bas

This program automatically normalizes a PL spectrum file to a value of 1 for the largest intensity value.

```
100 dim wavelength(1000) : dim intensity(1000)
```

```
200 input "Enter name of file to normalized: ";filein$
300 fileout$ = filein$+"-normalized"
400 print "Output file will be named: ";fileout$
1000 open filein$ for input as #1
1100 i = 0 : max = 1.000000E-99
1200 input #1,a$
1300 if a$ = "" then goto 1700
1350 i = i+1
1400 wavelength(i) = val(field$(a$,1,chr$(9)))
1500 intensity(i) = val(field$(a$,2,chr$(9)))
1550 if intensity(i) > max then max = intensity(i)
1600 goto 1200
1700 close #1
1800 if i = 0 then print chr$(7) : print "Input file
contained no data. No output file was created." : print :
print : goto 100
4000 open fileout$ for output as #1
4100 for j = 1 to i
4200 print #1,str$(wavelength(j)),str$(intensity(j)/max)
4300 next j
4400 close #1
4500 print "Finshed!";chr$(7) : print
```

Filename: smooth.bas

This program performs a smoothing operation on the intensity data of a text data file by averaging the numerical value of each data point with its neighbors. The user selects the amount of smoothing to be done (how many adjacent values to average over). This program takes care to smooth the data points near the beginning and end of the file correctly, which accounts for most of its complexity.

```
100 dim wavelength(1000) : dim intensity(1000) : dim
smoothintensity(1000)
200 input "Enter name of file to smooth: ";filein$
300 fileout$ = filein$+"-smoothed"
400 print "Output file will be named: ";fileout$
500 print "Enter number of points about which to average
each point"
600 input "an odd integer 3 or larger: ",wide
700 wide = 2*int((abs(wide)-3)/2)+3
800 if wide < 3 then wide = 3
900 print "averaging over ";str$(wide);" points." : print
: print " starting...";""
```

```
1000 open filein$ for input as #1
1100 i = 0
1150 i = i+1
1200 input #1,a$
1300 if a$ = "" then goto 1700
1400 wavelength(i) = val(field$(a$,1,chr$(9)))
1500 intensity(i) = val(field$(a$,2,chr$(9)))
1600 goto 1150
1700 close #1
1750 top = i-1
1800 for j = 2 to top-1
1900 low = j-(wide-1)/2
2000 high = j+(wide-1)/2
2100 if low < 1 then low = 1 : high = 2*j-low
2200 if high > top then high = top : low = 2*j-high
3000 sum = 0
3100 for k = low to high
3200 sum = sum+intensity(k)
3300 next k
3400 smoothintensity(j) = sum/(high-low+1)
3500 next j
3600 smoothintensity(1) = intensity(1) :
smoothintensity(top) = intensity(top)
4000 open fileout$ for output as #1
4100 for l = 1 to top
4200 print
#1,str$(wavelength(l)),str$(smoothintensity(l))
4300 next l
4400 close #1
4500 print "Finshed!";chr$(7) : print
```

Filename: peak finder.bas

This program uses the same smoothing algorithm as smooth.bas to apply sequentially more course smoothing operations to the PL intensity data file to assist the user in locating peak wavelengths of PL bands in a systematic manner. The local maxima of the data are printed at each step and the user is given the option of saving the smoothed file as well as whether to continue to the next incremental smoothing operation.

```
10 dim wavelength(1000) : dim intensity(1000) : dim
smoothintensity(1000)
```

```
20 input "Enter name of file to analized for peaks:
";filein$
90 rem Read in file to wavelength and intensity arrays.
100 open filein$ for input as #1
110 i = 0
120 i = i+1
130 input #1,a$
140 if a$ = "" then goto 180
150 wavelength(i) = val(field$(a$,1,chr$(9)))
160 intensity(i) = val(field$(a$,2,chr$(9))) :
smoothintensity(i) = val(field$(a$,2,chr$(9)))
170 goto 120
180 close #1
190 top = i-1
200 wide = 1
300 print : print "Filename: ";filein$
310 if wide = 1 then print "--Unsmoothed--"
315 if wide > 1 then print "--Averaging over
";str$(wide);" points--"
320 print "Peaks at:","Intensity: "
330 gosub 3000
333 print : if wide = 1 then goto 340
335 print "Save (Y/N):" : get cont$ : if (cont$ = "Y" or
cont$ = "y") then gosub 4000
340 print "Continue (Y/N):" : get cont$ : if (cont$ <>
"Y" and cont$ <> "y") then end
350 wide = wide+2 : gosub 1000
360 goto 300
900 end
1000 for j = 2 to top-1
1100 low = j-(wide-1)/2
1200 high = j+(wide-1)/2
1300 if low < 1 then low = 1 : high = 2*j-low
1400 if high > top then high = top : low = 2*j-high
1500 sum = 0
1600 for k = low to high
1700 sum = sum+intensity(k)
1800 next k
1900 smoothintensity(j) = sum/(high-low+1)
2000 next j
2100 smoothintensity(1) = intensity(1) :
smoothintensity(top) = intensity(top)
2200 return
3000 rem Find and print peaks
3100 for l = 2 to top-1
```

```
3200 if ((smoothintensity(l) > smoothintensity(l-1)) and
(smoothintensity(l) > smoothintensity(l+1))) then print
wavelength(l),,smoothintensity(l)
3300 next l
3400 return
4000 fileout$ = filein$+"-smoothed"+str$(wide)
4100 open fileout$ for output as #1
4200 for m = 1 to top
4300 print
#1,str$(wavelength(m)),str$(smoothintensity(m))
4400 next m
4500 close #1
4600 return
```

Programs to Analyze TRPL Data Files

The programs in this section are highly specialized and deal specifically with data files produced by proprietary software included with Edinburgh Analytical Instruments multi-channel analyzers, which is protected by a dongle (a hardware copy-protection device). These programs were used to analyze the time-resolved PL data files for this study.

Filename: time-resolved file convert.bas

This program converts tab-delimited PC/DOS text data files in the Edinburgh Analytical Instruments format to tab delimited Mac text files with time and intensity in columns. It assumes that the data were gathered with a timebase of 89 ps per channel. It automatically detects and corrects for a file with the time order reversed.

```
10 dim time(1022) : dim counts(1022) : dim
tempcounts(1022)
20 input "Enter the name of the file to be converted
(.txt assumed) or return to quit: ";filein$
25 if filein$ = "" then bye
30 fileout$ = filein$+"-conv.txt"
40 filein$ = filein$+".txt"
100 open filein$ for input as #1
105 maxtime = 0 : maxcounts = 0 : maxi = 0
110 for i = 1 to 1022
```

```
120 input #1,a$ : input #1,b$
130 time(i) = int(val(field$(a$,1," "))*1000+0.5)/1000
140 counts(i) = val(field$(a$,2," "))
150 if counts(i) > maxcounts then maxi = i : maxcounts =
counts(maxi) : maxtime = time(maxi)
160 next i
165 close #1
170 if time(2)-time(1) = 0.089 then goto 200
180 print : print : print : print "WARNING:  PROBLEM WITH
TIME-BASE OR COLLUMN DATA.  CHECK FILE." : print : print
: print
200 if maxi < 511 then goto 400
210 print "File reversal nessasary"
220  for k = 1 to 1022
230 tempcounts(k) = counts(1023-k)
240 next k
250 for l = 1 to 1022
260 counts(l) = tempcounts(l)
270 next l
280 maxi = 1023-maxi
290 maxtime = time(maxi)
400 for j = 1 to 1022
410 time(j) = time(j)-maxtime
420 next j
500 open fileout$ for output as #1
510 for m = 1 to 1022
520 print #1,str$(time(m)),str$(counts(m))
530 next m
535 close #1
540 print "Done." : filein$ = "" : goto 20
```

Filename: timebase converter.bas

This program allows the user to change the timebase of the data file. It is useful if the wrong timebase was entered when the time-resolved PL was first measured.

```
10 dim time(1022) : dim counts(1022)
20 print "Timebase Converter" : input "Enter the name of
the file you wish to convert or return to quit: ";filein$
30 if filein$ = "" then bye
40 open filein$ for input as #1
100 for i = 1 to 1022
110 input #1,a$
120 time(i) = val(field$(a$,1,chr$(9)))
```

```
130 counts(i) = val(field$(a$,2,chr$(9)))
140 next i
150 close #1
200 timebase = time(501)-time(500) : print : print "The
time base of ";filein$;"is: ";timebase;" ns."
210 input "Enter the new timebase: ";newtimebase
220 input "Enter the name of the file with the new
timebase in ns (return to overwrite origional file):
";fileout$
230 if fileout$ = "" then fileout$ = filein$
300 open fileout$ for output as #1
310 for j = 1 to 1022
320 ntime =
int((time(j)/timebase*newtimebase)*1000+0.5)/1000
330 print #1,str$(ntime),str$(counts(j))
340 next j
350 close #1
400 print "Done." : print
500 goto 20
```

Filename: baseline finder and convert.bas

This program normalizes an 89 ps timebase file to the 5 ps timebase measurements of the same sample in order to deconvolute the time-resolved data and obtain exponential fits of the PL decay processes. A working knowledge of Edinburgh Analytical Instruments multi-channel analyzers and software is essential to understanding this program.

```
10 dim time(1022) : dim counts(1022)
20 input "Enter the name of the file to be analized or
return to quit: ";filein$
25 if filein$ = "" then bye
100 open filein$ for input as #1
105 maxcounts = 0 : maxi = 0
110 for i = 1 to 1022
120 input #1,a$
130 time(i) = val(field$(a$,1,chr$(9)))
140 counts(i) = val(field$(a$,2,chr$(9)))
150 if counts(i) > maxcounts then maxi = i : maxcounts =
counts(maxi)
160 next i
165 close #1
195 sum = 0
```

```
200 for j = 1 to maxi-2
210 sum = sum+counts(j)
220 next j
230 average = sum/(maxi-2)
240 print "Background is ";average;" counts."
300 input "Enter the total counts in the 5 ps file:
";primarycounts
310 input "Enter the Residual (A) of the curve fit of the
5 ps file: ";a
320 background = average/10
330 input "Enter the channel in which the peak occurs in
the 5 ps scan: ";peakchannel
340 timerange = (1023-peakchannel)*5.000000E-03
400 primaryresidual = timerange*200*(a-background)
410 primaryfast = primarycounts-primaryresidual
450 intersection = int((timerange/0.089)+maxi)
455 sum = 0
460 for l = intersection-5 to intersection+5
470 sum = sum+counts(l)
480 next l
490 interaverage = sum/11-average
500 for k = 1 to 1022
510 counts(k) = (counts(k)-average)*(a-
background)/interaverage*17.8
520 if counts(k) < 0 then counts(k) = 0
530 next k
600 m = intersection : sum = 0
605 if m = 1023 then goto 640
610 if counts(m) = 0 then goto 640
620 sum = sum+counts(m)
630 m = m+1 : goto 605
640 secondaryresidual = sum : totalresidual =
primaryresidual+secondaryresidual
650 total = primaryfast+totalresidual
660 percenttail = int(totalresidual/total*10000+0.5)/100
670 percentfast = 100-percenttail
700 report$ = "analysis of "+filein$
710 open report$ for output as #1
1000 print "Tail analysis of ";filein$
1005 print #1,"Tail analysis of ";filein$
1007 print
1008 print #1
1010 print "The 5 ps scan had ";primarycounts;"counts
over ";timerange;"ns."
1015 print #1,"The 5 ps scan had ";primarycounts;"counts
over ";timerange;"ns."
```

```
1020 print "The residual from the curve fit was
";a;"counts of which ";background;"counts are estimated
to be background."
1025 print #1,"The residual from the curve fit was
";a;"counts of which ";background;"counts are estimated
to be background."
1030 print "The residual is estimated to account for
";primaryresidual;"counts in the 5 ps scan."
1035 print #1,"The residual is estimated to account for
";primaryresidual;"counts in the 5 ps scan."
1040 print "The background was subtracted from the 89 ps
scan and the scan was normalized to ";a-
background;"counts at ";timerange;"ns."
1045 print #1,"The background was subtracted from the 89
ps scan and the scan was normalized to ";a-
background;"counts at ";timerange;"ns."
1050 print "The total counts from ";timerange;"ns to the
first zero value or the end of the scan were multiplied
by 17.8 to convert from 89 ps per channel to 5 ps per
channel."
1055 print #1,"The total counts from ";timerange;"ns to
the first zero value or the end of the scan were
multiplied by 17.8 to convert from 89 ps per channel to 5
ps per channel."
1060 print "These counts totaled
";secondaryresidual;"counts."
1065 print #1,"These counts totaled
";secondaryresidual;"counts."
1067 print
1068 print #1
1070 print "The total 'tail' counts were
";totalresidual;"or ";percenttail;"percent of the
photons."
1075 print #1,"The total 'tail' counts were
";totalresidual;"or ";percenttail;"percent of the
photons."
1080 print "The total 'fast' counts were:
";primaryfast;"or ";percentfast;"percent of the photons."
1085 print #1,"The total 'fast' counts were:
";primaryfast;"or ";percentfast;"percent of the photons."
1100 close #1
```

REFERENCES

Aug95 Augustine, B. H., Hu, Y. Z., Irene, E. A., and McNeal, L. E., *Appl. Phys. Lett.* **67**(25), 3694 (1995).

Aug96 Augustin, A., Master's Thesis Technische Universität München, München (1996).

Aus85 Austin, I. G., Jackson, W. A., Searle, T. M., Bhat, P. K., and Gibson, R. A., *Philos. Mag. B* **52**, 271 (1985).

Bag95 Bagratashvili, V. N., Tsypina, S. I., Radtsig, V. A., Rybaltovskii, A. O., Chernov, P. V., Alimpiev, S. S., and Simanovskii, Y. O., *J. of Non-Cryst. Solids* **180**, 221 (1995).

Ber76 Bergh, A. A. and Dean, P. J., Light-emitting Diodes, Chap. 1, Clarendon Press, Oxford (1976).

Bim97 Bimberg, D., Ledentsov, N. N., Grundmann, M., Heitz, R., Böhrer, J., Ustinov, V. M., Kop'ev, P. S., and Alferov, Zh. I., *J. of Luminescence* **72-74**, 34 (1997).

Bla94 Blasse, B. C., and Grabmaier, B. C., Luminescent Materials, Chap. 4, Springer, Berlin (1994).

Blu74 Blundau, W., Onton, A, and Heinke, W., *J. Appl. Phys.* **45**, 1846 (1974).

Bru86 Brus, L. E., *J. Phys. Chem. Solids* **90**, 2555 (1986).

Bru94 Brus, L. E., *J. Phys. Chem.* **98**, 3537 (1994).

Bub60 Bube, R., Photoconductivity of Solids, Chap. 3, Wiley and Sons, New York (1960).

Byl78 Bylander, E. G., *J. Appl. Phys.* **49**, 1188 (1978).

Cal94 Calcott, P. D. J., Nash, K. J., Canham, L. T., and Kane, M. J., *Mat. Res. Soc. Symp. Proc.* **358**, 465 (1994).

Cam86 Campbell, I. H., and Fauchet, P. M., *Solid St. Commun.* **58**, 739 (1986).

Can90 Canham, L. T., *Appl. Phys. Lett.* **57**, 1046 (1990).

Cha94 Chang, S.-S., Doctoral Dissertation, University of Florida, Gainesville, FL (1993).

Cha00a Chang, S.-S., and Hummel, R. E., *J. Luminescence* **86**, 33 (2000).

Cha00b Chang, S.-S., Stora, M. E., and Hummel, R. E., *J. of Phys.: Condensed Matter* (in press).

Col80 Collins, R. W., Paesler, M. A., and Paul, W., *Solid State Commun.* **34**, 833 (1980).

Dea70 Dean, P. J., *J. of Luminescence* **1,2**, 398 (1970).

Del93 Delly, B. and Steigmeier, E. F., *Phys. Rev. B* **47**(3), 1397 (1993).

Dev54 De Vos, J. C., *Physica* **20**, 690 (1954).

Ebi97 Ebihara, K., Matsushita, S., Koshihara, S., Minami, F., Miyazawa, T., Obata, K., and Kira, M., *J. of Luminescence* **72-74**, 43 (1997).

Edw82 Edwards, A. H. and Fowler, W. B., *Phys. Rev. B* **26**(12), 6649 (1982).

Fau69 Faulkner, R. A., *Phys. Rev.* **184**, 713 (1969).

Fil98 Filonov, A. B., Kholod, A. N., and Borisenko, V. E., *Phys. Stat. Sol. (a)* **165**, 57 (1998).

Fow68 Fowler, W. B., Physics of Color Centers, Academic Press, New York (1968).

Fow86 Fowler, W. B., in Structure and Bonding in Noncrystalline Solids, G. E. Walrafen and A. G. Revesz, Eds., Plenum Press, New York (1986).

Fra97 Frame, J. W., Wheeler, D. J., DeTemple, T. A., and Eden, J. G., *Appl. Phys. Lett.* **71**(9), 1165 (1997).

Fri85 Friebele, E. J., Griscom, D. L., and Marrone, M. J., *J. of Non Cryst. Sol.* **71**, 133 (1985).

Fuc93 Fuchs, H. D., Stutzmann, M., Brandt, M. S., Rosenbauer, M., Weber, J., Breitschwerdt, A., Deák, P., and Cardona, M., *Phys. Rev. B* **48**, 8172 (1993).

Gee79 Gee, C. M., and Kastner, M., *Phys. Rev. Lett.* **42**(26), 1765 (1979).

Gib61 Gibbs, J. E. and Gordon-Smith, G. W., *Brit. J. of Applied Physics* **12**, 257 (1961).

Got98 Gotza, M., Dutoit, M., and Ilegems, M., *J. Vac. Sci. Technol. B* **16**(2), 582 (1998).

Gri91 Griscom, D. L., *The Centenial Memorial Issue of The Ceramic Society of Japan* **99**(10), 923 (1991).

Gro71 Groves, W. O., Herzog, A. H., and Craford, M. G., *Appl. Phys. Lett.* **19**(6), 184 (1971).

Hac97 Hack, J., Ludwig, M. H., Geertz, W., and Hummel, R. E., *Mat. Res. Soc. Symp. Proc.* **45**, 147 (1997).

Hau89 Haung, H. and Banyai, L, Eds., Optical Switching in Low-Dimensional Systems, Plenum Press with NATO Scientific Affairs Division, New York (1989).

Hay84 Hayes, W., Kane, M. J., Salminen, O., Wood, R. L., and Doherty, S. P., *J. Phys. C: Solid State Phys.* **17**, 2943 (1984).

Hen62 Henisch, H. K., Electroluminescence, Chap. 2, Pergamon Press, New York (1962).

Hsu95 Hsu, M. S., Meyers, M. A., and Berkowitz, A., *Scripta Metallurgica et Materialia* **32**(6), 805 (1995).

Hum92 Hummel, R. E., and Chang, S.-S., *Appl. Phys. Lett.* **61**, 1965 (1992).

Hum93 Hummel, R. E., Morrone, A., Ludwig, M. H., and Chang, S.-S., *Appl. Phys. Lett.* **63**, 2771 (1993).

Hum95a Hummel, R. E., Ludwig, M. H., and Chang, S.-S., *Sol. State Commun.* **93**, 237 (1995).

Hum95b Hummel, R. E., Ludwig, M. H., Chang, S.-S., and LaTorre, G., *Thin Solid Films* **255**, 219 (1995)

Hum95c Hummel, R. E., Ludwig, M. H., Hack, J., and Chang, *S.-S., Sol. State Commun.* **96**, 683 (1995.)

Hum98 Hummel, R. E., Shepherd, N., Ludwig, M. H., and Stora, M. E., *Thin Solid Films* **325**, 1 (1998).

Hum00 Hummel, R. E., Stora, M. E., Shepherd, N., Yu, S., and Fajardo, F., *J. Porous Materials* **7**, 131 (2000).

Hum01 Hummel, R. E., Silicon-Based Materials and Devices, H. S. Nalwa, Ed., Academic Press, Burlington, Mass (in press).

Hyb94 Hybersten, M. S., *Phys. Rev. Lett.* **72**, 1514 (1994).

Ima88 Imai, H., Arai, K., and Imagawa, H., *Phys. Rev. B* **38**(17), 12772 (1988).

Ito88 Itoh, C., Tanimura, K., and Itoh, N., *J. Phys. C: Solid State Phys.* **21**, 4693 (1988).

Ito89 Itoh, N., Tanimura, K., and Itoh, C., *Proc. of the Fifth Int. School on Condensed Matter Physics: Disordered Systems and New Materials*, Varna Bulgaria, Sept. 19-27, 1988, 564, M. Borissov, N. Kirov, and A. Vavrek, Eds., World Scientific, Singapore (1989).

Ive66 Ivey, H. F., *IEEE J. of Quantum Electronics* **QE-2**(11), 713 (1966).

Joe76 Jones, C. E. and Embree, D., *J. of Appl. Phys.* **47**, 5365 (1976).

Kay88 Kayanuma, Y., *Phys. Rev. B* **38**, 9797 (1988).

Ken96 Kenyon, A. J., Trwoga, P. F., Pitt, C. W., and Rehm, G.. *J. Appl. Phys.* **79**(12), 9291 (1996).

Khu96 Khurgin, J. B., Forsythe, E. W., Tompa, G. S., and Khan, B. A., *Appl. Phys. Lett.* **69**(9), 1241 (1996).

Kur97 Kurmaev, E. Z., Shamin, S. N., Galakhov, V. R., Sokolov, V. I., Ludwig, M. H., and Hummel, R. E., *J. of Physics: Condensed Matter* **9**, 2671 (1997).

Koc93 Koch, F., Petrova-Koch, V., and Muschik, T., *J. of Luminescence* **57**, 271 (1993).

Koh89 Kohketsu, M., Awazu, K., Kawazoe, H., and Yamane, M., *Jap. J. of Appl. Phys.* **28**, 615 (1989).

Kov94 Kovalev, D. I., Yaroshetzkii, I. D., Muschik, T., Petrova-Koch, and F. Koch, *Appl. Phys. Lett.* **64**, 214 (1994).

Koz93 Kozlowski, F., Steiner, P., Sauter, M., and Lang, W., *Journal of Luminescence* **57**, 185 (1993).

Kur97 Kurmaev, E. Z., Shamin, S. N., Galakhov, V. R., Sokolov, V. I., Ludwig. M. H., and Hummel, R. E., *J. of Physics: Condensed Matter* **9**, 2671 (1997).

Lar59 Larrabee, R. D., *J. of the Optical Soc. of America* **49**(4), 619 (1959).

Lev68 Levi, L., Applied Optics: A Guide to Optical System Design/Volume 1, Wiley & Sons, New York (1968).

Lin97 Linnros, J., Galeckas, A., Lalic, N., and Grivickas, V., *Thin Solid Films* **297**(1-2), 167 (1997).

Liu92 Liu, M., Kitai, A. H., and Mascher, P., *J. of Luminescence* **54**, 35 (1992).

Lor68 Lorentz, M. R., Reuter, W., Dumke, W. P., Chicotka, R. J., Pettit, G. D., Hilsum, C, and Porteus, P., *Proc. Int. Conf. on the Physics of Semiconductors*, Moscow, 1968 **2**, 1214, Nauka, Leningrad (1968).

Luc95 Lucovsky, G., Santos-Filho, P., Lu, Z., Jing, Z., and Whitten, J. L., *Non-Cryst. Solids*, **190**, 169 (1995).

Lud94 Ludwig, M. H., Hummel, R. E., and Chang, S.-S., *J. Vac Sci. Technol. B* **12**, 3023 (1994).

Lud95a Ludwig, M. H., Menniger, J., and Hummel, R. E., *J. of Physics: Condensed Matter* **7**, 9081 (1995).

Lud95b Ludwig, M. H., Hummel, R. E., and Stora, M. E., *Thin Solid Films* **255**, 103 (1995).

Lud96a Ludwig, M. H., *Critical Reviews in Solid State and Materials Sciences,* **21**(4), 265 (1996).

Lud96b Ludwig, M. H., Augustin, A., Hummel, R. E., and Gross, T., *J. Appl. Phys.* **80**, 8318 (1996).

Lud97 Ludwig, M. H., in Handbook of Optical Properties Volume II: Optics of Small Particles, Interfaces, and Surfaces, 103, R. E. Hummel and P. Wißmann, Eds., CRC Press, Boca Raton, FL (1997).

May90 Mayer, J. and Lau, S. S., Electronic Materials Science: For Integrated Circuits in Si and GaAs, Chap. 9, Macmillan, New York (1990).

Min96 Min, K. S., Shcheglov, C. M., Atwater, H. A., Brongersma, M. L., and Polman, A., *Appl. Phys. Lett.* **68**(18), 2511 (1996).

Möl88 Möller, K. D., Optics, University Science Books, Mill Valley, California (1988).

Mot75 Mott, N., F., Davis, E. A., and Street, R. A., *Philosophical Magazine* **32**(5), 961 (1975).

Mot77 Mott, N. F. and Stoneham, A. M., *J. Phys. C: Solid State Phys.* **10**, 3391 (1977).

Mus93 Muschik, T., Dissertation Technische Universität München, München (1993).

Nis92 Nishikawa, H., Shiroyama, T., Nakamura, R., Ohki, Y., Nagasawa, K., and Hama, Y., *Phys. Rev. B* **45**, 586 (1992).

Oha90 Ohanian, H.C., Principles of Quantum Mechanics, Chap. 3, Prentice-Hall, Englewood Cliffs, NJ (1990).

Oka97 Okamoto, S. and Kanemitsu, Y., *J. of* Luminescence **72-74**, 380 (1997).

Ook92 Ookubo, N., Ono, H., Ochiai, Y., Mochizuki, Y., and Matsui, S., *Appl. Phys. Lett.* **61**, 940 (1992).

Ort97 Ortiz, A., Falcony, C., Hernandez, J., Garcia, A. M., Alonso, *J. C.*, *Thin Solid Films* **293**, 103 (1997).

Pea88 Pearce, C. W., in VLSI Technology 2nd Ed., Chap. 1, S. M. Sze, Ed., McGraw-Hill, New York (1988).

Per92 Perry, C. H., Feng, L., Namavar, F., Kalkhoran, N. M., and Soref, R. A., *Appl. Phys. Lett.* **60**, 3117 (1992).

Pio90 Pio, F., Guzzi, M., Spinolo. G., and Martini, M., *Phys. Stat. Sol. B* **159**, 577 (1990).

Pou97 Poumellec, B., Taunay, T., Bernage, P., Cortes, R., and Krupa, J. C., *J. of Luminescence* **72-74**, 442 (1997).

Pre63 Preston, J. S., *Brit. J. of Applied Physics* **14**, 43 (1963).

Pro93 Prokes, S., *Appl. Phys. Lett.* **62**, 3244 (1993).

Pro94 Prokes, S. M., Carlos, W. E., and Glembocki, O. J., *Phys. Rev. B* **50**, 17093 (1994).

Pro95 Prosanov, I. Y., and Politov, A. A., *Inorg. Mater.* **31**, 663 (1995).

Rob85 Robertson, J., *Philosophical Magazine B* **52**(3), 371 (1985).

Ros93 Rosenbauer, M., Stutzmann, M., Fuchs, H. D., Finkbeiner, S., and Weber, J., *J. of Luminescence* **57**, 153 (1993).

Rup97 Rupp, S., Quilty, J., Trodahl, H. J., Ludwig, M. H., and Hummel, R. E., *Appl. Phys. Lett.* **70**(6), 723 (1997).

Rut94 Ruter, D., Kunze, T., and Bauhofer, W., *Appl. Phys. Lett.* **64**, 3006 (1994).

San92 Sanders, G. D., and Chang, Y. C., *Phys. Rev. B* **45**, 9202 (1992).

Shi94 Shimizo-Iwayama, T., Fujita, K., Nakao, S., Saitoh, K., Fujita, T., and Itoh, N., *J. Appl. Phys.* **75**(12), 7779 (1994).

Sil80 Silin, A. R., Skuja, L. N., Trukhin, A. N., *J. of Non-Cryst. Solids* **38 & 39**, 195 (1980).

Sku78 Skuja, L. N., Silin, A. R., and Mares, *J. Phys. Stat. Sol.* **50**, 149 (1978).

Sku84 Skuja, L. N., Streletsky, A. N., and Pakovich, A. B., *Solid State Commun.* **50**, 1069 (1984).

Sku92 Skuja, L. N., *Solid State Commun.* **84**, 613 (1992).

Sta84 Stathis, J. H. and Kastner, M. A., *Phys. Rev. B* **29**(12), 7079 (1984).

Sta87 Stathis, J. H. and Kastner, M. A., *Phys. Rev. B* **35**, 2972 (1987).

Stj97 St. John, J. V., Coffer, J. L., Rho, Y. G., Diehl, P., Pinizzotto, R. F., Culp, T. D., and Bray, K. L., *Chem. Mater.* **9**, 3176 (1997).

Sto00 Stora. M. E. and Hummel, R. E., *Proc. of the Third Annual Coherent Spectroscopy and Ultrafast Conference*, Orlando, FL, January 2000 (in press).

Stu64 Studer, F. J. and VanBeers, R. F., *J. of the Optical Soc. of America* **54**(7), 945 (1964).

Sui92 Sui, A., Leong, P. P., and Herman, I. P., *Appl. Phys. Lett.* **60**, 2086 (1992).

Sze81 Sze, S. M., *Physics of Semiconductor Devices* 2nd Ed., John Wiley & Sons, New York (1981).

Tak92 Takagahara. T. and Takeda, K., *Phys. Rev. B* **46**(23), 15578 (1992).

Tam94 Tamura, H., Rückschloss, Wirschen, T., and Veprek, S., *Appl. Phys. Lett.* **65**, 1537 (1994).

Tan85 Tanaka, T., Eshita, T., Tanimura, K., and Itoh, N., *Cryst. Latt. Def. and Amorph. Mat.* **11**, 221 (1985).

Tani83 Tanimura, K., Tanaka, T., and Itoh, N., *Phys. Rev. Lett.* **51**(5), 423 (1983).

Tani88 Tanimura, K., Itoh, C., and Itoh, N., *J. Phys. C: Solid State Phys.* **21**, 1869 (1988).

Tho65 Thomas, D. G., Hopfield, J. J., and Frosch, C. J., *Phys. Rev. Lett.* **15**, 857 (1965).

Thu75 Thurmond. C. D., *J Electrochem. Soc.* **122**, 1133 (1975).

Toh89a Tohmon, R., Mizumo, H., Ohki, Y., Sasagane, K., Nagasawa, K., and Hama, Y., *Phys. Rev. B* **39**(2), 1337 (1989).

Toh89b Tohmon, R., Shimogaichi, Y., Mizuno, H., Ohki, Y., Nagasawa, K., and Hama, Y., *Phys. Rev. Lett.* **62**, 1388 (1989).

Toh89c Tohmon, R., Shimogaichi, Y., Munekuni, S., Ohki, Y., Hama, Y., and Nagasamwa, K., *Appl. Phys. Lett.* **54**, 1650 (1989).

Tsu92 Tsu, R., Shen, H., and Dutta, M., *Appl. Phys. Lett.* **60**, 112 (1992).

Tsy94 Tsybeskov, L., Vandshev, J., and Fauchet, P. M., *Phys. Rev.* **B 49**, 7821 (1994).

Tur58 Turner, D. R., *J. Electrochem. Soc.* **105**, 402 (1958).

Uhl56 Uhlir, A., *Bell Syst. Tech. J.* **35**, 333 (1956).

Van96 Vanheusden, K., Seager, C. H., Warren, W. L., Tallant, D. R., and Voight, J. A., *Appl. Phys. Lett.* **68**, 403 (1996).

Vep97 Veprek, S., Wirschem, T., Dian, J., Perna, S., Merica, R., Veprek-Heijman, M. G. J., Heinecke, R., and Perina, V., *Thin Solid Films* **297**, 171 (1997).

Wak95 Wakita, K., Makimuri, S., and Nakayama, Y., *Jpn. J. Appl. Phys.* **34**, 1425 (1995).

Wil89 Wilson, J. and Hawkes, J. F. B., Optoelectronics: An Introduction, 2nd Ed., Chap. 4, Prentice Hall, New York (1989).

Wu_95 Wu, X. L., Yan, F., Zhang, M.-S., and Feng, D., *Physics Letters A* **205**, 117 (1995).

Wu_98 Wu, X. L., Siu, G. G., Tong, S., Gu, Y., Liu, X. N., Bao, X. M., Jiang, S. S., and Feng, D., *Phys. Rev. B* **57**(16), 9945 (1998).

Xu_96 Xu, J., Zhang, J., Ding, W., Yang, W., Cheng, G., Du, Y., Zao, J., Xu, C., Zhang, Y., and Du, Z., *Solid State Commun.* **99**, 987 (1996).

Yip98 Yip, R. Y.-F., Desjardins, P., Isnard, L., Aït-Quali, A., Bensaasa, A., Marchand, H., Brebner, J. L., Currie, J. F., and Masut, R. A., *J. Vac. Sci. Technol. A* **16**(2), 801 (1998).

Yua95 Yuan, J. and Haneman, D., *Appl. Phys. Lett.* **67**, 3328 (1995).

Zha97 Zhang, J. H., Lee, T. C., Lau, W. S., and Ai, X., *J. of Materials Processing Tech.* **68**, 83 (1997).

Zhe92 Zheng, X. L., Wang, W., and Chen, H. C., *Appl. Phys. Lett.* **60**, 986 (1992).

BIOGRAPHICAL SKETCH

The author was born October 3, 1970, in Teaneck, New Jersey, and spent most of his childhood in Midland, Michigan. He attended Redwood High School in Larkspur, California, graduating with honors in 1988. He attended the University of California at Davis completing the integrated studies freshman honors program as well as the honors math and chemistry curricula. He competed twice in the Putnam Invitational Math Exam and published technical literature as an undergraduate. He graduated in 1993 with a Bachelor of Science degree in applied physics with a concentration in materials science. He studied materials science and engineering with a specialization in electronic materials at the University of Florida and received a Master of Science degree in 1998. He has authored or co-authored seven technical papers with more pending. He has presented research at three technical conferences, winning a grand prize at the 2000 Joint Symposium of the American Vacuum Society and the Florida Society of Microscopy, a grand prize at the 2000 Coherent Spectroscopy and Ultrafast Conference, and third place at the 1995 Symposium of the Florida Chapter of the American Vacuum Society. He enjoys membership in several professional organizations including the American Institute of Physics, the American Society of Materials, the American Vacuum Society, the Minerals, Metals & Materials Society, and the Order of the Engineer. He has accepted a senior engineering position with Intel in Phoenix, Arizona.

I certify that I have read this study and that in my opinion it conforms to acceptable standards of scholarly presentation and is fully adequate, in scope and quality, as a dissertation for the degree of Doctor of Philosophy.

R. E. Hummel

Rolf E. Hummel, Chairman
Professor of Materials Science and
Engineering

I certify that I have read this study and that in my opinion it conforms to acceptable standards of scholarly presentation and is fully adequate, in scope and quality, as a dissertation for the degree of Doctor of Philosophy.

Robert T. DeHoff

Robert T. DeHoff
Professor of Materials Science and
Engineering

I certify that I have read this study and that in my opinion it conforms to acceptable standards of scholarly presentation and is fully adequate, in scope and quality, as a dissertation for the degree of Doctor of Philosophy.

Paul H Holloway

Paul H. Holloway
Distinguished Professor of Materials
Science and Engineering

I certify that I have read this study and that in my opinion it conforms to acceptable standards of scholarly presentation and is fully adequate, in scope and quality, as a dissertation for the degree of Doctor of Philosophy.

Wolfgang M. Sigmund
Assistant Professor of Materials
Science and Engineering

I certify that I have read this study and that in my opinion it conforms to acceptable standards of scholarly presentation and is fully adequate, in scope and quality, as a dissertation for the degree of Doctor of Philosophy.

RSrivastava

Ramakant Srivastava
Professor of Electrical and Computer
Engineering

This dissertation was submitted to the Graduate Faculty of the College of Engineering and to the Graduate School and was accepted as a partial fulfillment of the requirements for the degree of Doctor of Philosophy.

December, 2000

M. J. Ohanian
Interim Dean, College of
Engineering

Winfred M. Phillips
Dean, Graduate School

UNIVERSITY OF FLORIDA
3 1262 08555 1793

LD
1780
20 00
S883